A CENSUS OF DIVERSE ENVIRONMENTS IN STAR FORMING REGIONS: WHERE DO MASSIVE STARS FORM?

William Joseph Dirienzo
Franklin, WI

B.S., University of Wisconsin-Madison, 2008

M.S., University of Virginia, 2010

A Dissertation Presented to the Graduate
Faculty of the University of Virginia
in Candidacy for the Degree of
Doctor of Philosophy

Department of Astronomy

University of Virginia
August 12, 2014

Rémy Indebetouw

Crystal L. Brogan

Zhi-Yun Li

Eric Herbst

Abstract

Massive stars have profound effects on the interstellar medium that lead to chemical and dynamical evolution of the gas. This contributes to galaxy evolution and may also trigger new star formation. The physical conditions of massive star forming environments, and thus the formation mechanism, have been historically less well understood than their lower mass counterparts. This work discusses investigations into massive star formation, primarily in two different phases of the evolution of massive star forming regions.

First, we analyzed the environments of H II regions powered by massive stars for evidence of newly triggered star formation. Triggering may be an important mechanism through which massive star formation propagates through a cloud, contributing to the observed clustering of massive stars. We investigated six H II regions with infrared, bright rimmed bubble or cometary morphology, in search of quantitative evidence for triggered star formation, both "collect and collapse" (CnC) and "radiatively driven implosion" (RDI). We identified and classified 458 Young Stellar Objects (YSOs) in and around the H II regions. YSOs were determined by fitting a collection of radiative transfer model spectral energy distributions (SEDs) to infrared photometry for a large sample of point sources. We determined areas where there exist enhanced populations of relatively unevolved YSOs on the bright rims of these regions, suggesting that star formation has been triggered there. We further investigated the physical properties of the regions by using radio continuum emission as a proxy for ionizing flux powering the H II regions, and ^{13}CO J=1-0 observations to measure masses and gravitational stability of molecular clumps. We used an analytical model of CnC triggered star formation, as well as a simulation of RDI, and compare the observed properties of the molecular gas with those predicted in the triggering scenarios. Notably, those regions in our sample with cometary, or "blister,"

morphology are more likely to show evidence of triggering.

Second, we focused on Infrared Dark Clouds (IRDCs). IRDCs harbor the earliest phases of massive star formation, and many of the compact cores in IRDCs, traced by millimeter continuum or by molecular emission in high critical density lines, host massive protostars. We used the Robert C. Byrd Green Bank Telescope (GBT) and the Very Large Array (VLA) to map NH_3 and CCS in nine IRDCs to reveal the temperature, density, and velocity structures and explore chemical evolution in the dense ($> 10^{22}$ cm^{-2}) gas. Ammonia is an ideal molecular tracer for these cold, dense environments. The internal structure and kinematics of the IRDCs include velocity gradients, filaments, and possibly colliding sub-clouds that elucidate the formation process of these structures and their protostars. We find a wide variety of substructure including filaments and globules at distinct velocities, sometimes overlapping at sites of ongoing star formation. It appears that these IRDCs are still being assembled from molecular gas clumps even as star formation has already begun, and at least three of the IRDCs in our sample appear consistent with morphology of the "hub-filament structure" discussed in the literature. Furthermore, we find that these clumps are typically near equipartition between gravitational and kinetic energies, so these structures may survive for multiple free-fall times. We also have Combined Array for Research in Millimeter-wave Astronomy (CARMA) observations of dense gas tracers in a large IRDC with diverse physical conditions and star formation content. These data, preliminary analysis, and plans for future work are presented here.

Acknowledgements

I want to first and foremost thank my advisors, Rémy Indebetouw and Crystal Brogan. Their guidance, understanding, and support made the completion of this thesis possible. They taught me a great deal and always pushed me to achieve more. They have also spent countless hours reading drafts of papers and proposals and offered detailed comments that dramatically improved anything I had written. I also appreciate their concern for my future career and their efforts to have me work on tractable and interesting projects.

I want to thank my collaborators, Claudia Cyganowski, Ed Churchwell, Rachel Friesen, Claire Chandler, and Katie Devine for their helpful comments on paper drafts, as well. Claudia's comments were particularly plentiful, but thoughtful and probably saved me from a much longer referee process. Rachel generously provided GBT observing and reduction scripts and her IDL ammonia spectral line fitting program that gave me a head start on my own observations and fitting routine. Katy and Claire also observed and calibrated the VLA data in this thesis, and Katie observed some of the GBT data as well. I owe a great debt of gratitude to Rémy, Crystal, Zhi-Yun Li, and Ed Murphy for writing strong letters of recommendation for my job applications so that I have a job following graduation.

I also wish to thank Ed for serving as my advisor for the Tomorrow's Professor Today program, as well as the staff and volunteers at the Teaching Resource Center. When working on research was difficult or stressful, being involved with education and public outreach have helped me keep my sanity and remind me why I cared enough about astronomy to continue working on this thesis. Ed has been a very knowledgeable mentor, and I have learned a copious amount of pedagogy and education research from the TRC that has made me a much stronger educator and was a significant factor in being hired at my new job. The Physics Peer Mentor Tutor

program at UW-Madison takes credit for introducing me to this path and giving me a long-term vision for my career.

Amanda Kepley, Megan Johnson, Jay Lockman, and the rest of the GBT staff offered exceedingly valuable help with my GBT observations. Jim Braatz, Joe Masters, and Dana Balser were equally helpful with the GBT data reduction. The CARMA 2011 summer school staff taught me the basics of how to observe and reduce interferometric data and inspired me to submit my own CARMA proposal.

I could not have completed this work without the Jefferson Scholars Foundation. In addition to paying for most of my graduate education, I have had unique opportunities to meet students from other disciplines, work on conferences and journals, and attend amazing dinners. I made friends with people I never would have otherwise met, and grew personally and professionally in ways that I could not have imagined when I began. Thanks to Rachael Beaton for coaching me on my selection weekend presentation, and to the foundation staff, especially Karen Tapscott, for their tireless work.

Finally, I want to thank my parents, mostly for their support in various forms, but also for taking me to Kennedy Space Center as a three-year-old. That initiated my interest in space, which they encouraged throughout my childhood.

This thesis is dedicated to Tony Dirienzo, Tom Dirienzo, and Rose St. Louis.

This work is based (in part) on observations made with the *Spitzer Space Telescope*, which is operated by the Jet Propulsion Laboratory, California Institute of Technology under a contract with NASA. Support for this work was provided by NASA through an award issued by JPL/Caltech. Claudia J .Cyganowski is supported by an NSF Astronomy and Astrophysics Postdoctoral Fellowship under award AST-1003134. This publication makes use of data products from the Two Micron All Sky

Survey, which is a joint project of the University of Massachusetts and the Infrared Processing and Analysis Center/California Institute of Technology, funded by the National Aeronautics and Space Administration and the National Science Foundation. This publication makes use of molecular line data from the Boston University-FCRAO Galactic Ring Survey (GRS). The GRS is a joint project of Boston University and Five College Radio Astronomy Observatory, funded by the National Science Foundation under grants AST-9800334, AST-0098562, & AST-0100793. This research has made use of NASA's Astrophysics Data System Bibliographic Services. This research has made use of the SIMBAD database, operated at CDS, Strasbourg, France. This research has made use of SAOImage DS9, developed by Smithsonian Astrophysical Observatory. The National Radio Astronomy Observatory is a facility of the National Science Foundation operated under cooperative agreement by Associated Universities, Inc. This work was funded in part by the Jefferson Scholars Foundation at the University of Virginia. This work was funded in part by the Virginia Space Grant Consortium.

Table of contents

List of Figures

List of Tables

Chapter 1

Introduction

Star formation is among the most important processes in the universe, so a complete understanding is crucial to our comprehension of astronomy. Aside from directly creating new stars, the formation process also has a profound effect on its environment. Star formation involves a substantial reprocessing of gas in the interstellar medium and returns significant amounts of energy to its surroundings. Heating of the ambient gas, ionizing ultraviolet radiation, stellar winds, supernovae, and the creation of dust are some of the ways in which the youngest stars change the place where they are born. This drives evolution in the interstellar gas and, through the cumulative effect of many star-forming regions, the evolution of entire galaxies. Few aspects of astronomy are completely removed from the effects of star formation.

Massive star formation in particular provides strong feedback to the interstellar medium and is responsible for a significant fraction of the energy budget, thus greatly affecting the environment. Only massive stars are hot enough to produce ultraviolet (UV) radiation that ionizes the surrounding gas, or to end their lives in violent supernovae. Though massive stars are relatively short-lived and form in fewer numbers than low mass stars, they also produce the strongest effects on the shortest timescales. Often it is the UV radiation from these stars and the radio emission from the ionized gas that lead us to discover regions of star formation. Star forming regions, and massive ones in particular, have some of the most complex organic chemistry in the universe. The conditions in these environments are so extreme that even the best laboratory setting cannot replicate the physical parameters. Observational studies are thus crucial for informing theoretical chemical modeling. Given the relative importance of the most massive stars, it is unsettling and perhaps surprising that we do not have a satisfactory, comprehensive description of how they are born.

Several theoretical models and numerical simulations attempt to address these is-

sues and provide a plausible method of massive star formation. To test these models and provide constraints for future theoretical work, we need more (and better) observations of the earliest stages of massive star formation. The temperature and density structure, the kinematics (internal motions from accretion disks, jets, etc.), the magnetic fields, and the chemical composition of star-forming regions are all physical characteristics necessary to study this process.

1.1 Triggered Star Formation

While many of the details of isolated, low mass star formation are now understood, the precise process of massive star formation remains uncertain, mostly because of the additional difficulty of studying massive star forming regions. Most such regions are over 1 kpc away and their protostars are often observed through high extinction because the protostars evolve before the embedding envelope has dissipated (Zinnecker & Yorke 2007), which makes it difficult to identify and study these regions. Among the most important theoretical obstacles is the need for very high accretion rates to form a massive star in less time than it takes for radiation pressure, jets, outflows, stellar winds, etc. to halt formation.

High accretion rates may arise in the high-pressure environment hypothesized in triggered star formation scenarios. Originally termed "sequential star formation" by Elmegreen & Lada (1977), this theory posits that star formation, and massive star formation in particular, is self-propagating through molecular gas. If at least one massive star can be formed initially, then this star produces ionizing radiation that advances into the surrounding gas, creating an H II region. As the star continues to energize the region, the ionized gas expands and displaces the molecular gas, thus causing overdensities along the advancing boundary. If the expansion of the ionization

front is faster that the sound speed in the neutral gas, then the increase in pressure in these overdensities cannot be redistributed outward and the material continues to collect. Eventually this gas becomes so dense that it begins to fragment. These fragments will be compelled to collapse under self-gravity, and may form stars more quickly, and at preferentially higher mass, than quiescent, isolated star formation (see for example Motoyama & Yoshida 2003).

This triggering mechanism is typically termed "collect and collapse" (CnC; see Whitworth et al. 1994; Dale et al. 2007a), in contrast to other possible triggering processes, like 'radiatively driven implosion" (RDI; see for example Sandford et al. 1982). In the latter process, pre-existing overdensities in the molecular gas are enhanced when an ionization front sweeps away the less dense gas and begins to compress the overdensities from all sides, inducing collapse (Henney et al. 2009). While this can enhance the local density of Young Stellar Objects (YSOs), it may not necessarily lead to more massive stars, depending on the properties of the pre-existing overdensities. Bisbas et al. (2011) modeled RDI and determined a range of values of the ionizing flux for which star formation is triggered (10^{48} s^{-1} to 3×10^{50} s^{-1} for a 5 pc radius region, roughly a B0 or earlier type star), as well as a power law relationship between the ionizing flux and the timescale for collapse.

The theory of CnC makes quantitative predictions that can be tested observationally. The ages of triggered YSOs, as well as the masses, sizes, and densities of molecular cloud fragments in the spherically expanding shell, can be predicted from the flux of ionizing radiation powering the H II region and the initial density and sound speed of the molecular gas (Whitworth et al. 1994). Observationally, the initial density may be estimated from ^{13}CO (1-0) in these clouds as a tracer of the total molecular gas, and the ionizing flux can be determined from the properties of the

existing massive stars or from radio observations that trace the amount of ionized gas and thus the ionizing flux. It is important to test these predictions because the presence of YSOs and molecular gas clumps around a bubble, while suggestive, is not enough evidence alone to show that CnC triggering is taking place. For instance, simulations by Walch et al. (2011) show that this morphology may be replicated by the expansion of an ionization front into fractal molecular clouds, even when no stable, self-gravitating shell fragments have formed. Star formation may additionally be triggered by RDI in this scenario.

The available predictions that are readily applied to observations assume a simple spherically symmetric geometry. This type of study is best performed in relatively isolated, simple H II regions with dense rims, and the predictions will be best applied to regions that are round, closed bubbles. However, it is important to cover a range of morphologies and apparent evolutionary states to keep the sample unbiased, as few H II regions exhibit this ideal morphology.

Churchwell et al. (2006) cataloged 322 visually identified partial and complete mid-infrared (MIR) rings in the Galactic Legacy Infrared Mid-Plane Survey Extraordinaire (GLIMPSE). They found that these structures were ubiquitous (about 1.5 per square degree), 88% of them were less than 4' across, about 25% of them were coincident with H II regions known at the time, and 13% enclosed known star clusters. They proposed that these structures were in fact three-dimensional bubbles containing gas ionized by OB stars and surrounded by a photodissociation region (PDR). Churchwell et al. (2007) found an additional 269 bubbles, and more recent studies such as Simpson et al. (2012) have confirmed that these structures are common across the galactic plane. Since this type of structure is consistent with theoretical models of triggered star formation, recent studies of triggering have frequently drawn samples from this

catalog.

Previous observational searches for evidence of triggered star formation around Churchwell et al. (2006) bubbles have been conducted with varied results. Watson et al. (2008) studied three apparently wind-blown, parsec-sized mid-infrared bubbles, including N49, studied in this work. They identified central ionizing sources, as well as YSO populations around the rims, and determined all 3 regions to be possible sites of triggering. Watson et al. (2010) looked for YSOs around 46 infrared bubbles, but reported that only 20% of their sample showed a significant population of associated YSOs; however they did not use photometry at wavelengths longward of 8 μm, which is useful in identifying and classifying YSOs. Results from this work indicate that more than half of the YSO population in these environments are missed when 24 μm photometry is not used (see 2.2.2). Deharveng et al. (2010) investigated 102 bubbles, extending to the submillimeter wavelengths using the ATLASGAL survey at 870 μm to probe the cold dust, while also analyzing radio continuum and the YSO populations. They found that 86% of the bubbles enclosed H II regions, and 20% showed evidence of massive star formation on their rims. Thompson et al. (2012) analyzed the distribution of massive YSOs (MYSOs) seen by the *Midcourse Space Experiment* (MSX) from the Red MSX Source (RMS) survey compared to the locations of all 322 Churchwell et al. (2006) bubbles. They reported a statistically significant overdensity of MYSOs coincident with the bubbles, and the rims in particular, which was not explained by intrinsic clustering of MYSOs. They estimated that 14-30% of MYSOs in the Milky Way may be formed by triggering in bubbles, though they did not find any evidence that MYSOs associated with bubbles had higher luminosity (mass) than field MYSOs.

While the aforementioned studies have concentrated on the Churchwell et al.

(2006) bubbles, several studies have investigated regions not in that catalog as well, often with results consistent with triggering scenarios. Paron et al. (2011) studied the single H II region G35.673-00.847, a region with "semi-ring" mid-infrared morphology and two distinct but neighboring PDRs. They identified YSOs in the immediate vicinity of the region using infrared colors and then classified them using spectral energy distribution (SED) fitting. Using the same methods of testing CnC and most of the same datasets as this work, they rejected it as a plausible scenario for that region. Snider et al. (2009) identified YSOs in NGC 2467 using infrared colors (then confirmed by SED fitting) and found that they were largely located where the ionization front had compressed the molecular gas. They estimated that 25-50% of the YSOs in that region were triggered, though they ruled out RDI as the mechanism. Pomarès et al. (2009) found several YSOs on the boundary of RCW 82, but determined that the region was too young to have triggered star formation.

Koenig et al. (2008) analyzed the W5 H II region, which has two cometary regions in the same complex. YSOs within W5 were identified and classified using infrared colors and multiple clusters were seen. They found that both RDI and CnC were plausible scenarios in this region. Zavagno et al. (2006) studied RCW 79, a fairly isolated H II region with somewhat cometary morphology, and found several massive fragments identified by millimeter continuum in a shell around the ionized gas. Additionally, the locations of several Class I YSOs identified by infrared color selection coincident with these fragments are consistent with triggering by CnC. Deharveng et al. (2008) studied Sh2-212, a round, isolated H II region. They found fragments of molecular gas arranged in a shell around the region, with strong evidence for a massive YSO coincident with the most massive fragment. Studies of other individual H II regions with similar promising results have appeared in Zavagno et al. (2007,

2010a,b). The existing literature suggests that CnC is a viable star formation mechanism, but its relative importance and under which physical conditions it operates are still undetermined.

Several other studies searched for evidence of RDI in similar regions, and we summarize only a few here. Chen & Huang (2010) analyzed the Cepheus B molecular cloud and claimed it was a good RDI candidate because of its morphology, the presence of an age gradient in young stars leading back to the ionizing source, and the temperature, density, and velocity structure of the molecular gas around its bright rim. Urquhart et al. (2007) conducted a detailed study of the region BRC SFO 75 in millimeter continuum, ^{13}CO, and NH_3 emission. They identified two dense cores; one was being influenced by ionizing radiation while the other was still beyond the ionization front. They reported three YSOs near the core under the influence of the ionizing radiation, while the other core appears nearly spherical and devoid of stars. Morgan et al. (2010) observed the NH_3 (1,1), (2,2), (3,3), and (4,4) transitions towards 42 bright-rimmed regions under the influence of an ionizing source. Using previously published submillimeter continuum and CO data, as well as locations of known outflows and masers, they identified many of the regions with active star formation as likely sites of triggering. The NH_3 data showed that these regions have higher velocity dispersions than the counterparts that were not triggering candidates. They proposed that the higher velocity dispersions were an indication either that shock fronts induced star formation in these regions, or that they were a result of increased star formation activity. These studies have shown that RDI is also a viable mechanism for triggering star formation, though again its global importance is not known.

Dale et al. (2007b) performed SPH simulations of a molecular cloud with and

without a central ionizing source. They compared the cores that formed in each scenario and found that the star formation efficiency was approximately 30% higher when including the ionizing source. This increase in efficiency was due to both an acceleration in the formation time of cores that would have formed in the simulation without an ionizing source, as well as the formation of additional, apparently triggered cores. However, they did not see a significant change in the final mass distribution of the cores, indicating that the positive and negative feedback were of nearly equal importance, nor did they see an age gradient with position. Furthermore, the velocity of the cores primarily reflected the initial turbulent conditions rather than the velocity of the expanding shell. These simulations are consistent with an increase in star formation due to triggering, but show that it can be quite difficult to gather convincing observational evidence of this process.

Our investigation into triggering is presented in Chapter 2.

1.2 Infrared Dark Clouds

Infrared Dark Clouds (IRDCs) are dense ($> 10^5$ cm^{-3}) and cold (< 20 K) collections of dust and molecular gas, typically arranged in filamentary and/or globular structures with compact cores. IRDCs were first observed as regions of high extinction in silhouette against the galactic background infrared emission by the *Infrared Astronomical Satellite* (*IRAS*) (Wood et al. 1994), the *Midcourse Space Experiment* (*MSX*) (Egan et al. 1998; Carey et al. 1998), and the *Infrared Space Observatory* (*ISO*) (Hennebelle et al. 2001). The ability to identify and study these objects has been greatly improved by the *Spitzer Space Telescope*, and in particular surveys with two of its instruments: the Infrared Array Camera (IRAC) (Fazio et al. 2004) and Multiband Imaging Photometer for *Spitzer* (MIPS) (Rieke et al. 2004).

The Galactic Legacy Infrared Mid-Plane Survey Extraordinaire (GLIMPSE) (Benjamin et al. 2003; Churchwell et al. 2009) covered the region $|b| \leq 1^\circ$ and $10^\circ \leq |\ell| \leq 65^\circ$ in all the IRAC bands (3.6, 4.5, 5.8, and 8.0 μm) with $1\farcs5$ to $1\farcs9$ resolution, while the MIPS Galactic Plane Survey (MIPSGAL) (Carey et al. 2009) was a complementary survey in the 24 and 70 μm MIPS wavebands with $6''$ and $18''$ resolution, respectively. These surveys observed much of the galactic plane, imaged the structure of IRDCs at higher resolution than before, and revealed embedded protostars, typically 1 to 10 per IRDC. An extensive catalog of *Spitzer* IRDCs is given by Peretto & Fuller (2009), of which 80% were previously not identified from *MSX* images. Furthermore, Jackson et al. (2006) matched several hundred IRDCs to molecular clouds seen in ^{13}CO J=1-0 by the Boston University Galactic Ring Survey (BU-GRS), and thus determined velocities, kinematic distances, and physical properties of the population of clouds.

IRDCs are an active subject of study because they are nurseries of massive star formation and contain complex chemistry. It is now widely speculated that objects like these (whether or not they are in a position that allows them to be seen as IRDCs against background emission) contain the earliest stages of the formation of massive stars. Many IRDCs are seen in absorption even at wavelengths longer than 10 μm. These darkest clouds have very high column densities, as high as approximately 10^{24}-10^{25} cm^{-2}. The terms "core" and "clump" are frequently used in the literature, but the meanings are not standardized. We use the term "core" to refer to an unresolved or marginally resolved overdense structure <0.1 pc across and tens of solar masses. We then use the term "clump" to refer to a discrete structure in position-position-velocity space within an IRDC, typically 0.1 to 1 pc in size and hundreds of solar masses. We use the term "subcloud" to refer to any velocity component within an

IRDC that is distinct from other velocity components (Devine et al. 2011), and so a subcloud may be one or more nearby clumps at similar velocity.

Recent studies have revealed massive ($\gtrsim$10 $M_{\odot}$) protostars (Rathborne et al. 2005; Pillai et al. 2006b; Beuther & Steinacker 2007; Wang et al. 2008) and massive (10-1000 $M_{\odot}$) cores in IRDCs (Henning et al. 2010; Rathborne et al. 2006, 2007; Swift 2009; Rathborne et al. 2011). High mass protostars are identified in these studies by the presence of masers (indicating accretion disks or outflows), radio continuum emission (from ionized gas), or fitting spectral energy distributions (SEDs) consistent with massive protostars across mid-infrared and submillimeter wavelengths. Kim et al. (2010) found that about 13% of IRDC cores have protostars identified by their infrared or maser emission.

Rathborne et al. (2006) used the Institut de Radioastronomic Millimétrique (IRAM) telescope to make 11″ resolution 1.2 mm dust continuum maps of 38 IRDCs to investigate the structure and clumps of IRDCs traced by dust emission. They found that these clumps had similar masses, sizes, and densities as hot ($>$ 50 K) clumps with massive protostars, but were much colder (15-30 K), implying that the clumps were indeed an early evolutionary phase of massive star formation if the clumps subsequently collapsed. The authors further suggested IRDCs may be precursors to star clusters, as they have masses comparable to young clusters and contain several compact clumps. Finally, they also asserted that better resolution was needed to distinguish better individual cores and investigate fragmentation.

Other studies have begun to reveal the basic properties of IRDCs in more detail. Carey et al. (2000) observed 11 IRDCs at 850 and 450 μm continuum with the Submillimeter Common-User Bolometer Array (SCUBA) on the James Clerk Maxwell Telescope (JCMT) at 14″ and 8″ resolution, respectively. That study revealed clumps

with temperatures around 15 K, densities around 10^6 cm^{-3}, and masses of tens to about a thousand $M_\odot$ (the "cores" in their study were more like clumps by our definition because of the single-dish resolution).

Jackson et al. (2008) observed 316 IRDCs in CS (2−1) with the Australia Telescope National Facility (ATNF) Mopra Telescope with a single pointing at the darkest part of each cloud. They saw that 14% of the sample had two velocity components along the line of sight, which they interpreted as distinct IRDCs. Vasyunina et al. (2011) performed a single-dish study of 15 IRDCs using several dense gas tracers with the Mopra telescope, revealing the kinematics of the cores consistent with infall and outflows indicative of star formation. However, the study suffered from the 33″ limiting resolution of the 22 meter single-dish and thus results likely included the effects of including several cores along the line of sight. The authors noted that additional homogenous studies at better angular resolution were needed to make good statistical statements and to make analysis more clear.

Pillai et al. (2006a) performed Effelsberg 100 m observations of the NH_3 (1,1) and (2,2) transitions in 9 IRDCs to investigate the physical properties at 40″ and 0.2 km s^{-1} resolution. They found the morphology traced by NH_3 was in good agreement with infrared extinction and millimeter emission. They also found that temperatures of clumps were less than 20 K, and that there were many clumps in virial equilibrium with over 100 $M_\odot$ each (again, the clumps in their study were more like clumps by our definition because of the single-dish resolution). Velocity structures across the clouds they studied had widths of 1-3 km s^{-1}. It was found that temperatures and linewidths were lower in IRDCs with high NH_3 column than in high mass protostars and ultracompact H II regions. Two objects were found to have mid-infrared (MIR) peaks coincident with NH_3 peaks, indicating protostars. They observed clumps with

linewidths of about 1.7 km s^{-1}, sizes of about 0.57 pc, and masses of about 492 $M_{\odot}$.

Not all dense cores in IRDCs are obviously star forming, which raises the question: "Are these cores going to form stars and are just too young, or is there something fundamentally different about these cores preventing star formation?" To answer this question, we must know about the physical properties of both starless and star formation clumps in IRDCs. Disentangling the substructure of IRDCs is incredibly important to determining their formation and how it relates to subsequent star formation. Early studies of filamentary dark clouds with low spatial and velocity resolution appear to show that such structures are quasi-stable, i.e. approximately in pressure equilibrium with their environment and their lifetimes are long compared to the free-fall time (see for example Alves et al. 1998; Lada et al. 1999). Higher resolution studies show that IRDCs typically have complex substructure, spatially and kinematically. Some studies observe distinct subclouds within IRDCs, which themselves have slightly offset velocities from each other and may be colliding, and further suggest that the protostars are preferentially forming at the boundaries of these gas clumps (Sanhueza et al. 2013). Other studies observe collections of filaments with coherent velocity gradients consistent with gas flowing towards the most massive cores, perhaps guided by magnetic fields (Peretto et al. 2014). Myers (2009) and Li et al. (2013) described a "hub-filament structure", in which gas flows along filaments to a central hub where star formation is ongoing.

Ammonia is an ideal probe of the molecular gas in IRDCs. It is a relatively abundant species, typically about 10^{-9} to 10^{-7} fractional abundance relative to molecular hydrogen (Ragan et al. 2011; Chira et al. 2013). Unlike carbon-bearing species that are prone to freezing onto dust grains in these cold environments, NH_3 stays in the gas phase for a significant time. The ratio of the (1,1) to (2,2) line strengths leads

to a rotation temperature that has been shown to be a good tracer of the kinetic temperature of the gas to at least 30 K, within the typical range for IRDCs. Furthermore, the critical density of NH_3 is about 10^4 cm^{-3}, well matched to the gas being studied (Tafalla et al. 2002). Ammonia has hyperfine structure, allowing determination of the optical depth in the NH_3 lines by comparing the observed hyperfine component strengths to those set by molecular physics (Ho & Townes 1983). The direct measurement of the temperature and optical depth allows for an unambiguous determination of the column density, perfect for environments in which the column can vary significantly from optically thin to optically thick in the same cloud.

Devine et al. (2011) observed the NH_3 (1,1) and (2,2) and the CCS (2_1-1_0) transitions toward G19.30+0.07, and measured temperatures around 15-20 K, NH_3 column densities around 10^{15}-10^{16} cm^{-2}, and linewidths of about 2 km s^{-1}. They also observed that NH_3 and CCS generally had spatial distributions that were anticorrelated. Furthermore, they found that G19.30+0.07 was composed of four distinct clumps in three distinct velocity components. These clumps had masses of tens to hundreds of solar masses and were virially unstable against self-gravitating collapse. This complex substructure has also been investigated in other star forming regions with physical properties similar to IRDCs. Hacar et al. (2013) additionally found that molecular filaments in the Taurus molecular cloud, a lower mass star forming region, could be deconvolved into a hierarchy of several sub-filaments at distinct velocities leading to core formation. Rosolowsky et al. (2008) also saw multiple velocity components in NH_3 towards dense cores in the Perseus molecular cloud at 0.04 pc, 0.024 km s^{-1} resolution. These individual components often had such narrow linewidths ($\sim$0.1-0.3 km s^{-1}) that turbulence was unlikely to contribute significantly to slowing collapse. Lu et al. (2014) studied 62 high-mass star-forming regions with Very Large Array

(VLA) observations of the NH_3 (1,1) and (2,2) transitions. They found that parsec scale filaments were ubiquitous and often contained regularly spaced dense cores. Furthermore, they suggested that the filaments could be supported by turbulence and found that the dense cores were near virial equilibrium. Whether this also true of the more massive environment of IRDCs is not clear.

The combination of total power from single-dish observations along with the high resolution of an interferometer is critical for revealing the structure of filamentary clouds, such as IRDCs. For example, Pineda et al. (2010) identified a dense, coherent structure within the Perseus Molecular Cloud using GBT observations of the NH_3 (1,1) transition. The structure showed a dramatic increase in velocity dispersion going from the structure to the ambient gas. The GBT data had sufficient velocity resolution to identify this feature, however they did not have the spatial resolution to confirm a sharp transition in density of the gas. Pineda et al. (2011) followed with a combination of GBT and VLA data that identified dense structure that was significantly smaller than the GBT beam. These GBT observations of Perseus at about 250 pc had approximately 0.04 pc resolution, comparable to the resolution we achieve in this study with the VLA observations of IRDCs at several kpc distances.

Ragan et al. (2011, 2012) performed a study of NH_3 (1,1) and (2,2) with the Robert C. Byrd Green Bank Telescope (GBT) and the Very Large Array (VLA) in six IRDCs at $3\farcs7$-$8\farcs3$ and 0.6 km s^{-1} resolution. They found that the majority of the gas had kinetic temperatures 8-13 K, indicating that protostellar heating was not significant for most of the cloud. Furthermore, they found that velocity fields were generally coherent across the clouds, with local ($\sim$0.1 pc) disruptions of a few km s^{-1} coincident with sites of local star formation. They argued that neither turbulence nor thermal pressure were sufficient to support the IRDCs and that the observed velocity

structures were a result of ongoing collapse, fragmentation, and protostellar feedback.

Ragan et al. (2013) further investigated the differences in filamentary and globular IRDCs and their hierarchical structure. They studied 11 IRDCs, covering a range of morphology and star formation activity, with *Herschel* and the Submillimetre APEX Bolometer Camera (SABOCA) instrument on the Atacama Pathfinder Experiment (APEX) 12 m telescope at 350 μm, resolving structure down to $\sim$0.1 pc. They performed a dendrogram analysis on the APEX data found that filamentary IRDCs tended to be more massive and have more hierarchical structure than clumpy IRDCs. This suggests that IRDCs may be divided into two relatively distinct morphological families. Ragan et al. (2014) identified 7 Giant Molecular Filaments (GMFs) in which the molecular gas extend for $\sim$100 pc including IRDCs, infrared bright structures, and more diffuse gas this presumably enveloping these denser regions. The existence and structure of GMFs suggests that hierarchical structure may extend to even these large size scales.

Our study of IRDCs is presented primarily in Chapter 3, with some additional preliminary work in Chapter 4.

Chapter 2

Testing Triggered Star Formation in Six H II Regions

2.1 Introduction

The aim of this work is to study multiple isolated H II regions with varied morphologies in a homogeneous way to analyze triggered star formation in H II regions and determine whether the H II region morphology has any effect. Additionally, we use SED fitting to identify and classify YSOs not only in the immediate vicinity of the infrared bubbles and rims, but also in the surrounding field to quantify any enhancement in the YSO surface density. The benefit of SED fitting over infrared color selection is the improved ability to estimate the mass and other physical parameters of the YSOs.

We have adopted a sample of six previously identified H II regions that are relatively isolated and have simple morphologies, but range from round, closed bubbles to rims of so-called cometary, or "blister," H II regions. Israel (1978) developed the term "blister model" to describe cometary H II regions and asserted that most optically visible H II regions were in fact cometary. The sample is comprised of G028.83-0.25, G041.10-0.15, G041.91-0.12, G041.92+0.04, G044.28+0.11, and G044.34-0.82. Mid-infrared images of these regions are presented in Figure 2.1, and coordinates are given in Table 2.1. Churchwell et al. (2006) previously identified four of these regions, G028.83-0.25, G041.92+0.04, G044.28+0.11, and G044.34-0.82, as N49, N80, N91, and N92, respectively. They argue that nearly all of the bubbles of this type that they identified were formed by hot, young stars.

The determination of the distances to the regions in our sample is presented in §2.2.1. An overview of the infrared data and the YSO selection and categorization process is given in §2.2.2. The radio continuum images and its relationship to the ionizing sources powering these regions is discussed in §2.2.3. The analysis of molecular gas data is in §2.2.4. Tests of triggered star formation are discussed in §2.3.1. Results

Table 2.1: H II Region Sample

Regions	N#[a]	RA (J2000) hh:mm:ss.s	Dec (J2000) dd:mm:ss	Principle Morphology	$v_{\rm rad}$ (km s^{-1})	Distance (kpc)[b] Near	Far
G028.83-0.25	N49	18:44:44.3	-03:45:34	Bubble	90.6[c]	5.07	9.65
G041.10-0.15	···	19:06:48.9	07:10:55	Cometary	59.4[c]	3.99	8.67
G041.91-0.12	···	19:08:21.1	07:55:20	Cometary	18.1[d]	1.4	11.1
G041.92+0.04	N80	19:07:51.2	08:00:33	Bubble	17.7[e]	1.32	11.18
G044.28+0.11	N91	19:11:57.7	10:07:05	Cometary	59.6[c]	4.33	7.7
G044.34-0.82	N92	19:15:28.1	09:44:24	Cometary	62.0[e]	4.59	7.43

[a]Identifier in Churchwell et al. (2006).

[b]Using the galactic rotation curve of Reid et al. (2009)

[c]Radio recombination line velocity from Lockman (1989)

[d]Radio recombination line velocity from Lockman et al. (1996)

[e]JCMT CO J=3-2 velocity from Beaumont & Williams (2010)

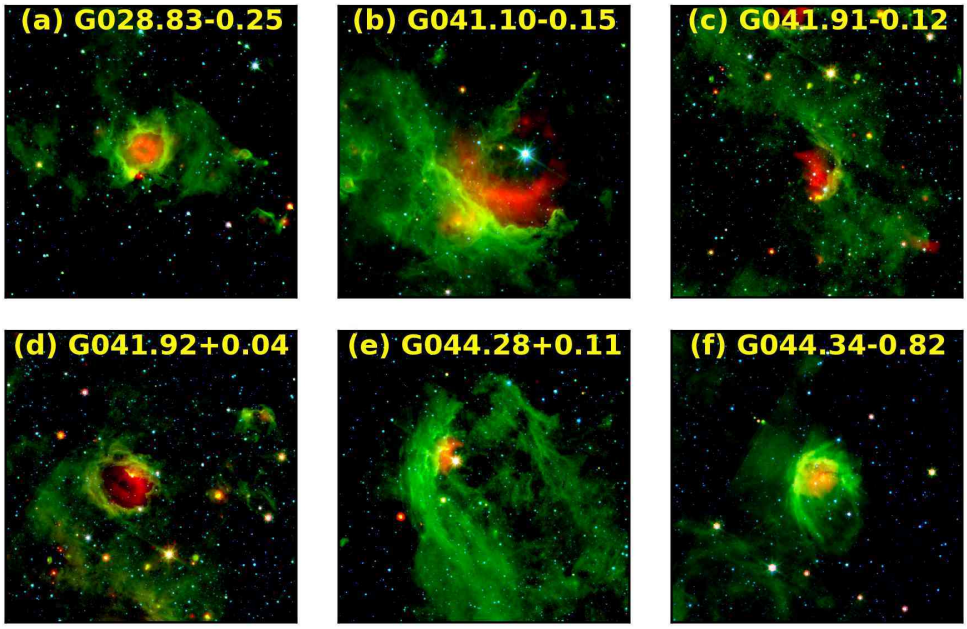

Fig. 2.1.— H II regions in our sample as seen by *Spitzer*, presented on a uniform angular scale 18′ across. Red is 24 μm, green is 8 μm, and blue is 3.6 μm. The strong 24 μm emission located within the bubbles is likely from heated dust grains within the H II regions, while the 8 μm emission along the rims of the bubbles is likely from PAHs. PAHs are destroyed within the H II regions, but on the edges are excited by the radiation leaking out of the region.

for each region are given in §2.3.2. Finally, a discussion of the evidence for triggering is presented in §2.4. The work in this chapter has appeared in the Astronomical Journal, Volume 144, Issue 6, article id. 173, 26 pp. (2012) under the title "Testing Triggered Star Formation in Six H II Regions" following advising and suggestions from the coauthors Rémy Indebetouw, Crystal Brogan, Claudia J. Cyganowski, Edward B. Churchwell, and Rachel K. Friesen.

2.2 Methodology and Analysis

2.2.1 Distance Determination

Many of our quantitative results depend on the distance to the H II regions. We calculated the kinematic distances using the galactic rotation curve of Reid et al. (2009). They adopted a galactocentric radius $R_\circ = 8.4 \pm 0.6$ kpc and a circular rotation speed $\Theta_\circ = 254 \pm 16$ km s^{-1} kpc^{-1}, based on the results of their measured trigonometric parallaxes of massive star-forming regions. Radio recombination line velocities are known for four of our regions from Anderson & Bania (2009): G028.83-0.25 at 90.6 km s^{-1}, G041.10-0.15 at 59.4 km s^{-1}, G041.91-0.12 at 18.1 km s^{-1}, and G044.34-0.82 at 59.6 km s^{-1}. All four of these regions have significant molecular gas emission at similar velocities. CO (3-2) velocities for G041.92+0.04 and G044.34-0.82 are known to be 17.7 km s^{-1} and 62.0 km s^{-1}, respectively, from Beaumont & Williams (2010).

All of the regions in our sample lie in the $|\ell| < 90°$ regime, so there is naturally a near-far distance ambiguity. Anderson & Bania (2009) attempted to resolve this ambiguity for 291 H II regions, including G028.83-0.25, G041.10-0.15, G041.91-0.12, and G044.28+0.11 (named C28.82-0.23, C41.10-0.21, D41.91-0.12, and U44.26+0.10

in their work, respectively). They did this by analyzing H I spectra using two different methods.

The first method is based on the features in the H I spectra due to absorption against the H II radio continuum by foreground H I clouds. Anderson & Bania (2009) searched for evidence of this absorption process by looking at the difference in spectra along the line of sight towards H II regions and towards nearby off-source positions. It is expected that all regions will show a difference in the H I emission and absorption features between the on and off source positions at velocities less than the radio recombination line velocity, but regions at the far distance will also show differences in these features between the recombination line velocity and the tangent point velocity.

The second method relies on the cold H I gas within the molecular clouds associated with the H II regions to absorb some of the emission from the warmer background H I. Narrow H I absorption at a velocity coincident with the velocity of ^{13}CO J=1-0 emission associated with the H II region indicates a source is at the near distance, while the absence of narrow H I absorption at the ^{13}CO J=1-0 velocity indicates the source is at the far distance.

Anderson & Bania (2009) used H I data from the Very Large Array (VLA) Galactic Plane Survey (VGPS) (Stil et al. 2006) and the ^{13}CO J=1-0 Boston University Galactic Ring Survey (BU-GRS) data (Jackson et al. 2006). The VGPS was a survey of the 21 cm H I line and 21 cm continuum, combining interferometric data from the VLA with single dish data from the Robert C. Byrd Green Bank Telescope (GBT). The data have angular resolution of $1'$, velocity resolution of 1.56 km s^{-1}, and 2 K root mean square (RMS) sensitivity. The BU-GRS is a large scale survey of the 110.2 GHz ^{13}CO J=1-0 transition in the disk of the Milky Way using the Five College

Radio Astronomy Observatory (FCRAO) 14 m single dish telescope. The publicly available data cubes have velocity resolution of 0.2 km s^{-1}, angular resolution of 46″, and typical antenna temperature RMS sensitivity of 0.13 K (Jackson et al. 2006).

The results of Anderson & Bania (2009) are summarized for the regions in our sample as follows. They find that G028.83-0.25 is likely at the near distance, G041.10-0.15 is likely at the far distance, G041.91-0.12 may be at the far distance, though with low confidence, and G044.28+0.11 is likely at the far distance. We also analyzed all six of our regions using the same methods and data. A detailed analysis of the spectra shows that the data remain at least consistent with the near distance for our sources. In particular, we note that the molecular gas associated with G041.10-0.15 shows a velocity gradient that should be considered when applying the H I self-absorption method. We thus assume the near kinematic distance for all of our sources for the remainder of this chapter. The resulting distances are presented in Table 2.1.

In the event that any of the regions lie at the far kinematic distance, the biggest effect will be that our bolometric luminosity estimates for the YSOs will be too low. For four of our sources, this effect would cause us to underestimate the bolometric luminosities by approximately a factor of four, since the far distances are about twice the near distances. The other two regions, G041.91-0.12 and G041.92+0.04, have a difference of about a factor of 8 between the near and far distances, and it is unlikely that the YSOs in these regions would be 64 times as bright as our current estimates. Our tests of triggered star formation (see §2.3.1) depend on the distance as well, though fairly insensitively. Our selection of YSOs is relatively insensitive to the distance, since the shapes of the SEDs will not be significantly changed. The longest wavelengths are the most important in the SED for identifying YSOs, and are also the least sensitive to a change in extinction associated with a change in distance.

2.2.2 Infrared Data and YSO Identification

The *Spitzer Space Telescope* has been revolutionary in collecting data of use for star formation studies. The Infrared Array Camera (IRAC) (Fazio et al. 2004) and Multiband Imaging Photometer for *Spitzer* (MIPS) (Rieke et al. 2004) instruments, together with the ground-based Two Micron All-Sky Survey (2MASS) (Skrutskie et al. 2006), provide the wide wavelength coverage important for reliable identification and classification of YSOs. The 2MASS Survey provides images at the near-infrared J (1.25 μm), H (1.65 μm), and K_s (2.16 μm) bands covering the entire sky. The Galactic Legacy Infrared Mid-Plane Survey Extraordinaire (GLIMPSE) (Benjamin et al. 2003; Churchwell et al. 2009) covers the region $|b| \leq 1^\circ$ and $10^\circ \leq |\ell| \leq 65^\circ$ in all the IRAC bands (3.6, 4.5, 5.8, and 8.0 μm) with $1\farcs5$ to $1\farcs9$ resolution, while the MIPS Galactic Plane Survey (MIPSGAL) (Carey et al. 2009) is a complementary survey in the 24 and 70 μm MIPS wavebands with $6''$ and $18''$ resolution, respectively. The GLIMPSE Point Source Catalog (GPSC) (Benjamin et al. 2003) is a publicly available, highly reliable catalog of automatedly identified point sources from the GLIMPSE survey. The catalog itself provides coordinates and flux density measurements from point spread function (PSF) fitting in each of the 2MASS and IRAC wavebands. Coordinates bounding the regions of the sky for which we used the GPSC and searched for YSOs are given in Table 2.2 and shown in Figure 2.2. We chose the regions to contain the entirety of the infrared bubbles and rims, as well as a significant area surrounding them for use as a control for comparisons of YSO spatial density.

In addition to the sources from the GPSC, we also identified point sources that were seen in IRAC 8 μm and/or MIPS 24 μm images but were missing from the catalog. The GPSC was finely tuned to have very high reliability in regions of complex diffuse emission, at the cost of the inevitable loss of some completeness. To improve

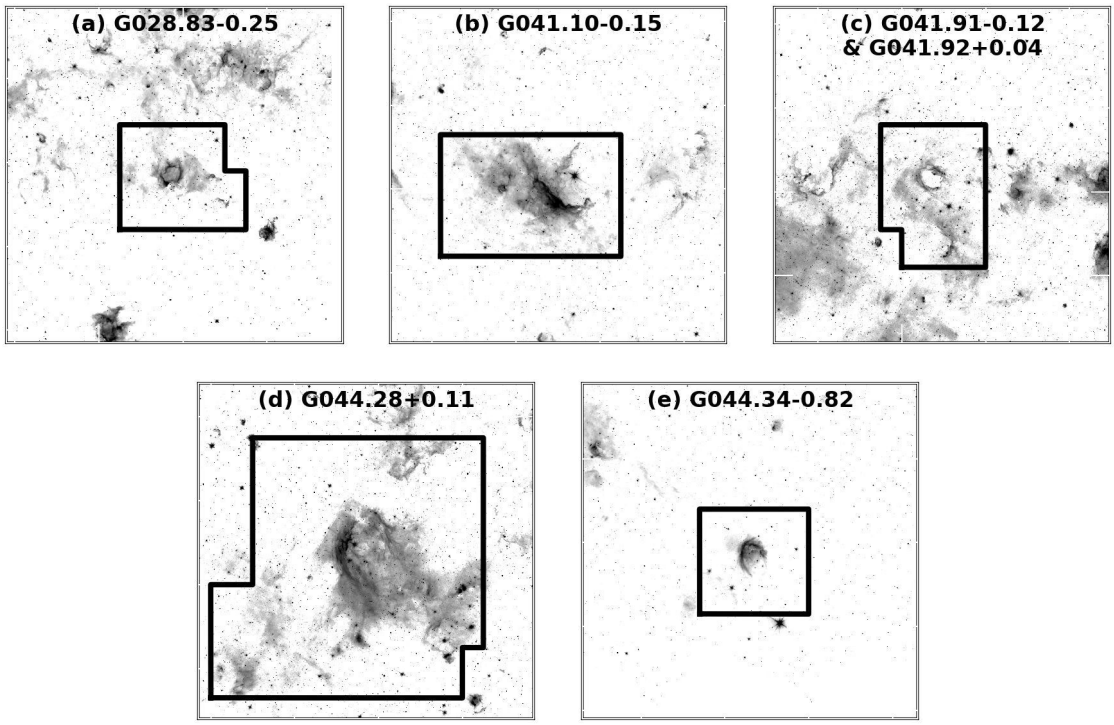

Fig. 2.2.— H II regions in our sample presented at uniform angular scale 48′ across. The grayscale images are IRAC 8 μm. The black boxes outline the areas of the sky over which we took point sources from the GPSC, identified additional point sources, and performed SED fitting to search for YSOs. The regions were chosen to include the entirety of the infrared bubble or rim, the associated molecular emission, and a significant field sample. Coordinates of the bounds of these boxes are given in Table 2.2.

the completeness of our final YSO list, we included these manually identified sources. An additional 179 sources were added to the sample in this manner, compared to 15,798 from the GPSC. We refer to these additional 179 sources as "MI" (manually identified) sources.

We employed a custom written Interactive Data Language (IDL) code to perform aperture photometry on all of the point sources in our sample. This was done to obtain photometry of the MI sources and MIPS photometry for all sources, as well as to obtain upper limits on nondetections from the GPSC. We used $3''$ radius circular apertures for the 2MASS and IRAC images, and $6''$ and $12''$ radius circular apertures for the MIPS 24 μm and 70 μm images, respectively, owing to the poorer resolution at longer wavelengths. In all cases the background emission was estimated from the mean value in an annulus extending 1.75 to 2.5 times the radius of the aperture. The criterion for detection was that the background-subtracted flux was at least one standard deviation of the background variation above the mean background level. We used this relatively low threshold above the background in individual bands because we later require detections in at least 4 photometric bands for a source to be considered part of our sample. In cases of a nondetection, we adopted the value of the background plus one standard deviation as an upper limit. We corrected for the fraction of missing flux from the comparison of aperture size to the PSF following Cohen et al. (2007). In the case of 70 μm, the images often suffered from their lower resolution as well as much more extended diffuse emission that made it nearly impossible to obtain reliable flux density measurements, except for the very brightest sources. We therefore only used the 70 μm images to determine upper limits for each source. Uncertainties were computed using Poisson counting statistics, with a minimum uncertainty of 10% of the photometric value used for all sources and wavebands.

When evaluating the aperture photometry values for sources in the GPSC within our sample, they generally agree with the GPSC photometry value to within ten percent. The biggest disagreements are at the very highest ($\gtrsim 0.5$ Jy) and very lowest ($\lesssim 2$ mJy) flux densities. Discrepancy at the highest flux densities is due to saturation in the images, which is better handled by PSF fitting than aperture photometry. In some cases, the aperture photometry allows us to obtain a measurement where the GPSC does not supply one, and so we adopted such values. In all other cases we adopt an uncertainty-weighted average of the values from the two methods. Since the two methods generally agree well, averaging the two does not significantly change the values, but we do get a larger, more realistic estimate of the uncertainty in cases where the two methods do disagree.

We required that only sources that are detected in at least four wavebands are analyzed, which helped to verify that sources are not spurious and that there was enough photometric information for each source to be studied reliably. Sources with fewer than four photometric data points were removed from further consideration. This requirement reduced our sample to 15,685 GPSC sources and 78 MI sources. The remaining sample sizes in each region are presented in Table 2.3.

With our sample of infrared point sources with flux density measurements or upper limits in nine wavebands, we begin to classify the sources using the SED fitter described in Robitaille et al. (2007). The fitter calculates a χ^2 value for each point source paired with each SED model from a selection of radiative transfer models. Because our point source sample contains sources with different numbers of photometric measurements, $n_{\rm data}$ (not counting upper limits), we use the χ^2 divided by the number of data points, $\chi^2/n_{\rm data}$, as a measure of goodness of fit.

To get a reliable list of YSO candidates, we took steps to remove sources that could

Table 2.2: YSO Fitting Parameters

Regions	$d_{\rm min}$[a] (kpc)	$d_{\rm max}$[a] (kpc)	Range of Sample Coverage[b] $(\ell, b : \ell, b)$	Coverage Area (arcmin^2)
G028.83-0.25	3.5	5.5	(28°.65, -0°.36 : 28°.95, -0°.22) (28°.7, -0°.22 : 28°.95, -0°.11)	250
G041.10-0.15	3.5	5.5	(40°.95, -0°.36 : 41°.38, -0°.07)	448
G041.91-0.12 and G041.92+0.04	0.5	2.5	(41°.80, -0°.18 : 42°.00, 0°.16) (42°.00, -0°.09 : 42°.05, 0°.16)	290
G044.28+0.11	3.5	5.5	(43°.95, -0°.15 : 44°.50, 0°.35) (44°.00, -0°.27 : 44°.60, 0°.00)	1303
G044.34-0.82	3.5	5.5	(44°.20, -0°.97 : 44°.46, -0°.72)	234

[a]Distance ranges for SED fitting are chosen to be consistent with the near kinematic distances from §2.2.1 while being as homogenous as possible across regions.

[b]Bounds of the area on the sky over which we searched for YSOs. These encompass significant area outside of the "bubble" or "cometary" regions to get a significant field sample as a control.

Table 2.3: Summary of Point Source Sample Sizes & Results

Region	Sample[a] (GPSC + MI)	Stellar[b] (GPSC + MI)	AGB[c] (GPSC + MI)	YSO[d] (GPSC + MI)
G028.83-0.25	1932 + 16	1614 + 2	32 + 0	48 + 4
G041.10-0.15	2250 + 13	1845 + 1	28 + 0	93 + 11
G041.91-0.12/G041.92+0.04	1749 + 11	1526 + 0	23 + 0	78 + 11
G044.28+0.11	8673 + 25	7911 + 1	46 + 1	155 + 23
G044.34-0.82	1081 + 13	995 + 1	9 + 1	26 + 9

[a]Includes sources from the GLIMPSE Point Source Catalog (GPSC) and additional sources identified visually in the 8 and 24 μm *Spitzer* images (MI). Only sources detected in at least four photometric bands are included in this count.

[b]Sources consistent with stellar atmosphere models from Brott & Hauschildt (2005).

[c]Sources initially identified as YSO candidates, but likely to be AGB stars (based on color-magnitude cuts) and thus removed from the final list of YSOs.

[d]Sources identified as YSOs by the SED fitter of Robitaille et al. (2007) and not likely to be AGB stars.

plausibly be main sequence or giant stars. We began by first fitting a grid of 7853 stellar atmosphere radiative transfer models from Brott & Hauschildt (2005) to our sample, using the SED fitter from Robitaille et al. (2007). The SED models spanned a range of effective temperatures, metallicities, and gravities ($2.7 \times 10^3 \mathrm{K} \leq T_{\mathrm{eff}} \leq 10^4 \mathrm{K}$, $-0.4 \leq [Z/H] \leq 0.5$, and $-0.5 \leq \log(g) \leq 5.5$, respectively). The extinction, A_V, along the line of sight to the source was a free parameter of the fitting process that we restricted to be between 0 and 20 magnitudes. The choice of this range was informed by Indebetouw et al. (2005) who found that A_V in the galactic plane is approximately 0.5-2 magnitudes kpc^{-1}. Since the A_V determination for each source is independent of every other source, this should account for variations in extinction across the field. The stellar atmosphere model fitting was distance independent, i.e. the absolute flux density scale is arbitrary at this stage, and only the SED shape is considered. Any source for which the best-fit SED met the criteria $\chi^2_{\mathrm{best}}/n_{\mathrm{data}} < 3$ was classified as "stellar," while the remaining sources were used as the sample for fitting YSO SEDs. The majority of GPSC point sources in our sample were well fit by the stellar atmosphere models (see Table 2.3). Removing these sources from further consideration, we were left with 1794 GPSC sources and 73 MI sources.

With sources consistent with stellar atmospheres identified and removed, we then performed SED fitting of YSO radiative transfer models from Robitaille et al. (2006) on the remaining sample. When performing the SED fitting, the line of sight extinction (to the "source," where source is defined as the outermost boundary of the radiative transfer model, not all the way to the surface of the central object) was again a free parameter between 0 and 20 magnitudes. The fitted distance was allowed to be within the ranges listed in Table 2.2, which were chosen to be consistent with the near kinematic distances following §2.2.1. The distance range for G041.91-0.12

and G041.92+0.04 was between 0.5 and 2.5 kpc, and 3.5 to 5.5 kpc for all the other regions. Again, any source for which the best-fit SED met the criteria $\chi^2_{\rm best}/n_{\rm data} < 3$ was classified as a good fit, while the remaining sources were excluded from further consideration. Examples of a good and marginally acceptable fit for each YSO stage (see below) are presented in Figure 2.3. A total of 598 YSO candidates (538 GPSC and 60 MI) were identified in this manner.

Once a source was identified as a YSO candidate, we also identified other SED models for which $\chi^2/n_{\rm data}$ was within 6 of the best fit, $\chi^2_{\rm best}/n_{\rm data}$. We did this so that once a source was reliably identified as a YSO candidate, we could investigate the full range of physical parameters that fit the data. We knew the central mass, accretion rate, disk mass, inclination angle, etc. of each model, so we calculated an average and uncertainty of several key physical parameters for each source based on the distribution "good fit" models, weighted by the probability, $\exp(-\chi^2/2)$, of each model. Most importantly, we estimated the mass and evolutionary stage of each of these YSO candidates. Using $(\chi^2 - \chi^2_{\rm best})/n_{\rm data} < 6$ as a threshold allowed for a more realistic estimate of the uncertainties in the physical parameters.

To check how much our YSO candidate sample depends on MIPS photometry, we repeated this same fitting process without 24 μm data. We find that 329 YSO candidates are recovered (55% of the YSO candidate sample using the MIPS photometry). This quantitatively illustrates the importance of long wavelength data for the identification of YSOs. We proceed with further analysis using the YSO candidate sample identified using the MIPS photometry. We note that of the 542 MIPS 24 μm point sources we report, 358 (66%) are detected at the 3σ level or greater.

A likely residual contaminant in this sample of YSO candidates is AGB stars, which tend to have SEDs similar to certain YSO models in this wavelength range.

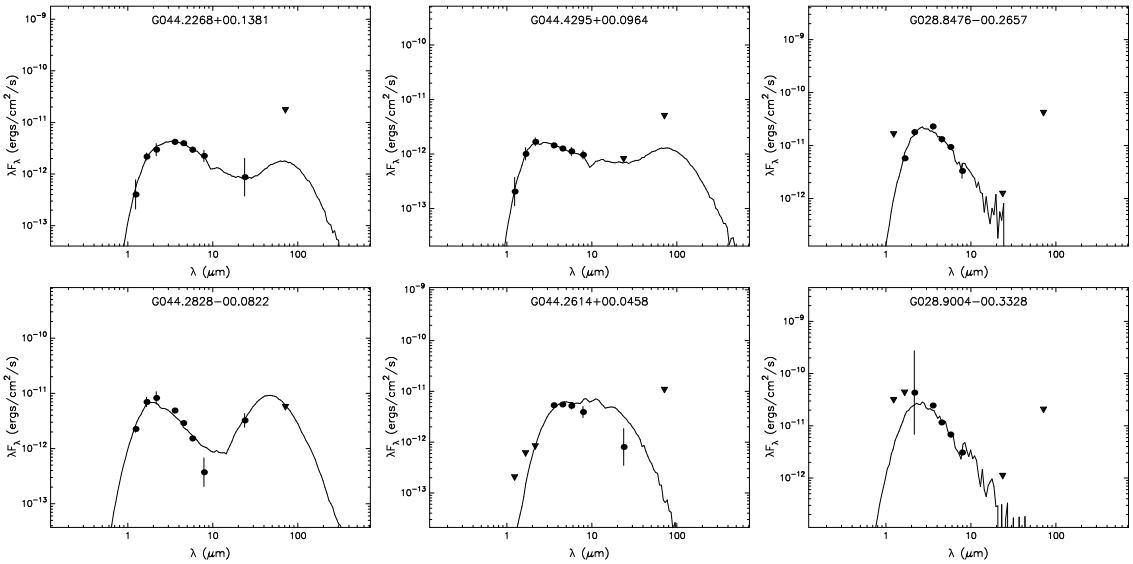

Fig. 2.3.— Examples of point source SEDs with best fit YSO models. All six objects have been identified as YSOs by our fitting method and were not removed as AGBs following our color cut. Stage I sources are in the left column, Stage II are in the middle column, and Stage III are in the right column. Examples that are typical of the lowest $\chi^2/n_{\rm data}$ are in the top row, while examples typical of highest $\chi^2/n_{\rm data}$ (marginally acceptable fit) are in the bottom row. Circles with error bars (often too small to see) represent detections, while downward arrows represent upper limits. The solid line is the best fit SED model.

In the absence of additional data to discern the true YSOs, such as spectroscopic observations, we evaluate our candidates in color-magnitude space. Robitaille et al. (2008) have analyzed AGB stars (both sAGB and xAGB) and clustered (likely YSO) sources to see where they each fall in [8.0]-[24.0] versus [4.5] space. They have determined areas in this space that are predominantly occupied by each population, however the populations do overlap somewhat in this space, and there will likely be contamination in both samples. The results of Robitaille et al. (2008) are derived for the entire galactic plane, so shifts in criteria to optimize the cut for each region are expected. We have determined our own selection criteria for removing AGB stars for each H II region using the Robitaille et al. (2008) results as a guide and being as conservative as possible in the removal of sources so as not to lower the completeness of our final YSO sample drastically. The decision to be conservative in this removal process is justified by our completeness estimates below. Color-magnitude diagrams of all YSO candidates are presented in Figure 2.4, showing our criteria for discrimination between AGB and YSO sources. Objects with limits on [4.5] or [8.0]-[24.0] are only removed if they lie entirely on the AGB side of our cuts.

One can see that each sample of YSO candidates roughly separates into two populations that are better separated in [4.5] than in [8.0]-[24.0]. The coordinates and properties of YSOs remaining after this color-magnitude cut are presented in Table 2.4. A comparison of the sample sizes to the numbers of stellar sources, YSOs, and AGBs are presented in Table 2.3. A total of 458 YSOs remained after 140 AGBs were removed. We refer to this final sample of 458 as "YSOs," while we refer to the previously combined sample of YSOs and AGBs as "YSO candidates." All additional analysis in this work only makes use of the YSO sample.

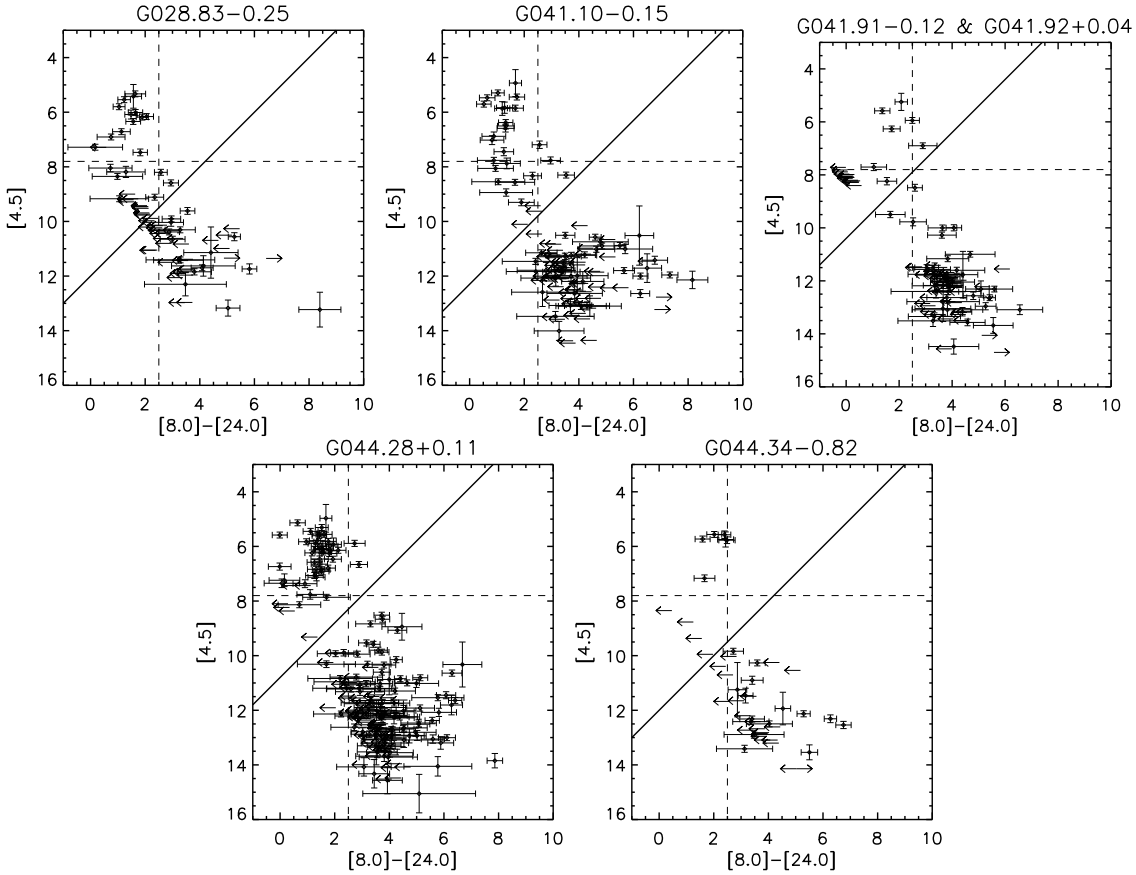

Fig. 2.4.— Color-magnitude plots for our initial sample of YSO candidates used to remove contamination by AGB stars. Sources with upper or lower limits are plotted as arrows. In general the samples separate into two populations. Following Robitaille et al. (2008), the brighter, bluer populations (upper left in this color space) are dominated by AGB stars over YSOs. We therefore exclude these objects from our final analysis. The dashed lines show the guidelines from Robitaille et al. (2008), while our cuts determined for each region are the solid line.

Table 2.4: YSOs Identified by SED Fitting

YSO	Stage[a]	$\frac{\chi^2_{\rm best}}{n_{\rm data}}$	24 μm?	$\log\left[\frac{M_*}{M_\odot}\right]$[b]	$\log\left[\frac{L_*}{L_\odot}\right]$	$\log\left[\frac{\dot{M}_{\rm env}}{M_\odot\ {\rm yr}^{-1}}\right]$[c]	$\log\left[\frac{M_{\rm disk}}{M_\odot}\right]$
G028.83-0.25							
G028.6534-00.2539	III	2.89	N	14.6±0.0	4.3±0.0	0.0±0.0	-8.0±0.0
G028.6608-00.2305	II	3.00	N	5.5±1.4	3.0±3.1	0.0±0.0	-2.1±-1.7
G028.6788-00.2786	I	0.05	N	3.8±1.1	2.3±2.6	-4.7±-4.1	-1.7±-1.4
G028.6879-00.2739	I	0.31	Y	3.6±1.3	2.0±2.1	-4.1±-3.8	-1.5±-1.2
G028.6962-00.2913	I	0.47	Y	5.0±1.6	2.9±3.1	-4.8±-3.9	-1.9±-1.5
G028.7020-00.2101	I	0.71	N	2.7±0.9	1.7±1.7	-5.5±-4.9	-2.1±-1.7
G028.7166-00.2231	I	0.01	N	2.0±1.1	1.5±1.9	-5.4±-4.8	-2.2±-1.8
G028.7190-00.1813	II	0.67	Y	4.3±1.1	2.6±2.9	-6.0±-4.8	-2.1±-1.7
G028.7191-00.2083	I	2.06	Y	1.1±1.2	1.7±2.1	-4.5±-4.0	-1.8±-1.6
G028.7347-00.1769	II	0.01	Y	4.5±1.0	2.6±2.6	-6.2±-4.8	-2.0±-1.6

[a] See §2.2.2 for explanation of evolutionary stages.

[b] Values for all quantities are determined by the parameters of model SEDs that fit the source such that $\left(\chi^2 - \chi^2_{\rm best}\right)/n_{\rm data} < 6$. Averages and uncertainties are the mean and standard deviation values of the fit parameters weighted by the probability of the corresponding model, $\exp\left(-\chi^2/2\right)$ (See §2.2.2). Uncertainties of 0.0 indicate no spread in the models that fit the data.

[c] The data are sometimes fit by disk-only models with no accreting envelope, represented by a value of 0.0.

(This table is available in its entirety in Appendix Table A.1. A portion is shown here for guidance regarding its form and content.)

YSO Classification

Historically, low-mass YSOs have been identified by their spectral indices and infrared colors. The reddest sources are classified as Class I objects, slightly bluer objects as Class II objects, and yet bluer objects as Class III objects. Class I corresponds to sources in a relatively early evolutionary phase, with significant accretion from a surrounding envelope. Class II objects have optically thick disks and potentially the remains of an envelope. Class III objects are the most evolved with only an optically thin disk remaining (Adams et al. 1987). We investigated both GPSC and MI sources using the color selection method of Allen et al. (2004) and found minimal differences between the YSOs identified by color and those identified by SED fitting. Most discrepancies were in confused regions of high background emission. This result

is in good agreement with a similar study in M16 (the Eagle Nebula) by Indebetouw et al. (2007). The major advantage of using the SED fitting method to identify YSOs, though it is more labor intensive than other methods, is that it allows an estimate of the physical properties of the source from the parameters of the radiative transfer models that best fit the data.

Throughout the remainder of this chapter, we adopt the YSO "Stage" classification scheme of Robitaille et al. (2006). This is physically similar to the common "Class" system corresponding to the relative evolutionary state of low-mass YSOs, described above, but can be simply determined in our case from the accretion rate, disk mass, and central source mass as determined by SED fitting and the Robitaille et al. (2006) models. As noted by Robitaille et al. (2006), the use of spectral index classification can lead to confusion as it is motivated more by observation than physical state and does not properly account for changes in viewing angle between individual sources. Furthermore, Whitney et al. (2004) note that for high mass sources, both $T_{\rm eff}$ and the evolutionary state affect the mid-infrared spectral index, so the model-derived "Stage" is less ambiguous than a simple spectral index. Stage I objects are defined as those that have $\dot{M_{\rm env}}/M_\star > 10^{-6}{\rm yr}^{-1}$, where $\dot{M_{\rm env}}$ is the envelope accretion rate and $M_\star$ is the mass of the central source. Stage II objects are defined by $\dot{M_{\rm env}}/M_\star < 10^{-6}{\rm yr}^{-1}$ and $M_{\rm disk}/M_\star > 10^{-6}$, where $M_{\rm disk}$ is the disk mass. Finally, Stage III objects are defined by $\dot{M_{\rm env}}/M_\star < 10^{-6}{\rm yr}^{-1}$ and $M_{\rm disk}/M_\star < 10^{-6}$.

Completeness

To estimate the completeness of our YSO sample, we determined which of the YSO SED models from Robitaille et al. (2006) would be both detectable by *Spitzer* and 2MASS and identifiable as YSOs by our selection method if the models represented

real YSOs within the bubble or cometary regions. To start, we calculated the flux density of each model SED in each waveband at the distance of each H II region and applied an extinction of $A_V = 1$ mag kpc^{-1}. For each H II region, we independently adopted values of the limiting flux density to qualify as a detection at each wavelength. These limiting values were determined by plotting the source counts from the GPSC in each region as a function of magnitude to identify the sensitivity limit in the bubble or cometary structures, which are known to have high backgrounds. We adopted a single value for each region and wavelength, though the actual background can vary by as much as a factor of five at the longer wavelengths. Furthermore, we applied the 2MASS and GLIMPSE saturation limits presented in Skrutskie et al. (2006) and Benjamin et al. (2003). We were thus able to determine the wavebands in which each YSO model would be detectable in each region, and so generate a set of simulated photometric data points for each YSO model. We then determined which of these model sources would be identified as YSOs following our selection method in §2.2.2.

We account for the fact that the distribution of physical parameters in the model grid does not necessarily represent the distribution of the true YSO population by using a simulated sample. Robitaille et al. (2006) simulated a large "virtual" cluster of YSOs drawing from a uniform age distribution (implying a constant rate of star formation) in the range from 10^3 years to 2 Myr, and a Kroupa (2001) IMF ranging from 0.1 to 30 solar masses. Robitaille et al. (2006) chose this mass range to approximate a real cluster, though the SED models have masses as high as 50 solar masses. They then calculated "weights" that scale with the likelihood of each model to appear in the simulated cluster. We used the list of models that would be detected and identified as YSOs within each region, weighted by these probabilities, to represent our simulated sample. We then plotted the mass distribution of this simulated pop-

ulation and compared it to the distribution of our observed YSO sample normalized by solid angle. The plots for each region are shown in Figure 2.5, using an arbitrary scaling of the simulated sample. For comparison, we also plotted the distribution of the virtual cluster without any observational or methodological effects considered, i.e. a simulated sample that is 100% complete across the entire mass range. The ratio of these two simulated distributions with and without observational effects, seen in Figure 2.6, provides a completeness estimate as a function of mass, while the correspondence between the simulated samples and the real samples seen in Figure 2.5 provides evidence that the completeness estimates are valid. We have not made an attempt to account for the effects of sampling small populations, so our simulated distributions are unable to account for stochasticity. For example, we do not detect any YSOs in G041.91-0.12 & G041.92+0.04 in multiple bins around 2-4 $M_{\odot}$ despite the fact that we estimate our completeness at over 50% in this mass range.

The loss of completeness at lower mass is dominated by photometric sensitivity limits, whereas the loss of completeness at high mass is dominated by AGB color-magnitude cuts that predominantly remove the sources among the brightest at 4.5 μm. The benefit of additional completeness at higher mass by altering or emitting the AGB color-magnitude cuts is outweighed by the likely contamination of AGBs falsely identified as high mass YSOs. The small number of massive YSO candidates makes it difficult to further investigate the uncertainty introduced by applying a population-based cut. Clearly G041.91-0.12 and G041.92+0.04 are the most complete samples, as is expected for the closest regions in this work, being over 50% complete between approximately 1.5 and 5 $M_{\odot}$. The remaining regions show a dramatic loss in completeness below 3-4 $M_{\odot}$.

We performed this completeness analysis only as a guide to interpreting our re-

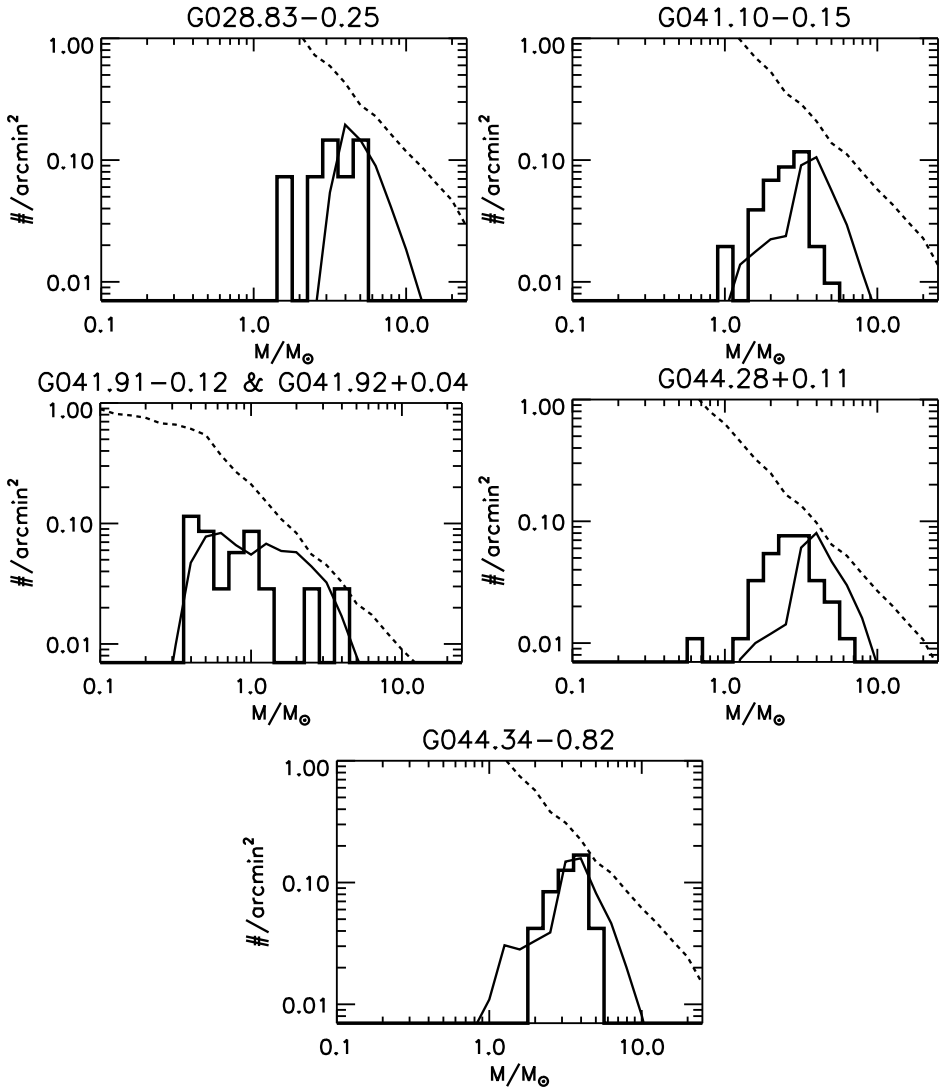

Fig. 2.5.— Mass distribution of our observed YSO samples from this work identified by SED fitting, with likely AGBs removed using color-magnitude cuts, restricted to YSOs within or on the bright rim regions, plotted by the thick-lined histogram. Overplotted are the distributions of the virtual cluster YSO populations from Robitaille et al. (2006). The dashed lines show the simulated populations ignoring any sources of completeness, while the thin solid lines show the distributions remaining after applying extinction corrections, considering sensitivity and saturation limits, fitting stellar atmosphere models to the SEDs, and applying color-magnitude cuts to remove AGB stars. Both simulated samples are presented with arbitrary scaling that is consistent within each region (see §2.2.2). The correspondence between the simulated sample with source incompleteness and the observed sample provides evidence that the completeness estimates are valid.

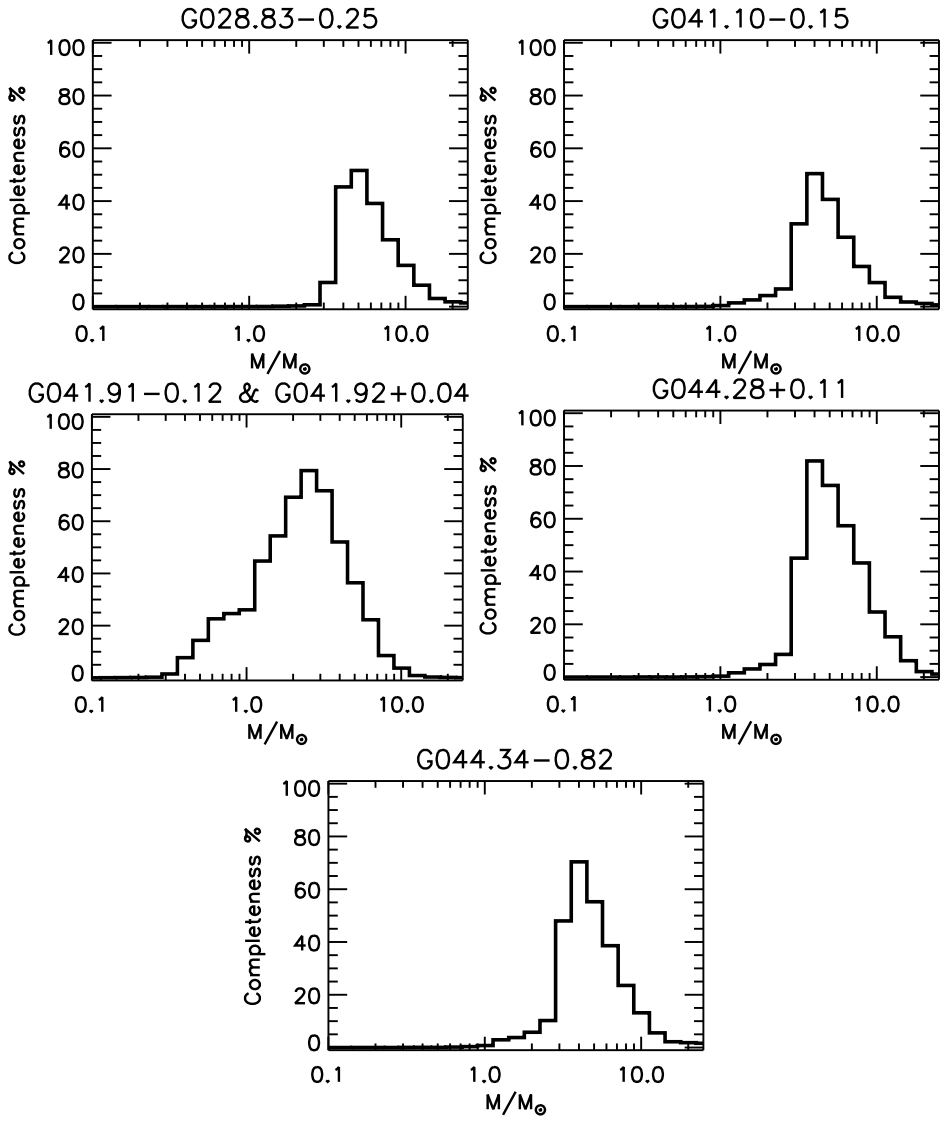

Fig. 2.6.— Ratio of the two simulated distributions from Figure 2.5 (with and without applying observational and methodological effects) as an estimate of completeness as a function of mass. The incompleteness at the low-mass end is dominated by photometric sensitivity, while the incompleteness at the high mass end is dominated by color-magnitude cuts removing AGB contaminants.

sults, especially in considering our estimated completeness of high mass YSOs. We do not apply any kind of completeness correction to our sample because of the relatively small number of YSOs in each region and the inherent uncertainty in applying such a correction. The incompleteness in our sample, particularly at the high mass end, precludes us from realistically analyzing whether possibly triggered YSOs have systematically higher masses than the field population.

We also note that the youngest, least evolved YSOs will be missed by our selection method regardless of mass because, while they may be bright in the far-infrared or in molecular tracers, they are not detectable in IRAC images shortward of 5 μm. Indeed, there is a small population of infrared sources in these regions that are identified in 24 μm and sometimes in 8 μm as well, but are not detectable in shorter wavelengths. However, these sources were excluded from our sample because they are detectable in fewer than the minimum four wavebands.

2.2.3 Ionizing Sources

Our analysis of the H II regions in the context of triggered star formation requires knowledge of the ionizing luminosity from stars that power the regions. To estimate this, we make use of the Very Large Array Galactic Plane survey (VGPS) 21 cm continuum data (approximately $1'$ resolution) described by Stil et al. (2006). Images of our sample regions with radio continuum contours are in Figures 2.7 to 2.12. We use custom apertures around the continuum emission associated with each H II region to measure the flux density. Carefully drawn source and background apertures are necessary because of the varying shapes of the radio continuum, as well as the varying background emission. For measurements of G041.10-0.15, we are particularly careful to avoid emission from the supernova remnant SNR G041.1-00.3 (3C 397) (Jiang et al.

2010).

Assuming the emission is optically thin free-free thermal continuum, we calculate the ionizing luminosity following Condon (1992):

$$Q_{\rm Ly} \gtrsim 7.54 \times 10^{46} \left(\frac{T_e}{10^4{\rm K}}\right)^{-0.45} \left(\frac{\nu}{\rm GHz}\right)^{0.1} \left(\frac{S_\nu}{\rm Jy}\right) \left(\frac{D}{\rm kpc}\right)^2 {\rm s}^{-1}, \qquad (2.1)$$

where T_e is the electron temperature, ν is the frequency of the observation, S_ν is the observed specific flux density, and D is the distance to the H II region. This quantity is a lower limit because the fraction of photons absorbed by dust or leaking out of the region is unknown. The regions in our sample that have observed recombination lines in Lockman (1989) or Lockman et al. (1996) are G028.83-0.25, G041.10-0.15, G041.91-0.12, and G044.34-0.82. The line widths are 19.9 ± 1.7 km s^{-1}, 26.7 ± 1.9 km s^{-1}, 36.7 ± 7.0 km s^{-1}, and 30.4 ± 4.7 km s^{-1}, respectively. These line widths imply temperatures of $0.87 \pm 0.15 \times 10^4$ K, $1.6 \pm 0.2 \times 10^4$ K, $2.9 \pm 1.1 \times 10^4$ K, and $2.0 \pm 0.6 \times 10^4$ K, respectively. Lockman (1989) notes that relatively large line widths, such as the one reported for G041.91-0.12, may be the result of multiple nebulae along the same line of sight that are not well separated in velocity. The resulting temperature should then be interpreted as an upper limit. Assuming a uniform value of 10^4 K for the electron temperature, we calculate the ionizing luminosity necessary to power each H II region. We estimate the uncertainty in the radio flux at 30%, the uncertainty in the electron temperature at a factor of 2 (100 %), and uncertainty in the distance at 50%, which yields an estimate of a factor of 1.75 uncertainty in the ionizing luminosity.

From $Q_{\rm Ly}$, we determined the spectral type of a single ionizing star using Vacca et al. (1996) and Smith et al. (2002). We also determined the spectral type of the most massive star in a cluster with a Salpeter (1955) IMF that would provide the

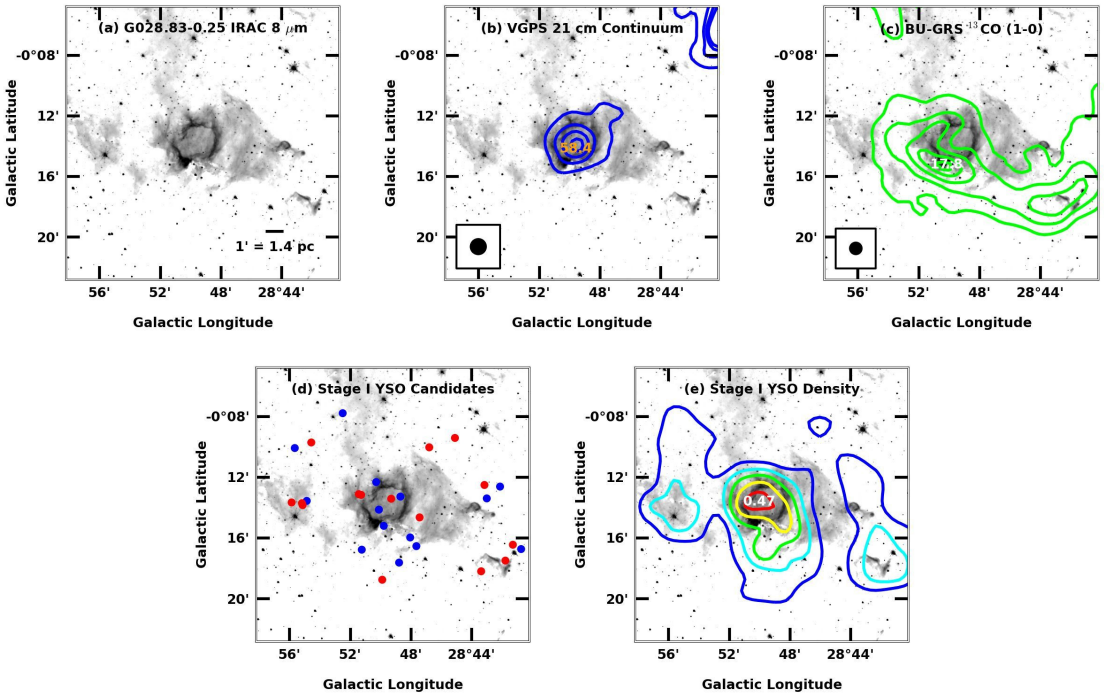

Fig. 2.7.— Results for G028.83-0.25. (a) A *Spitzer* 8 μm image. The dense rim is visible. A 1′ scale bar and physical scale at the assumed distance is in the lower right. (b) Radio continuum emission from the 21 cm VGPS. Contours are 95%, 80%, 60%, 40%, and 20% of the peak brightness temperature, 58.4 K in this region, labeled in the panel. The H II region emission is coincident with the infrared bubble. The images have approximately 1′ resolution, indicated by the beam in the lower left. (c) ^{13}CO J=1-0 emission from the BU-GRS over the velocity range 83.8 – 90.0 km s^{-1}. Contours are 95%, 80%, 60%, 40%, and 20% of the peak integrated antenna temperature, 17.8 K km s^{-1} in this region. The 46″ beam is in the lower left. (d) Stage I (least evolved) YSOs identified by SED fitting, plotted with circles.Red circles indicate sources with 24 μm photometry, while blue circles indicate sources with upper limits at 24 μm. Likely AGB contaminants have been removed. (e) Density of Stage I YSOs from SED fitting, sampled at 1.5 arcminutes. Contours are 95%, 80%, 60%, 40%, and 20% of the peak density, 0.47 YSOs per square arcminute in this region, labeled in the panel. Contour colors range from blue (low density) to red (high density). The maxima indicate areas of enhanced clustering of relatively unevolved YSOs. There is an enhanced YSO population at the center of the bubble as compared to the surrounding field.

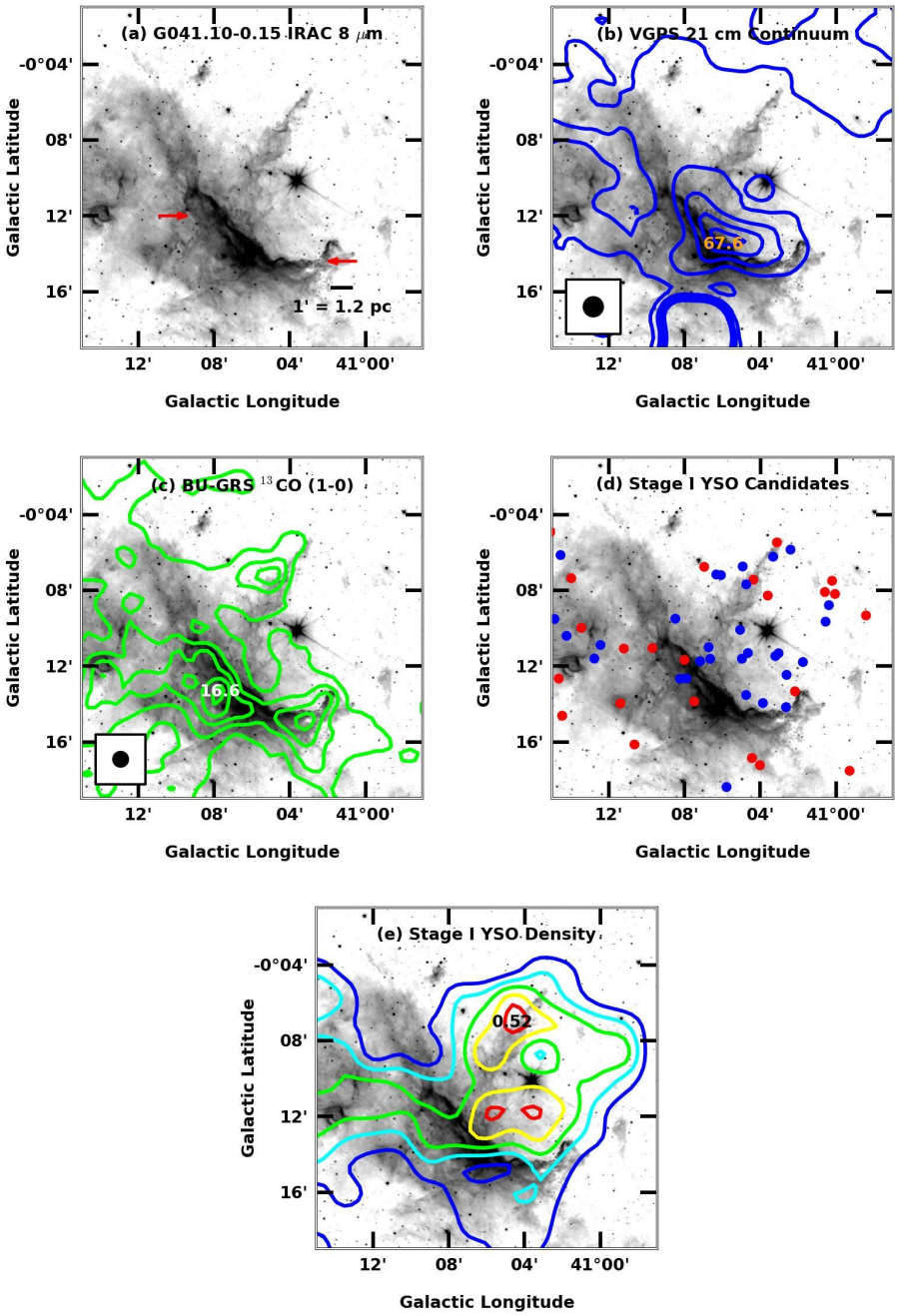

Fig. 2.8.— Results for G041.10-0.15. Panels are as in Figure 2.7. IRDCs are marked by red arrows in panel (a). The unrelated supernovae remnant 3C 397 (Jiang et al. 2010) is visible at the bottom of panel (b). The ^{13}CO J=1-0 emission in panel (c) is integrated over the velocity range 54.7 – 68.2 km s^{-1}. There is an enhanced YSO population located within and around the bubble as compared to the surrounding field, seen in panels (d) and (e).

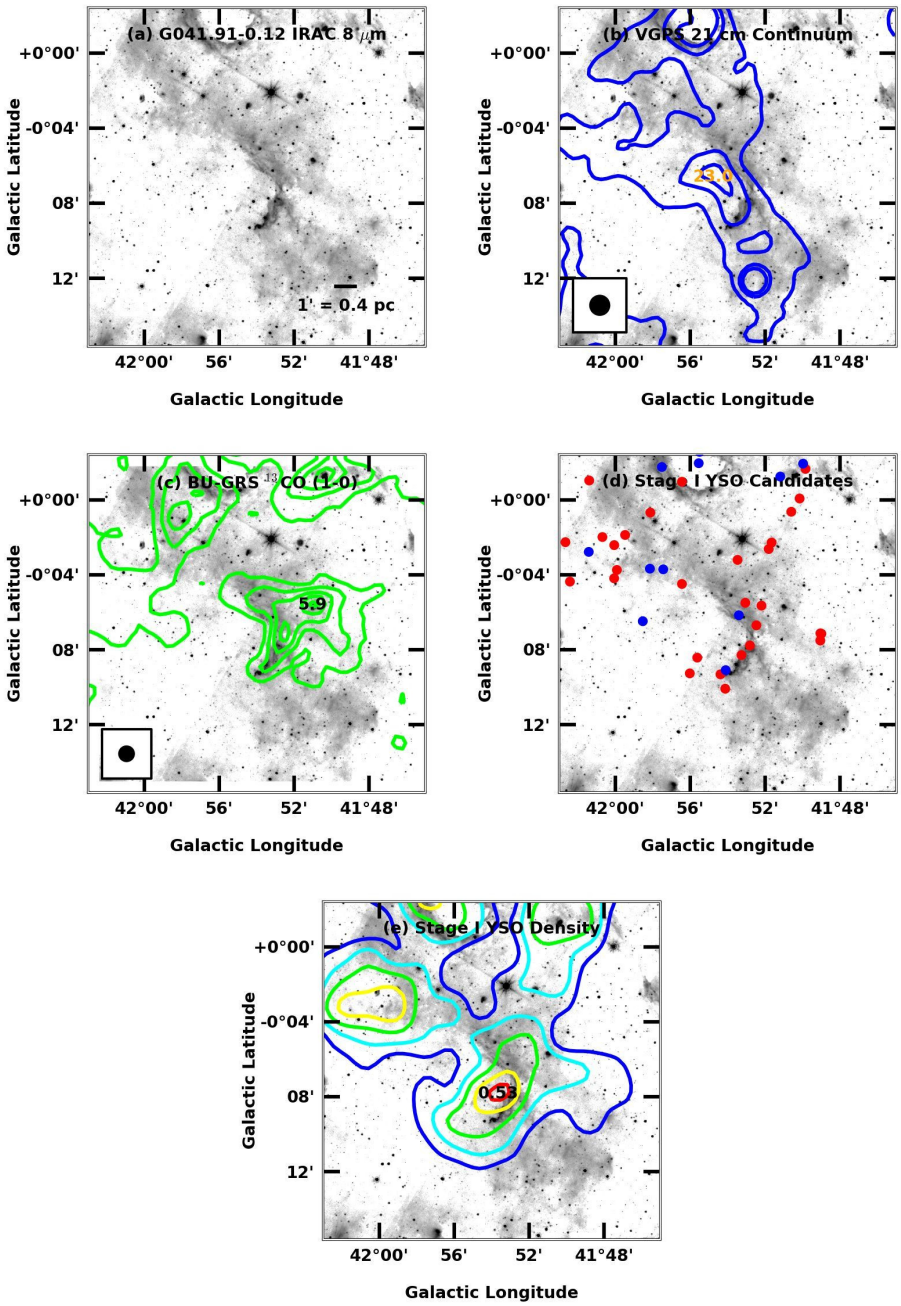

Fig. 2.9.— Results for G041.91-0.12. Panels are as in Figure 2.7. The ^{13}CO J=1-0 emission in panel (c) is integrated over the velocity range 12.0 – 20.8 km s^{-1}. There is an enhanced YSO population located around the infrared rim as compared to the surrounding field, seen in panels (d) and (e).

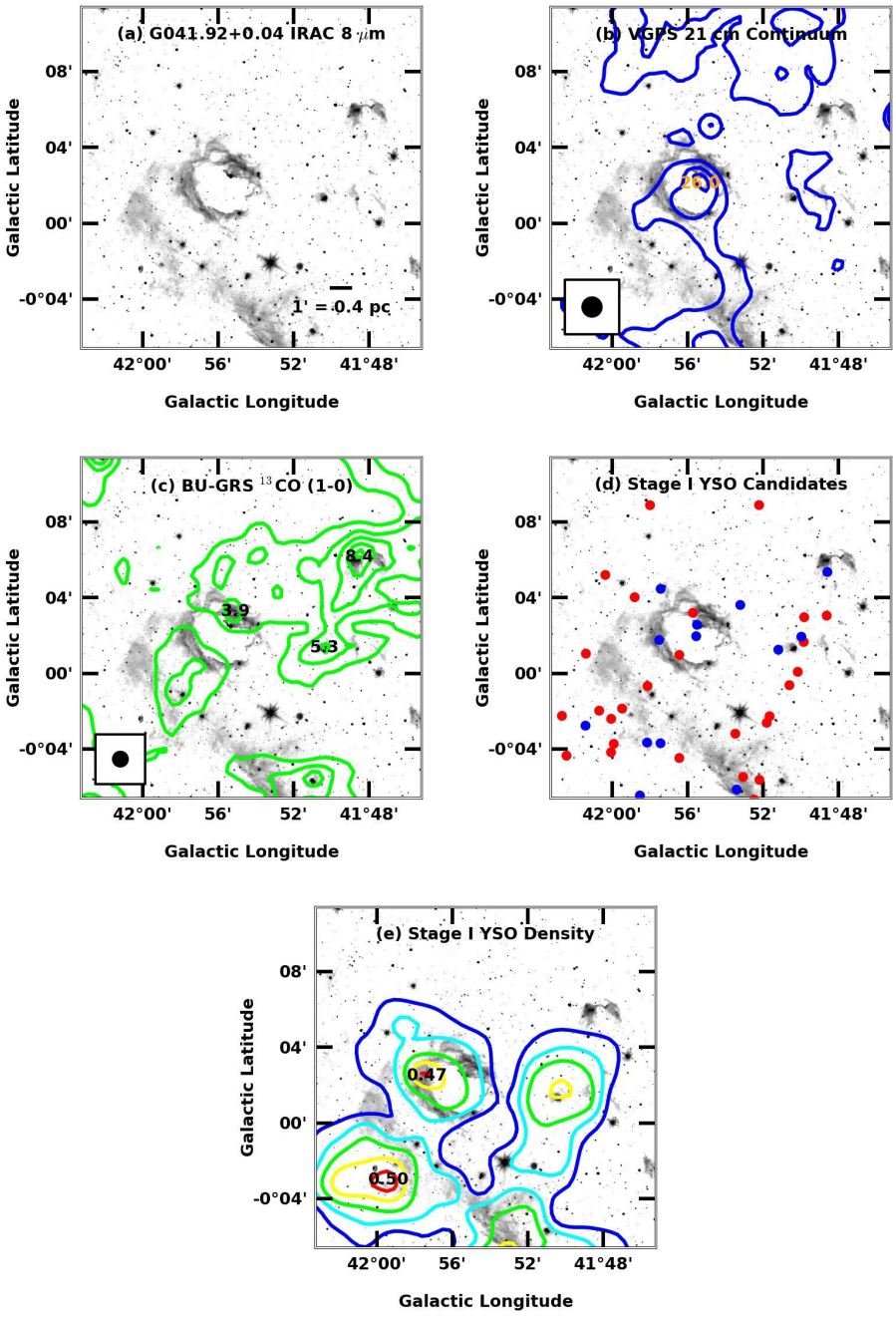

Fig. 2.10.— Results for G041.92+0.04. Panels are as in Figure 2.7. The ^{13}CO J=1-0 emission in panel (c) is integrated over the velocity range 12.0 – 20.8 km s^{-1}. There is a slightly enhanced YSO population located in the infrared bubble as compared to much of the surrounding field, seen in panels (d) and (e).

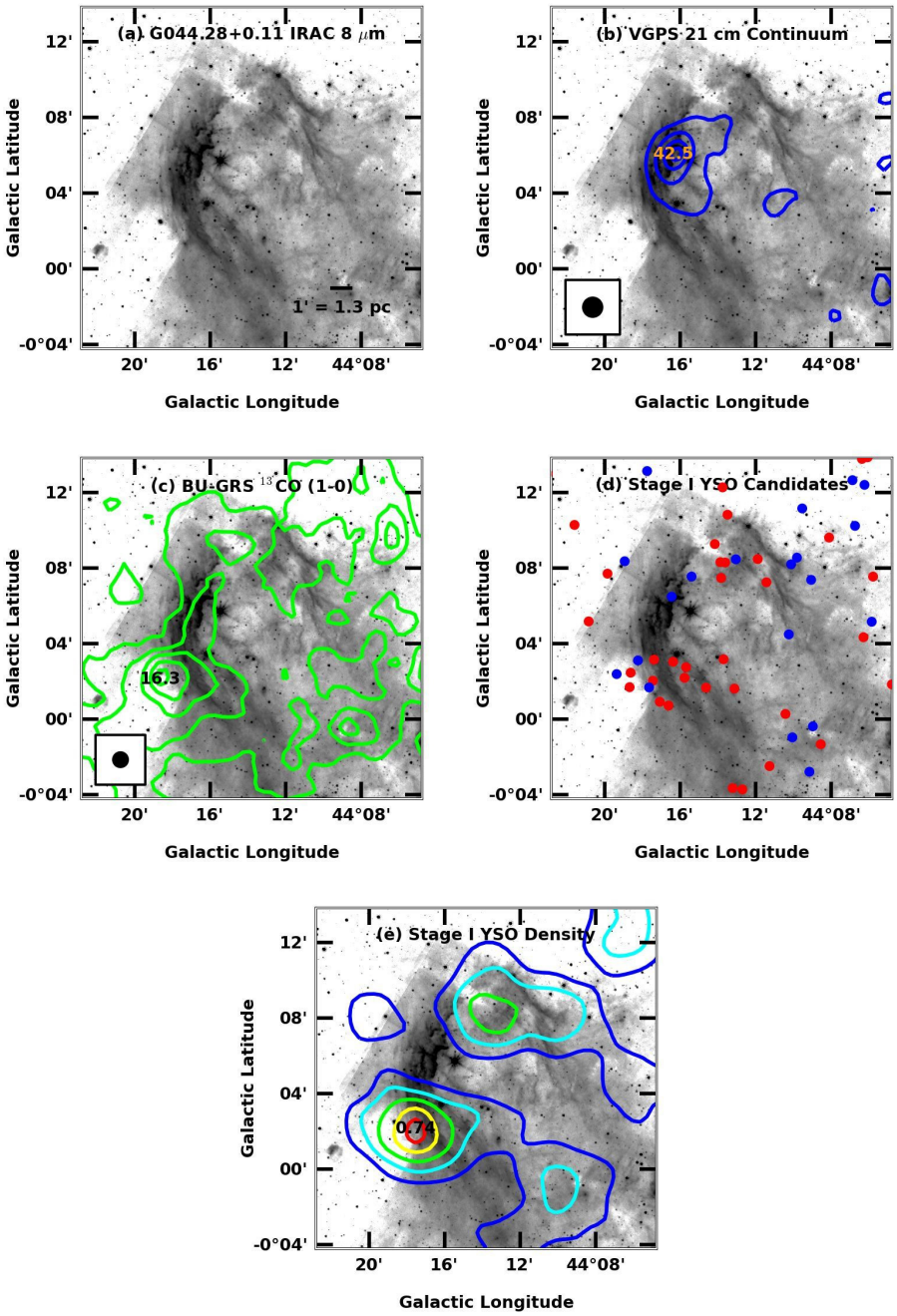

Fig. 2.11.— Results for G044.28+0.11. Panels are as in Figure 2.7. The ^{13}CO J=1-0 emission in panel (c) is integrated over the velocity range 52.2 – 68.4 km s^{-1}. There are enhanced YSO populations located on the infrared rim as compared to much of the surrounding field, seen in panels (d) and (e).

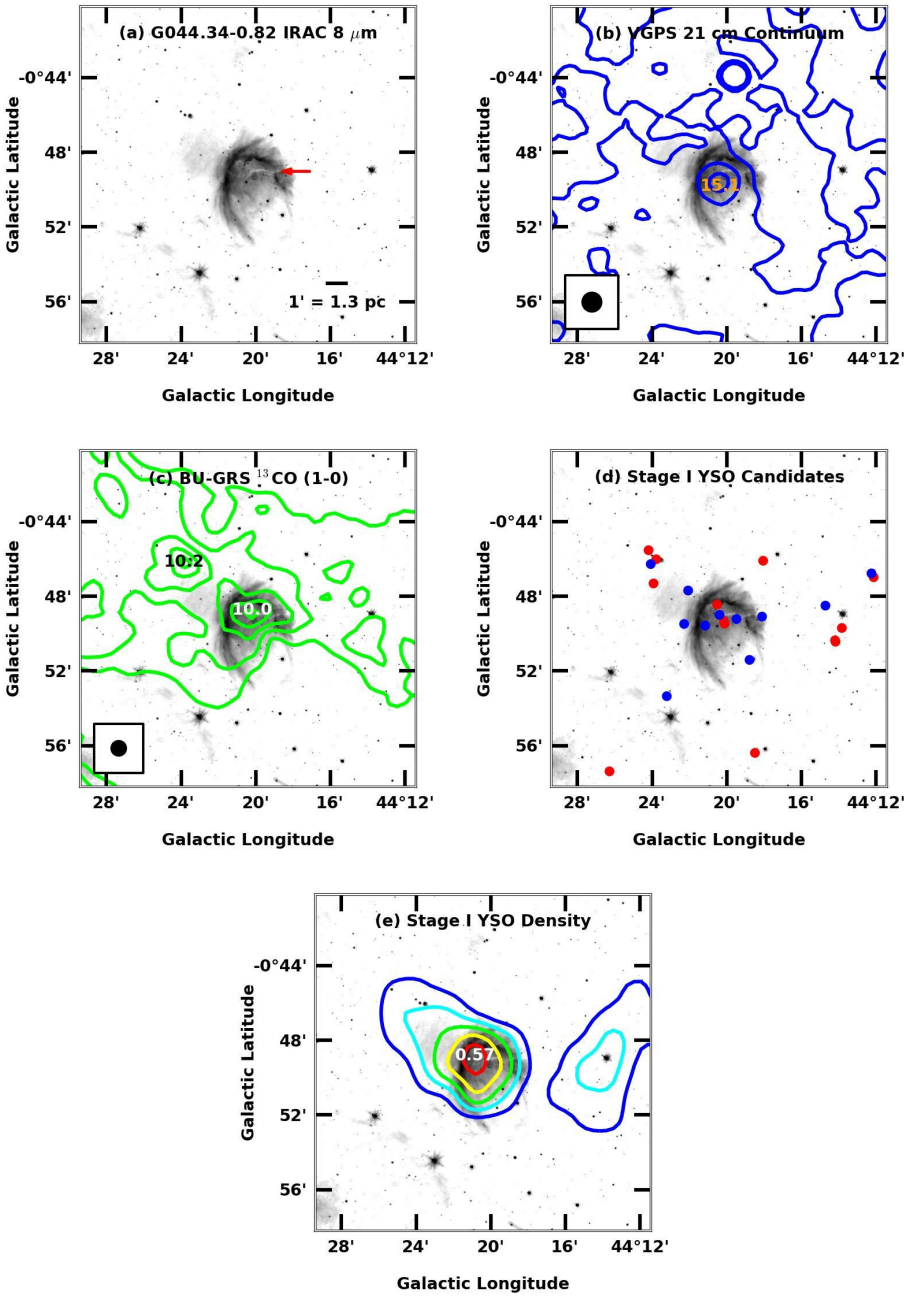

Fig. 2.12.— Results for G044.34-0.82. Panels are as in Figure 2.7. The IRDC is marked by a red arrow in panel (a). The ^{13}CO J=1-0 emission in panel (c) is integrated over the velocity range 56.4 – 67.1 km s^{-1}. There is an enhanced YSO population located in the infrared bubble as compared to the surrounding field, seen in panels (d) and (e).

same ionizing luminosity. Because of the steep relationship between mass and ionizing luminosity, the ionizing luminosity is dominated by the most massive member of the cluster, and therefore the star with the earliest spectral type. Thus, the results for a cluster were only approximately one spectral subtype later than when using a single star. We considered the effect of dust, by estimating that half of the ionizing luminosity was absorbed by dust grains (consistent with Wood & Churchwell 1989). The result was about one spectral subtype earlier. The factor of two uncertainty in the electron temperature also introduces an uncertainty of approximately one subtype. The $Q_{\rm Ly}$ values and the equivalent spectral types of a single ionizing source are presented in Table 2.5.

To verify whether the radio continuum emission is thermal, we calculated the spectral index from 11 cm to 21 cm, incorporating the Bonn 11 cm survey (Reich et al. 1984) from the Effelsburg 100 meter telescope. These single dish observations have angular resolution of about $4\farcm3$, and 50 mK RMS sensitivity. To get a consistent measurement, we smoothed the VGPS images to the resolution of the Bonn images and measured the photometry using the same apertures on each. Using $S_\nu \propto \nu^{\alpha_{\rm cm}}$, we calculated the spectral index, $\alpha_{\rm cm}$, for the regions and present the values in Table 2.5. We found that all of the regions have spectral indices of $\alpha_{\rm cm} \approx -0.1$ within uncertainties, consistent with optically thin free-free emission.

2.2.4 Molecular Gas

To fully understand whether star formation in these H II regions is triggered, we need to understand the molecular gas environment. We make use of the Boston University Galactic Ring Survey (BU-GRS) introduced in §2.2.1. The publicly available data cubes have velocity resolution 0.2 km s^{-1}, angular resolution of $46''$, and typical RMS

sensitivity of 0.13 K (Jackson et al. 2006). G028.83-0.25 has two velocity components seen in ^{13}CO J=1-0 at 88.0 and 95.6 km s^{-1} (see Figure 2.13), and either one or both may be associated with the H II region. We consider both, and they are evaluated separately for their triggering analysis (§2.3.2).

To calculate the ^{13}CO J=1-0 column density, we assume that the gas is in local thermodynamic equilibrium (LTE), fills the beam, and is optically thin, and thus use the standard equation:

$$N\left(^{13}\mathrm{CO}\right) = \frac{3k_B}{8\pi^3\nu_{\mathrm{GRS}}S(J_u)\mu^2_{\mathrm{GRS}}}\frac{Z_{\mathrm{GRS}}}{g_u g_K g_{\mathrm{nuclear}}}\exp\left(\frac{E_{u,\mathrm{GRS}}}{k_B T_{\mathrm{ex,GRS}}}\right)\int T_{B,\mathrm{GRS}}\,dv, \quad (2.2)$$

where $\nu_{\mathrm{GRS}} = 110.201353$ GHz, $S(J_u) = J_u/(2J_u+1)$ is the statistical weight of the upper level, $J_u = 1$ for the upper level, $\mu_{\mathrm{GRS}} = 0.112$ debye is the electric dipole moment, $g_u = 2J_u + 1$ is the rotational degeneracy, $g_K = 1$ is the K degeneracy for a linear molecule, $g_{\mathrm{nuclear}} = 1$ is the nuclear spin degeneracy, and $E_{u,\mathrm{GRS}}/k_B = 5.29$ K for the energy of the upper level. We assume a partition function of the form $Z_{\mathrm{GRS}} \approx 0.38(T_{\mathrm{ex,GRS}}/\mathrm{K}+0.88)$ (Wilson et al. 2009). We note the intrinsic assumption that the level populations are determined by a single parameter, the excitation temperature, which is not necessarily the same as the kinetic temperature.

For the excitation temperature, we adopt a value consistent with similar environments. Sridharan et al. (2002) reported ammonia temperatures of approximately 20 K for massive cores without strong centimeter continuum emission. Brogan et al. (2011) observed massive YSOs with the VLA and found ammonia temperatures in the 20-30 K range in kinematically simple cores. Rosolowsky et al. (2008) observed ammonia in dense cores in Perseus with the GBT, including sources both with and without submillimeter continuum, and found temperatures as low as 11 K in the cold gas. Admittedly Perseus is more quiescent than our regions. Furthermore, we do

Table 2.5: H II Region Properties

Region	Radio Continuum								
	Diameter		S_{21cm}	S_{21cm}[a]	$S_{11\ m}$	α_{cm}[b]	Q_{Ly}	Single Ionizing Source	
	(')	(pc)	(Jy)	(Jy)	(Jy)		(s^{-1})	Sp. Type[c]	Sp. Type[d]
G028.83-0.25	2.8	2.0	1.01	0.95	0.81	-0.24	$10^{48.3}$	O9.5-B0	O8-O9
G041.10-0.15	10.3	6.0	5.45	6.01	6.61	0.15	$10^{48.8}$	O8-O8.5	O7-O7.5
G041.91-0.12	4.0	0.8	0.5	0.57	0.45	-0.36	$10^{46.9}$	<B0.5	B0.5-B1
G041.92+0.04	3.2	0.6	0.45	0.4	0.23	-0.84	$10^{46.8}$	<B0.5	B0.5-B1
G044.28+0.11	8.9	5.6	1.32	1.3	1.22	-0.1	$10^{48.3}$	O9.5-B0	O8-O9
G044.34-0.82	5.1	3.4	0.12	0.1	0.09	-0.26	$10^{47.3}$	<B0.5	B0-B0.5

[a]Smoothed to the resolution of the 11 cm images for calculating the spectral index.

[b]Assuming 30% errors in the radio continuum measurements, the uncertainties in the spectral indices are approximately 0.7-0.8.

[c]Determined from $\log_{10}(Q_{Ly})$ and Vacca et al. (1996), assuming a dwarf (luminosity class V) star.

[d]Determined from $\log_{10}(Q_{Ly})$ and Smith et al. (2002), assuming solar metallicity and a dwarf (luminosity class V) star.

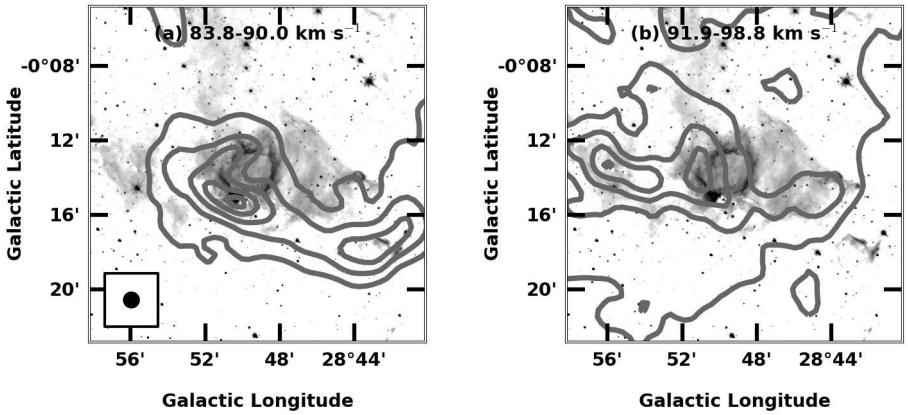

Fig. 2.13.— Contours of BU-GRS ^{13}CO J=1-0 emission integrated over two velocity components possibly associated with the H II region G028.83-0.25, plotted over the 8 μm IRAC image. The first component (*left*) is integrated over the velocity range 83.8 – 90.0 km s^{-1}, and the second component (*right*) is integrated over the velocity range 91.9 – 98.8 km s^{-1}. The 46″ beam is shown in the lower left corner of panel (a). Contours are plotted as 95, 80, 60, 40, and 20% of the peak value in panel (a), 17.8 K km s^{-2} antenna temperature.

not know that the ammonia and ^{13}CO have the same $T_{\rm ex}$ or trace the same volume. Paron et al. (2011) assumed $T_{\rm ex}$ = 20 K for similar analysis around the H II region G35.673-00.847. Deharveng et al. (2008) estimated the kinetic temperature of molecular gas to be between 14 K and 30 K in Sh2-212 based on ^{12}CO, ^{13}CO, and C^{18}O. We assume a value of $T_{\rm ex}$ = 20 K with an uncertainty of 10 K, and thus we obtain

$$N(^{13}\mathrm{CO}(1-0)) = 1.25 \times 10^{15} \frac{\int T_B \, dv}{\mathrm{K\ km\ s^{-1}}}\ \mathrm{cm^{-2}}. \tag{2.3}$$

We adopt a conversion factor $N(\mathrm{H_2})/N(^{13}\mathrm{CO}) = 5 \times 10^5$ from Simon et al. (2001) (assuming $R(^{12}\mathrm{CO}/^{13}\mathrm{CO}) = 45$ (Langer & Penzias 1990) and $X(^{12}\mathrm{CO}) = 8 \times 10^{-5}$ (Blake et al. 1987)), and thus the column density of the total molecular gas is

$$N(\mathrm{H_2}) = 6.24 \times 10^{20} \frac{\int T_B \, dv}{\mathrm{K\ km\ s^{-1}}} \mathrm{cm^{-2}}. \tag{2.4}$$

We note that a 50% uncertainty in $T_{\rm ex}$ (20 $\pm$ 10 K) introduces an uncertainty of about 35% in each of the column density and mass of molecular gas. Both column density and mass also scale linearly with our choice of $N(\mathrm{H_2})/N(^{13}\mathrm{CO}(1{-}0))$, and rely heavily on our assumption of LTE. The mass additionally depends our adopted distance. Contours of column density are shown in Figures 2.7, 2.8, 2.9, 2.10, 2.11, and 2.12. To calculate the mass of the gas in each region, we use

$$M = \mu m_{\rm H} D^2 \Omega \sum N(\mathrm{H_2}) = 1.19 \left(\frac{D}{\mathrm{kpc}}\right)^2 \left(\frac{\Omega}{\mathrm{arcmin^2}}\right) \frac{\int T_B \, dv}{\mathrm{K\ km\ s^{-1}}}\ M_\odot, \tag{2.5}$$

where μ is the mean molecular weight in multiples of the proton mass (assumed here to be 2.8), D is the distance to the region, and Ω is the solid angle occupied by the gas.

Next, we identify individual clumps within the molecular cloud structure using the Clumpfind code (Williams et al. 1994) that identifies local maxima in the data cubes and grows the clumps outward, down to lower evenly spaced signal levels until the noise floor is reached. We use the recommended value of twice the RMS for setting both the noise floor and the interval between adjacent contour levels. The result is a catalog of ^{13}CO J=1-0 clumps in position-position-velocity space, with size (full width at half maximum) measurements in galactic longitude ($\Delta\ell_{\rm FWHM,cl}$), galactic latitude ($\Delta b_{\rm FWHM,cl}$), and velocity ($\sigma_{\rm cl}$); we use the subscript "cl" to refer to clumps identified by Clumpfind. Clumpfind also calculates an effective radius, $R_{\rm cl}$, which is the radius of a circle that has the same solid angle on the sky as the clump, though the clump may itself be irregularly shaped.

There are a large number of unresolved or barely resolved clumps in this catalog that are near the noise floor, which are probably not real clumps. Clumpfind may provide several false positives in complex regions, so we apply additional "quality control" cuts to the list of clumps as follows. We first merge the clumps that have antenna temperature peaks in the data cube within $22''$ (1 pixel) of each other in ℓ or b and within $(\sigma_{{\rm cl},i} + \sigma_{{\rm cl},j})/2$ of each other, where the indices i and j correspond to two clumps. Then, we remove the clumps with $\Delta\ell_{\rm FWHM,cl}$ or $\Delta b_{\rm FWHM,cl}$ less than $66''$ (3 pixels), or $\sigma_{\rm cl}$ less than 0.6 km s^{-1} (3 channels), and all of the clumps that have an average antenna temperature below 3 times the RMS of the data. These criteria were determined to (1) produce a final catalog of high confidence clumps and (2) to balance the effects of Clumpfind's tendency to identify extraneous clumps in complicated data sets with the unintended consequence of merging clumps that are truly separate structures. Some of our H II regions still show a large number of clumps, but we consider them to be plausibly distinct structures in the data cubes.

For the remaining reliable catalog, we computed the mass, peak column density, average number density, and nearest neighbor (peak-to-peak) separation in the plane of the sky.

A plot of the masses and effective radii of all the clumps of molecular gas identified in our sample is presented in Figure 2.14. The distribution we find is consistent with the mass-size relation found empirically in 7 molecular clouds by Kauffmann et al. (2010), though our clumps do not reach the smallest scales as they do for the closer regions presented in that study. Ridge et al. (2003) observed ^{13}CO in 30 young stellar clusters within 1 kpc. The molecular clumps we identify in G041.91-0.12 and G041.92+0.04 are consistent with the range of cloud masses and radii seen in that study (marked in Figure 2.14), however we likely cannot resolve the fragments associated with individual clusters in the more distant regions. We interpret the agreement with Kauffmann et al. (2010) as an indication that our quality control cuts are sufficient to remove most spurious Clumpfind detections. However, our inability to resolve parsec-scale clumps must be considered when comparing the observed properties of these clumps to those predicted during "collect and collapse" (CnC).

As noted by Deharveng et al. (2005), dense molecular gas forming part or all of a shell can be an indication of CnC triggered star formation, particularly if the shell is composed of dense fragments of gas. We calculated the column densities and masses of each individual clump as outlined above. To get the number density of the gas, $n(\mathrm{H_2})$, we treat each clump as a sphere with a radius that is equal to the effective radius, $R_{\rm cl}$. We also calculate the virial parameter,

$$\alpha_{\rm vir} = \frac{M_{\rm vir}}{M_{\rm cl}} = \frac{5\sigma_{\rm cl}^2 R_{\rm cl}}{G M_{\rm cl}}, \tag{2.6}$$

for each clump. A virial parameter less than 1 indicates that the clump is likely to

collapse under self-gravity. This assumes that the clumps are spherically symmetric and isothermal, which is clearly not the case, so these values should be viewed with caution. The clumps typically have $\alpha_{\rm vir} \approx 1$, with 23% of all clumps prone to collapse.

All of the measured and calculated parameters for individual molecular clumps are presented in Table 2.6, with a summary of median values and region-wide parameters in Table 2.7.

Table 2.6: Molecular Gas Clump Parameters

$\ell_{\rm peak}$ (deg)	$b_{\rm peak}$ (deg)	$v_{\rm peak}$ (km s^{-1})	$R_{\rm cl}$[a] (pc)	$\sigma_{\rm cl}$ (km s^{-1})	$d_{\rm cl}$[b] (pc)	$N_{\rm cl}(H_2)$[c] (10^{21} cm^{-2})	$n_{\rm cl}(H_2)$ (cm^{-3})	$M_{\rm cl}(H_2)$ ($M_\odot$)	$\alpha_{\rm vir}$[d]
G028.83-0.25 (83.8-90.0 km s^{-1})									
28.850	-0.24	88.26	4.3	1.9	1.7	18.7	274	6103	0.5
28.844	-0.21	85.93	3.3	1.6	3.2	11.0	228	2311	0.8
28.887	-0.20	85.93	3.1	1.2	1.6	5.4	108	899	1.1
28.887	-0.22	87.41	3.5	1.0	1.1	7.1	121	1518	0.5
28.868	-0.24	86.14	2.7	1.5	1.7	7.4	298	1671	0.9
28.887	-0.23	85.93	2.1	1.2	1.1	5.2	233	625	1.0
28.887	-0.26	85.93	2.9	1.6	2.1	6.5	141	1010	1.8
28.795	-0.23	86.14	3.7	2.0	4.5	4.8	99	1478	2.1
28.868	-0.30	87.20	3.9	1.8	4.0	3.9	97	1645	2.0

[a] Clump effective radius

[b] Nearest neighbor (peak-to-peak) separation

[c] Peak column density

[d] $M_{\rm vir}/M_{\rm cl}$

(This table is available in its entirety in Appendix Table B.1. A portion is shown here for guidance regarding its form and content.)

2.3 Results

2.3.1 Assessment of Triggered Star Formation

There are two primary criteria we have checked to see if star formation is plausibly triggered by the CnC process. The first is that we expect an enhanced population of

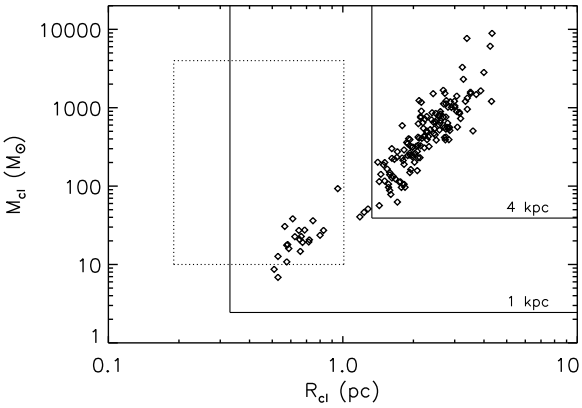

Fig. 2.14.— Effective radius, $R_{\rm cl}$, versus calculated mass of molecular gas, $M_{\rm cl}$, for every clump identified by Clumpfind remaining in our sample after our quality control cuts. The solid lines mark approximate sensitivity and resolution limits using Clumpfind and our quality control cuts on the BU-GRS data, assuming 1 kpc and 4 kpc as labeled. The dotted box shows the range of masses and radii of molecular clumps associated with young stellar clusters within 1 kpc as observed by Ridge et al. (2003).

Table 2.7: Summary of Molecular Gas Properties

	Median Clump Values				Region-wide Values			
Region	$\langle R_{\rm cl}\rangle$[c] (pc)	$\langle d_{\rm cl}\rangle$[d] (pc)	$\langle M_{\rm cl}\rangle$ ($M_\odot$)	$\langle N_{\rm cl}/10^{21}\rangle$ (cm^{-2})	M_{tot}[e] ($M_\odot$)	$n_i/10^3$ (cm^{-3})	$t_{\rm HII}$[f] (10^6 yr)	$\Phi_{\rm Ly}$[g] (cm^{-2} s^{-1})
G028.83-0.25[a]	3.3	1.7	1518	6.5	17264	4.79	0.79	$> 1.65 \times 10^{10}$
G028.83-0.25[b]	3.1	1.8	1194	2.8	31133	4.46	0.83	$> 1.65 \times 10^{10}$
G041.10-0.15	1.8	1.0	202	2.6	19913	1.35	2.1	$> 6.4 \times 10^{9}$
G041.91-0.12	0.58	0.7	18	3.4	177	3.13	0.31	$> 3.8 \times 10^{9}$
G041.92+0.04	0.67	0.3	23	2.3	357	3.27	0.19	$> 5.6 \times 10^{9}$
G044.28+0.11	2.5	1.7	534	3.7	29180	1.19	2.41	$> 2.1 \times 10^{9}$
G044.34-0.82	2.5	1.6	656	4.0	9534	1.73	2.12	$> 0.6 \times 10^{9}$

[a] 83.8 – 90.0 km s^{-1}

[b] 91.9 – 98.8 km s^{-1}

[c] Median molecular clump radius.

[d] Median clump peak-to-peak separation.

[e] Sum of molecular clump masses.

[f] Dynamical age of the H II region.

[g] Ionizing flux.

Stage I YSOs on or within the infrared bright bubbles and rims surrounding the H II regions (a similar enhancement is expected from "radiatively driven implosion" (RDI) as well). Second, Whitworth et al. (1994) predicted the fragmentation timescale and size, column density, mass, and separation of the typical fragments of the molecular gas comprising the expanding spherical shell of the H II region. Assuming a single (or compact) ionizing source and an initially uniform number density of gas, these values are given by:

$$t_{\rm frag} \approx 1.56 \left(\frac{a_s}{0.2 \text{ km s}^{-1}}\right)^{7/11} \left(\frac{Q_{\rm Ly}}{10^{49} \text{ s}^{-1}}\right)^{-1/11} \left(\frac{n_i}{10^3 \text{ cm}^{-3}}\right)^{-5/11} \text{Myr}, \quad (2.7)$$

$$R_{\rm frag} \approx 5.8 \left(\frac{a_s}{0.2 \text{ km s}^{-1}}\right)^{4/11} \left(\frac{Q_{\rm Ly}}{10^{49} \text{ s}^{-1}}\right)^{1/11} \left(\frac{n_i}{10^3 \text{ cm}^{-3}}\right)^{-6/11} \text{pc}, \quad (2.8)$$

$$N_{\rm frag} \approx 6.0 \times 10^{21} \left(\frac{a_s}{0.2 \text{ km s}^{-1}}\right)^{4/11} \left(\frac{Q_{\rm Ly}}{10^{49} \text{ s}^{-1}}\right)^{1/11} \left(\frac{n_i}{10^3 \text{ cm}^{-3}}\right)^{5/11} \text{cm}^{-2}, \quad (2.9)$$

$$M_{\rm frag} \approx 23 \left(\frac{a_s}{0.2 \text{ km s}^{-1}}\right)^{40/11} \left(\frac{Q_{\rm Ly}}{10^{49} \text{ s}^{-1}}\right)^{-1/11} \left(\frac{n_i}{10^3 \text{ cm}^{-3}}\right)^{-5/11} M_\odot, \text{ and} \quad (2.10)$$

$$d_{\rm frag} \approx 0.83 \left(\frac{a_s}{0.2 \text{ km s}^{-1}}\right)^{18/11} \left(\frac{Q_{\rm Ly}}{10^{49} \text{ s}^{-1}}\right)^{-1/11} \left(\frac{n_i}{10^3 \text{ cm}^{-3}}\right)^{-5/11} \text{pc}, \quad (2.11)$$

where a_s is the sound speed in the neutral gas, $Q_{\rm Ly}$ is the Lyman continuum (ionizing) luminosity in photons s^{-1}, n_i is the initial density of the molecular gas before H II region expansion, $t_{\rm frag}$ is the timescale for fragmentation to begin, $R_{\rm frag}$ is the radius of the fragments, $N_{\rm frag}$ is the column density of the fragments, $M_{\rm frag}$ is the mass of the fragments, and $d_{\rm frag}$ is the separation of fragments. We use the term "clump" to refer to collections of gas identified in the data by Clumpfind, and "fragment" to refer to theoretical collections of molecular gas predicted by Whitworth et al. (1994). Observing molecular cloud clumps consistent with the quantities predicted in Equations 2.7, 2.8, 2.9, 2.10, and 2.11 indicates that CnC is at least plausible in a

particular region.

Dale et al. (2007a) performed SPH simulations of expanding H II regions to test the validity of this analytical model. They found that fragmentation in the expanding shell did occur and that the time for fragmentation agreed with the prediction of Whitworth et al. (1994) to within 20%. Furthermore, they found that the fragment masses were approximately half of the values predicted by the analytical model.

The predicted values of Whitworth et al. (1994) all depend on three parameters: the sound speed, the ionizing luminosity, and the initial density. The sound speed of neutral gas is expected to vary in the range 0.2–0.6 km s^{-1}, and so without a method of measuring this parameter we assume a value of 0.2 km s^{-1} (Whitworth et al. 1994; Dunham et al. 2011). The predicted fragment masses can vary by an order of magnitude because of a factor of 2 uncertainty in the sound speed, whereas the other predicted molecular fragment properties are fairly insensitive to this uncertainty. We have the ionizing luminosity measurements with uncertainties from analyzing the 21 cm radio continuum. To estimate the initial density of the gas before H II region expansion, we calculate the average number density in the bubble region using the analysis from §2.2.4 to calculate the mass integrated over the gas apparently associated with the bubble or rim (i.e. the mass in the shell exterior to the ionization front). We integrate over the full velocity range of the associated emission and within an irregular aperture determined by eye, though using the distribution of positions in the molecular clump catalog as a guide. We then follow the method of Paron et al. (2011) to estimate the volume by assuming the thickness along the line of sight is equal to the radius of the region, $R_{\rm HII}$. If the gas is being collecting by an expanding shell, then the *average* density in this volume now should still be equal to the average density before expansion began (i.e. the same amount of gas in the same volume, but

distributed differently). Assuming 25% uncertainty in the angular size of the regions and using the uncertainties stated in §2.2.4, the initial densities of molecular gas are uncertain to within a factor of 3.6 larger or smaller than our quoted values. We assume uncertainty of a factor of 2 in the sound speed, thus the uncertainties in our CnC predictions for the formation time, size, column density, mass, and separation of molecular clumps are approximately factors of 2.4, 2.5, 2.2, 5.4, and 3.43, respectively.

We estimate the ages of the H II regions using a dynamical age from Dyson & Williams (1980), assuming spherical expansion:

$$t_{\rm HII} = 7.2 \times 10^4 \left(\frac{R_{\rm HII}}{\rm pc}\right)^{4/3} \left(\frac{Q_{\rm Ly}}{10^{49}\ {\rm s}^{-1}}\right)^{-1/4} \left(\frac{n_i}{10^3\ {\rm cm}^{-3}}\right)^{-1/2} {\rm yr}, \tag{2.12}$$

where $R_{\rm HII}$ is the radius of the region, $Q_{\rm Ly}$ is the ionizing luminosity, and n_i is the initial number density of the gas. We compare these ages with the fragmentation timescales for CnC from Whitworth et al. (1994) to see if they are consistent with the CnC scenario, $t_{\rm HII}/t_{\rm frag} \geq 1$. Following the uncertainties above, these ages may be a factor of 3 larger or smaller than our quoted values. Quantitative results are in §2.3.2.

Bisbas et al. (2011) modeled RDI through simulations of ionizing flux permeating into a molecular cloud. They find that for a 5 $M_\odot$ Bonnor-Ebert sphere, star formation is triggered by the radiation field if the ionizing flux, $\Phi_{\rm Ly}$, meets the criterion $10^9 \lesssim \Phi_{\rm Ly} \lesssim 3 \times 10^{11}$ cm^{-2} s^{-1}. The first stars then form when the age of the H II region is approximately

$$t_\star \approx 0.19 \left(\frac{\Phi_{\rm Ly}}{10^9\ {\rm cm}^{-2}\ {\rm s}^{-1}}\right)^{-1/3} {\rm Myr}. \tag{2.13}$$

We estimate the ionizing flux $\Phi_{\rm Ly}$ from the ionizing luminosity, $Q_{\rm Ly}$, and the size of the regions. We are then able to predict whether YSOs may have been formed from

RDI by taking the ratio of the dynamical age of the H II region and the time for RDI to begin: $t_{\rm HII}/t_\star \geq 1$. We note, however, that we used the current sizes of the regions to calculate $\Phi_{\rm Ly}$, while the size would have been smaller at any time in the past. Furthermore, sites of triggering may be closer to the ionizing sources than the rims, so our $t_\star$ values will be upper limits, whereas the values of $\Phi_{\rm Ly}$ and $t_{\rm HII}/t_\star$ will only be lower limits.

Due to the nature of RDI, quantitative predictions of the outcome of this process require detailed knowledge of the molecular gas before the expansion of the ionization front. This fact, combined with our ability to only place limits on the timescale for YSO formation, make it impossible to make strong statements about the contribution from RDI in our sample. We can only say that all of our regions are at least consistent with this scenario.

2.3.2 Results of Individual H II Regions

G028.83-0.25 (N49)

As seen in Figure 2.13 and previously mentioned, G028.83-0.25 (coincident with IRAS 18421-0348) has two velocity components in ^{13}CO J=1-0 possibly associated with the region, both part of larger structures. The components, located at about 87 and 95 km s^{-1}, are on either side of the recombination-line velocity, 90.6 km s^{-1}, from Anderson & Bania (2009). It may be that these two components are the front and back of an expanding shell of molecular gas, or they may be two unrelated clouds and either one could be association with the infrared bubble. We favor the 87 km s^{-1} component as the morphology in the integrated map better matches the infrared rim, but we present results below from analyzing the two components separately.

The infrared bubble is nearly circular and shows no indication of cometary mor-

phology. The region is 2.′8 across, corresponding to 2 pc at the near kinematic distance. The radio continuum seen by VGPS is highly peaked at the center of the infrared bubble, with a flux density of $\sim$ 1 Jy. We calculate the ionizing luminosity necessary to power the region, $Q_{\rm Ly}$, to be $10^{48.3}$ photons s^{-1}, which corresponds to a spectral type O8-O9, following Smith et al. (2002) (assuming solar metallicity and luminosity class V).

Deharveng et al. (2010) analyzed this region at 870 μm and reported a "half ring" of material with massive clumps coincident with the infrared rim. They concluded that this region is a good candidate for triggered star formation, specifically CnC. Furthermore, they determined the mass in the dense shell to be 4200 $M_\odot$, with clumps of 2300, 350, 240, and 190 $M_\odot$. Deharveng et al. (2010) also reported an ionizing luminosity of $10^{48.48}$ photons s^{-1} (corresponding to an O7 V - O7.5 V star) based on MAGPIS 20 cm radio continuum data. MAGPIS data have 6$''$ resolution images made from VLA B, C, and D array and Effelsburg 100 m observations (Helfand et al. 2006).

Cyganowski et al. (2008) found an Extended Green Object (EGO), G028.83-0.25, located on the southern portion of the bright rim ($(\alpha, \delta)_{\rm J2000} = (18^h44^m51.3^s, -03°45'48'')$) (in this chapter, we use the terms north, south, east, and west defined so that "north" describes the direction of increasing galactic latitude, and "west" describes the direction of increasing galactic longitude). EGOs are extended objects that are bright in the 4.5 μm IRAC band and are thought to be the result of jets or other outflow activity from a protostar (e.g. De Buizer & Vacca 2010; Ybarra et al. 2010). The emission is expected to be from shocked H_2 in the outflow. Additionally, this site is coincident with Class I and Class II methanol maser emission in the velocity range 79.5 - 92.67 km s^{-1} (Cyganowski et al. 2009), consistent with the lower velocity ^{13}CO

J=1-0 component. The EGO does not correspond to a YSO because there is not a source detectable in enough wavebands to be fit via our method (it is either not seen or only appears as an extended object larger than our aperture in our wavebands). A second nearby EGO, G28.28-0.36, is identified by Cyganowski et al. (2009) who, along with Walsh et al. (1998), report Class II methanol maser emission coincident with this EGO and with velocities consistent with the higher velocity ^{13}CO J=1-0 component. We describe these EGOs and masers here because they are evidence of massive star formation on the rim of this region. We do not identify YSOs at these locations, as no point source is visible in this portion of the rim longward of 4.5 μm. The absence of these two objects from the sample is not evidence that they do not contain protostars, but rather is consistent with heavily embedded MYSOs. We note that there is one Stage I YSO identified approximately 10$''$ to the west of the EGO.

Shown in Figure 2.7, the concentration of Stage I (unevolved) YSOs peaks on the infrared bubble. The peak density is more than three times the density of Stage I YSOs surrounding the region. The overall distribution of YSOs follows features in the molecular gas distribution from each velocity component.

Watson et al. (2008) analyze the structure and YSO population of G028.83-0.25 as part of their sample of 3 bubbles. They report an ionizing luminosity of $10^{48.89}$ photons s^{-1}, almost four times as large as our value. This is in part due to their adoption of a slightly larger distance to the region (5.7 kpc), and likely also because they use the MAGPIS 20 cm survey to measure the radio continuum. The MAGPIS data have 6$''$ angular resolution (Helfand et al. 2006), better than the VGPS images used in this work (we use the VGPS because it covers our entire sample). Due to the weak dependence on ionizing luminosity, the CnC predictions change by less than 15% from a factor of 4 difference in $Q_{\rm Ly}$ (see Equations 2.7, 2.8, 2.9, 2.10, and 2.11). Watson

et al. (2008) note that the local minimum in 24 μm emission at the center of the bubble suggests that there is a central wind from the ionizing star evacuating the dust in the central region. Watson et al. (2008) also identify the likely ionizing source, an O5 V star coincident with the bubble center and the 24 μm minimum. They additionally report 7 YSOs in the immediate vicinity of this region using the SED fitting method presented here. Our sample of YSOs includes 5 of the YSOs reported in Watson et al. (2008), and the reported physical parameters are generally in good agreement. We find discrepant values for one source in particular, the YSO G28.8299-00.2532. Watson et al. (2008) report a mass of 29 $M_{\odot}$ and accretion rate of $8.9 \times 10^{-4} M_{\odot}$ yr^{-1}, compared to our values of 6 $M_{\odot}$ and accretion rate of $8.0 \times 10^{-5} M_{\odot}$ yr^{-1}. The most likely reason for this discrepancy is that Watson et al. (2008) specifically decided to use a lower limit on the 24 μm photometry for this source, whereas our method applied an upper limit at a different value. This YSO is in a region of high, nonuniform background, so 24 μm photometry is not straightforward.

Everett & Churchwell (2010) modeled the dust distribution in this region with the Cloudy software package and simulated the 24 μm emission. They were able to match the observations using a model of a wind-blown bubble (WBB), providing further evidence that a stellar wind is at work in the central cavity. Their model is consistent with an age of 0.5-1 Myr. Whitworth et al. (1994) give a different set of equations to predict the properties of the molecular gas in regions triggered by stellar winds than by expanding H II regions. It is difficult to assess the relative contribution of these two reasons for region expansion with currently available data, particularly without a way to measure the power in the stellar wind. We therefore proceed with the analysis for an expanding H II for all of our sources. We do note that for G028.83-0.25, the estimated dynamical age ignoring the effects of wind agrees with the age

from the WBB model of Everett & Churchwell (2010), so our analysis is still viable when viewed with caution.

The identification of clumps of molecular gas and the characterization of this gas is more complicated for G028.83-0.25 than any other H II region in our sample. The two velocity components that lie along the line of sight to this region are marginally resolved in velocity in the BU-GRS data. In Table 2.6, one can see that over half of the clumps in each component have virial parameters indicating likelihood to collapse under self-gravity. Coincidentally, the average density of the gas over the bubble region is nearly the same for both velocity components, so our estimates of the dynamical age and expected fragment parameters for CnC are largely unaffected by our choice of component. If instead we included the total emission from both components but assumed the same volume occupied by the gas, the CnC predictions and dynamical age of the region would change by less than a factor of 1.4; $N_{\rm frag}$ and $t_{\rm HII}$ would increase, while the other quantities would decrease.

The ages of the regions using Dyson & Williams (1980) are presented in Table 2.7, and the predicted timescales and molecular fragment properties from Whitworth et al. (1994) and Bisbas et al. (2011) are given in Table 2.8. We find that G028.83-0.25 has a dynamical age of about 0.8 Myr and has a total mass in molecular gas of at least a few times 10^4 $M_\odot$. The dynamical age depends on the physical size of the region, the initial density, and the Lyman continuum luminosity. The mass is dependent on the distance, the integrated ^{13}CO intensity, and assumed values of the excitation temperature and the conversion factor $N(\mathrm{H_2})/N(^{13}\mathrm{CO}) = 5 \times 10^5$ (Simon et al. 2001). The mass we report is several times that reported by Deharveng et al. (2010), however they focused on a significantly smaller region immediately around the infrared rim (which we cannot probe with the resolution of the BU-GRS data).

For either velocity component, we calculate that the dynamical age of the region, 0.79 or 0.83 Myr for the low or high velocity component, respectively, is within uncertainty of being consistent with the timescale for CnC to begin, 0.9 Myr for both components. As happens to be true of all of our regions, the limits on the formation timescales for YSOs triggered by RDI, less than 0.08 Myr in the case of either velocity component of G028.83-0.25, are consistent with the dynamical ages of the H II regions. For this region, we predict that molecular fragments experiencing CnC should be approximately 2 pc in radius, have column densities of about 1×10^{22} cm^{-2}, be 13 $M_{\odot}$, and be separated by 0.5 pc. The median values of the observed molecular clumps for each of the two velocity components are about 3 pc in radius (for both components) and have column densities of 2.8×10^{21} cm^{-2} and 6.5×10^{21} cm^{-2}, 1200 and 1500 $M_{\odot}$, and have median separations of 1.8 pc and 1.7 pc for the high and low velocity components, respectively. For both velocity components the dynamical ages and median clump sizes are consistent with CnC predictions. The median column density of clumps in the lower velocity component is also consistent with CnC. The median separation of clumps in each component is approximately at the edge of the uncertainty range for being consistent with the CnC prediction. These values are presented in Table 2.7.

Zavagno et al. (2010a) presented a case study of G028.83-0.25 using *Herschel*-PACS and -SPIRE data from the Hi-GAL survey, in addition to GLIMPSE, MIPSGAL, and ATLASGAL 870 μm data, to investigate this region as a candidate for triggering. They identified four condensations at 870 μm, and applied the same SED fitter and YSO models used here, though using apertures 40-100$''$ in size and only employing *Herschel* photometry. Four of our YSOs (as well as the EGO identified by Cyganowski et al. (2008)) are coincident with three of their condensations. We

determine all four of these YSO to be Stage I, with masses 1.5-6.2 $M_{\odot}$. They further use Whitworth et al. (1994) to estimate the parameters $t_{\rm frag}$, $R_{\rm frag}$, and $N_{\rm frag}$ for CnC as 0.5 Myr, 1.55 pc, and 1.6×10^{22} cm^{-2}, respectively. These values agree with ours, taking into account that Zavagno et al. (2010a) used a slightly larger distance (5.5 kpc). They also conclude that this region would be better evaluated using a model accounting for the dynamics of the apparent stellar wind.

Beaumont & Williams (2010) performed a study of several infrared bubbles, including G028.83-0.25, G041.92+0.04, and G044.34-0.82, using JCMT CO (3-2) and MAGPIS survey 20 cm emission. For G028.83-0.25, they analyze the molecular gas at 87.5 $\pm$ 3.1 km s^{-1}. They list the size of the bubble as 1.77 $\pm$ 0.43 pc, the 20 cm flux as 0.985 Jy, and an ionizing luminosity of $10^{48.21}$ photons s^{-1}. These quantities are all consistent with ours.

G041.10-0.15

G41.1-0.15 is a cometary region in 8 μm emission, and spans 6 pc at 4 kpc. The morphology of the molecular gas very closely follows the 8 μm rim, but also extends to the east. The radio continuum peaks very close to the infrared rim, and has a total flux density of 5.5 Jy. We calculate the ionizing luminosity necessary to power the region, $Q_{\rm Ly}$, to be $10^{48.8}$ photons s^{-1}, which corresponds to a spectral type O7-O7.5, following Smith et al. (2002). The supernova remnant 3C 397 (also known as SNR G041.1-00.3) is seen in the 24 μm and radio continuum images to the south of the region. At a distance of 10.3 kpc (Jiang et al. 2010), it is unrelated to G041.10-0.15.

One might naively assume that the very bright point source present near the center of the bubble is the star powering this region; in fact this region shows a minimum in the 24 μm emission around this source, which may be evidence of a

central stellar wind as in G028.83-0.25. However, this star is identified as V844 Aql, an M6 variable AGB star (Høg et al. 2000). We verified this classification with spectral observations performed with the Fan Observatory Bench Optical Spectrograph at the Fan Mountain Observatory operated by the University of Virginia. V844 Aql is thus most likely in the foreground and unrelated to the region of interest. G041.10-0.15 may contain a wind-blown bubble (WBB), though the true ionizing source may be obfuscated by V844 Aql. The morphology of the 24 μm emission may also be explained by the cometary nature of the region.

G041.10-0.15 has a very clearly enhanced population of Stage I YSOs around and in the bubble region (Figure 2.8). The area of enhanced YSO density follows the molecular gas in general, however the Stage I YSOs show the greatest density within the bubble only and not as greatly in the extended molecular gas. The collection of YSOs in the eastern portion of the bubble shows preferentially less evolved YSOs compared to the field YSOs in this region. There are multiple 24 μm point sources located around the rim that were not detected at shorter wavelengths and thus not identified as YSOs by our SED fitting, but are candidate embedded protostars. In addition, there are two infrared dark clouds (IRDCs) seen against the emission of the rim; one in the east and one in the south-southwest. We cannot be certain whether or not these clouds are part of the same structure as the infrared rim.

Unlike G028.83-0.25, the molecular gas around the rim is easily separated into distinct clumps with Clumpfind, particularly the gas coincident with the infrared rim (see Table 2.6). The total mass in molecular gas is about 2×10^4 $M_\odot$. There are over 60 distinct clumps, however only about 15% of them are prone to collapse. The region has a dynamical age of about 2.1 Myr, and we calculate the expected timescale for CnC to begin to be 1.4 Myr. The limit on the timescale for RDI is less than 0.10

Myr. The CnC fragments are predicted to be 4.8 pc in radius and have 6.6×10^{21} cm^{-2} column density, 20.8 $M_{\odot}$, and 0.7 pc separation. The observed clumps have typical radius 1.8 pc, 2.6×10^{21} cm^{-2} column, 202 $M_{\odot}$, and 1 pc separation (see Table 2.8). The dynamical age and separations of clumps are within uncertainties of the values necessary for CnC, but the sizes, column densities, and masses are not.

G041.91-0.12

G041.91-0.12 is a great example of a so-called cometary, or blister, H II region. The morphology indicates that after some initial expansion it opened on one side, possibly due to ambient gas of lower density on the side of the opening. The opening is currently 0.8 pc across. Nevertheless, G041.91-0.12 is interesting as a potential location for triggered star formation because of its bright rim and very closely matching morphology in molecular gas. The H II region is seen immediately to the east of the infrared rim, with a flux density of 0.5 Jy. We calculate the ionizing luminosity necessary to power the region, $Q_{\rm Ly}$, to be $10^{46.9}$ photons s^{-1}, which corresponds to a spectral type B0.5-B1. The image of radio continuum emission (Figure 2.9) confirms that the ionized gas is extended in the direction of the opening.

G041.91-0.12, seen in Figure 2.9, is in close proximity on the sky and in radial velocity to G041.92+0.04 (Figure 2.10), so we surveyed one continuous region from the GLIMPSE point source catalog to search for YSOs and to provide the field sample. We then performed the clump decomposition and evaluated the evidence for triggering in each region separately. Both regions are part of the same larger, diffuse structure of molecular gas that is continuous in position-position-velocity space, though the dense shells where distinct clumps were identified were well separated. The spatial density of Stage I YSOs seen in Figure 2.9 peaks on the infrared rim coincident with

a molecular gas peak.

Despite being much closer than most of the other regions in our sample, it is still very difficult to resolve distinct clumps in the molecular gas. Only 6 distinct clumps are identified in Table 2.6, with a total mass of less than 200 $M_{\odot}$, and none of them have virial parameters indicating likelihood to collapse. The region has a dynamical age of 0.3 Myr, which is about 1 Myr less than the predicted time for fragments to start experiencing CnC. The limit on the timescale for RDI is less than 0.12 Myr. The fragments are predicted to be 2 pc in radius and have 6.5×10^{21} cm^{-2} column density, 21.3 $M_{\odot}$, and 0.8 pc separation. The observed clumps have typical radius 0.58 pc, 3.4×10^{21} cm^{-2} column, 18 $M_{\odot}$, and 0.7 pc separation (see Table 2.7). The median column density, mass, and separation of the molecular clumps are consistent with CnC.

G041.92+0.04 (N80)

G041.92+0.04, seen in Figure 2.10, has a round geometry, and is 0.6 pc across. The radio continuum peaks within the bubble, with a total flux density of 0.45 Jy at 21 cm. There is a local minimum in the 24 μm emission at the center of the bubble, possibly indicating this is a WBB. We calculate the ionizing luminosity necessary to power the region, $Q_{\rm Ly}$, to be $10^{46.8}$ photons s^{-1}, which corresponds to a spectral type B0.5-B1. The molecular gas emission, though relatively weak, shows two spatially separated components around the bubble, one to the northwest and one to the southeast. Deharveng et al. (2010) reported that the 870 μm emission shows several clumps located around the bubble, indicating this region is a good candidate for CnC triggering.

A look at the YSO sample reveals that there is only slight evidence that there is

a significant YSO population on the rim in Figure 2.10. The enhancement of YSO density coincident with the bubble is weaker than the enhancement to the southeast that is not coincident with strong molecular gas or radio continuum emission (see above). Watson et al. (2010) reported that they also did not find a significant YSO population associated with this bubble. Of the four brightest point sources on the rim, three are classified as Stage II YSOs.

Like G041.91-0.12, the molecular gas is not readily identified as distinct clumps. A total of 16 clumps are found, presented in Table 2.6, with a total mass of about 350 $M_{\odot}$, though again none are prone to collapse as determined by their virial parameters. The dynamical age for this region is 0.2 Myr, which is over 1 Myr less than the calculated time for CnC to begin triggering. The limit on the timescale for RDI is less than 0.11 Myr. CnC fragments are predicted to be 1.9 pc in radius and have 6.5×10^{21} cm^{-2} column density, 21.3 $M_{\odot}$, and 0.8 pc separation. The observed clumps have a median radius 0.67 pc, 2.3×10^{21} cm^{-2} column, 23 $M_{\odot}$, and 0.3 pc separation (see Table 2.7). The median column density, separation, and mass of the molecular gas clumps are within uncertainty of the CnC predictions.

Beaumont & Williams (2010) found that G041.92+0.04 has a size of 0.48 $\pm$ 0.11 pc, a 20 cm flux of 0.254 Jy, and an ionizing luminosity of $10^{46.21}$ photons s^{-1}. We measured a radio continuum flux about a factor of two higher using the VGPS data, but the other quantities are consistent with ours.

G044.28+0.11 (N91)

G044.28+0.11, seen in Figure 2.11, is among the more interesting regions in the sample. It is the largest in both angular and physical extent. There is a portion of a round, bright rim in the east, but is a cometary H II region overall. The radio

continuum peaks immediately to the west of the 8 μm rim, coincident with the 24 μm emission. The total flux density from VGPS is 1.3 Jy, indicating an ionizing luminosity of $10^{48.3}$ photons s^{-1}, which corresponds to a spectral type O8-O9. The molecular gas is concentrated along the infrared rim, and the region is approximately 5.6 pc across. Deharveng et al. (2010) noted several 870 μm condensations, including one coincident with the PDR. They suggest this region is a good candidate for triggering through either CnC or RDI.

Seen in Figure 2.11, the YSO sample clearly shows locations of enhanced densities of Stage I YSOs coincident with the bright rim and the molecular gas. The greatest concentration is in the southeastern portion of the rim, which has 14 Stage I YSOs, though there are also concentrations on the northern portion of the rim and near the end of the southern portion of the rim. The estimated evolutionary stages of the YSOs show that these areas also have systematically less evolved YSOs than the surrounding regions. MSX6C G044.3103+00.0416 is a MYSO previously identified by Urquhart et al. (2009) as part of the RMS survey. They further detected a 6.4 mJy 6 cm continuum source toward this source with the VLA. This source was classified as a Stage I YSO by our YSO fitting (as G044.3102+00.0410), with a mass of 7.5$\pm$1.79 $M_{\odot}$ and luminosity $10^{3.19\pm3.17}$ $L_{\odot}$. The SED fitting determines a distance of 4.48$\pm$0.8 kpc and A_V=14.05$\pm$5.73. Pandian et al. (2007) also report a Class II methanol maser coincident with this location.

There is a lack of YSOs in the center of the infrared rim, neighboring the radio continuum peak and the 24 μm emission. There is a fairly sharp transition in 8 μm emission, and there is an "elephant trunk," or pillar, feature in the rim with one faint, moderately extended source near the end of it. This feature is an indication of RDI (Lefloch & Lazareff 1994). The faint point source may be an embedded

protostar missed by our SED fitting, and the trunk structure may be formed by the advancing ionization front clearing away gas surrounding the overdensity progenitor to this protostar.

Like G041.10-0.15, a large number of molecular clumps are easily identified by Clumpfind in this region, particularly along the infrared rim (see Table 2.6). A total of 45 clumps are identified, with a total mass of 3×10^4 $M_\odot$, of which 20% are prone to collapse. The dynamical age of G044.28+0.11 is 2.4 Myr, and the CnC fragmentation timescale is only 1.7 Myr. The limit on the timescale for RDI is less than 0.15 Myr. CnC fragments are predicted to be 4.5 pc in radius and have 5.6×10^{21} cm^{-2} column density, 24.7 $M_\odot$, and 0.9 pc separation. The observed clumps have a median radius of 2.5 pc, column density of 3.7×10^{21} cm^{-2}, 534 $M_\odot$, and 1.7 pc separation (see Table 2.7). The dynamical age of the region and the median size, separation, and column density of the molecular clumps are consistent with the predicted values for CnC.

G044.34-0.82 (N92)

G044.34-0.82, seen in Figure 2.12, is 3.4 pc across. It does appear to be a cometary H II region, though it is still fairly round and contained. We may be seeing the back wall of an open shell. The radio continuum and molecular gas emission are concentrated on the infrared rim. With a 21 cm flux density of 0.1 Jy, the region is expected to be powered by a B0-B0.5 star. The molecular gas observations show that it is part of the same larger structure as G044.28+0.11. G044.34-0.82 is far enough away in angular extent from G044.28+0.11 that we use separate YSO field samples. Deharveng et al. (2010) reported 870 μm emission coincident with the IRDC crossing the region.

Shown in Figure 2.12, there is a greatly enhanced population of YSOs, mostly Stage I, near the center of the region, rather than on the rim. One of the YSOs is

coincident with the IRDC. G044.34-0.82 shows the greatest contrast in YSO density between the center of the region and the surrounding field seen anywhere in this study. Watson et al. (2010) also reported a significant YSO population in this region using the same SED fitting method used here, though without 24 μm photometry. They identified 7 YSOs within 3 bubble radii of the center; we identify 14 in the same region.

A total of 13 clumps, with 38% prone to collapse, have a combined mass of 10^4 $M_\odot$ (see Table 2.6). The dynamical age of G044.34-0.82 is 2.1 Myr, while the CnC fragmentation timescale is 1.7 Myr. The limit on the timescale for RDI is less than 0.23 Myr. CnC fragments are predicted to be 3 pc in radius and have 5.4×10^{21} cm^{-2} column density, 25.5 $M_\odot$, and 0.9 pc separation. The observed clumps have a median radius 2.5 pc, 4×10^{21} cm^{-2} column density, 656 $M_\odot$, and 1.6 pc separation (see Table 2.7). The dynamical age of the region and the median size, separation, and column density of the molecular clumps are consistent with the predicted values for CnC.

Beaumont & Williams (2010) found that G044.34-0.82 has a size of 2.09 $\pm$ 0.57 pc, but did not measure the radio continuum.

2.4 Discussion

Every one of our H II regions shows at least some enhancement of the density of YSOs, particularly Stage I YSOs, on the infrared bubbles or rims. The YSO density enhancements also often follow the molecular gas. An overdensity of relatively unevolved YSOs on the rims is suggestive of triggering as opposed to spontaneous collapse throughout the cloud. The rims have the highest and most complex diffuse emission complicating the extraction of point source photometry, so it is even more remarkable that so many YSOs can be identified in such areas. Because the ages

of individual YSOs have considerable uncertainty, the relative evolutionary states of YSOs are a more robust measure than the absolute ages. Images of the YSO density maps are in Figures 2.7, 2.8, 2.9, 2.10, 2.11, and 2.12. All of our regions are consistent with RDI, though we cannot be more precise given that we can only put limits on the expected ionizing fluxes and timescales. We do however note the morphology on the infrared rim/PDR boundary in G044.28+0.11 suggestive of RDI.

For CnC models, the observed values that match the theoretical predictions are summarized in Table 2.9. We first consider the dynamical ages, the time required for fragments to begin to form YSOs, and the molecular gas fragment sizes. We note that, when considering the uncertainties in the parameters, only G041.91-0.12 and G041.92+0.04 are too young to have CnC triggered star formation. G041.91-0.12 is decidedly not a round H II region, so the quantitative predictions of fragment properties we perform should be viewed with caution. The opening would cause the intact portion of the region to cease or significantly slow its expansion, thus causing our estimated age to be a lower limit. A change in the expansion speed would also likely change the time for the shell to collect enough neutral gas to begin fragmentation and collapse. Thus we cannot be certain that this region is in actuality too young to experience CnC without a method of age estimation that correctly accounts for the geometry. In regard to the sizes of the molecular clumps, G041.10-0.15, G041.91-0.12, and G041.92+0.04 do not have any clumps physically large enough to be consistent with CnC in the simple model of Whitworth et al. (1994).

Again referring to Table 2.9, only G028.83-0.25 has clump separations not consistent with the predicted separation within our estimated uncertainty, though only just. The peak column densities we observe are consistent with the predicted values within the uncertainties, with the exceptions of G041.10-0.15 and the higher velocity

Table 2.8: Predicted Molecular Fragments Properties for Triggering

Region	$t_\star$ (10^6 yr)	$t_{\rm HII}/t_\star$ [c]	$t_{\rm frag}$ (10^6 yr)	$R_{\rm frag}$ (pc)	$N_{\rm frag}$ (10^{21} cm^{-2})	$M_{\rm frag}$ ($M_\odot$)	$d_{\rm frag}$ (pc)	$t_{\rm HII}/t_{\rm frag}$ [d]
G028.83-0.25[a]	<0.08	>9.9	0.9	2.1	10.5	13.1	0.5	0.9
G028.83-0.25[b]	<0.08	>10.4	0.9	2.2	10.3	13.4	0.5	0.9
G041.10-0.15	<0.10	>21.0	1.4	4.8	6.6	20.8	0.7	1.5
G041.91-0.12	<0.12	>2.6	1.4	2.0	6.5	21.3	0.8	0.2
G041.92+0.04	<0.11	>1.7	1.4	1.9	6.5	21.3	0.8	0.1
G044.28+0.11	<0.15	>16.1	1.7	4.5	5.6	24.7	0.9	1.4
G044.34-0.82	<0.23	>9.2	1.7	3.0	5.4	25.5	0.9	1.2

[a] 83.8 – 90.0 km s^{-1}

[b] 91.9 – 98.8 km s^{-1}

[c] The ratio of the dynamical age of the region to the timescale for RDI to begin. A value greater than 1 indicates that this is a plausible triggering scenario.

[c] The ratio of the dynamical age of the region to the timescale for CnC to begin. A value greater than 1 indicates that this is a plausible triggering scenario. The ratios for G028.83-0.25 are within uncertainty of a value of 1.

Table 2.9: Correspondence Between CnC Predictions and Observations

Region	$t_{\rm frag}$	$R_{\rm frag}$	$N_{\rm frag}$	$M_{\rm frag}$	$d_{\rm frag}$
G028.83-0.25[a]	Y[c]	Y	Y	N	Y
G028.83-0.25[b]	Y	Y	N	N	N
G041.10-0.15	Y	N	N	N	Y
G041.91-0.12	N	N	Y	Y	Y
G041.92+0.04	N	N	Y	Y	Y
G044.28+0.11	Y	Y	Y	N	Y
G044.34-0.82	Y	Y	Y	N	Y

[a] 83.8 – 90.0 km s^{-1}

[b] 91.9 – 98.8 km s^{-1}

[c] Cell values indicate whether the median clump values are (Y) or are not (N) consistent with the predicted values for CnC. In the case of $t_{\rm frag}$, the value is consistent if the dynamical age of the region is at least as the lower bound on the uncertainty range.

component of G028.83-0.25. The peak column densities in the lower velocity component, however, are consistent with the predictions. Finally, the predicted masses of the clumps for all the regions are in the range 13-26 $M_{\odot}$. Only G041.91-0.12 and G041.92+0.04 have observed clumps consistent with their predicted values; the other regions have clumps much more massive than the predicted values. This is the reverse of the situation with the clump sizes. We note that many of the clumps we identify are at the limit of what we are able to resolve and detect in ^{13}CO J=1-0. The 46″ resolution corresponds to 0.3 pc at 1.35 kpc and 1.0 pc at 4.5 kpc, roughly representative of the distances in our sample. It is possible that the physical clumps are actually smaller than what we have identified. This may account for this mass discrepancy, however it is difficult to reconcile this scenario with the clumps appearing too small to be CnC fragments in some regions.

Given this evidence, we conclude the following. G041.10-0.15, G041.91-0.12, G044.28+0.11, and G044.34-0.82 are good candidates for triggered star formation. G044.28+0.11 is almost certainly experiencing ongoing RDI in the center of its infrared bright rim, if not also CnC around the rest of the edges of the region. G041.10-0.15 and G044.34-0.82 show great enhancement of unevolved YSOs around the bubble region. As seen in Table 2.9, G044.28+0.11 is consistent with all the predictions for CnC fragments from Whitworth et al. (1994) except the masses. G041.10-0.15 is only consistent with the timescales and fragment separations, which might indicate that RDI is more important in this region. The inconsistency with Whitworth et al. (1994) may also be explained by deviations from the assumed, simple geometry. G041.91-0.12 has the least quantitative evidence for CnC of these four, however the incredible match of Stage I YSOs to the infrared rim cannot be ignored, and the excellent example of cometary morphology can easily account for the discrepancy between the

predicted and observed parameters. To illustrate this point, we note that Zuckerman (1973) originally proposed the idea of a blister in the Orion Nebula to resolve an apparent discrepancy between the age of the Trapezium stars and the H II region.

G028.83-0.25 appears morphologically to be a good candidate for triggering given the enhanced density of YSOs. The presence of EGOs and several masers coincident with both the infrared rim and a peak in ^{13}CO J=1-0 emission is highly suggestive, however the quantitative analysis shows that the molecular gas clumps do not have properties consistent with this scenario. Invoking the two velocity components of molecular gas to increase the density estimate is not sufficient to improve the correspondence between predictions and observations. The resulting increase in $t_{\rm HII}$ and decrease in $t_{\rm frag}$ in that scenario makes the timescales consistent with CnC, however the other predicted physical parameters of the molecular gas fragments would show larger disagreement with observed properties.

Finally, G041.92+0.04 is unlikely to be a good example of triggered star formation. The YSO density enhancement is moderate, and predicted CnC parameters typically do not agree with the observed parameters in this region. Since there is no compelling geometric reason to doubt the calculated parameters, it is likely true that this region is not yet old enough to experience CnC. We note that it may in the future, and it is also possible that RDI is responsible for the slight enhancement of YSOs along the infrared rim.

Deharveng et al. (2010) report that most of the bubbles in their sample that were good candidates for triggering were large and apparently evolved regions. They note that G028.83-0.25 (N49) is a relatively smaller and less evolved region despite being a good candidate for triggering, though this can be explained by a relatively high, homogeneous ambient density of gas into which the region is expanding. This

assessment is consistent with our findings. We see the greatest evidence for triggering in regions with cometary morphology, which we interpret as an age effect, consistent with Deharveng et al. (2010). This is, however, at odds with Thompson et al. (2012), who find that bubbles with overdensities of YSOs are systematically the smaller bubbles, which they interpret as the youngest bubbles. It may be that at least some of these bubbles appear small because they are expanding into relatively denser gas, or that they are cometary regions that have slowed their expansion, rather than being younger. Further study, particularly with large samples, is necessary to resolve this issue.

Molecular gas observations with better angular and spectral resolution, thus allowing for more reliable clump decomposition and analysis, would allow for stronger conclusions to be drawn. Also, better estimates of the age of the H II region that do not assume a spherical geometry could provide stronger evidence. The results of Dale et al. (2007a) indicate that the problem is well enough understood that more complex geometries and sets of initial conditions may be explored in simulations.

2.5 Conclusions

The importance of triggered star formation is a key open question in understanding star formation on Galactic scales. Many recent studies of triggering have focused on the sample of MIR-bright bubbles identified in the GLIMPSE survey of the Galactic Plane (see §2.1); the citizen-science Milky Way Project has recently increased the number of such bubbles cataloged in GLIMPSE by an order of magnitude (Simpson et al. 2012). With this explosion in the number of candidate triggered regions, it is important to understand whether the presence or absence of triggering around any given H II region can be reliably evaluated based on existing survey data.

We have performed SED fitting on a large number of infrared point sources around several H II regions, using 2MASS and *Spitzer* near to mid-infrared photometry. We identified 458 objects that are consistent with radiative transfer models of YSOs, but not with stellar atmosphere models or AGB colors. We report properties of the individual candidates, including mass, evolutionary stage, and accretion rate, based on the physical parameters of the best matching model SEDs. The distribution of the YSOs along the bright rims of infrared bubbles as compared to the field populations, as well as their relatively early evolutionary state, provides evidence that triggered star formation is at work. We find that the regions with cometary morphology are the strongest candidates for triggered star formation.

We searched for further evidence of triggered star formation by *quantitatively* comparing the predictions of CnC and RDI triggering models to observations for 6 H II regions spanning a range of morphologies. To evaluate the consistency of models and data from as many angles as possible, we combined publicly available MIR, cm continuum, and ^{13}CO (1-0) surveys to constrain the properties of YSOs and ionized and molecular gas. While the results for many of our regions are suggestive of triggering, the data are insufficient to draw firm conclusions about the triggering mechanism(s). Our analysis suggests that to distinguish CnC and RDI in an individual region, additional data and modeling would be required, including: (1) high-resolution molecular line data to resolve clumps; (2) additional long-wavelength data to identify younger and more deeply embedded YSOs and improve SED coverage; and/or (3) models that account for source geometry to better constrain H II region ages. While (1) would require dedicated observations for each source of interest, the necessary data for (2) will be provided by *Herschel* survey catalogs, allowing the application of statistical techniques (e.g. Thompson et al. 2012; Kendrew et al. 2012) to younger YSOs.

Chapter 3

Single-Dish and Interferometric Observations of Ammonia and CCS in Infrared Dark Clouds

3.1 Introduction

In this study, we mapped the NH_3 (1,1) and (2,2) and the CCS (2_1-1_0) transitions across nine IRDCs containing both ongoing star formation and more quiescent environments. Single-dish data are necessary for determining whether sharp transitions at the edges of the dense structures are real and not a consequence of filtering the extended emission. Fortunately, the NH_3 (1,1) and (2,2) and the CCS (2_1-1_0) transitions may be observed simultaneously with the GBT. It is also important to remember that we likely do not resolve the smallest substructure in these clouds and that interferometric data are even more important. The combination of interferometric and single-dish radio data from the VLA and the GBT gives us the high resolution we need to separate better individual cores and other structures compared with previous work, while also not resolving out emission. The limited number of studies in this regime suggest that the substructure is present because IRDCs represent a phase in which star formation proceeds even as the IRDC itself is still being constructed from colliding clumps and/or gas flowing into the cloud along filaments. A homogeneous study of several representative IRDCs combining total power and high resolution is thus necessary.

We describe the IRDC sample, with distance determination and previous studies of these clouds, in §3.2. Observations and data reduction are described in §3.3. Our methodology is presented in §3.4, including NH_3 spectral line fitting, clump deconvolution, and infrared extinction. Results of investigating the kinematics, the spectral line fitting, and clump properties are in §2.3. A discussion of the results relating to kinematics, structure, gravitational stability, and chemical evolution is presented in §2.4, and conclusions are in §3.7. The work presented in this chapter has been submitted to the Astronomical Journal on 25 June 2014 under the title

"Physical Conditions of the Earliest Phases of Massive Star Formation: Single-Dish and Interferometric Observations of NH_3 and CCS in Infrared Dark Clouds" with the help of coauthors Crystal Brogan, Rémy Indebetouw, Claire J. Chandler, Rachel K. Friesen, and Kathryn E. Devine.

3.2 Sample Selection & Distance Determination

This sample of nine IRDCs, ranging approximately $1'$-$10'$ across, was originally selected in 2005 from extinction features in the 8 μm GLIMPSE images, chosen to cover a wide range of physical parameters. The IRDCs subsequently appeared in a catalog compiled by Simon et al. (2006a), identified by their high contrast against background emission in the 8.3 μm *MSX* images. The sample size is large enough to contain a statistically significant number of cores, but small enough for each object to be studied in detail. The sample contains tens of cores identified by dust thermal continuum, including about half that are coincident with infrared point sources indicating ongoing star formation. The larger IRDCs show both quiescent, starless cores and protostars in close proximity to each other.

We include both filamentary and globular morphologies, apparently starless and protostellar cores, and ranges of physical sizes, masses, linewidths, distances, and infrared contrast. A comparison of this sample with all the IRDCs analyzed by Jackson et al. (2006) in the Boston University Galactic Ring Survey (BU-GRS) data is shown in Figure 3.1 (except G010.74-00.13, which is not covered by the BU-GRS).

We calculated the kinematic distances using the galactic rotation curve of Reid et al. (2009) as described in §2.2.1. All of the regions in our sample were in the $|\ell| < 90^\circ$ regime, so there was naturally a near-far distance ambiguity. Since IRDCs are seen in absorption, we assumed for the rest of this work that all of the regions were

at the near kinematic distance, except for G034.43+00.24. Kurayama et al. (2011) performed parallax measurements of an H_2O maser associated with G034.43+00.24 using Very Long Baseline Interferometry (VLBI) as part of the VLBI Exploration of Radio Astrometry (VERA) project and determined the distance to be $1.56^{+0.12}_{-0.11}$ kpc, which we adopt, less than half of the near kinematic distance of $3.55^{+0.36}_{-0.36}$. A summary of the sample is presented in Table 3.1.

3.3 Observations and Data

3.3.1 GBT Observations

Data from the GBT provide total flux on large spatial scales, which is not measured by our VLA observations. Dates of GBT observations for Project IDs AGBT05C_14 and AGBT12B_283 are listed for each source in Table 3.2. The data are dual polarization taken in frequency switching mode using a 5 MHz shift. Observations in 2005 are in PointMap mode with the single pixel K-band receiver, while data in 2012 are in on-the-fly (OTF) mapping mode using beams 1 and 4 of the 7 possible beams in the K-band Focal Plane Array (KFPA). All observing configurations include simultaneous observation of the NH_3 (1,1) and (2,2) inversions lines and the CCS (2_1-1_0) line, with rest frequencies of 23.6945 GHz, 23.72263 GHz, and 22.34403 GHz, respectively. The expected beam full width at half maximum (FWHM) at these frequencies is approximately $32\farcs$ Hourly pointing scans indicated the actual FWHM of the beam during observing varied between $32''$ and $34''$, and the pointing correction was typically $6\farcs$

The spectral resolution of the raw data varied with telescope configuration, so all data were smoothed to the limiting velocity resolution of approximately 0.15 km s^{-1}.

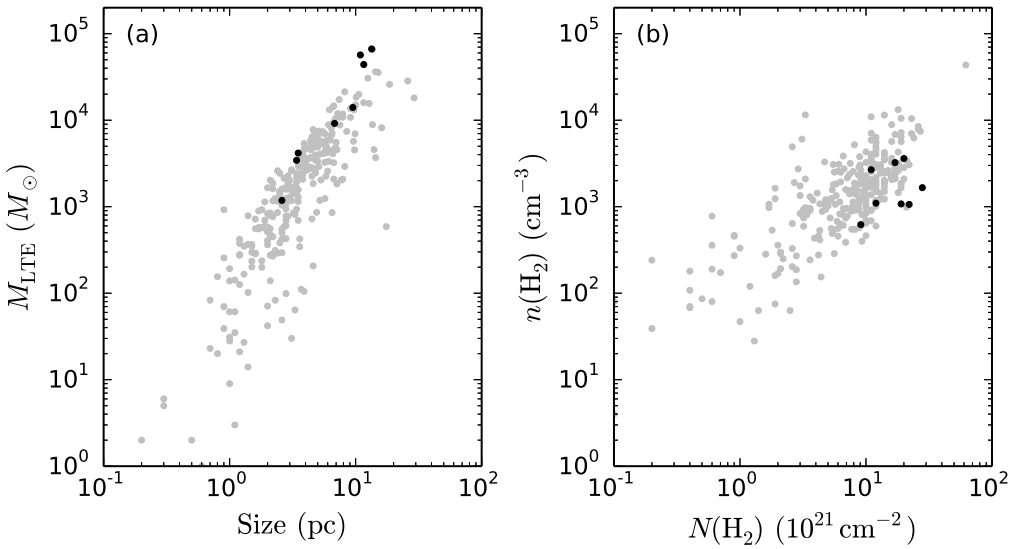

Fig. 3.1.— A comparison of physical parameters of the IRDCs in this sample to all of those in the BU-GRS (Jackson et al. 2006) as analyzed by Simon et al. (2006b). The black points represent IRDCs from this sample (except G010.74-00.13, which was not covered by the BU-GRS).

Table 3.1. IRDC Sample

IRDC	R.A. (J2000) hh:mm:ss.s	Decl. (J2000) dd:mm:ss	$v_{\rm LSR}$ (km s^{-1})	D (kpc)
G010.74-00.13	18:09:45.9	-19:42:04	29.0	$3.46^{+0.46}_{-0.55}$
G022.56-00.20	18:32:59.6	-09:20:08	76.8	$4.55^{+0.26}_{-0.27}$
G024.60+00.08	18:35:39.7	-07:18:52	53.4	$3.45^{+0.32}_{-0.34}$
G028.23-00.19	18:43:30.2	-04:12:56	80.0	$4.50^{+0.30}_{-0.30}$
G031.97+00.07	18:49:30.6	-00:48:18	96.0	$5.60^{+0.42}_{-0.42}$
G032.70-00.30	18:52:06.2	-00:20:26	90.2	$5.23^{+0.45}_{-0.39}$
G034.43+00.24	18:53:18.7	01:25:51	58.0	$1.56^{+0.12}_{-0.11}$
G035.39-00.33	18:57:09.4	02:07:48	44.5	$2.98^{+0.37}_{-0.38}$
G038.95-00.47	19:04:08.4	05:09:12	42.2	$2.80^{+0.40}_{-0.40}$

Table 3.2. GBT Observations

Date	Session #	IRDC	Zenith Opacity
Project ID AGBT05C_14			
2005 Oct 19	1	G010.74-00.13	0.123
2005 Oct 19	2	G038.95-00.47	0.115
2005 Oct 23	3	G010.74-00.13	0.128
2005 Oct 30	6	G022.56-00.20	0.057
2005 Oct 31	7	G022.56-00.206	0.083
2005 Oct 31	7	G024.60+00.08	0.084
2005 Oct 31	7	G032.70-00.30	0.084
2005 Nov 02	8	G032.70-00.30	0.067
2005 Nov 03	8	G038.95-00.47	0.067
2005 Nov 17	9	G032.70-00.30	0.039
2005 Nov 17	9	G038.95-00.47	0.04
2005 Nov 18	11	G028.23-00.19	0.058
2005 Nov 19	11	G038.95-00.47	0.056
2005 Dec 24	12	G028.23-00.19	0.066
Project ID AGBT12B_283			
2012 Nov 05	2	G034.43+00.24	0.048
2012 Nov 14	3	G034.43+00.24	0.043
2012 Dec 05	4	G031.97+00.07	0.041
2012 Dec 05	4	G035.39-00.33	0.040

System temperatures typically varied between 40 and 60 K. Absolute flux calibration of the 2012 observations was tied to beam nodding scans of Venus on 2012-12-05. We utilized the Green Bank Telescope Interactive Data Language (GBTIDL) procedures `venusmodel`, `venuscal`, and `venuscalget`, documented in GBT memo #275,[1] to model the antenna temperature of Venus at a given date, time, and elevation, and to calculate the aperture efficiency. This model corrected for the distance to Venus and any beam dilution if it was unresolved, but did not account for variations across the surface of Venus. The determined aperture efficiency, η_A, of 0.64 was in good agreement with the value of 0.63 from the Ruze equation and the GBT sensitivity calculator. From this value, we also calculated the main beam efficiency to be $\eta_{\rm mb} = 1.37\eta_A = 0.88$ as noted in "Calibration of GBT Spectral Line Data in GBTIDL v2.1."[2]

The primary uncertainty in the efficiency estimates come from the possibility of pointing errors in the observations of Venus, which will tend to cause us to underestimate the aperture efficiency. Given typical pointing scan corrections, we do not expect this effect to be bigger than about 30%, which would result in the fluxes in our final maps being 30% higher. The good agreement between the measured aperture efficiency and the prediction form the Ruze equation implies that the errors are not this large.

Inspection of the observations taken in 2012 show that while the relative flux scales of dates 2012 November 14 and 2012 December 5 agree, observations on day 2012 November 5 have a lower flux scale. This effect is seen in the maps of the same regions on different days, the peak antenna temperature in the Focus scans of our pointing source 1851+0035 (observed approximately every hour), and calibration observations of DR21. To determine the relative flux scale, we averaged the results

[1] `https://safe.nrao.edu/wiki/bin/view/GB/Knowledge/GBTMemos`
[2] `http://www.gb.nrao.edu/GBT/DA/gbtidl/gbtidl_calibration.pdf`

of the fractional difference in the maps and the Focus scans. We excluded DR21 in this calculation because the measured ratio may be affected by pointing errors since we neither mapped DR21 nor performed a pointing correction on it. We measured the flux scale on 2012 November 5 to be 0.7 relative to that of the other days, so we adopted values of the aperture efficiency and main beam efficiency of 0.46, and 0.63, respectively, to bring data from that day into agreement with the others. This discrepancy may be a result of atmospheric effects, dish surface effects, or pointing or focus errors not accurately corrected by the standard calibration procedure.

No flux calibrators were observed during the 2005 observations, so we adopted 0.58 and 0.8 as the aperture efficiency and main beam efficiency, respectively, because the aperture efficiency at these frequencies in 2005 was typically 91% of what is is now (Todd Hunter, private communication). We inspected the peak antenna temperature of the focus scans on the pointing sources across multiple epochs to look for variations in the relative flux scales, assuming the fluxes of these sources to be stable over the approximately two month timescale of these observations. The most frequently observed pointing source was 1733-1304, being observed every day of the observations in 2005 except 2005-12-24, when only 1743-0350 was used. Additionally, 1751+0939 was observed sporadically on 2005 October 19, 2005 November 17, and 2005 November 18. We found that the aperture efficiency only changed significantly over the course of 2005 December 24, possibly affecting the flux scale by about 20% across the maps of G028.23-00.19.

Initial calibration of the frequency switching data and conversion to main beam temperature was performed with the GBT pipeline for the KFPA provided by the National Radio Astronomy Observatory (NRAO). The pipeline queried the weather data from the GBT weather forecast database to determine the zenith opacity for

each observing block. The pipeline also accepted values for the aperture efficiency and the main beam efficiency as inputs, determined as above.

After the initial calibration, we used GBTIDL to fit and subtract baselines from the spectra. Many of the baselines contained complex shapes with large amplitudes. We averaged the spectra for each individual combination of scan number, IF, polarization, and beam, then fit the line-free regions with a high order polynomial. The baseline shapes varied considerably between different IFs, beams, and polarizations, and showed moderate variation with time among different scans. We determined that the variation between individual integrations was within the noise of an individual integration, so that we could average over whole scans. For the 2012 observations taken in OTF mode, a single scan consisted of one row or column in the map. Since the 2005 observations were taken in PointMap mode, each scan was a single pointing. Baselines in the 2005 observations were generally less complex, so we used lower order polynomials at this stage.

Imaging was performed also using the GBT pipeline for the KFPA, which uses ParselTongue to call AIPS tasks from Python. Data were gridded using the `SDGRD` task. Since lower amplitude baseline effects were noticed on shorter timescales, we additionally performed lower order polynomial fitting and subtraction on an individual line of sight basis in the final imaged data cubes using the `imcontsub` task in the Common Astronomy Software Applications (CASA) package (`http://casa.nrao.edu`). By combining two baseline subtraction methods, we could address both the time variability in neighboring scans before the imaging step while also taking care to get the flattest baselines possible in the final data cubes. The data were converted from main beam temperature to Jy beam^{-1} by multiplying by $(2k_B\eta_{\rm mb})/(A_p\eta_A) = 0.483$, where k_B is the Boltzmann constant and A_p is the physical collecting area of the GBT.

Typical RMS noise in the final data cubes was 25-40 mJy beam^{-1} per 0.15 km s^{-1} channel. We estimate our absolute flux uncertainty to be approximately 20%.

3.3.2 VLA Observations

NH_3 (1,1) and (2,2) and CCS (2_1-1_0) emission in our sample of IRDCs was observed with the VLA in D configuration, primarily in 2005 and 2006 (NRAO Proposal ID AD0516), with observations of CCS in G028.83-00.19, G031.97+00.07, and G034.43+00.24 in 2007 (NRAO Proposal ID AD0556). The 3.125 MHz bandwidth covered only the main and innermost satellite hyperfine lines of the NH_3 (1,1) and (2,2) transitions. The spectral setup had 24.414 kHz resolution. Different numbers of pointings per IRDC were used to fully cover the highest opacity regions with the approximately 1.′9 (FWHM) primary beam, as determined from the 8 μm images. G031.97+00.07 and G034.43+00.24 each were observed with five pointings (though only four were observed in CCS), G028.83-00.19 was observed with two pointings, and the remaining IRDCs were observed with one pointing each. J1820-254 was used as the phase and amplitude calibrator for G010.74-00.13, while J1832-105 was used for G022.56-00.20 and G024.60+00.08, and J1851+005 was used for the remaining IRDCs. 3C286 (J1331+305) and 3C48 (J0137+331) were used as flux density calibrators. Table 3.3 summarizes the parameters of the VLA observations, including bandpass calibrators, beam sizes, and flux-density-to-temperature conversion factors.

All data were calibrated using AIPS. The 2007 CCS observations were conducted during the EVLA upgrade, and eight of the twenty-seven antennas had been converted to EVLA antennas. Data were obtained using both the VLA and EVLA antennas. Doppler tracking could not be used during the upgrade period, so the AIPS task `CVEL` was applied during calibration to correct for motion of the Earth relative to the

Table 3.3. VLA Observations

IRDC	Project ID	Bandpass Calibrator[a]	Synthesized Beam Major Axis × Minor Axis ($''$) × ($''$)	(pc)×(pc)	PA (deg)	Flux to T_B (K Jy^{-1})
			NH_3 (1,1) 23.6945 GHz			
G010.74-00.13	AD0516	J1851+005	4.8×3.4	0.081×0.057	-4.6	134.6
G022.56-00.20	AD0516	J1832-105	4.3×3.3	0.095×0.073	-2.3	155.3
G024.60+00.08	AD0516	J1832-105	4.2×3.3	0.070×0.055	7.3	158.2
G028.23-00.19	AD0516	J1851+005	4.0×3.6	0.087×0.079	-9.6	154.2
G031.97+00.07	AD0516	J1851+005	3.9×3.6	0.106×0.010	30.3	153.6
G032.70-00.30	AD0516	3C273, J1851+005	3.8×3.8	0.096×0.096	64.9	149.3
G034.43+00.24	AD0516	3C273, J1851+005	3.8×3.7	0.029×0.028	79.2	156.3
G035.39-00.33	AD0516	3C273, J1851+005	4.2×3.6	0.061×0.052	62.6	143.8
G038.95-00.47	AD0516	3C273, J1851+005	3.9×3.6	0.053×0.049	87.0	154.2
			NH_3 (2,2) 23.72263 GHz			
G010.74-00.13	AD0516	J1832-105	4.7×3.4	0.079×0.057	-7.6	134.0
G022.56-00.20	AD0516	3C273, J1832-105	4.4×3.3	0.097×0.073	-6.3	149.3
G024.60+00.08	AD0516	3C273, J1832-105	4.2×3.3	0.070×0.055	1.7	154.8
G028.23-00.19	AD0516	3C273, J1851+005	4.2×3.5	0.092×0.076	-23.1	149.3
G031.97+00.07	AD0516	3C273, J1851+005	3.9×3.6	0.106×0.098	-9.1	154.3
G032.70-00.30	AD0516	3C273, J1851+005	4.1×3.7	0.104×0.094	-45.2	144.3
G034.43+00.24	AD0516	3C273, J1851+005	3.8×3.7	0.029×0.028	-69.3	153.0
G035.39-00.33	AD0516	3C273, J1851+005	4.2×3.7	0.061×0.053	64.9	141.0
G038.95-00.47	AD0516	3C273, J1851+005	4.0×3.7	0.054×0.050	-78.4	148.9
			CCS (2_1-1_0) 22.34403 GHz			
G010.74-00.13	AD0516	3C454.3	5.4×3.2	0.091×0.054	15.8	140.3
G022.56-00.20	AD0516	3C454.3	4.4×3.5	0.097×0.077	8.0	160.9
G024.60+00.08	AD0516	3C273, 3C345, 3C454.3	4.3×3.6	0.072×0.060	-0.5	158.5
G028.23-00.19	AD0556	3C345	4.8×3.5	0.105×0.076	-5.3	147.5
G031.97+00.07	AD0556	3C345	5.0×3.4	0.136×0.092	-9.2	142.5
G032.70-00.30	AD0516	3C273, 3C454.3	4.3×3.6	0.109×0.091	-46.2	159.8
G034.43+00.24	AD0556	3C345	4.8×3.4	0.036×0.026	-10.8	147.1
G035.39-00.33	AD0516	3C84, 3C345, 3C454.3	4.1×3.6	0.059×0.052	-49.2	162.5
G038.95-00.47	AD0516	3C84, 3C345, 3C454.3	4.1×3.6	0.056×0.049	-55.1	166.7

[a]Bandpass calibrators were selected by the best bandpass solution for each observing date. CCS observations often also used the phase and amplitude and/or flux density calibrators to improve the bandpass solution. 3C273 is also known as J1229+020, 3C454.3 is also known as J2253+161, 3C345 is also known as J1642+398, and 3C84 is also known as J0319+041.

local standard of rest (LSR) during the observations. In the 22 GHz data sets, the uncertainty of the absolute flux densities was estimated to be 10%. We estimated the absolute positional accuracy to be better than 1″.

Before imaging, data were Hanning smoothed, bringing the effective velocity resolution to approximately 0.6 km s^{-1}. Continuum subtraction was performed with the CASA task `uvcontsub` on all the data for G034.43+00.24 and the CCS observations of G031.97+00.07, as there were significant continuum point sources seen in these four dirty images. The data were imaged in CASA using the `clean` task in mosaic mode with natural weighting of the visibilities, deconvolved with 0.33 km s^{-1} channels and 0.″7 pixels. We also employed the multiscale capability of `clean` to include clean components approximately one and three times the size of the synthesized beam, as well as the standard point-like components. The CASA task `pbcor` was used to apply a primary beam correction. The mosaics were imaged to the 35% power level relative to the peak of the mosaic primary beam response.

The synthesized beam in the images is 3-5″. The RMS noise is 1-4.5 mJy beam^{-1} per 0.33 km s^{-1} channel. The conversion between from flux density in Jy beam^{-1} to brightness temperature, T_B (K), for the various data cubes are listed in Table 3.3.

3.3.3 Combining Single-Dish and Interferometric Data

Successful combination of single dish and interferometric data relies upon good astrometric alignment and calibration between the two data sets. The estimated positional accuracy of our GBT observations, 6″, while small compared to the GBT beam, were larger than the VLA beam. This allowed for positional errors that might introduce significant artifacts in our combined maps. For example, using the GBT as a clean model for the VLA with a positional offset between the two can cause negative fea-

tures neighboring the emission in the combined image. To address this issue, we computed the amount of positional shift required to align the GBT and VLA data by smoothing our VLA-only (1,1) cubes to the GBT angular resolution and smoothed the GBT-only (1,1) cubes to the VLA velocity resolution. We then determined the positional shift required to align the maxima in the emission. Shifts were restricted to integer numbers of pixels (6″ each) in the native GBT images. The largest total shift was 18″, or approximately half a GBT beam, for G035.39-00.33. All other IRDCs required shifts less than 10″, and three IRDCs (G032.70-00.30, G034.43+00.24, and G038.95-00.47) did not require any shift.

The GBT data were combined with the VLA data in a two-stage process. First, the GBT cube was used as a starting model for the VLA data in the CASA task `clean`, and then cleaning proceeded as for the VLA only, described above in §3.3.2. The resulting cube was then combined with the GBT cube again, using the CASA task `feather`. No relative calibration factor was applied in this combination, implicitly assuming that there was no systematic offset in the absolute calibration of the datasets.

Feathering Fourier transforms the two images, multiplies the single dish image by the Fourier transform of the single dish beam, multiplies the high-resolution image by the complement of that transfer function, adds the two filtered Fourier cubes, and transforms back. Feathering two images is a simple way to combine the two data sets, but can be sensitive to the shape of the tapering function and to relative calibration uncertainties. Using a cleaned image that has the single dish data as a starting model, rather than the cleaned VLA image alone, mitigates these effects because the cleaning process can correct any potential issues with the feathered image that might be inconsistent with the interferometric visibilities. Combining the data sets by using

a clean model alone, however, is also sensitive to calibration errors and can result in a cube with more total flux than the single dish alone, which is not physical. Feathering these resulting cubes with the single-dish brings the total flux in the final combined images back into agreement with the single-dish data.

Using both methods produced a result that is as consistent as possible with the both the GBT and VLA data taken individually. The RMS noise was approximately the same as the VLA-only cubes. The synthesized beams, and thus the conversion between brightness temperature and flux density, were exactly the same as for the VLA data alone (Table 3.3).

As a check on the flux in our combined cubes, we smoothed them to the resolution of the GBT and divided by the GBT cubes. This should have produced a cube of values close to 1, as the GBT is sensitive to total flux. We found that within regions of significant emission, our smoothed, combined cubes were almost always within the 20% flux uncertainty of the GBT. Our final cubes were therefore within the uncertainty of recovering the correct total flux. Comparing to the VLA data cubes alone, the morphology of the combined data cubes is similar on size scales approximately the size of the synthesized beam, however using the VLA alone misses most the extended, diffuse emission. The fluxes of clump-sized sources seen in the VLA are tens of percent lower than what is seen in the combined images because of the contribution of this diffuse gas across the IRDCs. The total flux in the VLA cubes is typically less than half of the total flux measured by the GBT, and thus the combined images. An image showing the comparison between GBT-only, VLA-only, and GBT+VLA images is shown in Figure 3.2.

3.4 Methods

3.4.1 Clump Deconvolution

Detailed knowledge of the kinematic and spatial structure of these IRDCs provides constraints on the NH_3 spectral line fitting (see §3.4.3). It is readily apparent in the data that regions containing at least two strong, distinct velocity components, if not three or four, are common. Attempts to fit a single velocity component to the NH_3 spectra in these regions result in poor fits with unphysically large linewidths and optical depths, so multiple components must be included. By performing clump deconvolution on the data before fitting, it is trivial to determine the number of components to include at each line of sight. Sophisticated clump deconvolution algorithms make use of the data cube and its noise properties as a whole, and so are more robust determinations of the number of components to fit than any method making this determination on a line of sight (pixel-by-pixel) basis. Additionally, identifying significant, coherent emission in the data allows us to make very good initial estimates of the central velocities and velocity widths at each line of sight for each component by making first- and second-order moment maps (velocity field and velocity dispersion, respectively) restricted to emission within the identified clump. Finally, using these clumps provides a straightforward and physically motivated way to analyze the physical parameter results from the fitting for different substructures within the clouds.

We perform clump deconvolution on the NH_3 (1,1) data using the `cprops` package described by Rosolowsky & Leroy (2006). We use the main hyperfine component of the (1,1) line because it typically has the highest signal-to-noise ratio and the (2,2) line does not trace the coldest, and often lowest column density, gas. The velocity

offsets between cospatial velocity components are sometimes comparable to the NH_3 hyperfine splitting, so the deconvolution must be performed carefully. We use the GBT and VLA combined data cubes before primary beam correction (so the noise is roughly constant across the images) to generate the clump assignment cubes. The initial mask only includes voxels (single elements in the position-position-velocity cubes, akin to pixels in position-position images) with values greater than 7σ, and then the mask is expanded to include voxels above 5σ that are connected to initial mask via a path only passing through significant emission. The `cprops` algorithm then identifies "kernels" in the data, consisting of local maxima significantly above a "merge level" – the contour value at which multiple kernels are connected in the data and the significant emission cannot be uniquely assigned to one kernel over another. The `cprops` documentation refers to this unassigned emission as the "watershed." We further restrict the list of kernels to those that lead to clumps with projected area on the sky greater than three times the synthesized beam area, i.e. only well-resolved clumps are assigned as independent structures so that we can accurately probe their physical properties. Kernels that lead to these unresolved clumps are rejected before the final `cprops` assignments are determined, so the voxels, and thus emission, from these clumps is free to be reassigned to another clump or the watershed. This algorithm produces clump assignments from our data that map excellently to clumps discerned by eye.

An alternate method in the `cprops` package uses the `clumpfind` algorithm (Williams et al. 1994) to assign emission to the same kernels list as the standard `cprops` algorithm, but proceeds by assigning voxels to clumps in discrete contours continuing all the way to the noise floor. Assignment degeneracies in this method are broken by evaluating the proximity of voxels to the clump peaks in position-position-velocity

space. This method has the advantage of assigning all of the significant emission into clumps, however the assignment cubes tend to have a "patchwork" appearance that likely does not represent physically accurate clump boundaries.

The `clumpfind` algorithm is also fairly sensitive to the input parameters that determine the contouring scheme used to make the clump assignments. This will in turn affect the clump parameters we calculate in §2.4. The `cprops` algorithm is generally less sensitive than `clumpfind` to the inputs. The specific assignments can be altered by varying the parameters, but the typical clump sizes, aspect ratios, etc. are not significantly affected.

For our study, we start with the standard `cprops` assignments, and then further used the `clumpfind` assignments to assign the watershed emission. The result is an assignment cube in which all of the significant emission is assigned to exactly one clump, and the patchwork assignments from the clumpfind algorithm are restricted to the weakest emission. The clump-averaged properties discussed in this work will be dominated by the strongest emission, and thus by the `cprops` assignments. Results of the deconvolution are presented in §3.5.1 and discussed in §3.6.4.

3.4.2 Infrared Extinction

IRDCs are initially identified by their apparent absorption in mid-infrared images, so it is natural to use their contrast with the background emission as a measure of physical properties in the cloud. In the simplest terms, a greater contrast, i.e. darker cloud compared to the background, indicates a greater column of dust. It is rather straightforward to generate extinction maps if one has an estimate of the background, and with a few assumptions the dust mass surface density may also be calculated across a map.

Any method of estimating this optical depth must account for the following complications: (1) we do not have a direct measurement of the background infrared (IR) emission at the location of the cloud, so it must be estimated from an irregular, varying background measured off the cloud while attempting to avoid contamination from foreground objects, such as other dark clouds and bright nebulae; (2) there exists foreground emission from the dust between the clouds and the observer; and (3) dark clouds often contain embedded point sources that do not probe the full column of the clouds and contaminate our contrast measurements.

We adopt a modified version of the Large Median Filter (LMF) method presented by Butler & Tan (2009) to map the 24 μm optical depth, $\tau_{24\mu\mathrm{m}}$, using the *Spitzer* MIPSGAL data. This method is summarized in detail as follows. First, a model of the infrared background is generated using a $40'$ square median filter sampled every $24''$, and then smoothed by a $24''$ Gaussian filter. The median filter preferentially skews the model towards pixels lacking strong emission or absorption, provided the size of the filter is larger than the typical size of a dark cloud or other nearby structures. Increasing the size of the filter also causes the model to be less local, so it is not beneficial to sample the model at the same pixel scale as the original images. The Gaussian smoothing removes unphysically discrete (sharp) features introduced by the discrete sampling of the model.

The fraction of the infrared emission that is foreground to the cloud, f_{fore}, is estimated assuming a galactic dust distribution, adopting a solar galactocentric radius of 8.4 kpc (consistent with our distance determination in §3.2), and using the galactic longitude and distance for each cloud. Following Butler & Tan (2009), we assume the hot dust follows an azimuthally symmetric distribution matching the surface density

of Galactic OB associations,

$$\Sigma_{\rm OB} \propto \exp\left(-\frac{R}{3.5\ {\rm kpc}}\right), \tag{3.1}$$

where R is the galactocentric radius extending to 16 kpc. The values of $f_{\rm fore}$ are listed in Table 3.4, and range from 0.058 to 0.328. If $I_{\lambda,0}$ is the intensity of radiation just behind the cloud and $I_{\lambda,1}$ is the intensity of radiation just in front of the cloud, then they are related to the optical depth through the cloud, τ_λ, by

$$I_{\lambda,1} = I_{\lambda,0} \exp\left(-\tau_\lambda\right). \tag{3.2}$$

Accounting for the foreground contribution, the intensity of our background model, $I_{\lambda,0,{\rm obs}}$, is related to the true intensity just behind the cloud by

$$I_{\lambda,0} = \left(1 - f_{\rm fore}\right) I_{\lambda,0,{\rm obs}}. \tag{3.3}$$

Similarly, the observed intensity in the images, $I_{\lambda,1,{\rm obs}}$, is related to the true intensity just in front of the cloud by

$$I_{\lambda,1} = I_{\lambda,1,{\rm obs}} - f_{\rm fore} I_{\lambda,0,{\rm obs}}. \tag{3.4}$$

Therefore, the optical depth through the cloud is obtained by

$$\tau_\lambda = -\ln\left(\frac{I_{\lambda,1,{\rm obs}} - f_{\rm fore} I_{\lambda,0,{\rm obs}}}{\left(1 - f_{\rm fore}\right) I_{\lambda,0,{\rm obs}}}\right). \tag{3.5}$$

Battersby et al. (2010) make the point that extended sources in IRAC must be corrected for internal scattering in the instrument, and they include this correction for

their analysis of the optical depth at 8 μm. Engelbracht et al. (2007), however, find there is no need to apply such a correction for 24 μm images from MIPS over a range of a factor of about five in background level, so we do not apply a scattering correction in our calculations.

An optical depth map is then generated on the same pixel scale as the infrared images. Point sources and other emission features appear as negative optical depth in the maps, and are thus excluded from analysis. Featureless portions of the infrared image correspond to approximately 0 in the optical depth maps as expected. We see that the clouds typically peak at optical depth of about 0.25-0.5. G028.23-00.19 has noticeably higher optical depth than the other clouds by about a factor of two, and peaks at an approximate optical depth of 1. Further results of this analysis are presented in §3.5.2.

3.4.3 Ammonia Spectral Line Fitting

We fit the spectra along individual lines of sight in our combined GBT and VLA data. The (1,1) and (2,2) lines were fit simultaneously. The fitting routine was written in Python using the `nmpfit` package, which performed a least-squares (Levenberg-Marquardt algorithm) fit and returned the fit parameters and the full covariance matrix. We include the full hyperfine structure of NH_3 from the components and intrinsic strengths documented in Kukolich (1967). The limiting bandwidth of the VLA data restricted our fit in practice to the main and inner satellites components of the spectral lines. We simultaneously fit the central velocity ($v_{c,\mathrm{LSR}}$), velocity FWHM (Δv), total optical depth in the (1,1) component ($\tau_0(1,1)$, abbreviated henceforth as τ_0), excitation temperature (T_{ex}), and rotation temperature (T_R).

There is a natural degeneracy between the excitation temperature and optical

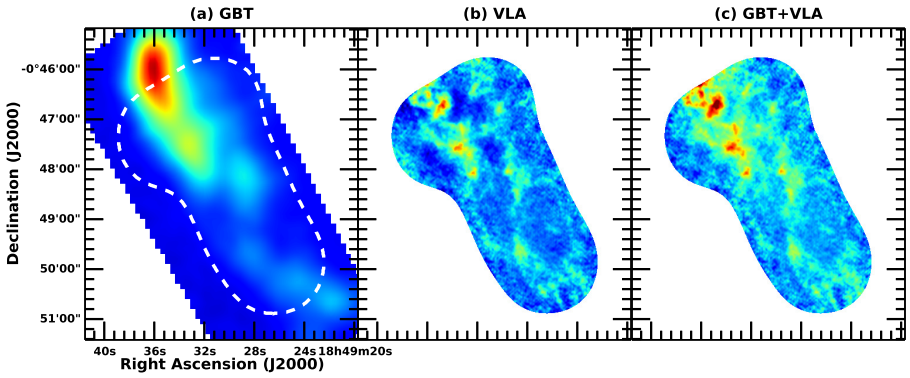

Fig. 3.2.— A comparison of the NH_3 (1,1) data for the GBT-only, VLA-only, and combined images. Images of G031.97+00.07 are integrated from 94 km s^{-1} to 97 km s^{-1}. The VLA footprint is plotted on the GBT image as a reference. The VLA and combined images have both been corrected for the response of the primary beam and are shown on the same flux scale (all three flux scales are linear). Aside from the improved resolution over the GBT along, the combined image also recovers more extended emission than the VLA alone. The combined image recovers the total flux of the GBT image, and recovers more flux than the VLA for even relatively compact, marginally resolved sources.

Table 3.4. Clump Properties

Peak Coordinates			cprops		*Herschel*	Spectral Line Fitting				*Spitzer*
R.A. (J2000) hh:mm:ss	Decl. (J2000) dd:mm:ss	v_{LSR} (km s^{-1})	R_{eff} (pc)	A_0	70 μm source?	$\langle\sigma_{line}\rangle$ (km s^{-1})	$\langle\tau_0\rangle$	$\langle T_K\rangle$ (K)	$\langle N(NH_3)\rangle$ (10^{23} cm^{-2})	$\langle\tau_{24\mu m}\rangle$[a]
G010.74-00.13 (f_{fore} = 0.095)[b]										
18:09:45	-19:42:29	28.50	0.17	2.1	N	1.0	7.3	14.1	0.8	0.35
18:09:45	-19:42:07	28.50	0.16	1.2	Y	1.0	8.3	15.1	1.1	0.34
18:09:44	-19:42:06	29.16	0.11	2.1	N	0.7	7.9	14.0	0.6	0.37
18:09:46	-19:41:47	29.82	0.16	2.5	Y	1.0	8.1	14.7	0.9	0.27
G022.56-00.20 (f_{fore} = 0.173)										
18:33:00	-09:19:59	74.84	0.15	3.0	Y	1.3	6.7	16.5	1.0	0.20
18:33:01	-09:19:56	76.82	0.09	1.6	N	1.6	6.0	15.7	0.9	0.19
18:33:00	-09:20:04	78.14	0.09	2.8	N	1.6	5.1	16.3	0.7	0.22
G024.60+00.08 (f_{fore} = 0.127)										
18:35:40	-07:18:36	52.49	0.12	1.4	Y	1.4	4.5	19.8	0.8	0.19
18:35:39	-07:18:55	53.15	0.17	1.5	N	0.8	6.1	14.0	0.6	0.28
18:35:40	-07:19:06	53.81	0.09	1.2	N	0.6	6.1	14.2	0.4	0.23

[a] $\tau_{24\mu m}$ cannot be computed for some clumps because IR emission covers their entire angular extent or the contrast with the background is too low.

[b] f_{fore} is the estimated fraction of diffuse galactic IR emission that is foreground to the cloud, and is used to calculate $\tau_{24\mu m}$ (see §3.4.2).

Note. — (This table is available in its entirety in Appendix Table D.1. A portion is shown here for guidance regarding its form and content.)

depth if they are low. However, we observe lines that are typically optically thick in this study (see §3.5.3), and so the degeneracy is broken. Since we observe lines that are so optically thick ($\tau_0 > 5$), our fitted values of τ_0 may only be lower limits. The fitting routine is capable of handling multiple velocity components simultaneously and independently along the same line of sight (see Section 3.4.1).

The basic functional form of the fit to a single NH_3 inversion line is

$$\Delta T^*_{A,\nu}(J,K) = \eta_{\rm mb}\Phi\left[\mathcal{J}\left(T_{\rm ex}(J,K)\right) - \mathcal{J}\left(T_{\rm bg}(J,K)\right)\right]\left[1-\exp\left(-\tau_\nu(J,K)\right)\right], \quad (3.6)$$

where $\Delta T^*_{A,\nu}(J,K)$ is the increase in corrected antenna temperature at the telescope from the line emission, $\eta_{\rm mb}$ is the main beam efficiency, Φ is the beam-filling factor, $T_{\rm ex}(J,K)$ is the excitation temperature of the line, $T_{\rm bg}(J,K)$ is the background temperature of the line, $\tau_\nu(J,K)$ is the frequency-dependent optical depth, and

$$\mathcal{J}(T) = \frac{h\nu}{k_B}\left[\exp\left(\frac{h\nu}{k_B T}\right) - 1\right]^{-1} \quad (3.7)$$

is the Rayleigh-Jeans temperature for the Planck constant h, the Boltzmann constant k_B, and frequency ν (Ho & Townes 1983). We assume $\Phi = 1$ (i.e the brightness temperature, T_B, equals the main beam temperature, $T_{\rm mb}$). In principle the background temperature includes a contribution from the continuum temperature, $T_C(J,K)$, such that $T_{\rm bg}(J,K) = T_C(J,K) + T_{\rm CMB}$, where $T_{\rm CMB} = 2.73$ K is the contribution of the cosmic microwave background. In this study, our data have already been baseline subtracted and we do not expect a background continuum source, so we set $T_C(J,K) = 0$.

The line shape as a function of frequency, ν, is primarily determined by the optical

depth profile:

$$\tau_\nu(J,K) = \tau_0(J,K) \sum_{i=1}^{\mathcal{N}(J,K)} a_i(J,K) \times \exp\left(-4\ln 2\left(\frac{\nu - \nu_c(J,K) - \delta\nu_i(J,K)}{\Delta\nu(J,K)}\right)^2\right), \tag{3.8}$$

where $\tau_0(J,K)$ is the opacity in the (J,K) line, $\mathcal{N}(J,K)$ is the number of hyperfine components in the (J,K) line, i is the index for the hyperfine components, $a_i(J,K)$ is the scale factor for the relative intensity contained in each hyperfine component, $\nu_0(J,K)$ is the rest frequency of the (J,K) line, $\nu_c(J,K)$ is the Doppler shifted cental frequency of the (J,K) line, $\delta\nu_i(J,K)$ is the difference in frequency of the ith hyperfine component of the (J,K) line and the main hyperfine component, and $\Delta\nu(J,K)$ is the FWHM of the (J,K) line (Friesen et al. 2009).

Treating NH_3 as a two-state system, the ratio between the optical depths of two different fine structure lines is given by Ho & Townes (1983) as

$$\frac{\tau_0(J',K')}{\tau_0(J,K)} = \left(\frac{\nu_0(J',K')}{\nu_0(J,K)}\right)^2 \left(\frac{\Delta\nu(J',K')}{\Delta\nu(J,K)}\right)^{-1} \left(\frac{T_{\rm ex}(J',K')}{T_{\rm ex}(J,K)}\right)^{-1} \times \left(\frac{|\mu(J',K')|^2}{|\mu(J,K)|^2}\right) \left(\frac{g(J',K')}{g(J,K)}\right) \exp\left(-\frac{\Delta E(J',K';J,K)}{k_B T_R(J',K';J,K)}\right), \tag{3.9}$$

where $\Delta E(J',K';J,K)$ is the difference in energy of the lower levels of the transitions, $T_R(J',K';J,K)$ is the rotation temperature of the lines, $|\mu(J,K)|^2 = \mu_D^2 K^2/\left(J(J+1)\right)$ for the electric dipole moment of the molecule μ_D, and $g(J,K)$ is the statistical weight given by Osorio et al. (2009) as

$$g(J,K) = \begin{cases} 4(2J+1) & \text{for } K \neq \dot{3} \text{ or } K = 0 \\ 8(2J+1) & \text{for } K = \dot{3} \text{ and } K \neq 0, \end{cases} \tag{3.10}$$

where $\dot{3}$ denotes being a multiple of 3. This accounts for the rotational degeneracy ($g_u = 2J_u + 1$), the K degeneracy ($g_K = 1$ for $K = 0$ or $g_K = 2$ for $K \neq 0$ in symmetric top molecules like NH_3), and the nuclear spin degeneracy ($g_{\rm nuclear} = 4$ for $K = \dot{3}$ (ortho-NH_3) or $g_{\rm nuclear} = 2$ for $K \neq \dot{3}$ (para-NH_3)). We further assume the excitation temperature, the central velocity, and the velocity FWHM are constant for all (J, K) (thus $\Delta\nu(J', K')/\Delta\nu(J, K) = \nu_0(J', K')/\nu_0(J, K)$).

From the fit parameters, it is straightforward to calculate the kinetic temperature of the gas and the total column density of the NH_3. The kinetic temperature, T_K, is given by Tafalla et al. (2004) as

$$T_K = T_R(2,2;1,1) \times \left[1 - \left(\frac{T_R(2,2;1,1)}{42\ \mathrm{K}}\right) \ln\left(1 + 1.1 \exp\left[-\frac{16\ \mathrm{K}}{T_R(2,2;1,1)}\right]\right)\right]^{-1}, \tag{3.11}$$

and the column density of NH_3 in the (1,1) state is given by Friesen et al. (2009) as

$$N(1,1) = \frac{8\pi\nu_0^2}{c^2 A(1,1)} \frac{g_1}{g_2} \frac{1 + \exp\left(h\nu_0/\left[k_B T_{\rm ex}\right]\right)}{1 - \exp\left(h\nu_0/\left[k_B T_{\rm ex}\right]\right)} \int \tau_\nu \, d\nu, \tag{3.12}$$

where the Einstein A coefficient $A(1,1) = 1.68 \times 10^{-7}\ \mathrm{s}^{-1}$ (Pickett et al. 1998), $g_1 = g_2$ for the statistical weights of the upper and lower energy levels of the (1,1) transition, and

$$\int \tau_\nu \, d\nu = \left(\frac{\sqrt{\pi}\tau_0(1,1)\Delta\nu(1,1)}{2\sqrt{\ln 2}}\right). \tag{3.13}$$

The total NH_3 column density can then be calculated by considering the partition function for NH_3 and using the relation $N(NH_3) = N(1,1)Z_{\rm tot}/Z(1,1)$ (Friesen et al.

2009). The terms of the partition function are calculated by

$$Z(J,J) = (2J+1)\,S(J)\exp\left(\frac{-h\left[BJ(J+1)+(C-B)J^2\right]}{k_B T_R(2,2;1,1)}\right), \tag{3.14}$$

where the rotational constants are $B = 298.117$ GHz and $C = 186.726$ GHz (Pickett et al. 1998), and $S(J)$ is the statistical weight for ortho- or para-NH_3. For ortho-NH_3 (J a multiple of 3), $S(J) = 2$, and otherwise $S(J) = 1$ for para-NH_3, such as (1,1). $Z_{\rm tot}$ is then just the sum of the $Z(J,J)$ terms over all J, which quickly converges. In the rest of this paper, we drop the $(2,2;1,1)$ notation for simplicity.

A list of key parameters for the analysis, including the parameters used in the spectral line fitting, is given in Table 3.5. Results of the spectral line fitting are presented in §3.5.3. An example spectrum and fit of a single line of sight with two distinct velocity components is shown in Figure 3.3.

3.5 Results

Images of the sample from the *Spitzer Space Telescope* and the *Herschel Space Observatory* with the GBT and VLA data are shown in Figures 3.4, 3.5, 3.6, 3.7, 3.8, 3.9, 3.10, 3.11, and 3.12. The NH_3 (1,1) distribution generally traces the infrared extinction very closely and peaks around infrared point sources and, to a lesser extent, the IR extinction peaks. The NH_3 (2,2) distribution is more compact and generally correlates with stronger (1,1) emission. The CCS emission had systematically lower signal-to-noise ratio ($< 5\sigma$) than the NH_3 and is typically only marginally detected. The CCS that is observed, however, does not typically cover the full spatial extent of the NH_3.

Table 3.5. Selected Physical Parameters of Interest

Parameter	Description
	Line of sight Parameters
Calculated Directly from the Radio Data:	
$I_{(1,1)}$	Moment 0 (integrated intensity) of the NH_3 (1,1) line
$\langle v_{(1,1)} \rangle$	Moment 1 (intensity-weighted velocity field) of the NH_3 (1,1) line
$\langle \sigma_{v,(1,1)} \rangle$	Moment 2 (intensity-weighted velocity dispersion) of the NH_3 (1,1) line
$I_{\rm CCS}$	Moment 0 (integrated intensity) of the CCS line
Calculated Directly from the IR Data:	
$\tau_{24\mu{\rm m}}$	Optical depth at 24 μm from IR extinction
From NH_3 (1,1) and (2,2) Spectral Line Fitting[a]	
ν_c	Central Doppler shifted NH_3 frequency
$\Delta\nu$	NH_3 frequency FWHM
τ_0	Total optical depth in the NH_3 (1,1) line
$T_{\rm ex}$	NH_3 excitation temperature
T_R	NH_3 rotation temperature
χ^2	Goodness of fit statistic
Calculated from Spectral Line Fitting Results[a]	
T_K	Kinetic Temperature
$v_{c,{\rm LSR}}$	Central NH_3 LSR velocity
Δv	NH_3 velocity FWHM
$\sigma_{\rm obs}$	Observed line of sight velocity dispersion
$\sigma_{\rm line}$	Line of sight velocity dispersion corrected for spectral resolution
σ_T	NH_3 Thermal velocity dispersion
$\sigma_{\rm NT}$	NH_3 Nonthermal velocity dispersion
$\mathcal{M}$	Nonthermal (turbulent) Mach number
$N(NH_3)$	Total column density of NH_3
$N(H_2)$	Column density of molecular Hydrogen
	Clump-by-clump Parameters
Directly from cprops for each clump:	
R.A. (J2000)	Right Ascension of the peak NH_3 (1,1) main beam temperature
Decl. (J2000)	Declination of the peak NH_3 (1,1) main beam temperature
$R_{\rm eff}$	Effective radius of a circle with the same projected area as the clump
A_0	(Initial) Aspect ratio projected onto the sky
Calculated clump-by-clump:	
$M_{\rm cl}$	Clump mass from total NH_3 and $X(NH_3)$
$t_{\rm ff,sph}$	Spherical free-fall time
$t_{\rm ff,cyl}$	Cylindrical free-fall time along the axis
$M_{\rm vir,sph}$	Spherical virial mass
$M_{\rm vir,cyl}$	Cylindrical virial mass
$\alpha_{\rm vir,sph}$	Spherical virial parameter
$\alpha_{\rm vir,cyl}$	Cylindrical virial parameter
$B_{\rm min}$	Minimum magnetic field strength to support cloud against collapse
	Whole IRDC (Cloud) Parameters
D	Distance to cloud
$f_{\rm fore}$	Fraction of IR galactic emission that is foreground to the cloud
$M_{\rm IR}$	Mass lower limit from 24 μm extinction
$M_{\rm GRS}$	Mass lower limit from BU-GRS ^{13}CO (J=1-0)
$M_{\rm mm}$	Mass from BGPS 1.12 mm emission

[a]These parameters may also be evaluated as clump-averaged values, weighted by the $(\chi^2_{\rm red})^{1/2}$ statistic over the clump. Both line of sight and clump-averaged values separate different velocity components that overlap spatially.

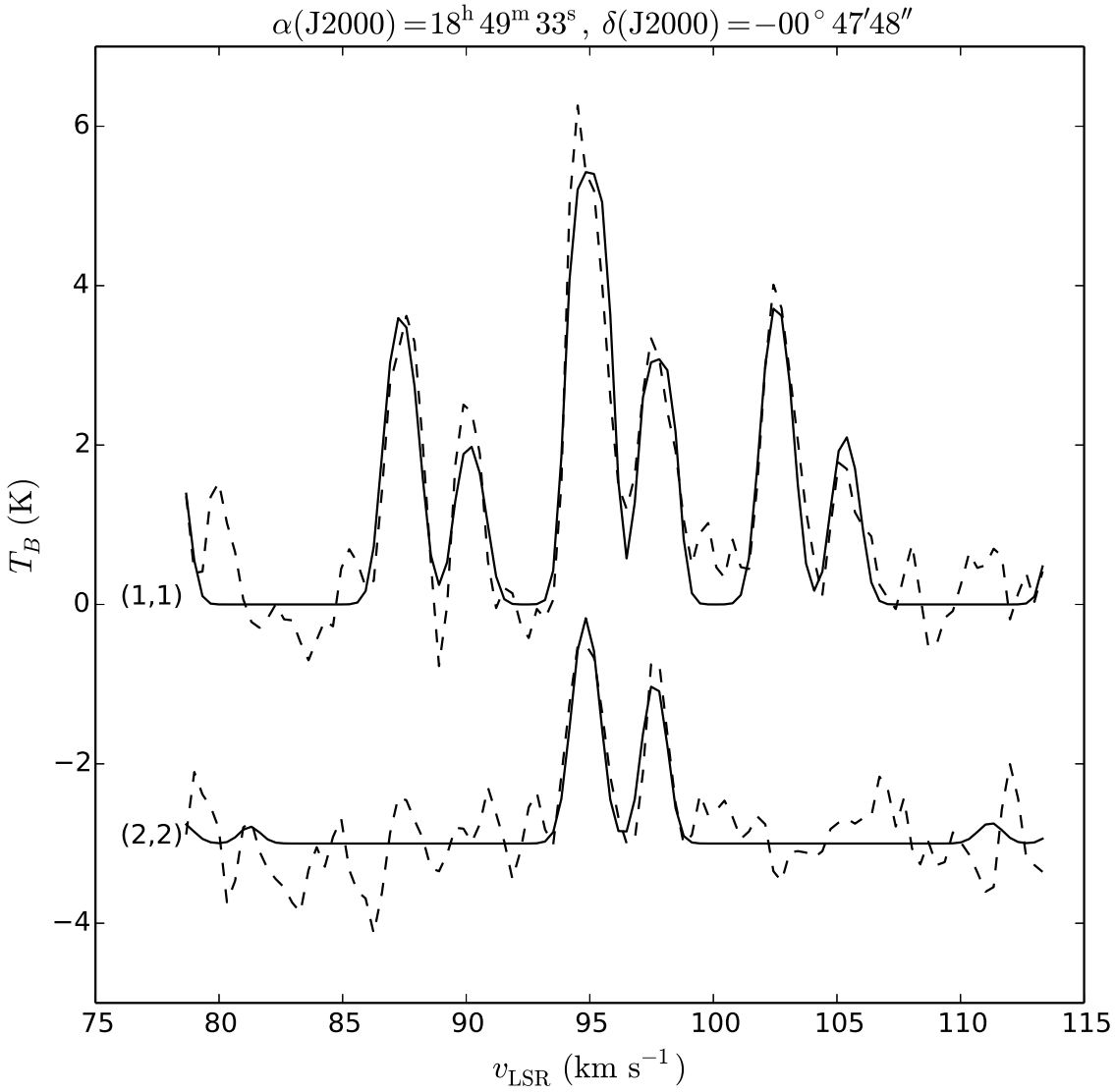

Fig. 3.3.— An example spectrum of the NH_3 (1,1) and (2,2) lines with fit to the spectrum. This spectrum is from one line of sight toward G031.97+00.07 with two distinct velocity components. The data are the dashed lines and the fit is the solid line. The (2,2) spectrum and fit have been vertically offset by -3 K for clarity. The brightness temperature scale assumes a beam filling factor of unity.

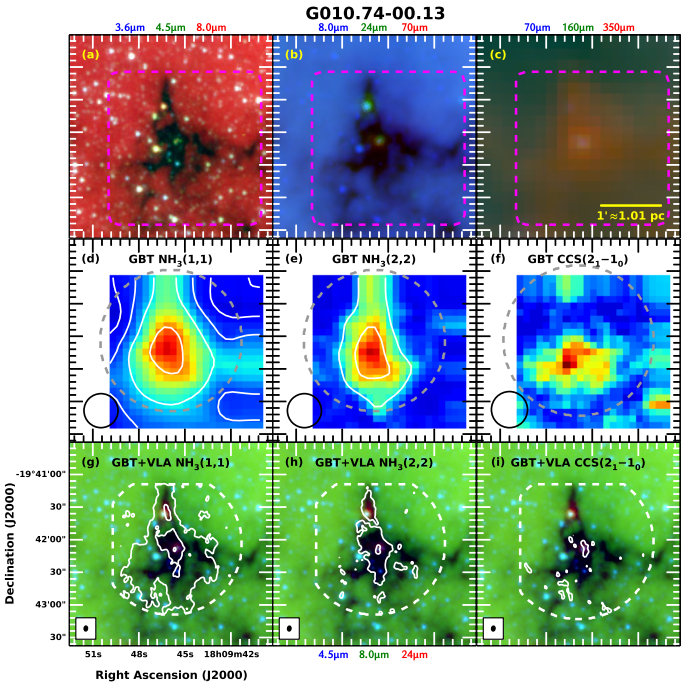

Fig. 3.4.— *Spitzer Space Telescope* and *Herschel Space Observatory* images of G010.74-00.13, along with our GBT and VLA data. The IRDC is seen against the diffuse mid-infrared emission of the galaxy toward the shorter wavelengths (panels (a) and (b)), though embedded infrared point sources are visible. At longer wavelengths (panel (c)), the IRDC becomes visible in the thermal emission of the dust. The highest 24 μm optical depth, $\tau_{24\mu\mathrm{m}}$, that we calculate in this cloud is 0.42. A yellow scalebar representing 1′ with the physical size at our adopted distance is shown at the lower right of (c). The GBT footprint is overplotted in dashed magenta in panels (a), (b), and (c). Panels (d), (e), and (f) show the NH_3 (1,1), NH_3 (2,2), and CCS emission, respectively, as seen by the GBT. An arbitrary linear color stretch is shown with white contours showing the signal-to-noise ratio at 5σ, 10σ, 20σ, and 40σ. The size of the GBT beam is shown in the lower left of each panel, and the VLA footprint is overplotted in dashed gray. Panels (g), (h), and (i) show *Spitzer* images of G010.74-00.13 with contours of the combined GBT and VLA NH_3 (1,1), NH_3 (2,2), and CCS emission, respectively. The contours show the signal-to-noise ratio at 5σ, 25σ, and 50σ. The NH_3 generally traces the MIR extinction and peaks near IR point sources. The NH_3 (2,2) is generally less extended than the (1,1), as it traces warmer gas. The CCS, though weak, typically follows the highest extinction parts of the clouds when it is detected. The combined footprint of the GBT and VLA observations (their intersection) is shown in dashed white. The synthesized beam is shown at the lower left of each panel.

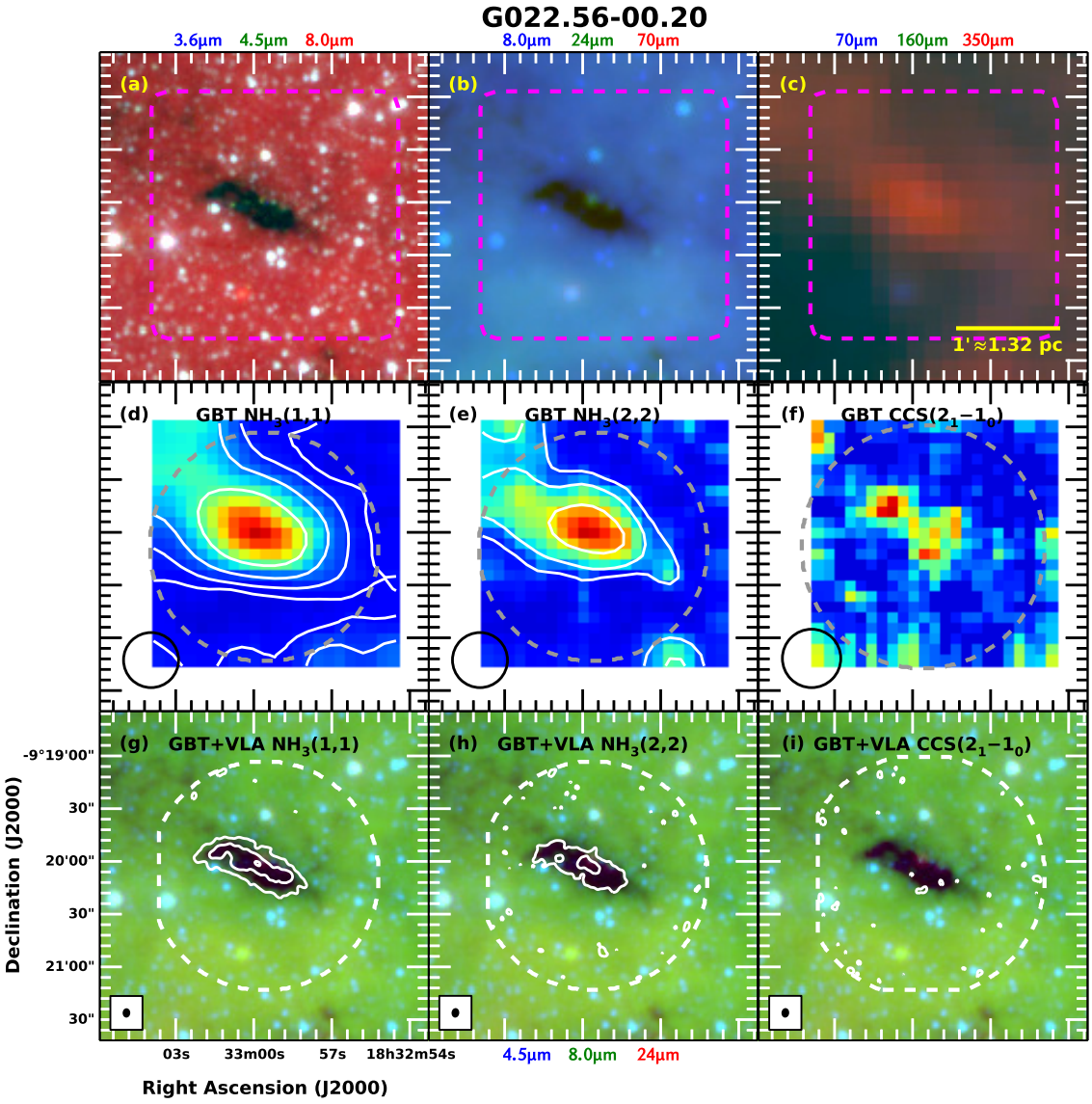

Fig. 3.5.— Same as Figure 3.4 but for G022.56-00.20. The highest value of $\tau_{24\mu m}$ is 0.27.

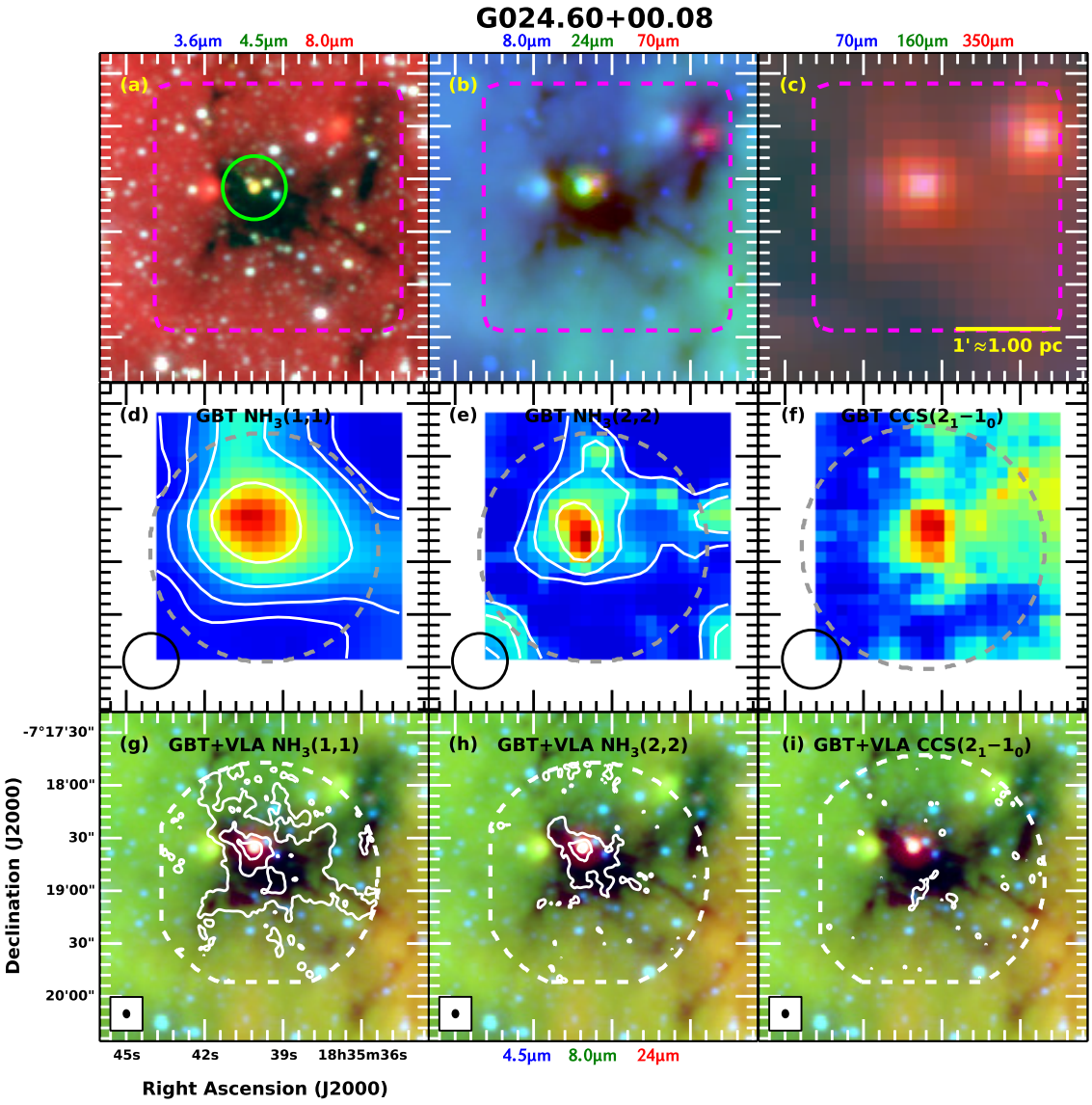

Fig. 3.6.— Same as Figure 3.4 but for G024.60+00.08. The highest value of $\tau_{24\mu m}$ is 0.47. The green circle in panel (a) shows the location of the extended green object (EGO) identified by Cyganowski et al. (2008).

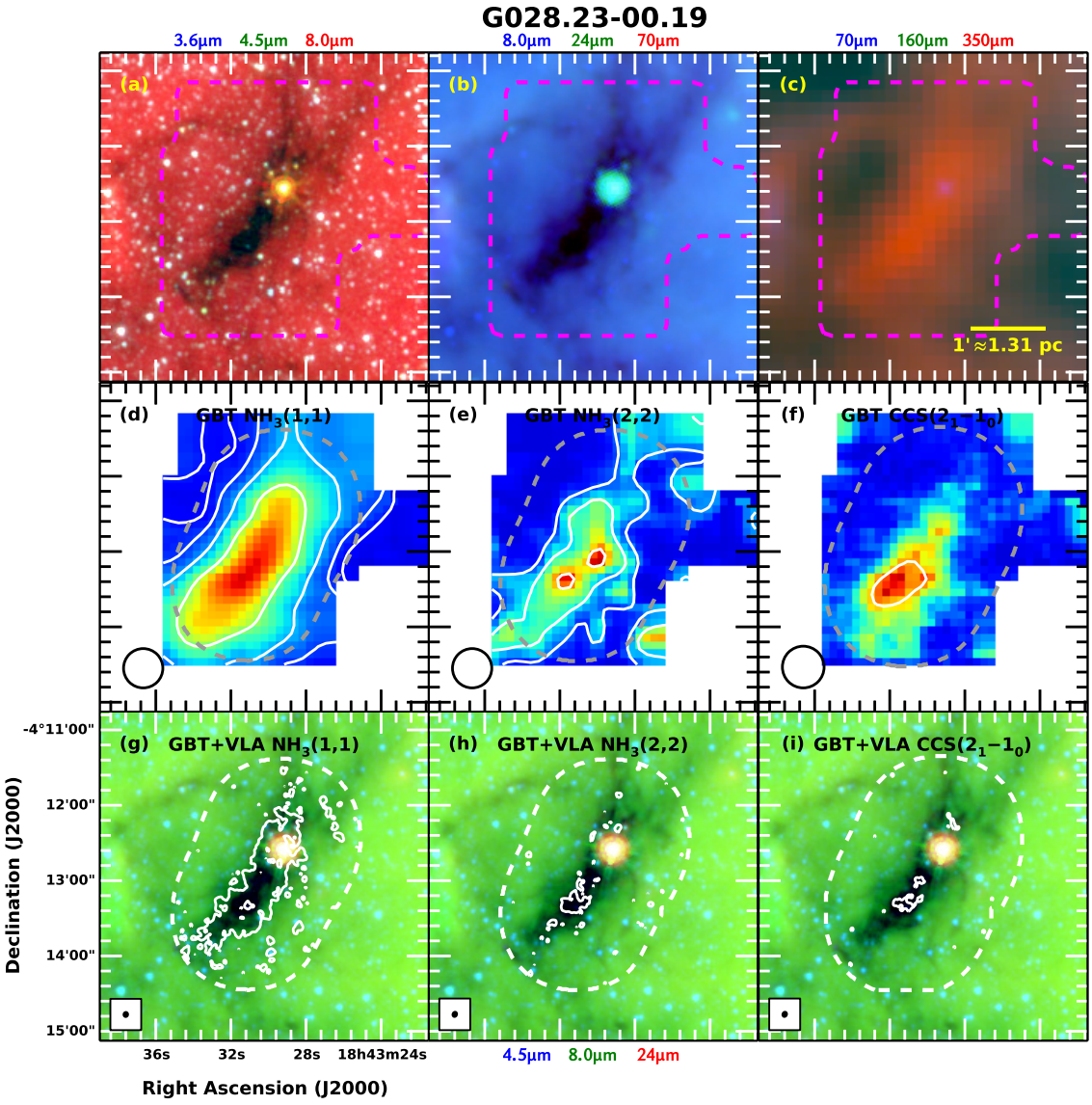

Fig. 3.7.— Same as Figure 3.4 but for G028.23-00.19 with GBT+VLA contours at 5σ and 25σ. The bright point source is an unrelated, foreground late-type star (Bowers & Knapp 1989). The highest value of $\tau_{24\mu m}$ is 0.89.

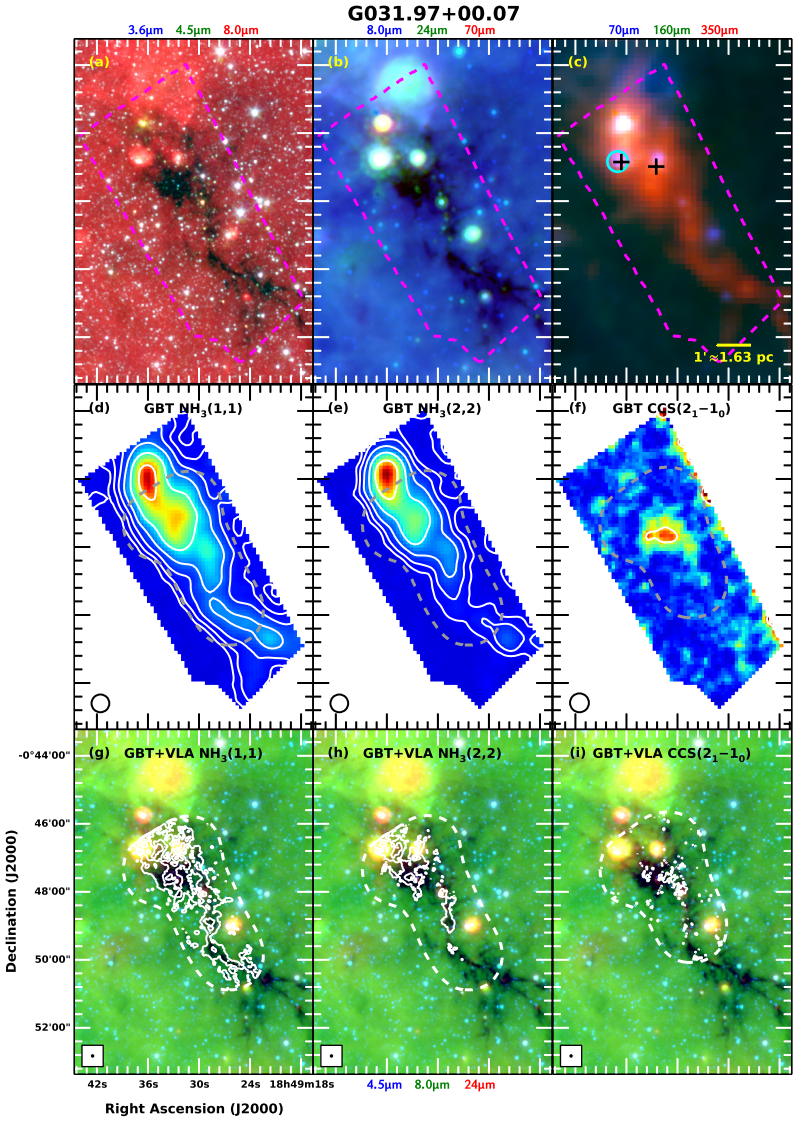

Fig. 3.8.— Same as Figure 3.4 but for G031.97+00.07 with GBT contours at 5σ, 10σ, 20σ, 40σ, 80σ, and 160σ, and with GBT+VLA contours at 5σ, 25σ, 50σ, and 100σ. The highest value of $\tau_{24\mu m}$ is 0.43. The cyan circle in panel (c) shows the location of the H II region identified by Urquhart et al. (2009). The black crosses are H_2O masers reported by Wang et al. (2006).

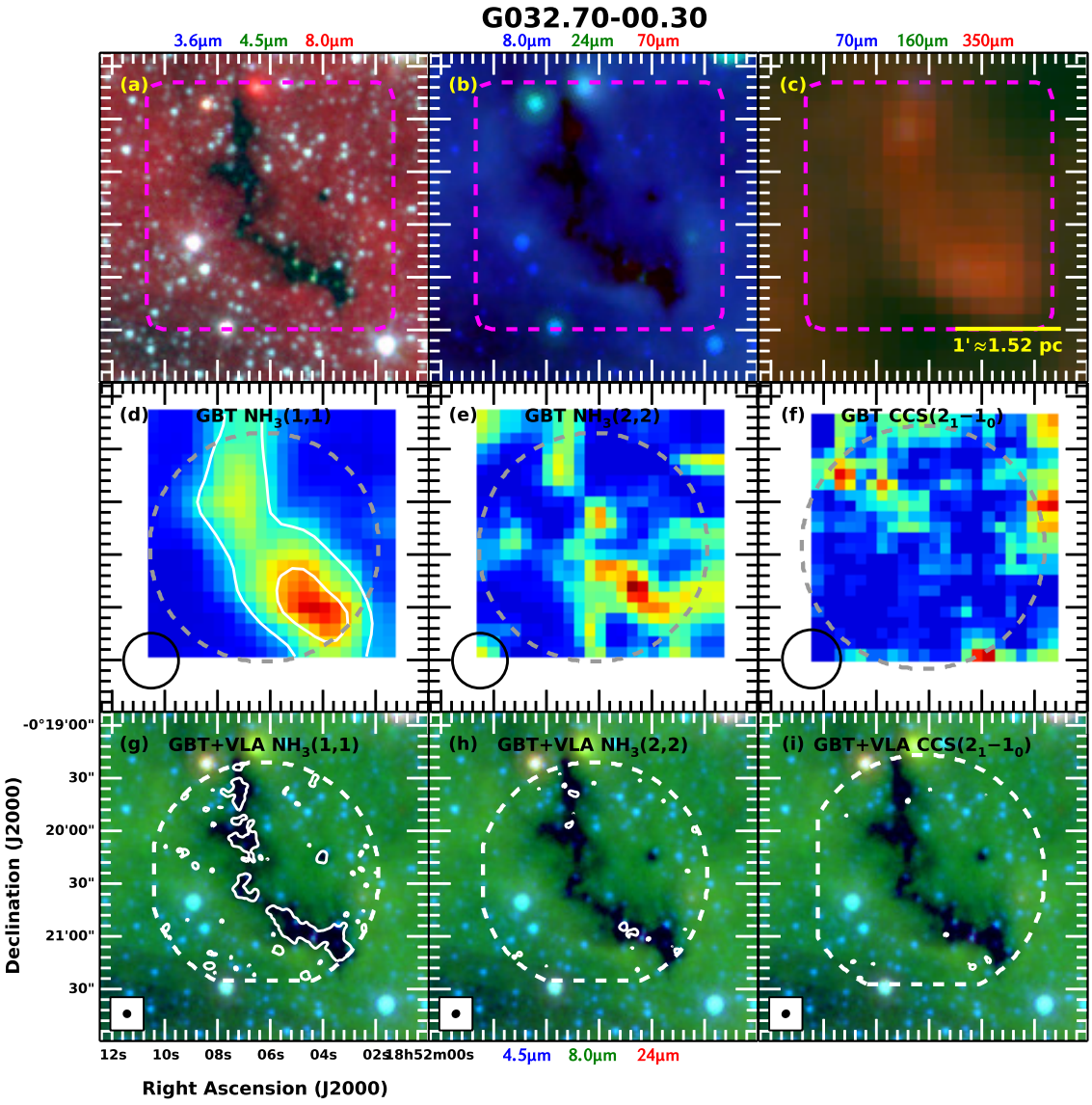

Fig. 3.9.— Same as Figure 3.4 but for G032.70-00.30 with GBT contours at 5σ and 10σ, and with GBT+VLA contours at 5σ. The highest value of $\tau_{24\mu m}$ is 0.36.

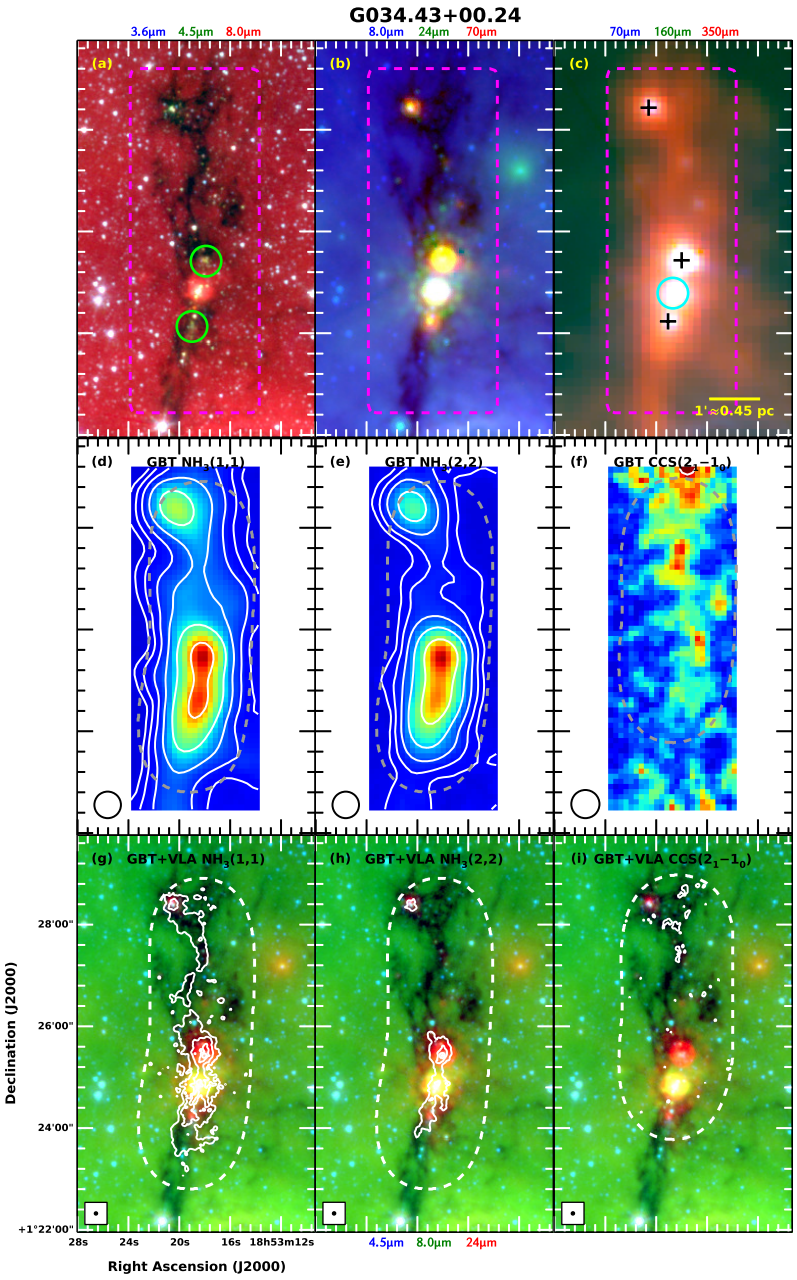

Fig. 3.10.— Same as Figure 3.4 but for G034.43+00.24 with GBT contours at 5σ, 10σ, 20σ, 40σ, 80σ, and 160σ, and GBT+VLA contours at 5σ, 25σ, 50σ, and 100σ. The highest value of $\tau_{24\mu m}$ is 0.14. The green circles in panel (a) show the location of the extended green objects (EGOs) identified by Cyganowski et al. (2008). The cyan circle in panel (c) shows the location of the H II region identified by Urquhart et al. (2009). The black crosses are H_2O masers reported by Wang et al. (2006).

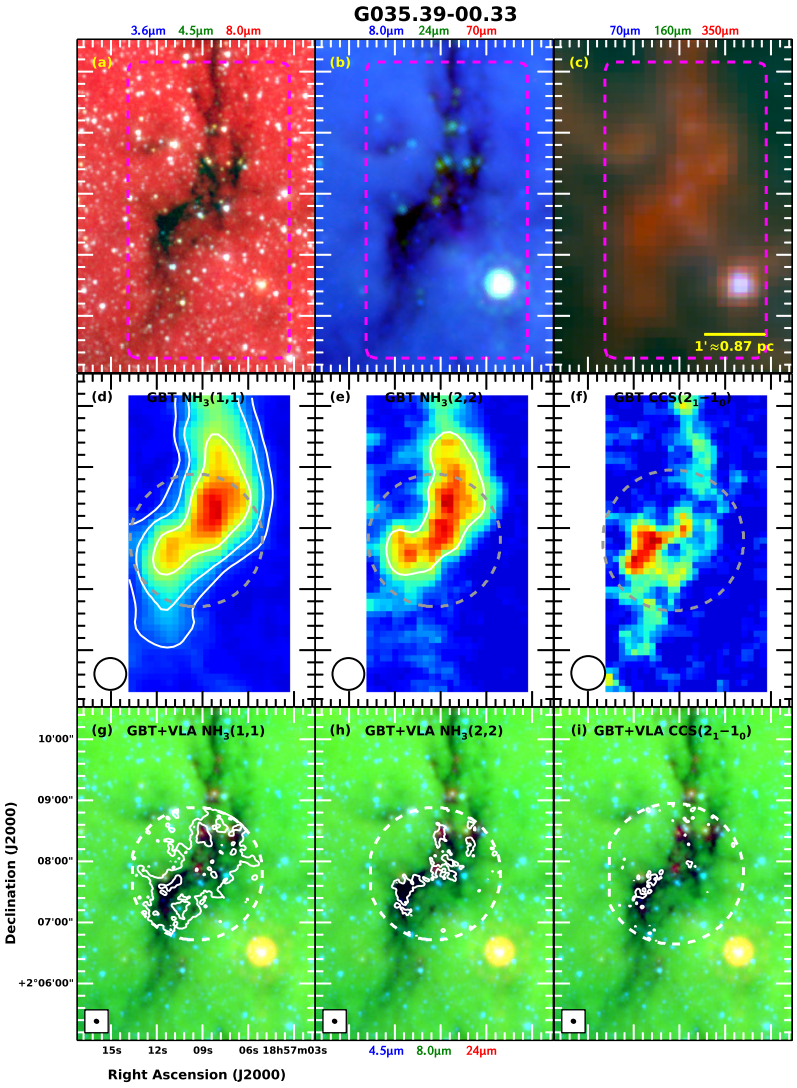

Fig. 3.11.— Same as Figure 3.4 but for G035.39-00.33 with GBT contours at 5σ, 10σ, and 20σ. The highest value of $\tau_{24\mu m}$ is 0.44.

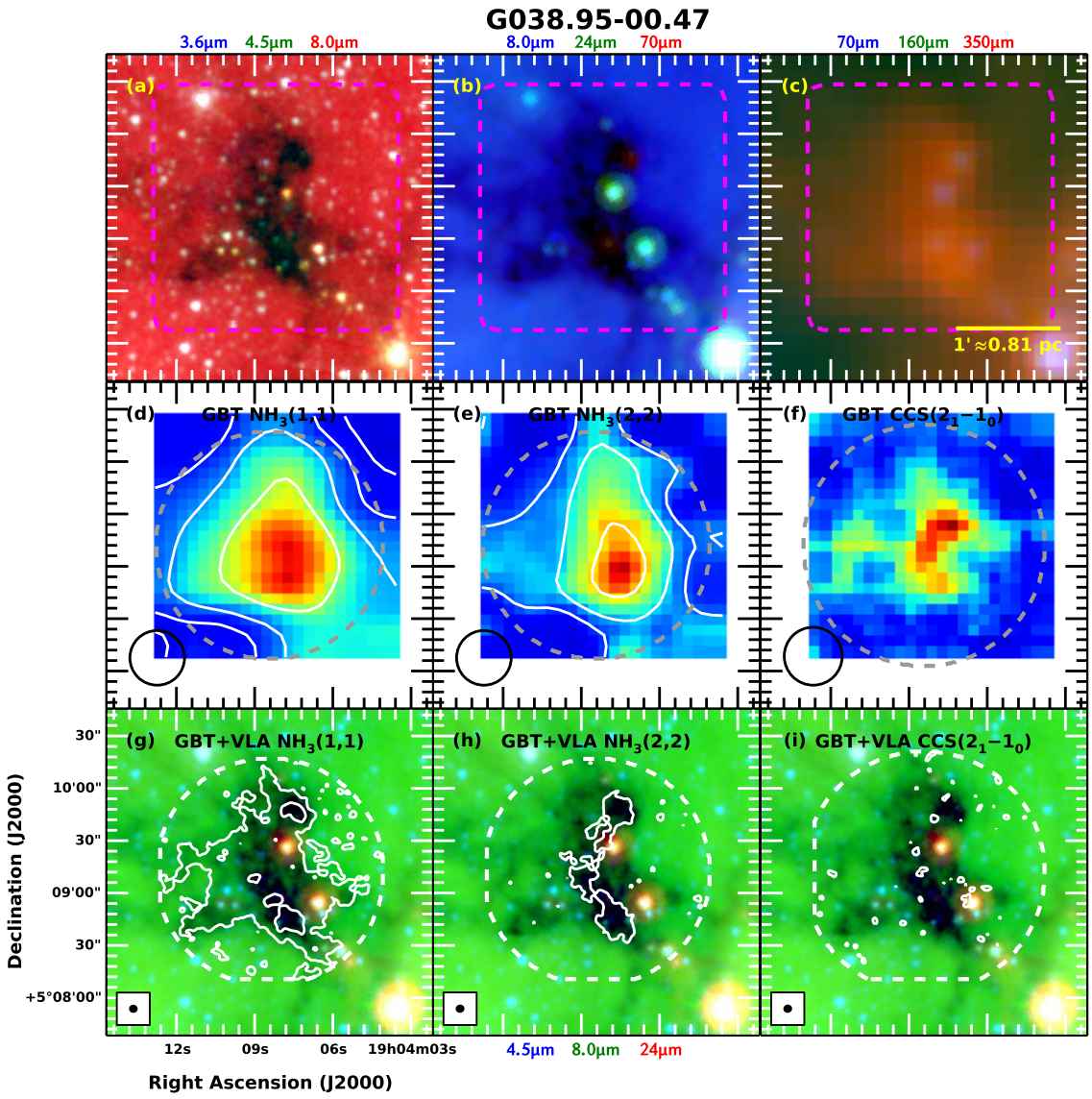

Fig. 3.12.— Same as Figure 3.4 but for G038.95-00.47 with GBT+VLA contours at 5σ and 25σ. The highest value of $\tau_{24\mu m}$ is 0.34.

3.5.1 Clump Deconvolution Results

A summary of the clump properties is presented in Table 3.4. Coordinates and velocities are given at the peaks of the emission. The effective radius, $R_{\rm eff}$, is the radius of a circle on the sky that has the same projected area as the full extent of the clump, which ranges from approximately 0.02 pc to 0.28 pc in our sample, with a median of about 0.16 pc. The physical resolution (i.e. synthesized beam) of the (1,1) cubes ranges from 0.02 pc to 0.1 pc, so clumps are typically well resolved.

Additionally, `cprops` performs an elliptical fit to each clump with a flexible position angle to determine sizes along the major and minor axes. The aspect ratio, A_0, is calculated from the `cprops` results as the ratio of the major axis length to the minor axis length, which is confirmed visually to be an accurate method. The aspect ratios of most of the clumps are approximately 1-2, but extend to about 3 to 4 for the more filamentary clumps, while the highest aspect ratio in our sample is 6.

3.5.2 Infrared Extinction Results

The infrared optical depth, $\tau_{24\mu\rm m}$, is calculated as described in §3.4.2 and then averaged over the full extent of the clump on the sky. Since the extinction is calculated from two-dimensional images, we cannot accurately separate the extinction from multiple components along the same line of sight, however the majority of individual pixels in the extinction maps are included in at most one velocity component. Values of $\tau_{24\mu\rm m}$ range from approximately 0 to 0.85. Clumps at the lower end of this distribution are those dominated by infrared point sources or other emission, such that we cannot reliably determine an infrared optical depth. Since none of the optical depths averaged over a whole clump are greater than 1, we can conclude that while the centers of clumps may be very optically thick, there are at least significant

outer portions of the clumps that are susceptible to heating by external or internal infrared radiation fields. They are, however, still opaque to optical and ultraviolet radiation since the extinction at 550 nm is approximately 50 times greater than at 24 μm (Draine 2003).

3.5.3 Spectral Line Fitting Results

Plots of the results of pixel-by-pixel NH_3 spectral line fitting are shown in Figure 3.13, as well as averages over clumps (also in Table 3.4) and whole clouds. The parameter averages are weighted by the square root of the reduced chi-squared statistic from the fit,

$$\left(\chi^2_{\rm red}\right)^{1/2} = \left(\frac{\chi^2}{n_{\rm dof}}\right)^{1/2}, \tag{3.15}$$

where χ^2 is the goodness of fit statistic and $n_{\rm dof}$ is the number of degrees of freedom, i.e. the difference between the number of data points and the number of fit parameters (five per velocity component). This is a natural choice for the weighting because the relative uncertainties of the fit parameters scale with $(\chi^2_{\rm red})^{1/2}$. Experimentation shows that the averages are not very sensitive to the exact weighting scheme; for example, the results change by only a few percent if weighting by $\chi^2_{\rm red}$ is used instead of $(\chi^2_{\rm red})^{1/2}$.

The typical uncertainties for single lines of sight and single velocity components for $v_{c,\rm LSR}$, Δv, τ_0, $T_{\rm ex}$, and T_R are 0.04 km s^{-1}, 0.09 km s^{-1}, 1.4, 0.58 K, and 1.1 K, respectively. The velocity FWHM, kinetic temperature, optical depth in the (1,1) line, and column density are generally correlated. G034.43+00.24 (cyan) is notable as having the highest Δv, T_K, and $N(NH_3)$ in the sample, dominated by the emission surrounding the bright protostars with outflows as traced by masers and extended green objects (EGOs; bright 4.5 μm sources often attributed to shocked molecular

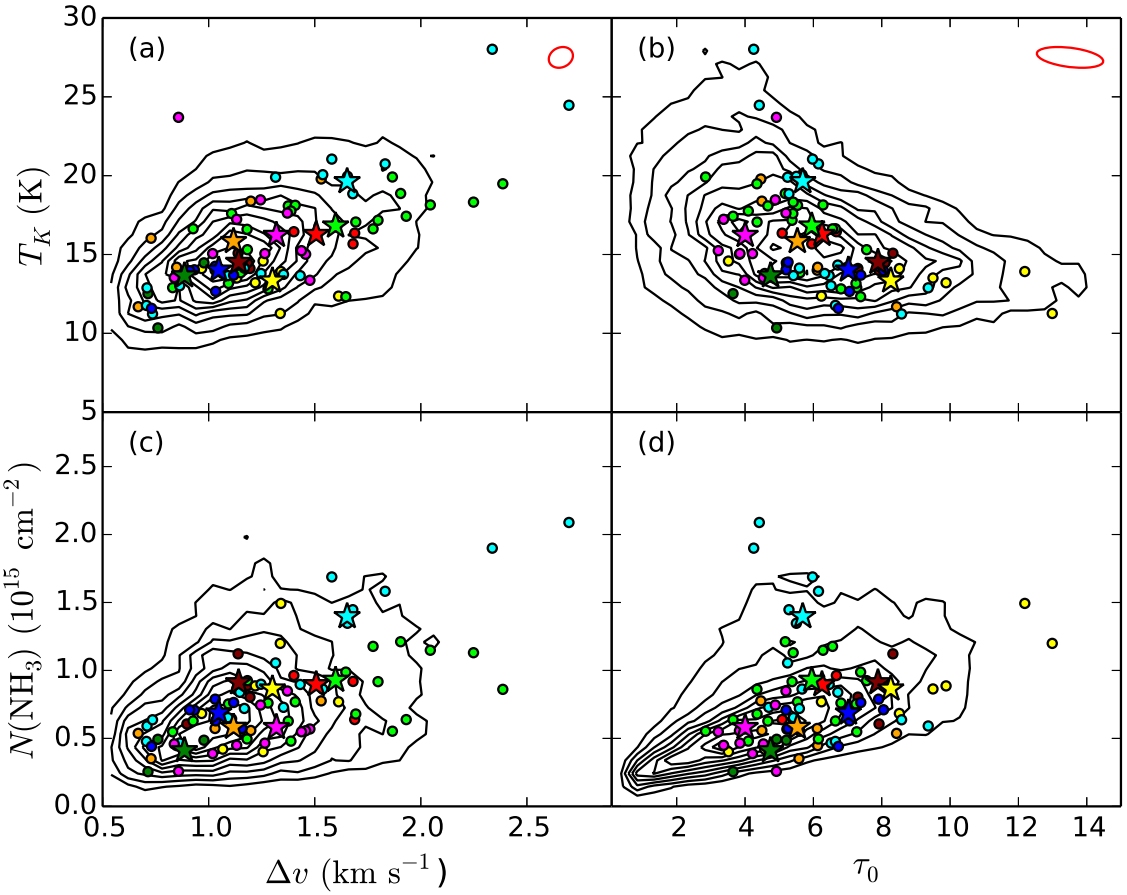

Fig. 3.13.— Plots of the results of NH_3 spectral line fitting. The circles are $(\chi^2_{\rm red})^{1/2}$-weighted averages over clumps defined by `cprops`, and stars are $(\chi^2_{\rm red})^{1/2}$-weighted averages over whole IRDCs. Symbols are colored by cloud: G010.74-00.13, G022.56-00.20, G024.60+00.08, G028.23-00.19, G031.97+00.07, G032.70-00.30, G034.43+00.24, G035.39-00.33, and G038.95-00.47 are maroon, red, orange, yellow, bright green, dark green, cyan, blue, and magenta, respectively. The background black contours show the $(\chi^2_{\rm red})^{1/2}$-weighted density of all lines of points in the sample (individual lines of sight and separated by distinct velocity components). Panels (a) and (b) also show red representative covariance ellipses from the spectral line fitting in the upper right.

hydrogen emission in protostellar outflows). G028.23-00.19 is also notable for being apparently starless throughout, and is colder and has a higher τ_0 than the rest of the sample.

The clump-averaged values quoted for the optical depth, τ_0, and the kinetic temperature of the gas, T_K, are averages weighted by the reduced $(\chi^2_{\rm red})^{1/2}$ value from the spectral line fitting, and can be separated kinematically by individual clump even when they overlap spatially. Most of the clumps have an average NH_3 optical depth τ_0 greater than 5 and all are greater than 1, indicating that these clumps are typically optically thick in NH_3 emission. We note that G028.83-00.19 shows significantly higher NH_3 optical depth than the rest of the sample, matching its high infrared optical depth.

Linewidths

In further analysis we adjust the values of the velocity dispersion to account for observational effects. We first convert the linewidth from the fit to a velocity dispersion, $\sigma_{\rm obs} = \Delta v (8 \ln 2)^{-1/2}$. The data are discretely sampled along the spectral axis and thus limited by the spectral resolution of the VLA observations. The effective velocity resolution is $\sigma_{\rm res} \approx 0.6$ km s^{-1}. Then

$$\sigma_{\rm line} \approx \sqrt{\sigma^2_{\rm obs} - \sigma^2_{\rm res}} \tag{3.16}$$

is the "true" velocity dispersion along the line of sight. These values of the velocity dispersion averaged over the `cprops` clump boundaries are listed in Table 3.4.

We further calculate the one-dimensional thermal linewidth calculated from the kinetic temperature,

$$\sigma_T = \sqrt{\frac{k_B T_K}{\mu_{\rm NH_3} m_{\rm H}}}, \tag{3.17}$$

where $\mu_{\rm NH_3} = 17.03$ is the mean molecular weight of ammonia and $m_{\rm H}$ is the mass of a hydrogen atom. We can then calculate the nonthermal contribution to the velocity

dispersion via

$$\sigma_{\rm NT} = \sqrt{\sigma^2_{\rm line} - \sigma^2_T}. \tag{3.18}$$

We see dispersion typically around 2 km s^{-1}, greater than the thermal linewidths, which are typically less than 0.1 km s^{-1}. The effect of this nonthermal dispersion is discussed in §3.6.4.

Comparison to Previous Studies

Taking the optical depth to be typically 5-10 for the majority of clumps, and the kinetic temperature to be 12-25 K for the majority of the clumps, we compare our results to similar studies. These values are in agreement with the dense clumps in G19.30+0.07 observed by Devine et al. (2011) with the VLA and the same spectral lines. Compared to the sample of Ragan et al. (2011), who also used the (1,1) and (2,2) lines observed by the GBT and the VLA, we find slightly higher kinetic temperatures in our study. They measured kinetic temperatures in the range of about 8 K to 13 K., however their sample was selected to be devoid of star formation indicators and thus be in the earliest evolutionary phases. It is possible that our sample generally reflects a slightly later stage in IRDC evolution, in which star formation activity has increased and the gas is showing the affects of protostellar heating.

Our clumps are slightly different than dense cores and core candidates in Perseus observed by Rosolowsky et al. (2008) with the GBT, also with the same spectral lines. They found colder kinetic temperatures around 10-12 K and optical depths usually less than 5, but as high as 15 in the densest cores. Furthermore, they observed column densities around 5×10^{14} cm^{-2} with only the densest cores exceeding 10^{15} cm^{-2}, while we observe column densities 10^{14}-10^{16} cm^{-2} and nearly all of our clumps peak at about 3×10^{15} cm^{-2}. Their GBT observations of cores at 260 pc have comparable

physical resolution (0.04 pc) to our study (0.02-0.1 pc), so the differences cannot be explained by beam dilution effects. The higher column densities in our study can be partially explained by using a slightly different method of calculation that includes a correction for both parity states of the (1,1) (Friesen et al. 2009). This correction typically increases the column densities by less than a factor of two for the measured excitations temperatures. We therefore are observing slightly warmer gas and slightly higher column densities in IRDCs than lower mass and apparently more quiescent star forming environments like Perseus. This is not surprising if star formation activity is largely controlled by mass surface density; the average mass surface density in Perseus is approximately 90 $M_{\odot}$ pc^{-2} (Heiderman et al. 2010), but is approximately 150 $M_{\odot}$ pc^{-2} in IRDCs (based on masses and sizes reported by Simon et al. (2006b)).

3.6 Discussion

3.6.1 Kinematics and Previous Studies of Individual Sources

All nine IRDCs show evidence of clumps and velocity substructure. The IRDCs are generally composed of many distinct clumps that sometimes can be grouped into subclouds of similar velocities. These subclouds and clumps also overlap spatially and show apparent interactions in position-position-velocity space, with star formation tracers (infrared point sources, masers, H II regions, etc.) coincident with these overlapping sites. We also see smoother velocity gradients along the most filamentary (high aspect ratios, $A_0 \gtrsim 3$) clumps and across clouds as a whole.

G010.74-00.13

G010.74-00.13 shows a clear velocity gradient west to east across the cloud. Channel maps of the NH_3 (1,1) emission are presented in Figure 3.14. At low velocity ($v_{\rm LSR} \approx$ 28 km s $^{-1}$), the NH_3 morphology appears filamentary, however it gradually transitions to a more globular morphology at higher velocity ($v_{\rm LSR} \approx 30$ km s^{-1}). This structure appears to be two distinct subclouds of different morphologies and velocities. It is notable that both infrared point sources (possible protostars; see Figure 3.4) are coincident with the filamentary component. There is an elevated velocity dispersion (peak in the second-moment maps of about 0.9 km s^{-1}) in the center of the cloud where these two subclouds overlap and may be colliding in this scenario. This location is also coincident with one of the protostellar candidates. The majority of the NH_3 (2,2) emission is within the filamentary velocity component, whereas the CCS more closely follows the 30 km s $^{-1}$ globular component. In G010.74-00.13, it may be that this cloud-cloud collision has triggered both the formation of the protostar and the high velocity dispersion, or it may be that the protostar is responsible for the high velocity dispersion directly and its location is coincidental.

G022.56-00.20

G022.56-00.20 is deconvolved into three subclouds with `cprops`. The central velocity component ($v_{\rm LSR} \approx 77$ km s^{-1}) is located at the northeastern end of the cloud, while the high ($v_{\rm LSR} \approx 78$ km s^{-1}) and low ($v_{\rm LSR} \approx 75$ km s^{-1}) velocity components have high aspect ratios ($A_0 \approx$3) and run nearly parallel to each other along the cloud's major axis. The 75 km s^{-1} velocity component is located slightly to the north of the 78 km s^{-1} velocity component, though they overlap spatially, and the cloud shows a high velocity dispersion of about 2 km s^{-1} in the overlap region. It is noteworthy

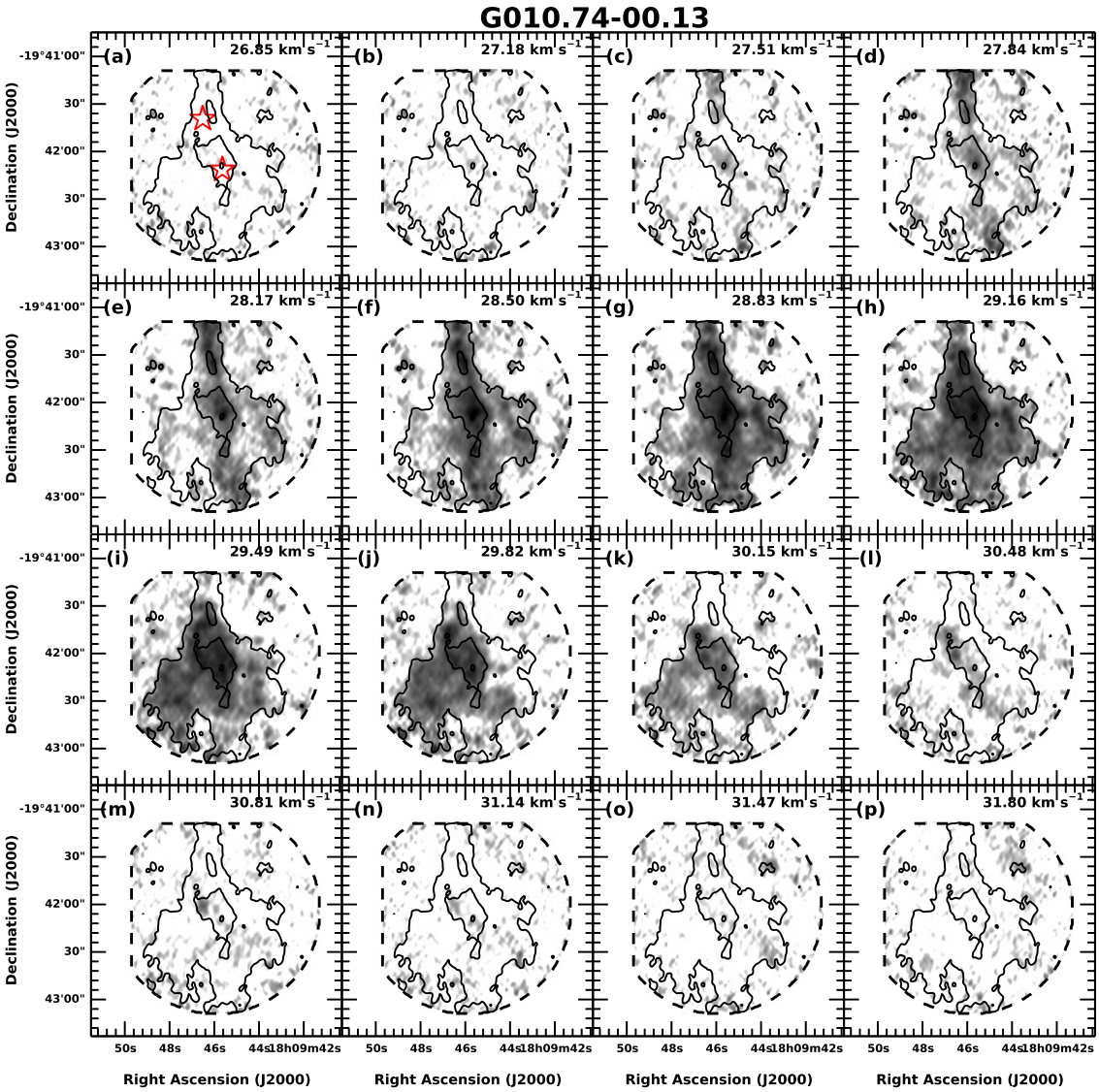

Fig. 3.14.— Channel maps of the main hyperfine component of the NH_3 (1,1) emission in G010.74-00.13, shown in a logarithmic scale from 5 mJy beam^{-1} to 70 mJy beam^{-1}. Black contours show the integrated NH_3 (1,1) intensity and overlapping GBT and VLA footprint, same as the white contours in Figure 3.4. Channel velocities, $v_{\rm LSR}$, are labeled in the upper right corner of each panel in km s^{-1}. The 70 μm infrared point sources are marked by stars in panel (a) (red in the online figure). There is a clear gradient from the filamentary structure running north to south into the globular structure extending to the southeast. The largest linewidth is at the center of the cloud, coincident with both structures and with an embedded infrared point source.

that the peak in integrated intensity, the peak in velocity dispersion, and an infrared point source are all coincident in the center of this overlap region, as can be seen in Figures 3.5 and 3.15. In Figure 3.16, the position-velocity diagrams taken across the cloud parallel to the minor axis clearly show these major velocity components and their interaction. We identify two possible scenarios for G022.56-00.20: (1) this cloud is a collision of multiple subclouds, apparently triggering the formation of the protostar; or (2) the protostar is driving expansion of the molecular gas around it. The separation between the two primary components is $\lesssim 5$ km s^{-1} and they extend $\lesssim 1$ pc, making either scenario plausible.

G024.60+00.08

G024.60+00.08 shows a clear gradient in the velocity field from about $v_{\rm LSR} \approx 50.5$ km s^{-1} in the west to about $v_{\rm LSR} \approx 55$ km s^{-1} in the east-southeast. Channel maps of the cloud in Figure 3.17 do not clearly distinguish between the possibility of two distinct components or a single gradient across one major component. There is a velocity dispersion peak of about 1.2 km s^{-1}, cospatial with a large NH_3 clump and an infrared point source near the center of the cloud (see Figure 3.6). Rathborne et al. (2007) identified two protostellar condensations (bright, compact, millimeter cores with infrared emission indicative of star formation) in G024.60+00.08 with IRAM Plateau de Bure 1.3 and 3 mm continuum and *Spitzer* images, one of which is the central IR point source. Cyganowski et al. (2008) identified an EGO in G024.60+00.08. The position of the EGO is marked in Figure 3.6, and is also coincident with the protostellar candidate.

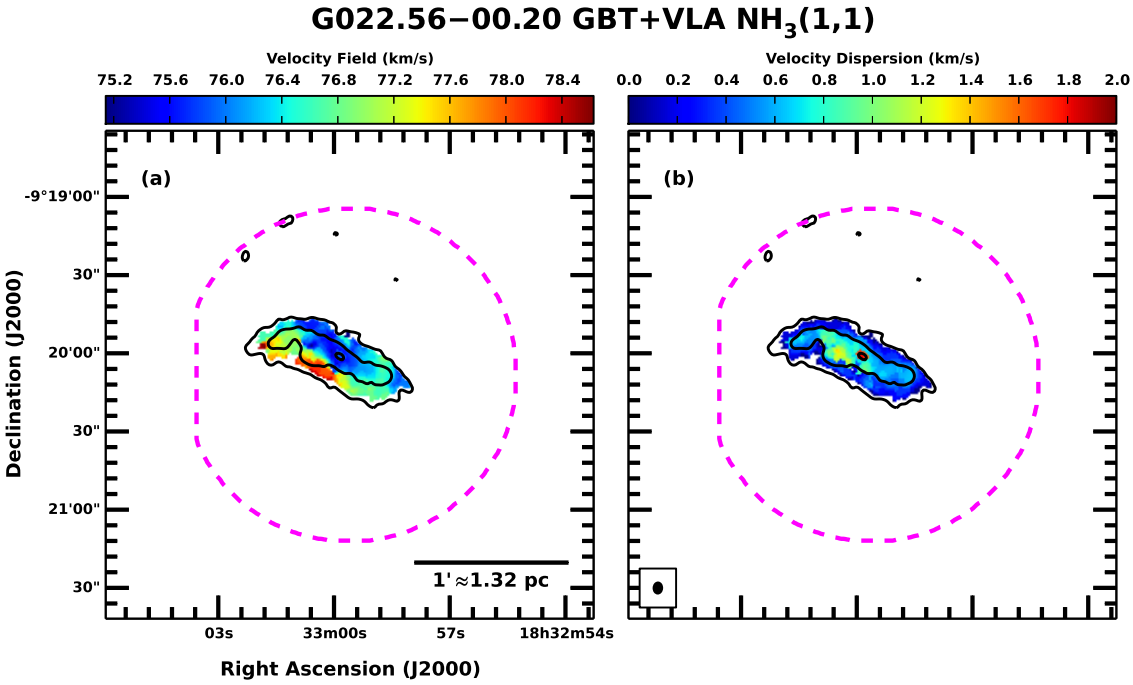

Fig. 3.15.— Moment 1 and moment 2 maps showing the velocity field ($\langle v_{(1,1)} \rangle$) and velocity dispersion ($\langle v^2_{(1,1)} \rangle$), respectively, from the NH_3 (1,1) emission in G022.56-00.20. Clump deconvolution with `cprops` identifies three subclouds: one filament running along the northwestern edge, one globule at the northeastern end, and one filament running along the southeastern edge. The gradient in the velocity velocity field is explained by the velocity offset between the two filaments, and the elevated velocity dispersion through the center of the cloud is coincident with the overlap of the two filaments. The peak in the velocity dispersion, the peak in the integrated NH_3 emission, and an infrared point source are all coincident at the center of the cloud.

G028.23-00.19

G028.23-00.19 is an apparent starless, dark cloud. The bright point source (Figure 3.7) is an unrelated, foreground late-type star (Bowers & Knapp 1989). Rathborne et al. (2006) made millimeter continuum maps of G028.23-00.19 with the IRAM 30 m single dish telescope and observed three dense clumps at 11″ resolution with masses ranging from 38 to 705 $M_\odot$. The primary cloud has one filament, with at least 4

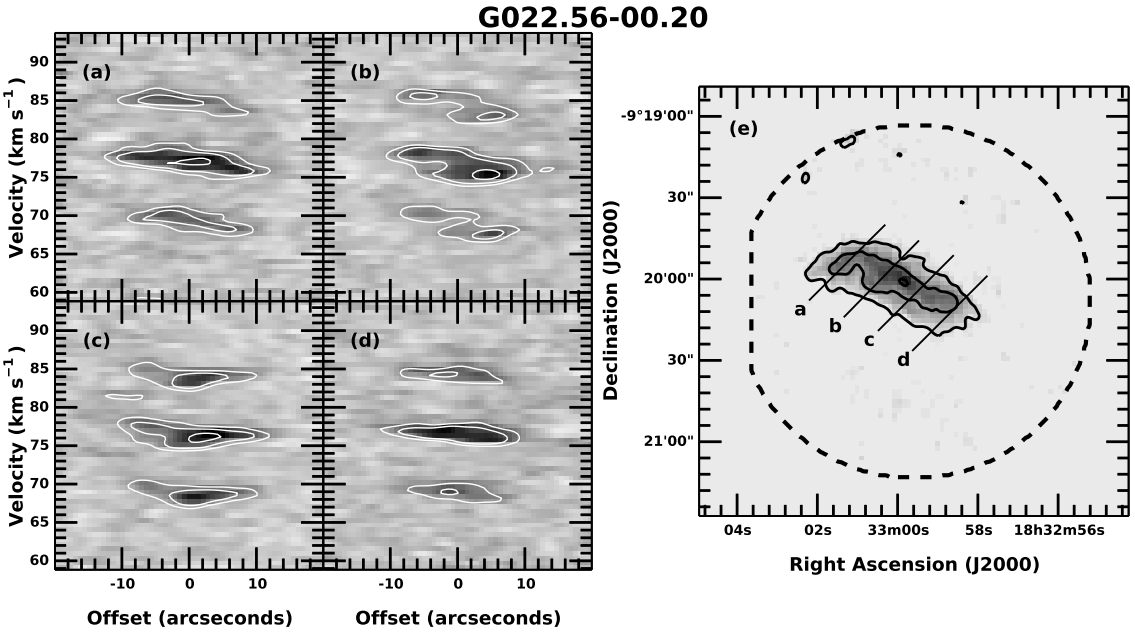

Fig. 3.16.— Position-velocity diagrams in (a) through (d), with white contours at 2σ, 4σ, and 8σ. Slices for the diagrams are labeled and overplotted on the integrated intensity map of G022.56-00.20 in (e) in grayscale with a linear stretch. The black contours for the integrated intensity and combined GBT and VLA footprint are the same as the white contours in Figure 3.5. The angular offsets in the diagrams increase from east to west. The three most distinct structures in each diagram are the main and two inner satellite hyperfine components of the NH_3 (1,1) line. The velocity offset between the two primary filaments is most apparent through the center of the cloud.

connecting filaments extending beyond our maps, but seen in infrared extinction. Sanhueza et al. (2013) found two distinct velocity components in CARMA observations of this cloud, with 0.3 km s^{-1}, 10.″9 resolution. The presence of SiO emission and the strength of the CH_3OH emission in the absence of an apparent protostar lead them to conclude further that the two components were colliding and exciting the emission. In our data, the position-velocity diagram shows that the velocity structure in NH_3 is a smoother gradient across the filament, from about $v_{\rm LSR} \approx 79$ km s^{-1} to $v_{\rm LSR} \approx 82$ km s^{-1}. It is unlikely that we are seeing a resolution effect, given that we

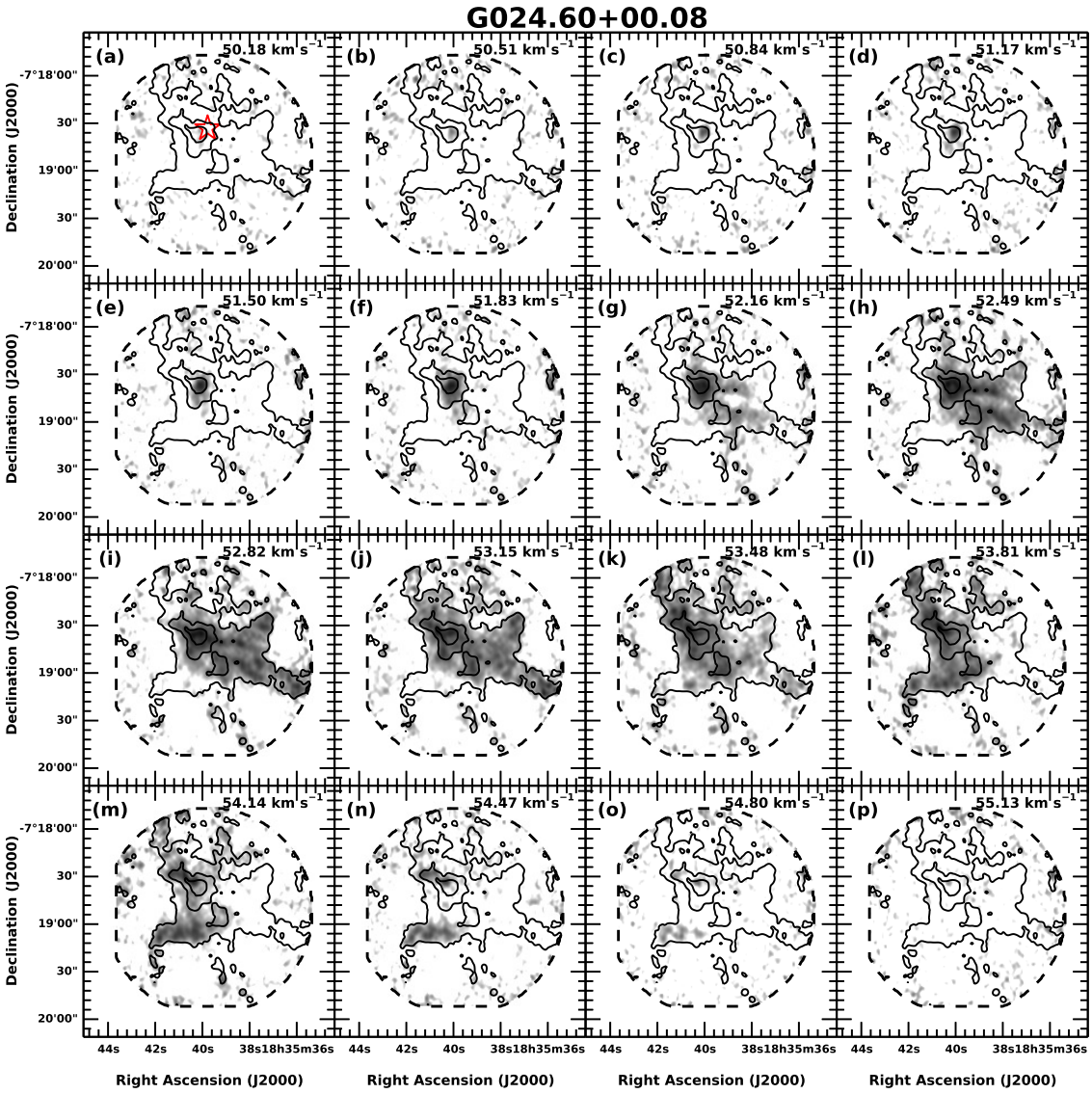

Fig. 3.17.— Channel maps of the NH_3 (1,1) emission as in Figure 3.14 but for G024.60+00.08, with contours and field of view matching Figure 3.6, and only one 70 μm source. There is a clear gradient from the northwest to southeast along the filamentary structures. These filaments extend further in the infrared extinction maps beyond the coverage of the NH_3 observations. Deconvolution with `cprops` identifies multiple subclouds with offset velocities along these filaments. The largest linewidth is at the center of the cloud, coincident with both structures and with an embedded infrared point source.

have comparable velocity resolution and higher angular resolution than the CARMA study. The discrete clumps may be explained by a combination of chemical differentiation across the cloud and/or missing the largest spatial scales in the CARMA data. There is also an ammonia velocity dispersion peak of about 0.9 km s^{-1} coincident with the optical depth peak. We propose a possible explanation that the core in G028.83-00.19 may be a deeply embedded protostar with an outflow exciting the SiO and CH_3OH.

G031.97+00.07

G031.97+00.07 has the most complex substructure in our sample. Rathborne et al. (2006) made millimeter continuum maps of G031.97+00.07 with the IRAM 30 m single dish telescope at 11″ resolution and observed nine dense clumps with masses ranging from 151 to 1890 $M_\odot$. Urquhart et al. (2009) identified an H II region in G031.97+00.07 and Wang et al. (2006) reported H_2O masers in G031.97+00.07, all marked in Figure 3.8. The infrared morphology has a long, thin filamentary structure leading to a higher contrast globule neighbored by at least 3 protostars with H II regions and masers. The cloud itself is part of a much larger molecular complex seen in ^{13}CO in the BU-GRS with infrared dark filaments extending beyond our observations.

Seen in Figure 3.8, The NH_3 emission closely matches the infrared contrast, and it is deconvolved into 21 distinct clumps. As seen in the position-velocity slices in Figure 3.18, the structures are a mix of filaments and globules, and tend to fall in one of two distinct velocity ranges: $v_{\rm LSR} \approx$ 92-99 km s^{-1} and $v_{\rm LSR} \approx$ 97-102 km s^{-1}. The majority of the emission is in the 92-99 km s^{-1} velocity range, however the 97-102 km s^{-1} velocity range is coincident with at least one protostar. The filamentary

structures also show velocity gradients spanning about 2 km s^{-1} along their major axis, as seen in Figure 3.19. This cloud also has the strongest CCS emission in our sample, with a peak signal-to-noise ratio of about 22. G031.97+00.07 may be a region where several weaker filaments extending tens of parsecs are feeding molecular gas and star formation is progressing most quickly at the collision points. The morphology and velocity structure of this cloud is consistent with the "hub-filament structure" described in Myers (2009) and Li et al. (2013), in which gas flows along the filaments to a central hub where it feeds star formation.

Battersby et al. (2014b) recently studied G031.97+00.07 (called G32.02+0.06 in their work) in the NH_3 (1,1), (2,2), and (4,4) transitions with the VLA and discussed the environment of the larger molecular complex. They observed two pointings, one towards the active region at the north end of the cloud, and one quiescent region near the south end of the cloud (their pointings partially overlap our combined maps, but do not cover the central portion of the cloud). They found dense parsec scale filaments of 10 to 100 $M_\odot$ with dense cores less than 0.1 pc in size, in agreement with our findings. The authors reported that the dense cores were virially unstable to gravitational collapse, and that turbulence likely set the fragmentation length scale in the filaments. In the quiescent region, they observed the two distinct velocity components that we see continue along the cloud towards the more complex active region. Finally, they note the existence of at least three bubbles all seen in *Spitzer*, *Herschel*, and the BU-GRS that are likely older H II regions from previous generations of massive stars, and may have compressed the molecular gas to form and/or shape the IRDC and trigger more recent massive star formation.

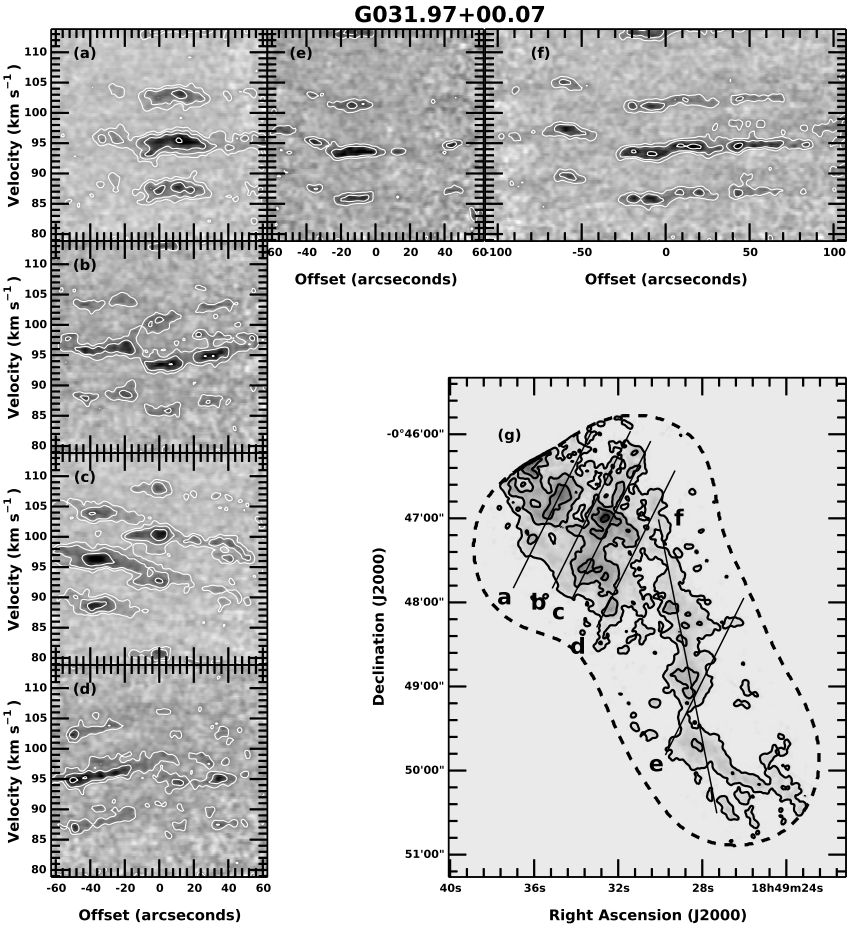

Fig. 3.18.— Position-velocity diagrams in (a) through (f) as in Figure 3.16, but for G031.97+00.07 with white contours at 2σ, 4σ, 8σ, and 16σ. Slices and the integrated intensity map are shown in (g) also as in Figure 3.16, but with contours taken from Figure 3.8. G031.97+00.07 contains a complex substructure of globules and filaments at offset velocities and with internal velocity gradients.

G032.70-00.30

G032.70-00.30 has the weakest NH_3 emission in our sample. As shown in Figure 3.5, the (2,2) line is only marginally detected, and there is no detected CCS. Weak infrared point sources indicate protostellar candidates at both ends of the cloud. There is a velocity gradient from $v_{\rm LSR} \approx 89$ km s^{-1} to $v_{\rm LSR} \approx 91$ km s^{-1} across the filament

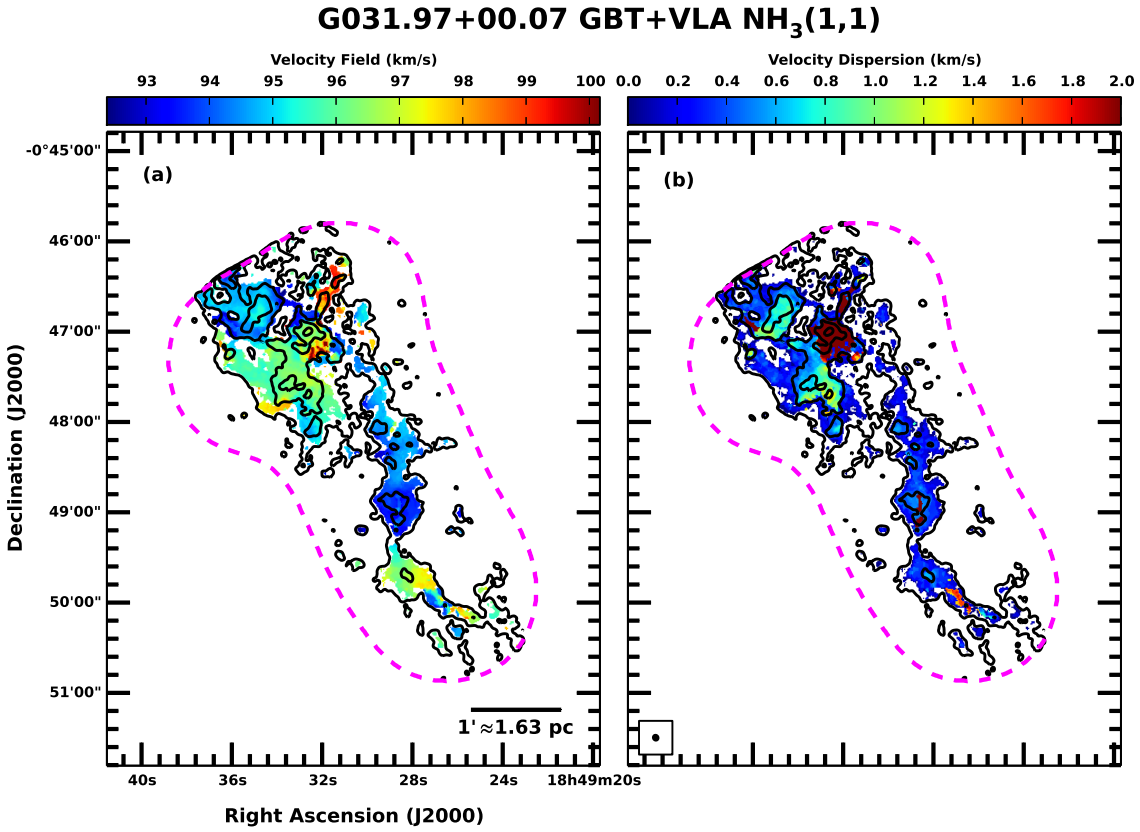

Fig. 3.19.— Moment 1 and moment 2 maps showing the velocity field ($\langle v_{(1,1)} \rangle$) and velocity dispersion ($\langle v^2_{(1,1)} \rangle$), respectively, from the NH_3 (1,1) emission in G031.97+00.07. Deconvolution with `cprops` reveals a complex substructure with 21 globules and filaments. The majority of the emission is in a lower velocity component around 92-99 km s^{-1}, though a few clumps form a higher velocity component around 97-102 km s^{-1}. These velocity components are cospatial, as shown by the elevated values in the velocity dispersion map. There are additionally velocity gradients along the substructures with higher aspect ratios, such as the filament in the middle of the cloud.

from southeast to northwest, with the highest velocity dispersion of 0.8 km s^{-1} near the southwestern end.

G034.43+00.24

Urquhart et al. (2009) identified an H II region in G034.43+00.24 and Wang et al. (2006) reported H_2O masers in G034.43+00.24, all marked in Figure 3.10. Rathborne et al. (2005) observed the millimeter/submillimeter continuum in G034.43+00.24 with IRAM, the James Clerk Maxwell Telescope (JCMT), and the Caltech Submillimeter Observatory (CSO). They identified three compact clumps of several hundred solar masses each. The spectral energy distributions (SEDs) stretching from the millimeter to the infrared indicated high luminosities consistent with protostars of $\sim$10 $M_\odot$ each. Moreover, Rathborne et al. (2005) also observed HCN, CS, and SiO in G034.43+00.24 with IRAM and CSO. The large line widths of $\sim$10 km s^{-1} in HCN and CS along with the detection of SiO indicated outflows and shocked gas, further evidence of ongoing star formation. Cyganowski et al. (2008) identified two EGOs, marked in Figure 3.10. Sanhueza et al. (2010) observed this region in multiple molecular gas tracers with the Atacama Pathfinder Experiment (APEX) 12 m telescope, the Nobeyama Radio Observatory (NRO) 45 m, and the Swedish-ESO 15 m Submillimeter Telescope (SEST). They found 4 molecular cores with velocity profiles indicative of outflows and large scale infall towards the most massive core, further strengthening the evidence for ongoing massive star formation in this cloud.

G034.43+00.24 has a complex substructure. The overall shape is very filamentary (see Figure 3.10), and it is a portion of the Giant Molecular Filament GMF38.1-32.4a identified by Ragan et al. (2014). The cloud is known to have three protostars with masers, EGOs, and millimeter cores along the primary filament, with an additional

protostar at the northern end of the cloud. Shown in Figure 3.20, The velocity dispersion is elevated to over 2 km s^{-1} at two of the protostar positions. There is an overall gradient from the southwest to the northeast. The major filament has a velocity gradient from the west to the east, leading into a gradient from south ($v_{\rm LSR} \approx$ 56 km s^{-1}) to north ($v_{\rm LSR} \approx 60$ km s^{-1}) along the weaker filament toward the northern protostar. This gradient may be the result of gas flowing along the larger GMF, or may be composed of multiple subclouds not resolved in velocity.

G035.39-00.33

G035.39-00.33 is a long, filamentary, high IR contrast cloud with protostellar candidates (see Figure 3.11). The velocity structure shows two distinct velocity components: a $v_{\rm LSR} \approx 43$ km s^{-1} velocity subcloud at the northern end of our observations, and a $v_{\rm LSR} \approx 45$ km s^{-1} velocity filament in the main cloud with a gradient from the southeast to the northwest. The two components are well separated in velocity space, and position-velocity slices do not show any apparent interaction between the two. We see high velocity dispersion around most of the protostars, only one of which is coincident with the lower velocity component. Our GBT data, which cover much more of the cloud and have higher velocity resolution, show that the velocity gradient in the 45 km s^{-1} component continues along the northern extent of the filament.

Jiménez-Serra et al. (2010) observed G035.39-00.33 in the SiO J=2-1 line (a shock tracer) with the IRAM 30 m, and found both bright, compact emission with broad linewidths and weaker, extended emission with narrow linewidths. The compact emission was consistent with protostellar outflows, and they proposed three explanations for the extended emission: (1) a collection of low mass outflows throughout the cloud, (2) a recently processed more massive outflow whose energy was distributed through-

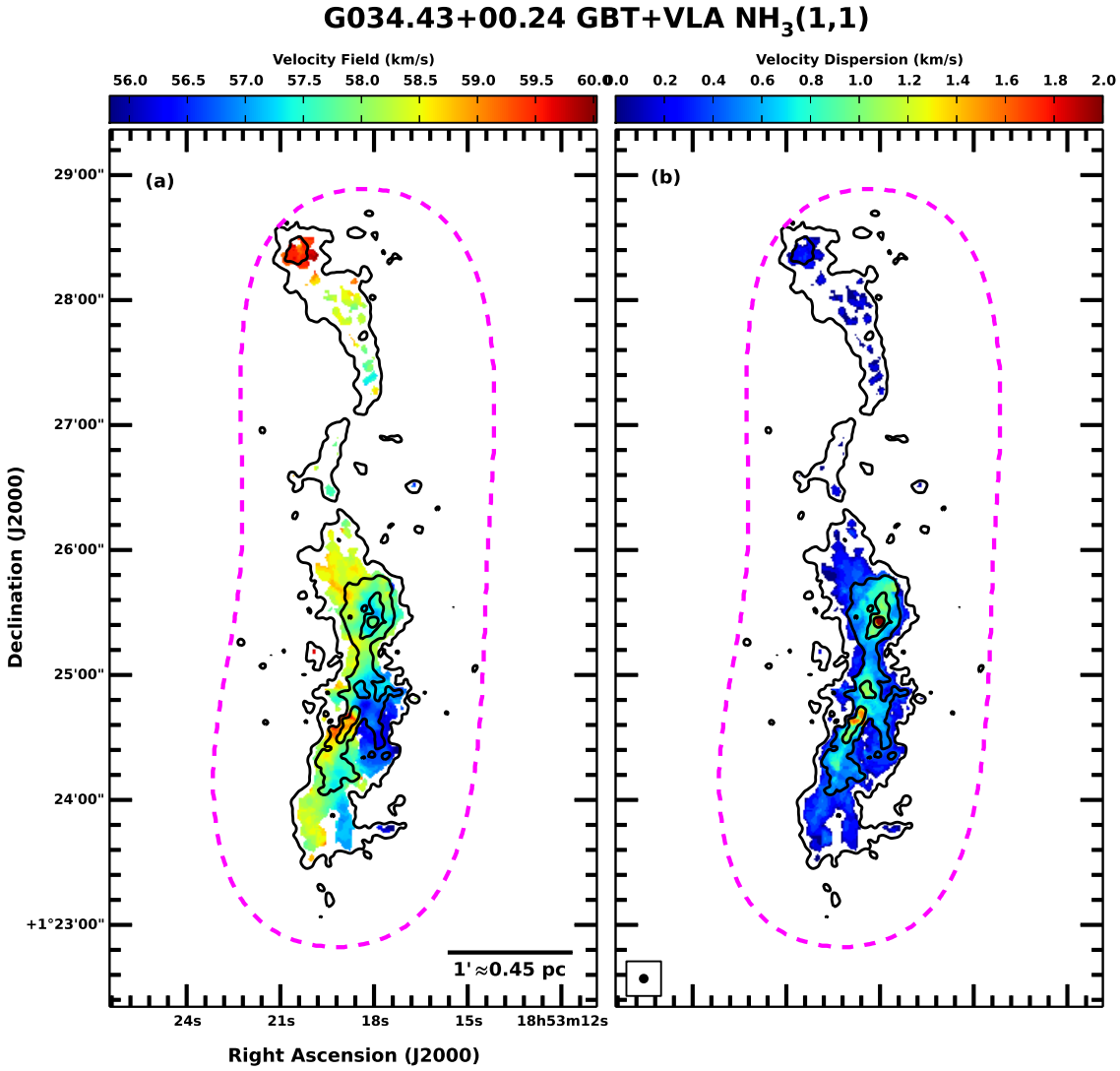

Fig. 3.20.— Moment 1 and moment 2 maps showing the velocity field ($\langle v_{(1,1)} \rangle$) and velocity dispersion ($\langle v^2_{(1,1)} \rangle$), respectively, from the NH_3 (1,1) emission in G034.43+00.24. The cloud as a whole is very filamentary, but deconvolution with `cprops` reveals subclouds ranging from globule to filamentary within the larger filamentary structure. The southern half of the cloud contains three strong protostellar candidates. The two with known EGOs, indicative of molecular outflows, are coincident with the peaks in the velocity dispersion. An overall velocity gradient in the cloud is seen from the western edge to the eastern edge in this part of the cloud, then continues along the fainter filament to the protostar in the north.

out the cloud, or (3) the IRDC was recently assembled from collisions of smaller clouds or filaments. They detected three filaments with distinct velocities at approximately 44.1 km s^{-1}, 45.3 km s^{-1}, and 46.6 km s^{-1}. Jiménez-Serra et al. (2014) further found velocity gradients of 0.4 to 0.8 km s^{-1} pc^{-1} from north to south along the filaments, as seen in multiple transitions of ^{13}CO and $C^{18}O$ with the IRAM 30 m and the JCMT. They further found that dense cores were preferentially located at the intersection of the (possibly interacting) filaments. Henshaw et al. (2014) observed N_2H^+ (1-0) in G035.39-00.33 with the Plateau de Bure Interferometer (PdBI) array and noted that the local kinematics of the filaments were affected the dense cores, either through accretion or expanding envelopes. Hernandez et al. (2012) found that this parsec-scale region was consistent with being in virial equilibrium without requiring support from magnetic fields, and that the timescale for achieving equilibrium was less that the estimated 1.4 Myr for formation from two converging flows.

While these studies focused primarily on the narrower portion of the cloud north of our VLA maps, our larger GBT maps cover the region in these studies, and we also detect these three velocity components in NH_3 (though the 46.6 km s^{-1} component is seen only weakly). The two velocity components we observed in our combined maps are the extensions of two of these filaments to the south. Most of the emission we detected here is part of the 45 km s^{-1} velocity component, and this southern region is both wider and darker (in MIR extinction) than the northern portion of the cloud. We suggest that this IRDC may also represent an example of the hub-filament structure, in which gas is flowing along the parsec-scale 45 km s^{-1} filament to the region we studied, where it feeds the ongoing star formation traced by infrared point sources.

G038.95-00.47

G038.95-00.47 is a globular IRDC with long, low infrared contrast filaments extending from a few parsecs away from it to the east. Seen in Figure 3.12, it also contains at least 2 protostellar candidates along the western edge, and neighbors two infrared bubbles to the southeast and southwest. The velocity field shows a clear gradient from the southwest to the east ($v_{\rm LSR} \approx 40.5$ km s^{-1}) and north ($v_{\rm LSR} \approx 43.5$ km s^{-1}). This cloud is also consistent with the "hub-filament structure" described in Myers (2009) and Li et al. (2013).

Xu et al. (2013) studied G038.95-00.47 in relationship to its environment, specifically the two adjacent H II regions G38.91-0.44 (N74) and G39.30-1.04 (N75). They used 1.4 GHz radio continuum and single dish ^{12}CO, ^{13}CO, and C^{18}O J=1-0 observations to probe the physical characteristics of the bubbles and used GLIMPSE data to identify young stellar objects (YSOs) in the region. They found a molecular clump associated with G038.95-00.47 that showed a sharp integrated intensity gradient towards the H II regions consistent with it being compressed by their expansion. They further identify an overabundance of YSOs in the IRDC and propose that star formation was triggered via "radiatively driven implosion" (RDI).

3.6.2 Mass Estimates

We estimate the H_2 masses for IRDCs from three independent methods: dust extinction, dust thermal emission, and ^{13}CO emission, described below. Total IRDC masses for our sample for all three methods are shown in Figure 3.21, with a comparison discussed below. All masses were measured by integrating over the footprint of our combined GBT+VLA observations.

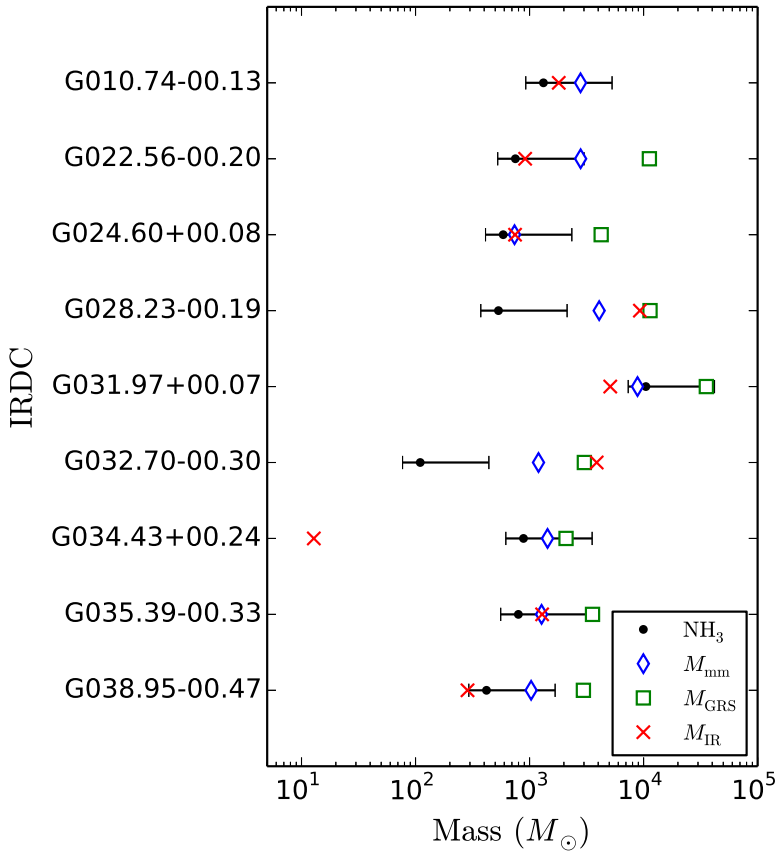

Fig. 3.21.— Total molecular gas masses for our IRDC sample using three different method of estimation, along with the mass inferred from NH_3 assuming a relative abundance of 10^{-8} compared to molecular hydrogen. The error bars represent a factor of three variation in this abundance. Values of $M_{\rm IR}$ are the masses estimated from dust absorption, i.e. 24 μm contrast. Because of the infrared emission from protostellar candidates, IR bubbles, etc., the dust extinction method is not viable everywhere. The mass estimates may therefore be lower limits, particularly for G034.43+00.24. Values of $M_{\rm mm}$ are the masses estimated from dust emission at 1.12 mm, observed in the BGPS. Values of $M_{\rm GRS}$ are masses estimated from ^{13}CO J=1-0 in the BU-GRS, except for G010.74-00.13, which was not covered in that survey. The emission is probably optically thick, but also includes the contribution of the lower density molecular envelopes. The masses estimated from the BGPS and the BU-GRS data are typically well-correlated, but the BU-GRS masses are higher by factors of a few.

IR Extinction Mass Estimates

For the dust extinction method, we continue to follow the analysis presented by Butler & Tan (2009) used to calculate infrared extinction maps described in §3.4.2. The mass surface density is determined from the optical depth by

$$\Sigma_\lambda = \frac{\tau_\lambda}{\kappa_\lambda}, \tag{3.19}$$

where κ_λ is the dust opacity per gas mass at wavelength λ. Our choice of dust opacity from the literature will affect the mass estimate by as much as factors of a few. For MIPS 24 μm, we adopt $\kappa_{24\mu\mathrm{m}} = 13.3$ cm^2 g^{-1} from the dust model of Ossenkopf & Henning (1994) for 10^5 year-old, 10^6 cm^{-3} dust with thin ice mantles and assuming a dust-to-gas mass ratio of 1:100. This value has an uncertainty of about a factor of three given the full range of possible κ_ν values, depending on the age, thickness of ice mantles, and number density of dust grains, which results in a factor of about three uncertainty in the mass estimates. The angular resolution of the 24 μm images, and thus our extinction and mass surface density maps, is $6''$, compared to the $3\farcs2$-$5\farcs4$ resolution of the NH_3 maps. This is the closest resolution match of the three mass estimates, however it lacks any velocity information to disentangle multiple clumps along a single line of sight.

For the total mass, we simply sum over the IRDC:

$$M_{\mathrm{IR}} = D^2 \Omega \sum_{\mathrm{IRDC}} \Sigma_\lambda = 30 \left(\frac{D}{\mathrm{kpc}}\right)^2 \left(\frac{\Omega}{\mathrm{arcmin}^2}\right) \left(\sum_{\mathrm{IRDC}} \tau_\lambda\right) M_\odot. \tag{3.20}$$

Cloud masses estimated with this method range from about 280 $M_\odot$ to 3900 $M_\odot$, excluding G034.43+00.24. In this cloud, M_{IR} is a very weak lower limit on the mass because there is significant infrared emission from IR point sources that prevents us

from calculating the extinction across most of the IRDC.

BU-GRS ^{13}CO J=1-0 Mass Estimates

Next, we estimate the gas mass from the ^{13}CO J=1-0 BU-GRS data cubes. Because the spectral line data have velocity information, we restrict measurements from this emission to velocity ranges with NH_3 (1,1) emission greater than 5σ. While the velocity resolution of 0.2 km s^{-1} is in fact better than our 0.6 km s^{-1} resolution NH_3 data cubes, the beam FWHM is 46″, so we are not able to resolve individual clumps. G010.74-00.13 is outside the coverage of the BU-GRS, and so is not included in this analysis.

To calculate the ^{13}CO J=1-0 column density, we use the method described in §2.2.4, though this time we assume an excitation temperature $T_{\rm ex,GRS} = 10$ K. Using a higher excitation temperature of 20 K would raise the mass estimates by approximately 40% compared to 10 K. The column density of the total molecular gas is

$$N_{\rm GRS}({\rm H_2}) = 4.2 \times 10^{20} \left(\frac{\int T_{B,{\rm GRS}}\, dv}{\rm K\ km\ s^{-1}} \right) {\rm cm^{-2}}. \tag{3.21}$$

To calculate the total mass of the gas, we sum over the cloud and use

$$\begin{aligned} M_{\rm GRS} &= \mu m_{\rm H} D^2 \Omega \sum_{\rm IRDC} N_{\rm GRS}({\rm H_2}) \\ &= 0.7 \left(\frac{D}{\rm kpc} \right)^2 \left(\frac{\Omega}{\rm arcmin^2} \right) \left(\frac{I_{\rm GRS}}{\rm K\ km\ s^{-1}} \right) M_\odot, \end{aligned} \tag{3.22}$$

where μ is the mean molecular weight in multiples of the proton mass (assumed to be 2.33), D is the distance to the region, Ω is the solid angle occupied by the gas, and $I_{\rm GRS}$ is the sum of $T_{B,{\rm GRS}}$ over the IRDC in position and velocity.

Cloud masses estimated with this method range from about 2090 $M_\odot$ to 36000

$M_\odot$. We note that our mass estimates from this method are systematically lower than those reported by Simon et al. (2006b) by factors of about two to six. However, the Simon et al. (2006b) analysis uses ellipses larger than the IRDCs themselves, sometimes including complex networks of filaments extending beyond our maps, to get total masses, and so they expect their own values to be overestimates. Both our mass estimates with this method and those of Simon et al. (2006b) are systematically higher than those derived from IR extinction. We discuss this further below.

BGPS Dust Emission Mass Estimates

To calculate the gas mass from thermal dust emission, we follow the method of Friesen et al. (2009) applied to $\lambda = 1.12$ mm maps from the Bolocam Galactic Plane Survey (BGPS) (Aguirre et al. 2011). The hydrogen column can be estimated by

$$N_{\rm mm}({\rm H_2}) = \frac{S_{1.12{\rm mm}}}{\Omega_{\rm mb}\mu m_{\rm H}\kappa_{1.12{\rm mm}}B_\lambda(T_d)}, \tag{3.23}$$

where $S_{1.12{\rm mm}}$ is the flux density of the Bolocam emission, $\Omega_{\rm mb}$ is the solid angle of the main beam (33″ FWHM), μ is the mean molecular weight, $m_{\rm H}$ is the mass of a hydrogen atom, $\kappa_{1.12{\rm mm}}$ is the dust emissivity per unit gas mass, and $B_\lambda(T_d)$ is the Planck function for a dust temperature T_d. We adopt $\kappa_{1.12{\rm mm}} = 0.012$ cm^2 g^{-1}, again assuming a dust-to-gas mass ratio of 1:100 and using the dust model of Ossenkopf & Henning (1994) for 10^5 year-old, 10^6 cm^{-3} dust with thin ice mantles. The total mass summed over the IRDC is then

$$\begin{aligned} M_{\rm mm} &= \mu m_{\rm H} D^2 \Omega \sum_{\rm IRDC} N_{\rm mm}({\rm H_2}) \\ &= 41 \left(\frac{S_\nu}{\rm Jy}\right)\left(\frac{D}{\rm kpc}\right)^2\left(\frac{\Omega}{\rm arcmin^2}\right)\left(\exp\left[\frac{12.85\ {\rm K}}{T_d}\right]-1\right) M_\odot. \end{aligned} \tag{3.24}$$

Our choice of dust temperature is informed by the findings of Battersby et al. (2014a). They compared the dust temperature inferred from *Herschel* SEDs to the gas (kinetic) temperature measured from the NH_3 (1,1), (2,2), and (4,4) transitions with the VLA in G031.97+00.07 (called G32.02+0.05 in their work). The dust temperatures, 11.6±0.2 K, were systematically lower than the gas temperatures, 15.2±1.5 K, however the two temperatures were generally correlated regardless of local star formation activity. We therefore adopt the median of the clump-averaged kinetic temperatures in Table 3.4 for each IRDC multiplied by the ratio 11.6/15.2 as the dust temperature for each cloud. We do not use our T_K maps directly because of the resolution mismatch and the lack of kinematic information in the Bolocam data to separate multiple velocity components. Cloud masses estimated with this method range from about 740 $M_\odot$ to 8900 $M_\odot$. It should be noted that the resolution of the BGPS is poorer than that of the ammonia maps by a factor of a few, and also does not contain velocity information.

Comparison of Mass Estimates

The cloud mass estimates from the three methods are shown in Figure 3.21. For the majority of our sample, the masses derived from dust emission are typically consistent with those estimated from the IR extinction within a factor of a few, well within our estimated uncertainties. We note that in G028.23-00.19 and G032.70-00.30 , $M_{\rm IR}$ and $M_{\rm GRS}$ agree well, but $M_{\rm mm}$ is well below the other estimates. These are both quiescent clouds, so it is possible that the typical dust temperature in these clouds is lower than the median clump-averaged kinetic temperature we used, and so the dust emission mass estimate is low. In G034.43+00.24, $M_{\rm IR}$ is a very weak lower limit on the mass because of infrared emission from IR point sources, as discussed above.

In every case, $M_{\rm GRS}$ is greater than $M_{\rm mm}$ by at least factors of a few, and greater than an order of magnitude in G024.60+00.08. However, these two estimates are clearly well correlated. The ^{13}CO J=1-0 emission is probably optically thick, and may miss gas mass because of CO depletion, but also includes the contribution of the lower density molecular envelopes surrounding the IRDCs. Hernandez & Tan (2011) compared the mass surface density estimates from 8 μm extinction to that from the BU-GRS, taking care to subtract the contribution from the molecular envelope surrounding the IRDC itself (their study was performed in G034.43+00.24 and G035.39-00.33, though selected slightly different portions of the clouds that we studied here). Their mass estimates were also well-correlated though systematically offset, and they estimated the mass surface density of the envelopes to be about 50% higher that within the IRDC itself. Considering that the envelopes have a greater physical extent than the IRDCs, this effect can easily explain the offset that we see.

3.6.3 Ammonia Abundance

Total masses of the individual clumps are necessary to investigate their stability against gravitational collapse to form stars. We cannot use any of the three methods used above for the total IRDC masses because none of the datasets have both sufficient angular and velocity resolution to be used on individual clumps. It is straightforward to calculate a total NH_3 column from the spectral line fit, as shown in §3.4.3. We then must assume a fractional abundance, $X(NH_3)$, to convert from NH_3 to H_2. Our ability to compute the total mass of molecular gas in clumps, and thus their gravitational stability, is limited by our knowledge of the ammonia abundance relative to molecule hydrogen. Previous studies of the fractional abundance of NH_3 in physically similar environments yield a range of values from 10^{-9} to 10^{-7} (see for example Ragan

et al. 2011; Chira et al. 2013; Battersby et al. 2014a), and may depend on Galactocentric radius and the local chemistry, depending on and cloud age and physical environment (Battersby et al. 2014a). The uncertainty in this conversion factor will translate linearly to the uncertainty in clump masses, and so will affect our analysis of gravitational stability.

Because of the different resolutions and the fact that our ammonia column and mass measurements are restricted to the dense gas, we cannot probe how the abundance varies with environment. However, as shown in Figure 3.21, adopting a value of $X(\mathrm{NH_3}) = 10^{-8}$ for the ammonia abundance relative to hydrogen typically gives good agreement with dust emission and infrared extinction estimates within a factor of about three. We therefore assume a nominal value of 10^{-8} for calculating the masses of clumps, $M_{\rm cl}$, however the uncertainty of any individual clump mass is likely at least a factor of three.

3.6.4 Gravitational Stability

From the mass and size of a clump, we can calculate the mean mass density ρ_0, and thus the spherical free-fall time,

$$t_{\rm ff,sph} = \sqrt{\frac{3\pi}{32 G \rho_0}} = \sqrt{\frac{\pi^2 R_{\rm eff}^3}{8 G M_{\rm cl}}} = 16.6 \left(\frac{R_{\rm eff}}{\rm pc}\right)^{3/2} \left(\frac{M_{\rm cl}}{M_\odot}\right)^{-1/2} \mathrm{Myr}, \tag{3.25}$$

or the filament free-fall time for a cylinder collapsing along its axis,

$$t_{\rm ff,cyl} = \sqrt{\frac{2}{3}} A_0 t_{\rm ff,sph} = 13.5 A_0 \left(\frac{R_{\rm eff}}{\rm pc}\right)^{3/2} \left(\frac{M_{\rm cl}}{M_\odot}\right)^{-1/2} \mathrm{Myr}, \tag{3.26}$$

where A_0 is the initial aspect ratio of the filament (Pon et al. 2011). We adopt the current aspect ratio of the clumps for A_0, implicitly assuming that these structures

are either young or have not evolved substantially since their formation, so our values of $t_{\rm ff,cyl}$ will be lower limits. Spherical free-fall times for these clumps range from 2×10^4 to 2×10^5 years, and cylindrical free-fall times range from 2×10^4 to 10^6 years. These timescales are consistent either with the expectation that these clouds are still in the earliest phases of star formation or that they are supported against free-fall collapse.

The first models of filamentary structures collapsing along characteristic length scales was presented by Chandrasekhar & Fermi (1953). They determined that a cylindrical cloud of incompressible fluid with an axial magnetic field separated into collapsing fragments whose length was initially 12 times the diameter of the cylinder. Following collapse and redistribution of mass, the length to diameter ratio shrinks to 4.5 if the average density remains unchanged, or 2 if there is no magnetic field. Schneider & Elmegreen (1979) identified filaments in optically dark nebulae and measured ratios of core separation to filament diameter of 3 ± 1, consistent with these predictions. The aspect ratios of approximately two-thirds of the clumps in our sample are between 1 and 2, but the most filamentary of our clumps have aspect ratios greater than 3, consistent with these predictions and studies.

It is common to calculate the virial mass and virial parameter for spherical clumps via

$$\alpha_{\rm vir,sph} = \frac{M_{\rm vir,sph}}{M_{\rm cl}} = \frac{5\sigma^2_{\rm line} R_{\rm eff}}{G M_{\rm cl}}, \tag{3.27}$$

using the total clump mass determined from NH_3, $M_{\rm cl}$, the line of sight velocity dispersion $\sigma_{\rm line}$, and the effective radius. A virial parameter less than 1 indicates a spherical clump prone to collapse, and greater than 1 is resistant to collapse. To calculate a similar virial parameter for filamentary clumps, we use the equilibrium

relation from Chandrasekhar & Fermi (1953) for an infinite, isothermal cylinder:

$$2\left(\gamma-1\right)\left(\frac{\mathcal{U}}{L}\right)+2\left(\frac{\mathcal{B}}{L}\right)-G\left(\frac{M_{\rm vir,cyl}}{L}\right)=0. \tag{3.28}$$

We take $\gamma = 7/5$ for the adiabatic index of diatomic gas, $(\mathcal{U}/L)$ is the internal kinetic energy of the clump per unit length, $(\mathcal{B}/L)$ is the magnetic energy per unit length, and $(M_{\rm vir,cyl}/L)$ is the cylindrical virial mass per unit length. We ignore the contribution from magnetic fields for now, and assume the internal kinetic energy is turbulence dominated since the linewidths are largely nonthermal, such that

$$\frac{\mathcal{U}}{L}=\frac{3}{2}\left(\frac{M_{\rm vir,cyl}}{L}\right)\sigma^2_{\rm line}. \tag{3.29}$$

For cylinders of finite length, we note that the $L \approx 2R_{\rm eff}\sqrt{A_0}$ by approximating the filament as an ellipse (as in `cprops` to calculate the aspect ratio) and noting that it has a projected area equal to $\pi R^2_{\rm eff}$. We then recover an equivalent virial parameter for cylindrical clumps:

$$\alpha_{\rm vir,cyl}=\frac{M_{\rm vir,cyl}}{M_{\rm cl}}=\frac{12}{5}\sqrt{A_0}\frac{\sigma^2_{\rm line}R_{\rm eff}}{GM_{\rm cl}}=\frac{12}{25}\sqrt{A_0}\alpha_{\rm vir,sph}. \tag{3.30}$$

For the most filamentary clumps in our sample $A_0 \gtrsim 3$ (with one being approximately 6), so $\alpha_{\rm vir,cyl} \approx \alpha_{\rm vir,sph}$. For clumps with smaller aspect ratios $\alpha_{\rm vir,cyl} < \alpha_{\rm vir,sph}$, however this estimate is less reliable because the initial assumption of a cylinder of infinite length is certainly violated in this case. The median value of $M_{\rm vir,sph}$ is about 1.5, and is about 1 for $M_{\rm vir,cyl}$.

Given the factor of three uncertainty in the individual clump masses and the assumption of relatively simple geometry, we cannot confidently say which individ-

ual clumps are gravitationally bound; however, it is significant that across our large sample most clumps are approximately in equipartition of gravitational and kinetic energies. For clumps that are interacting and not in isolation, then the simple assumptions of virial equilibrium are not met and it becomes more difficult to determine if these structures are bound. However, if the clumps are completely collapsing, then the kinetic energy should be twice that of the gravitational energy. Since the sample average kinetic and potential energies are approximately equal it is more likely that these clumps are prevented from collapsing by their internal motions, rather than that they are already collapsing. This is consistent with the fact that the star formation is not predominantly in the center of the clumps, but at the interfaces between clumps.

We further investigate the role of turbulent support in these clumps by calculating the sound speed of the gas as given by Chandrasekhar & Fermi (1953),

$$c_s = \sqrt{\frac{\gamma k_B T_K}{\mu m_{\rm H}}}, \tag{3.31}$$

and then the Mach number,

$$\mathcal{M} = \frac{\sigma_{\rm NT}}{c_s}. \tag{3.32}$$

We take $\gamma = 7/5$ as above, and list the sound speeds and Mach numbers for the clumps in Table 3.6. The Mach numbers are typically 3 to 5 and all greater than 1 (with the exception of one clump in G034.43+00.24 for which the linewidth is approximately the thermal linewidth). This implies that the clumps are dominated by nonthermal motions. These nonthermal motions may be dominated by turbulence that provides support against gravitational collapse of the cloud, but it is also possible that high nonthermal motions arise from protostars, for example from infall motions, which do not provide support. We generally cannot separate these effects in our data, though

we expect both to contribute. It is unlikely that gas motions directly associated with protostars can explain the high nonthermal motions across the entire IRDCs, so turbulence is likely an important source of support for these clumps.

In the absence of magnetic field strength measurements, we can estimate the minimum field strength required to support these clumps against gravitational collapse by taking the condition that

$$\frac{3GM_{\rm cl}^2}{5R_{\rm eff}} \approx \frac{B_{\rm min}^2}{8\pi}\frac{4}{3}\pi R_{\rm eff}^3, \tag{3.33}$$

so that

$$B_{\rm min} \approx 1.02 \times 10^{-4} \left(\frac{M_{\rm cl}}{M_\odot}\right) \left(\frac{R_{\rm eff}}{\rm pc}\right)^{-2} {\rm mG}. \tag{3.34}$$

For the clumps in our sample, we find that 13 μG $\lesssim B_{\rm min} \lesssim$ 3.5 mG, well matched to the typical magnetic field strengths measured in molecular clouds (Crutcher 2012). These values of $B_{\rm min}$ are upper limits on the minimum field strength when the support from turbulence and thermal motions is included, so even smaller magnetic fields will be sufficient to stabilize the clumps. Magnetic fields may therefore be an important source of pressure support in these clumps.

Comparing the free-fall times, the virial parameters, and the turbulent and magnetic support, the majority of clumps in these IRDCs appear to be supported against collapse. The observed nonthermal motions and typical magnetic field strengths in molecular clouds are sufficient to stabilize these clumps against self-gravity. It is likely that many of these clumps are then at least quasi-stable, and may be long-lived compared to the free-fall times. This may explain why we see quiescent regions that are devoid of any signs of ongoing star formation, and why protostellar candidates are typically found at the sites where clumps overlap. The clumps that are apparently

interacting in position-position-velocity space are not evolving in isolation, and so collapse may be progressing in places where clumps are compressed by collisions with each other.

Size-linewidth Relation

We can place the clumps identified in this study in the context of other molecular gas clumps in varying environments and physical characteristics by putting them on a plot of size versus linewidth or, equivalently, size and spherical virial mass. In Figure 3.22, red diamonds mark the dense clumps seen in 30 Doradus in the Small Magellanic Cloud in ^{13}CO J=2-1 with ALMA (Indebetouw et al. 2013). Green circles mark dense CS J=2-1, 3-2, and 5-4 clumps from a previous study of IRDCs by Gibson et al. (2009) with the 14 m Five College Radio Astronomy Observatory (FCRAO). Caselli & Myers (1995) observed massive cores in Orion in ^{13}CO and C^{18}O J=1-0, shown in blue crosses. Purple triangles mark galactic clouds listed by Heyer et al. (2009) as observed in ^{12}CO and ^{13}CO 1-0 with the FCRAO, with their observed relation plotted in black (extended as a dotted line): $M_{\rm vir,sph} = 300\ M_{\odot} R_{\rm pc}^2$. Oka et al. (2001) observed clouds in the Central Molecular Zone in the galactic center in ^{12}CO 1-0 with the NRO 45 m telescope (plotted as orange X's), and determined the relation $M_{\rm vir,sph} = 2 \times 10^4\ M_{\odot} R_{\rm pc}^2$. Finally, Falgarone et al. (1992) observed quiescent molecular clouds in ^{13}CO 1-0 and 2-1 with the IRAM 30 m, shown as maroon squares.

We additionally use the presence or absence of a 70 μm point source within the boundaries of a clump to classify it as "protostellar" or "starless," respectively. This classification is listed in Table 3.4. Clumps from this work are shown as black stars in Figure 3.22; protostellar clumps are filled, while starless clumps are empty. It is notable that the trend seen across different studies between radius and linewidth

Table 3.6. Clump Stability

$M_{\rm cl}$ ($M_\odot$)	$t_{\rm ff,sph}$ (Myr)	$t_{\rm ff,cyl}$ (Myr)	$M_{\rm vir,sph}$ ($M_\odot$)	$M_{\rm vir,cyl}$ ($M_\odot$)	$\alpha_{\rm vir,sph}$	$\alpha_{\rm vir,cyl}$	c_s (km s^{-1})	$\mathcal{M}$	$B_{\rm min}$ (mG)
G010.74-00.13									
409	0.06	0.10	217	152	0.53	0.37	0.26	3.9	1.37
454	0.05	0.05	171	91	0.38	0.20	0.27	3.5	1.88
112	0.06	0.10	59	41	0.53	0.36	0.26	2.5	0.87
348	0.06	0.12	195	149	0.56	0.43	0.27	3.8	1.36
G022.56-00.20									
486	0.05	0.11	287	238	0.59	0.49	0.29	4.4	2.09
162	0.04	0.05	264	158	1.63	0.97	0.28	5.6	1.95
103	0.04	0.10	257	207	2.50	2.01	0.28	5.5	1.33
G024.60+00.08									
174	0.05	0.06	271	155	1.56	0.89	0.31	4.5	1.28
243	0.07	0.09	136	80	0.56	0.33	0.26	3.2	0.88
63	0.06	0.06	40	21	0.63	0.33	0.27	2.2	0.72

Note. — Clumps appear in the same order as Table 3.4. (This table is available in its entirety in Appendix Table E.1. A portion is shown here for guidance regarding its form and content.)

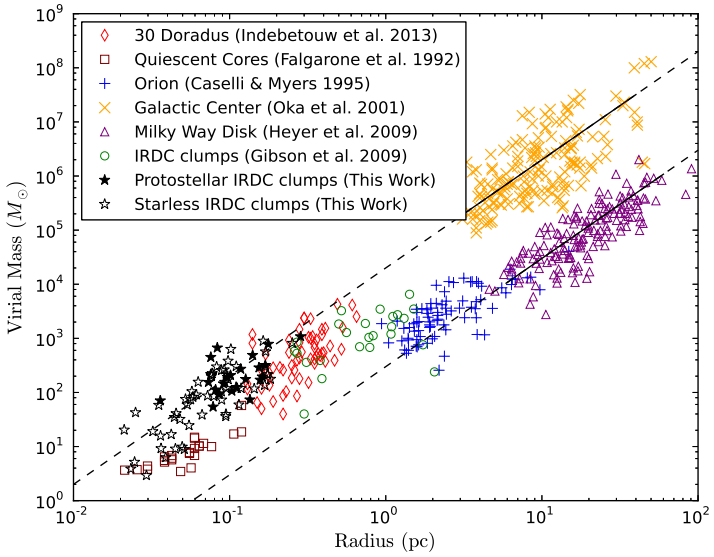

Fig. 3.22.— A comparison of radius and spherical virial mass (a proxy for linewidth) for the clumps in our sample (using $R_{\rm eff}$ and $M_{\rm vir,sph}$) to other studies of molecular gas in different environments. Filled stars indicate clumps from our work that are determined to be protostellar due to the presence of a 70 μm point source within the clump boundary. Open symbols are starless clumps that lack a 70 μm point source. See §3.6.4 for descriptions of the different populations.

extends over more than 3 orders of magnitude in size, regardless of the molecular line tracers and observations used. We note that both classes of our clumps are along the same trend, though the protostellar clumps are typically larger in size and virial mass (i.e. linewidth). Recall that the thermal linewidths for even $T_K = 50$ K gas is only 0.12 km s^{-1}, and so the linewidths are largely nonthermal.

Zhang et al. (2011) observed ammonia among other molecular tracers, and also saw that linewidths were elevated around protostellar candidates and were more elevated for more evolved sources. They further found that nonthermal velocity dispersions were supersonic. Urquhart et al. (2011) found that in massive cores the column densities, kinetic temperatures, and linewidths seen in ammonia are all correlated with each other and with bolometric luminosity, indicating that these values are driven largely by the central source. We also see strong correlations between the column densities, kinetic temperatures, and linewidths in the clumps in our sample.

Molecular clumps may be virialized but still have higher velocity dispersions (and thus virial masses) than Larson's relation for galactic disk clumps if there exists some external pressure. Elevated linewidths may be a result of chaotic gravitational collapse, in which the turbulent motion arises from the collapse. An alternative explanation is pressure from the gravity of the larger IRDC cloud as a whole. In this sample, we have already shown that the clumps have strong supersonic turbulence, which likely accounts for the relationship between the size and velocity dispersions (Ballesteros-Paredes et al. 2011). However, the velocity dispersions being elevated above the typical Milky Way relation requires the clumps to not be in equilibrium (as in the case of outflows), or have additional external pressure beyond that of the warm ISM.

3.6.5 $N(\mathrm{CCS})/N(\mathrm{NH_3})$

Suzuki et al. (1992) showed that a relative lack of CCS compared to NH_3 is an indication of a more evolved core. Hirota et al. (2009) observed varying abundances of carbon-chain molecules relative to NH_3 in dark cloud cores and interpreted the variation as an indication of the evolution stage of the cores. Sakai et al. (2008) observed 55 millimeter cores in IRDCs with the NRO 45 m telescope and the Atacama Submillimeter Telescope Experiment (ASTE) 10 m telescope, looking at N_2H^+, HC_3N, CCS, NH_3, and CH_3OH at $18''$ to $73''$ and 0.12 km s^{-1} to 0.5 km s^{-1} resolution. They found that the [CCS]/[N_2H^+] ratios of even 24 μm dark cores were typically less than 1 and concluded that these cores were more chemically evolved than low-mass starless cores where the ratio is 2.6 to 3.2. Marka et al. (2012), however, found no variation in the column density ratio, $N(\mathrm{CCS})/N(\mathrm{NH_3})$, with evolutionary state of Bok globules, the low-mass dark cloud analogs to IRDCs. All of these studies targeted dense cores but were performed with single-dish observations. Devine et al. (2011) used the VLA and demonstrated that the spatial distributions of the NH_3 and CCS were highly anticorrelated in a single IRDC. Since these NH_3 and CCS transitions have similar excitation conditions (i.e critical densities), these studies show that neither molecule traces all of the gas.

The spatial distributions of NH_3 and CCS in our sample are shown in Figures 3.4-3.12. Because of the low signal-to-noise in the CCS line, the GBT observations give a clearer impression of where the CCS is. The CCS generally is not detected over the full spatial extent that NH_3 is. In the scenario where the ratio of these abundances is a viable method for tracing evolutionary stage, we would expect the most evolved (i.e protostellar) cores would have a lower CCS abundance than starless cores.

We investigate the possibility of chemical evolution of different clumps by com-

paring the column densities of NH_3 and CCS. Lai et al. (2003) calculate the column density of CCS in lower mass star forming regions from the 22.34403 GHz line using an updated form of the relation from Suzuki et al. (1992):

$$N(\mathrm{CCS}) = 5.1\times10^{11}\tau_{\mathrm{CCS}}\left(\frac{\Delta v_{\mathrm{CCS}}}{\mathrm{km\ s^{-1}}}\right) Z_{\mathrm{CCS}}\frac{\exp\left(E_{u,\mathrm{CCS}}/\left[k_B T_{\mathrm{ex,CCS}}\right]\right)}{\exp\left(E_{u,\mathrm{CCS}}/\left[k_B T_{\mathrm{ex,CCS}}\right]-1\right)}\mathrm{cm^{-2}}, \quad (3.35)$$

where Δv_{CCS} is the FWHM of the CCS line, Z_{CCS} is the partition function (24 to 62 for low rotational transitions), $E_{u,\mathrm{CCS}} = 1.12$ cm^{-1} is the energy level of the upper state, $T_{\mathrm{ex,CCS}}$ is the excitation temperature of the line, and τ_{CCS} is the peak optical depth. The peak optical depth is related to the peak main beam temperature by

$$T_{\mathrm{mb,CCS}} = \Phi T_{B,\mathrm{CCS}} = \Phi\left[\mathcal{J}(T_{\mathrm{ex,CCS}}) - \mathcal{J}(T_{\mathrm{bg}})\right]\left[1-\exp(-\tau_{\mathrm{CCS}})\right], \quad (3.36)$$

where $T_{\mathrm{mb,CCS}}$, $T_{B,\mathrm{CCS}}$, and $\mathcal{J}(T)$ are the same as given in §3.4.3 but for CCS, $T_{\mathrm{bg}} = 2.73$ K is the background CMB temperature, and $\Phi = 1$ is the assumed beam-filling factor. Linewidths are difficult to measure for the CCS given that it is only detected with a signal-to-noise ratio greater than 5 along few lines of sight (refer to Figures 3.4-3.12). We therefore take Δv_{CCS} from the ammonia velocity dispersion (second order moment) maps, $U = 43$, and $T_{\mathrm{ex,CCS}} = 5$ K. With these assumptions, we calculate column densities of approximately 10^{11} cm^{-2} and as high as 10^{12} cm^{-2} , similar to those observed by Lai et al. (2003) and Suzuki et al. (1992). Given the scatter in the points, the low signal-to-noise ratio of the CCS emission, and the assumptions made to obtain N(CCS) we cannot determine the column densities along individual lines of sight to better than an order of magnitude. We therefore only use the clump averaged values of N(CCS) to compare to the column density of the NH_3.

We expect from previous studies that CCS will be relatively depleted in the more

chemically evolved gas, if at all. Without a direct probe of the age of the clumps, we use star formation activity as a proxy. Using the simple classification scheme mentioned in §3.6.4, the presence or absence of a 70 μm point source within the boundaries of a clump are used to classify it as "protostellar" or "starless," respectively. We also consider the possibility that temperature and/or density may have an effect on the depletion of CCS onto dust grains. Figure 3.23 shows a comparison of the ratio of the column densities of CCS and NH_3 against the kinetic temperature and the ammonia column density, averaged over clumps defined by `cprops`. We do not see a clear distinction between protostellar and starless clumps in $N(\mathrm{CCS})/N(\mathrm{NH_3})$ as we would expect. This is weak evidence of trend for CCS to be relatively depleted compared to NH_3 in the highest column density gas, but one should be extremely cautious of interpreting this as a true correlation given the uncertainties involved. More sensitive high resolution studies of CCS, preferably including more than one spectral line, are necessary to say whether or not CCS is relatively depleted in certain environments in IRDCs.

3.7 Conclusions

In this study, we have mapped the NH_3 and CCS in nine Infrared Dark Clouds, combining single dish and interferometric data from the GBT and the VLA. From fitting the NH_3 spectral lines, we probed the physical conditions of these regions. We find typical values of physical parameters in agreement with other studies: kinetic temperatures around 12-25 K, linewidths around 1-2 km s^{-1}, clump sizes from <0.1 to 0.2 pc, and clump masses of tens to thousands of $M_\odot$.

The kinematics seen in NH_3 reveal a diverse set of configurations and substructure. It appears that no one description of internal structure works for all IRDCs. We see

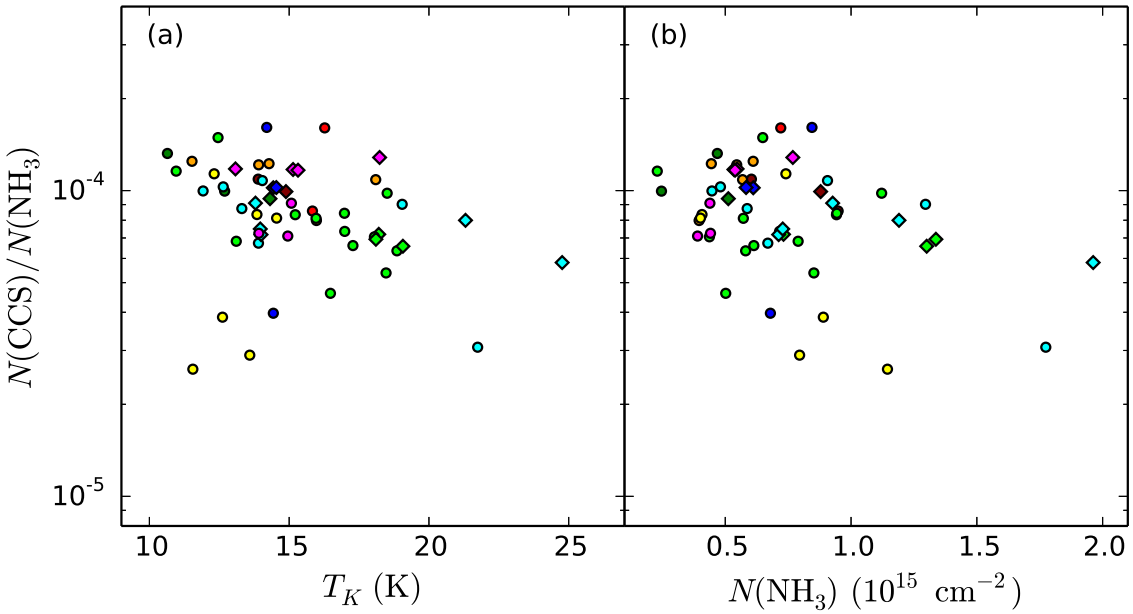

Fig. 3.23.— A comparison of the ratio of the column densities of CCS and NH_3 against the kinetic temperature and the ammonia column density, averaged over clumps defined by `cprops`. Colors are as in Figure 3.13. Diamonds represent clumps that are coincident with a 70 μm point source (protostellar), and circles represent clumps without such a point source (starless). We do not see a clear distinction between protostellar and starless clumps in $N(\mathrm{CCS})/N(\mathrm{NH_3})$ as we would expect from previous studies. Given the scatter in the points, the low signal-to-noise ratio of the CCS emission, and the assumptions made to obtain $N(\mathrm{CCS})$, more sensitive high resolution studies of CCS, preferably including more than one spectral line, are necessary to say whether or not CCS is relatively depleted in certain environments in IRDCs.

clouds with gradients in the velocity field and velocity dispersion, clouds with discrete clumps possibly interacting with each other, and clouds that clearly have both of these scenarios occurring simultaneously in different locations. Protostars have a tendency to form at the interface of different subclouds. We find that these clumps are typically near virial equilibrium and can easily be supported by typical molecular cloud magnetic field strengths, so these structures may survive for multiple free-fall times. At least three of these IRDCs are consistent with the picture of hub-filament

structure, in which filaments feed molecular gas toward a cental, dense structure harboring star formation. All nine of these IRDCs have lower contrast IR extinction features that extend beyond our molecular maps, and so it is possible that all of these IRDCs are consistent with hub-filament structure. High resolution studies of other physical probes, including shock tracers like SiO, are necessary to further test whether the gas is in fact colliding in these regions.

The signal-to-noise ratio of the CCS line is typically weak, and so deeper observations and observations of other CCS lines are necessary to better probe the possible chemical differentiation and evolution in IRDCs.

Chapter 4

Preliminary Analysis of CARMA Observations of Dense Gas in G031.97+00.07

4.1 Introduction

Our study of the NH_3 and CCS in IRDCs has revealed some of their internal structure and kinematics, but there is much left unknown. Interpreting discrete velocity components, velocity gradients, and elevated velocity dispersions as evidence of colliding clumps and/or gas flowing along filaments can be misleading because of the lack of information in the third spatial dimension and the velocities in the plane of the sky. Our analysis of the NH_3 and CCS abundances was limited by several assumptions. To move forward with understanding the kinematics and the chemistry in IRDCs, we observed G031.97+00.07 in a suite of molecular lines (Table 4.1) and 3 mm continuum with the Combined Array for Research in Millimeter-wave Astronomy (CARMA). This cloud was chosen because of the diversity of internal conditions: long, thin filaments, globular structures, dark, quiescent gas, embedded MIR point sources, and brighter point sources associated with masers and/or H II regions.

Our selection of lines includes the traditional dense gas tracers HCO^+, HNC, and N_2H^+ with higher critical densities (10^5 to a few times 10^6 cm^{-3}) than NH_3 (HNC was chosen instead of HCN because of the limitations of the CARMA spectral setup). The ratios of these lines have been shown to trace evolutionary state of cores and gas, including within IRDCs (Turner & Thaddeus 1977; Lo et al. 2009; Daniel et al. 2013). We expect these lines to be optically thick in IRDCs because of the high column densities, and so we also include the isotopologues $H^{13}CO^+$ and $HN^{13}C$ as more robust column density tracers for the highest column density locations. Previous studies of star forming regions have observed HCO^+ and HNC in self-absorption with inverse P Cygni profiles indicative of infall within cores (Sanhueza et al. 2012, e.g.). The N_2H^+ line has hyperfine structure, and so we can determine the optical depth and thus still have measure the column density in regions of high column density Daniel

et al. (2006); Di Francesco et al. (2004). N_2H^+ is further interesting as a tracer of chemistry because it is a precursor to the formation of NH_3 (Scott et al. 1997). Furthermore, NH_2D is also interesting to compare to NH_3 as the relative abundance of deuterated species of molecules has been shown to change with evolutionary state (Tiné et al. 2000; Shah & Wootten 2001). The simple carbon chain molecule C_2H, similar to CCS, is also expecting to trace evolutionary state as it is created in the early phases of dense gas before freezing onto dust grains; unlike CCS it also has hyperfine structure that probes the optical depth (Tucker et al. 1974). The traditional shock tracer SiO is used to find regions of activity (Martín-Pintado et al. 1992) including jets, outflows, expanding shells around H II regions, and possibly the collisions of subclouds. These interactions cause Si to sputter off the dust grains and leads to the formation of SiO in the gas phase (Schilke et al. 1997; Caselli et al. 1997). Finally, CH_3OH can also sputter off dust grains in outflows (Gómez et al. 2011), and its masers trace protostellar activity (Fontani et al. 2010). The continuum is expected to be dominated by the thermal emission of the dust, and so we have an additional probe of the dust column density and temperature at higher resolution than the BGPS. Analysis of these observations is preliminary; data reduction and promising early results are presented here.

4.2 CARMA Observations and Data

Nine dense gas tracers were observed in G031.97+00.07 with CARMA between 2012 April 11 and 2012 April 23 (Project ID c0874) in D configuration (the second most compact configuration; E configuration would have lead to "shadowing" of some dishes for this source). Table 4.1 lists the observed lines. The spectral setup had 97 kHz resolution and 31 MHz bandwidth, which corresponded to a velocity resolution

of approximately 0.3 to 0.4 km s^{-1}. In addition, continuum emission was observed at 90.172 GHz and 93.664 GHz with 500 MHz bandwidths. We mosaicked 21 pointings to cover fully the highest opacity regions as determined from the 8 μm images. The CARMA footprint is slightly narrower than the VLA footprint but still covers the significant NH_3 emission, however the CARMA footprint is more extended along the major axis of the cloud than the VLA footprint and is similar to the extent of our GBT observations. The primary beam of the largest (10 m) antennas at the highest frequency of our observations was approximately 1.′3 (FWHM), which is comparable to the largest recoverable angular scale for a single pointing in D configuration. We used 1743-038 as the phase, amplitude, and bandpass calibrator. MCW349 was used as the flux density calibrator except on April 23, 2012, when Neptune was used.

The data were calibrated using Miriad, and then were imaged in CASA using the `clean` task in mosaic mode with natural weighting of the visibilities, deconvolved with 0.5 km s^{-1} channels. We also employed the multiscale capability of `clean` to include clean components approximately one and three times the size of the synthesized beam, as well as the standard point-like components. The CASA task `pbcor` was used to apply a primary beam correction. The mosaics were imaged to the 35% power level

Table 4.1: Lines Observed with CARMA

Species	Rest Frequency (GHz)	Transition(s)	Name
CH_3OH	96.741	$J_K = 2_{-1} - 1_{-1}E$	Methanol
		$J_K = 2_0 - 1_0A$	
		$J_K = 2_0 - 1_0E$	
N_2H^+	93.174	$JF_1F = 112 - 012$	Diazenylium
		$JF_1F = 123 - 012$	
		$JF_1F = 101 - 012$	
HNC	90.664	$J = 1 - 0$	Hydrogen Isocyanide
HCO^+	89.188	$J = 1 - 0$	Formylium
C_2H	87.319	$NJF = 1(3/2)2 - 0(1/2)1$	Ethynyl
$HN^{13}C$	87.091	$J = 1 - 0$	Hydrogen Isocyanide
SiO	86.847	$J = 2 - 1$	Silicon Monoxide
$H^{13}CO^+$	86.754	$J = 1 - 0$	Formylium
NH_2D	85.926	$J_{K_a,K_c} = 1_{1,1} - 1_{0,1}$	Deuterated Ammonia

relative to the peak of the mosaic primary beam response.

The synthesized beams in the cubes are 5″ to 6.″2, which is 0.14 to 0.17 pc. The RMS noise in the cubes is typically near 40 mJy beam^{-1} per 0.5 km s^{-1} channel.

4.3 Methods

We fit the spectra along individual lines of sight in our CARMA data using variations of the method described in §3.4.3. For the preliminary work, we focus on analysis of the SiO and N_2H^+ fitting and only fit one velocity component per line of sight instead of performing clump deconvolution. SiO is of particular interest as a tracers of shocks from protostellar outflows, for example. SiO emission apparently unassociated with these outflows can also provide evidence of collisions between subclouds within the IRDCs. N_2H^+ is a common dense gas tracer. It is part of the NH_3 formation pathway so it is reasonable to assume they trace similar gas and might reveal conditions of the chemistry. The poorer signal-to-noise ratio of the CARMA data compared to our GBT and VLA NH_3 data make it more difficult to distinguish multiple components. We include the full hyperfine structure of N_2H^+ from the components and intrinsic strengths documented in Daniel et al. (2006) in the same manner as for NH_3. We simultaneously fit the central velocity, velocity FWHM, optical depth, and the excitation temperature assuming LTE and beam filling factor of unity. We are unable to fit a rotation temperature like NH_3 without an additional N_2H^+ transition. The SiO $J = 2 - 1$ transition has no hyperfine structure, so we fit a further simplified model of a single gaussian with central velocity, velocity FWHM, and the peak temperature.

From the fit parameters, it is straightforward to calculate the total column density of the molecular species. Following Di Francesco et al. (2004), the column density of

N_2H^+ is

$$N\left(\mathrm{N_2H^+}\right) = \frac{3h}{8\pi^{5/2}\mu^2}\frac{\Delta v}{(8\ln 2)^{1/2}}\frac{\tau}{(J_l+1)\exp\left(-E_J/\left[k_B T_{\mathrm{ex}}\right]\right)} \times\left[\frac{k_B T_{\mathrm{ex}}}{hB}+\frac{1}{3}\right]\frac{1}{1-\exp\left(-h\nu/\left[k_B T_{\mathrm{ex}}\right]\right)}, \tag{4.1}$$

where $\mu = 3.40$ debye is the dipole moment, Δv is the velocity FWHM, $J_l = 0$ is the lower rotational quantum number, $E_J = J_l(J_l+1)hB$ is the energy of the rotational level, T_{ex} is the excitation temperature, $B = 46.586871$ GHz is the rotational constant, and τ is the optical depth. Our fitting routine provides values for Δv, T_{ex}, and τ. Simplifying, the equation becomes

$$N\left(\mathrm{N_2H^+}\right) = 7.379\times10^{11}\tau\left(\frac{\Delta v}{\mathrm{km\ s^{-1}}}\right)\frac{T_{\mathrm{ex}}/\left[2.24\ \mathrm{K}\right]+1/3}{\exp\left(-\left[2.24\ \mathrm{K}\right]/T_{\mathrm{ex}}\right)} \times\frac{1}{1-\exp\left(-\left[4.47\ \mathrm{K}\right]/T_{\mathrm{ex}}\right)}\ \mathrm{cm^{-2}}. \tag{4.2}$$

For SiO, we follow the column density calculation of Sanhueza et al. (2012),

$$N\left(\mathrm{SiO}\right) = \frac{3k_B}{8\pi^3 B\mu^2}\frac{\left(T_{\mathrm{ex}}+hB/\left[3k_B\right]\right)}{(J_l+1)}\frac{\exp\left(E_J/\left[k_B T_{\mathrm{ex}}\right]\right)}{1-\exp\left(-h\nu/\left[k_B T_{\mathrm{ex}}\right]\right)} \times\frac{1}{\mathcal{J}\left(T_{\mathrm{ex}}\right)-\mathcal{J}\left(T_{\mathrm{bg}}\right)}\int T_{\mathrm{mb}}\ dv, \tag{4.3}$$

though now $\mu = 3.1$ debye, $B = 21.711979$ GHz, and $E_J/k_B = 6.25$ K. The integrated main beam temperature is taken from moment 0 SiO maps, and the excitation temperature is taken to be the amplitude of the gaussian fit. The equation then simplifies

to

$$N\,(\mathrm{SiO}) = 4.00 \times 10^{11} \frac{\exp\left(\left[6.25\ \mathrm{K}\right]/T_{\mathrm{ex}}\right)}{1 - \exp\left(-\left[4.17\ \mathrm{K}\right]/T_{\mathrm{ex}}\right)} \times \frac{\left(T_{\mathrm{ex}} + 0.35\ \mathrm{K}\right)}{\mathcal{J}\left(T_{\mathrm{ex}}\right) - \mathcal{J}\left(T_{\mathrm{bg}}\right)} \int T_{\mathrm{mb}}\ dv\ \mathrm{cm}^{-2}. \tag{4.4}$$

The results of the spectral line fitting and column densities are found in §4.4.4.

4.4 Results & Discussion

4.4.1 Overview

All nine species were detected in G031.97+00.07, as shown in the integrated intensity contours in Figures 4.3, 4.4, 4.5, 4.6, 4.7, 4.8, 4.9, 4.10, and 4.11. We see that N_2H^+, HNC, and HCO^+ are detected throughout most of the cloud, tracing the infrared contrast as NH_3 does. Similarly strong detections (1 to 2 Jy beam^{-1} at the peak) are observed in the CH_3OH maps as well, though the emission is not quite as widespread. The remaining molecules are only detected towards the northeastern end of the cloud and one dark clump in the southwestern end of the cloud. Spectra towards these locations are shown in Figures 4.1 and 4.2. The molecules with the stronger detections peak in these same locations, which are towards the highest contrast parts of the IRDC and towards brightest IR point sources associated with masers and/or H II regions.

In the velocity field maps shown in Figures 4.3, 4.4, 4.5, 4.6, 4.7, 4.8, 4.9, 4.10, and 4.11, we see that the molecular species are consistent with the NH_3 velocity field (see Figure 3.19; repeated as Figure 4.12 below), specifically the two distinct velocity components around 92-99 km s^{-1} and 97-102 km s^{-1}. There do appear to be some

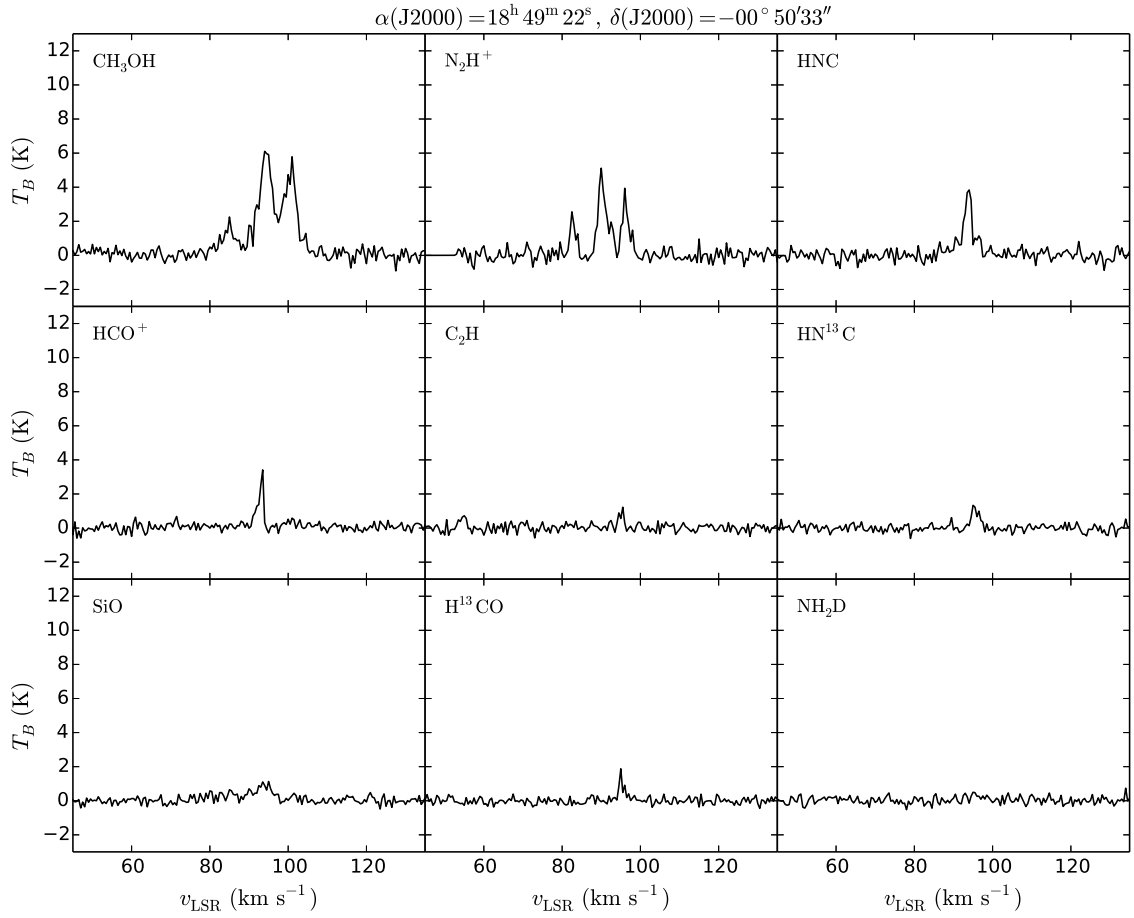

Fig. 4.1.— Spectra of all molecular species towards the southern IR source at the apparent junction of filaments. The brightness temperature scale assumes a beam filling factor of unity.

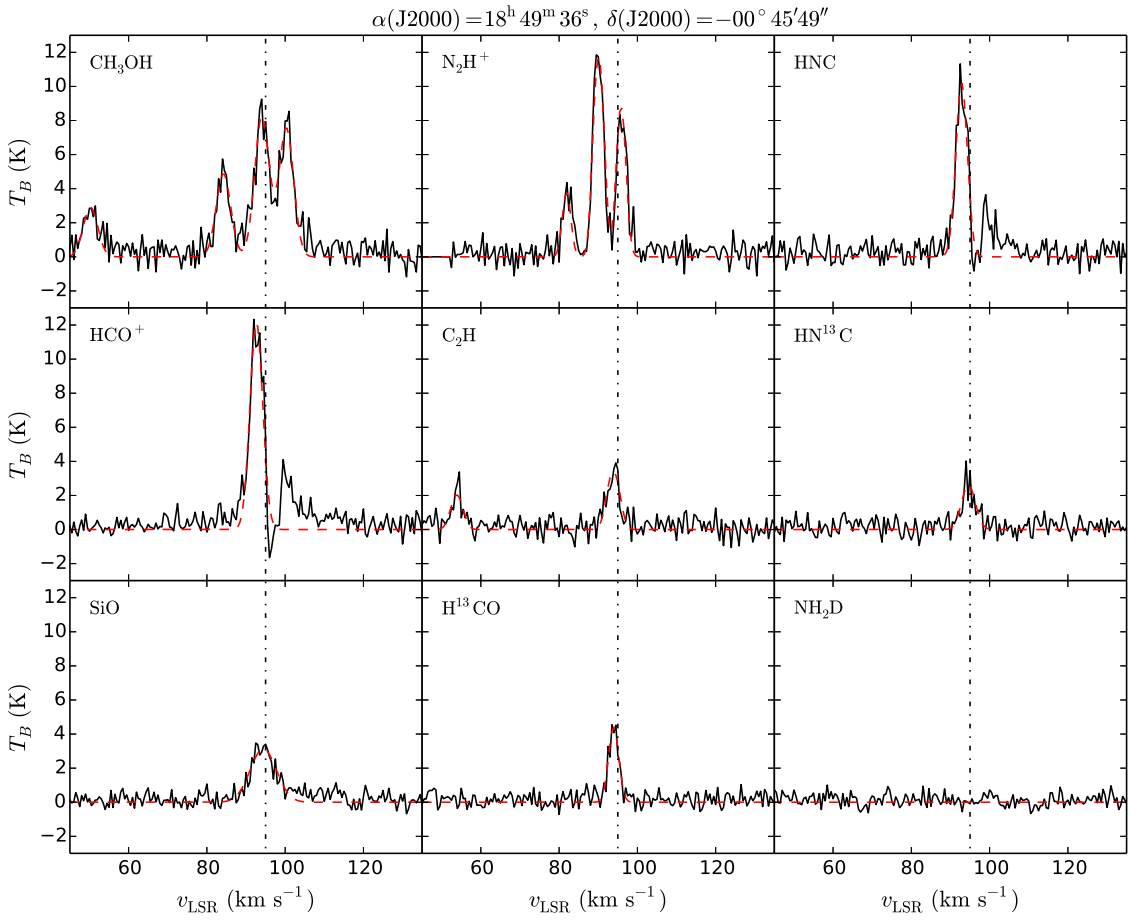

Fig. 4.2.— Spectra of all molecular species towards the bright IR source at the northeastern end of the cloud. The data are shown in solid black, and the best fits are shown in dashed red. A vertical black dashed-dotted line at 95 km s^{-1} is shown for comparing the line centers. The brightness temperature scale assumes a beam filling factor of unity.

systematic offsets between the precise velocity of the the lower velocity component from species to species. Closer inspection of these velocities and their angular extent with the higher angular and spectral resolution NH_3 observations shows that different species observed with CARMA are associated more strongly with some NH_3 clumps than others. We may be seeing some indication of different relative abundances in different clumps at slightly different velocities, similar to what was reported by Sanhueza et al. (2013) (see 3.18 for the complex velocity substructure). Further investigation of this effect is necessary to say more, however we may ultimately be hindered by the resolution of the CARMA observations.

4.4.2 Sources of Interest

There are two particular locations of special note. The first is the aforementioned clump towards the southwestern end of the cloud. The clump corresponds to a local IR extinction peak and a weak 24 μm point source. At least four distinct filaments appear to be connected to this clump, and so its morphology is consistent with a hub of star formation in the hypothesized hub-filament structure. The only species not detected in this clump is NH_2D. Spectra towards this location are shown in Figure 4.1.

The second noteworthy location is the bright IR point source at the far north-eastern end of our observations, marked in Figure 4.3. This point source was beyond the coverage of our VLA NH_3 and CCS observations, however our GBT maps showed the NH_3 (1,1) and (2,2) maxima to be centered on this source (spectra are shown in Figure 4.13). The strongest detection of most of the species in this study is located towards this source, except for HNC and N_2H^+, which still have strong detections there, and NH_2D, which was not detected there at all. Both HNC and HCO^+ have pro-

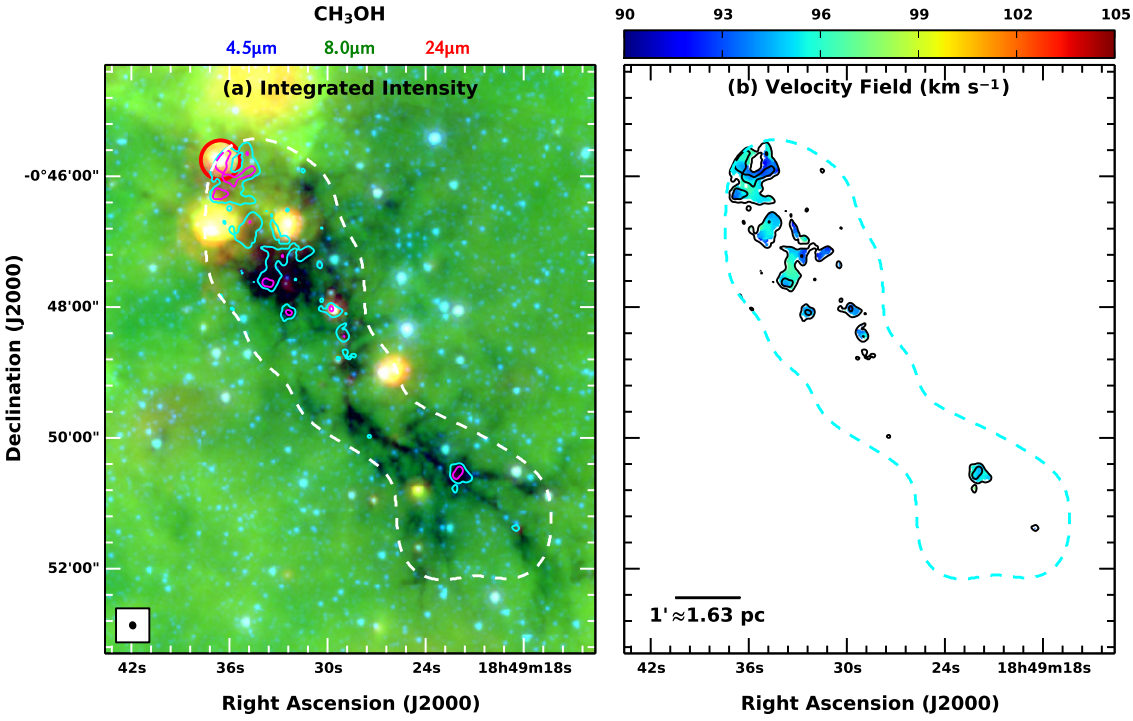

Fig. 4.3.— (a) Integrated intensity (moment 0) map of the CH_3OH emission. The background *Spitzer* image is as in Figure 3.8. Cyan contours are at 5σ and magenta contours are at 50σ. The white dashed contour shows the CARMA footprint. The synthesized beam is shown in the lower left. The red circle marks the location of the IR point source discussed in §4.4.2. (b) Velocity field (moment 1) map of the CH_3OH emission. Black contours match the cyan and magenta contours in (a). Dashed cyan contours show the CARMA footprint. A $1'$ scale bar is shown in the lower left.

files consistent with self-absorption towards this source, and the detections of $HN^{13}C$ and $H^{13}CO^+$ provide further evidence that HNC and HCO^+ are optically thick along this line of sight. The nondetection of NH_2D is not surprising given that this source is probably a relatively evolved protostar, and the relative abundance of deuterated ammonia is typically lower in protostellar sources (Busquet et al. 2010). Spectra for all emission lines towards the peak of this source are shown in Figure 4.2.

We also detect a distinct subcloud in HNC and HCO^+ at a velocity approximately 30 km s^{-1} lower than the main cloud. An integrated intensity map of HCO^+ over

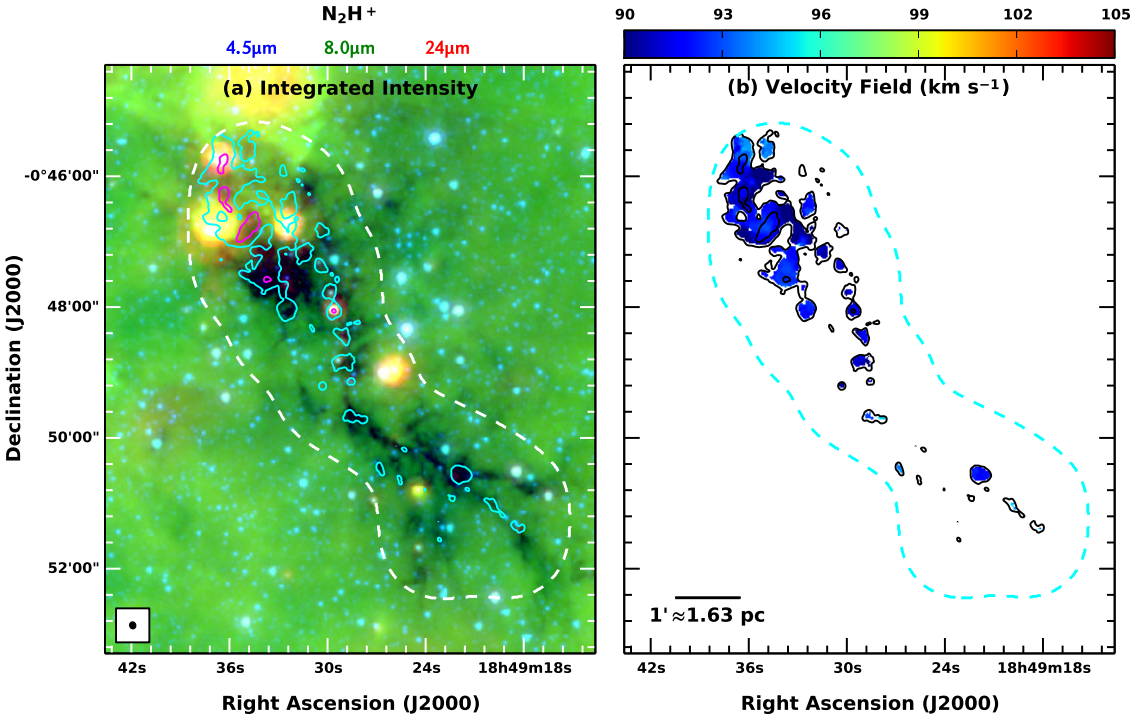

Fig. 4.4.— Same as Figure 4.3, but for N_2H^+.

the range 65 to 67 km s^{-1} is shown in Figure 4.14, and the spectra are shown in Figure 4.15. The moment map also reveals weaker emission at the same velocity just to the north. This second cloud is along roughly the same line of sight as the edge of a dark filament, but there is no indication of interaction or other emission in the entire intermediate velocity range. The IR extinction along this line of sight may then contain contributions from both the main cloud and this second cloud. Our VLA NH_3 and CCS observations do not extend to this velocity, however our GBT observations show a weak NH_3 (1,1) detection at this location and velocity. This cloud is probably unrelated to the IRDC, though if it contains significant dust then the 24 μm optical depth through the main IRDC we calculated in Chapter 3 in this location is an overestimate.

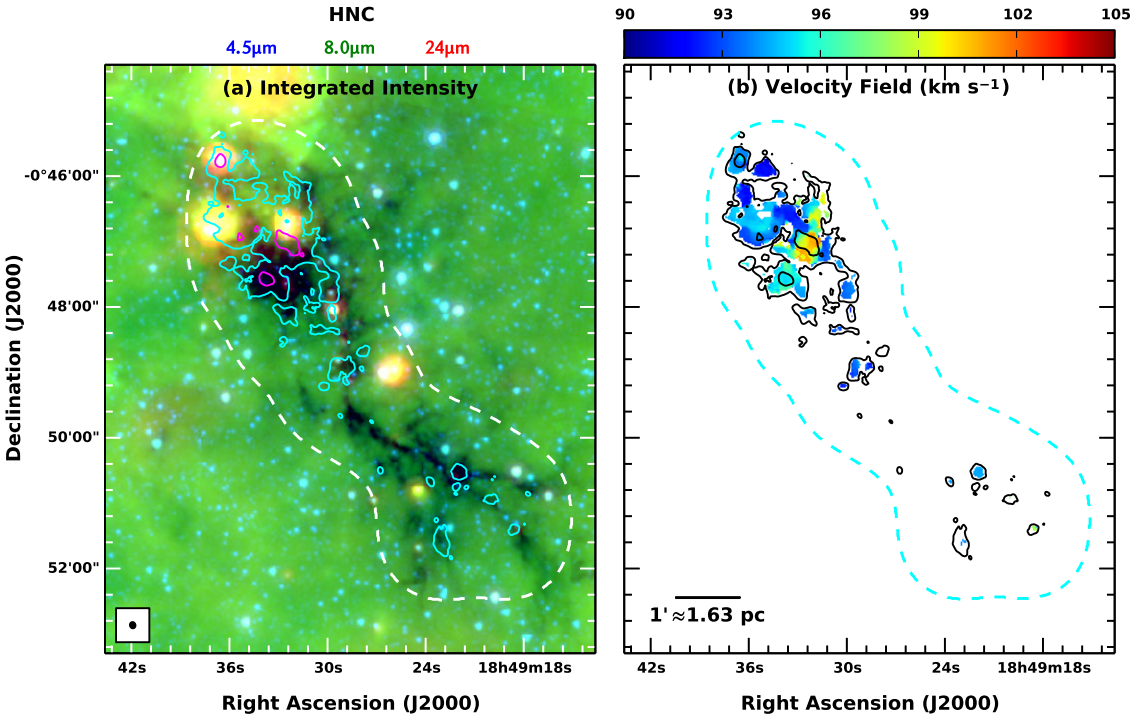

Fig. 4.5.— Same as Figure 4.3, but for HNC.

4.4.3 SiO as a Shock Tracer

We note that the detection of SiO is an indication of shocks (Martín-Pintado et al. 1992). Shocks or other activity cause dust grains to sputter and release silicon and silicates into the gas phase, leading to the formation of SiO in the gas phase (Schilke et al. 1997; Caselli et al. 1997). The values of velocity FWHM from SiO line fitting also show elevated linewidths compared to the other species. While the NH_3 profiles in the GBT and VLA combined data are typically <2 km s^{-1} wide, the SiO is typically greater than 5 km s^{-1}, often greater than 10 km s^{-1}, and peaks around 25 km s^{-1} toward the bright IR source at the northeastern end of the cloud. Sanhueza et al. (2012) found in their survey of the chemistry in IRDC cores with Mopra that SiO had a low detection rate (less than 10%), but was predominantly seen in more evolved

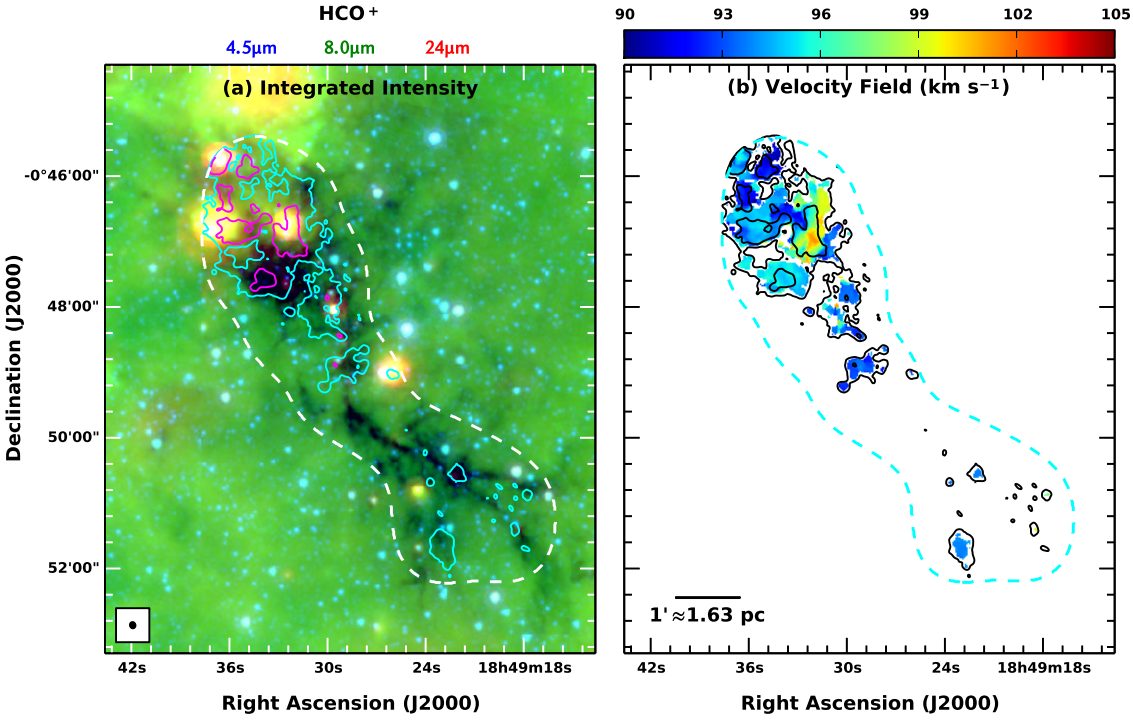

Fig. 4.6.— Same as Figure 4.3, but for HCO^+.

clumps with indications of active star formation activity (detection rate near 20%). They also reported a large scatter in the SiO linewidths, but that active clumps typically had linewidths greater than 6 km s^{-1}.

Jiménez-Serra et al. (2010) observed G035.39-00.33 in the SiO J=2-1 line with the IRAM 30 m, and found both bright, compact emission with broad linewidths and weaker, extended emission with narrow linewidths. The compact emission was consistent with protostellar outflows, and they proposed three explanations for the extended emission: (1) a collection of low mass outflows throughout the cloud, (2) a recently processed, more massive outflow whose energy was distributed throughout the cloud, or (3) the IRDC was recently assembled from collisions of smaller clouds or filaments. The majority of SiO emission we detect has high linewidths and is

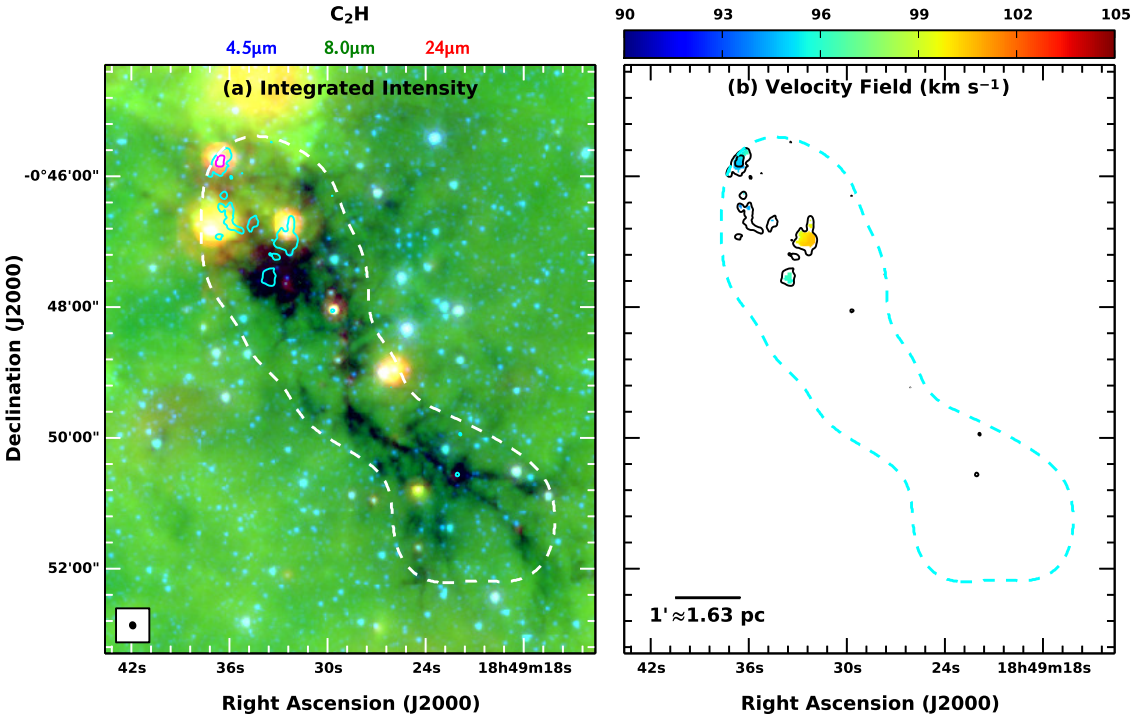

Fig. 4.7.— Same as Figure 4.3, but for C_2H.

coincident with or adjacent to IR point sources, so the majority of the emission is probably tracing outflows from protostars. There is however, significant emission located towards the higher IR contrast regions. For this emission, we cannot distinguish between the three mechanisms proposed by Jiménez-Serra et al. (2010).

4.4.4 Spectral Line Fitting Results

Example plots of fits to the data for N_2H^+ and SiO are shown in Figure 4.2. Results of the spectral line fitting are shown in Figure 4.16 and Figure 4.17. The typical uncertainties for single lines of sight of N_2H^+ for $v_{c,\mathrm{LSR}}$, Δv, τ, and T_{ex} are 0.05 km s^{-1}, 0.5 km s^{-1}, 1.5, and 1 K, respectively. The typical uncertainties for single lines of sight of SiO for $v_{c,\mathrm{LSR}}$, Δv, and T_{mb} are 0.05 km s^{-1}, 1 km s^{-1}, and 0.1 K,

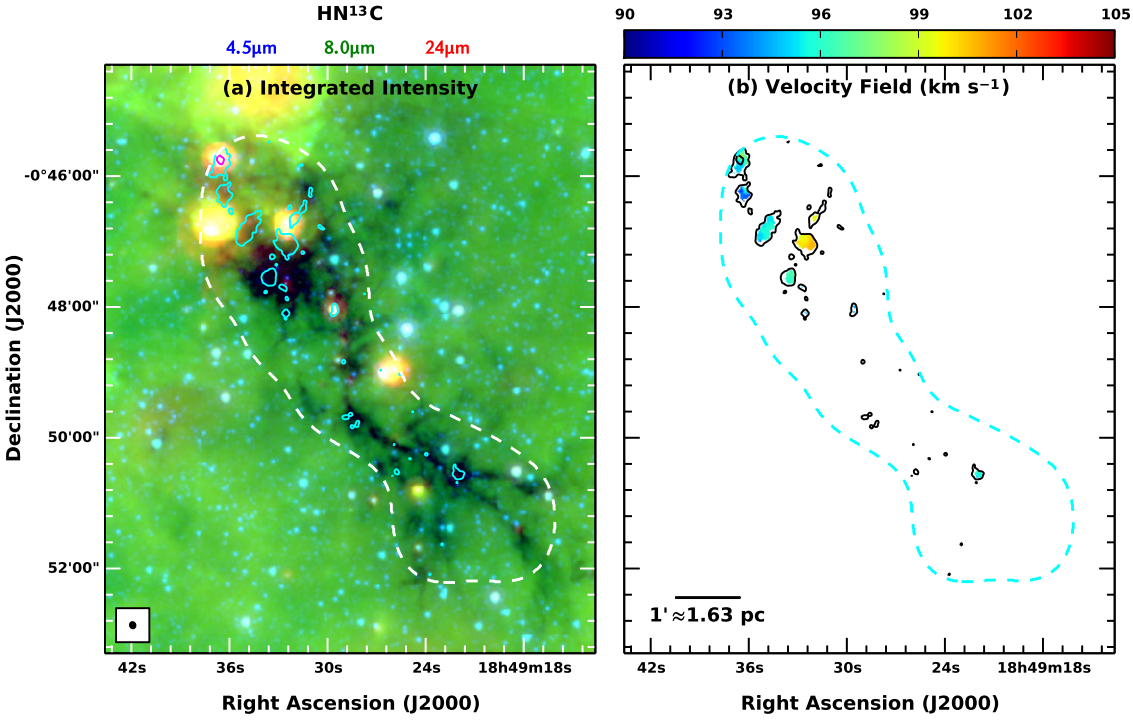

Fig. 4.8.— Same as Figure 4.3, but for $HN^{13}C$.

respectively. Comparison to our ammonia fitting results in Figure 3.13 reveals that N_2H^+ has similar distributions of optical depths and linewidths to NH_3, but that SiO clearly has elevated linewidths, as previously stated. The column densities of N_2H^+ and SiO each range from about 10^{13} to over 10^{14} cm^{-2}, and so their abundances relative to NH_3 are of order 0.01 to 0.1. Assuming a fractional abundance of NH_3 compared to H_2 of $X(NH_3) = 10^{-8}$ as in Chapter 3, the fractional abundances of N_2H^+ and SiO with respect to H_2 are 10^{-10} to 10^{-9}.

These column densities are a factor of a few to ten higher than what was reported in Sanhueza et al. (2012), who observed IRDC cores with the Mopra 22 m, however our relative abundances are in agreement and the total column density is sensitive to beam dilution. Taking our NH_3 column densities and assuming an abundance relative

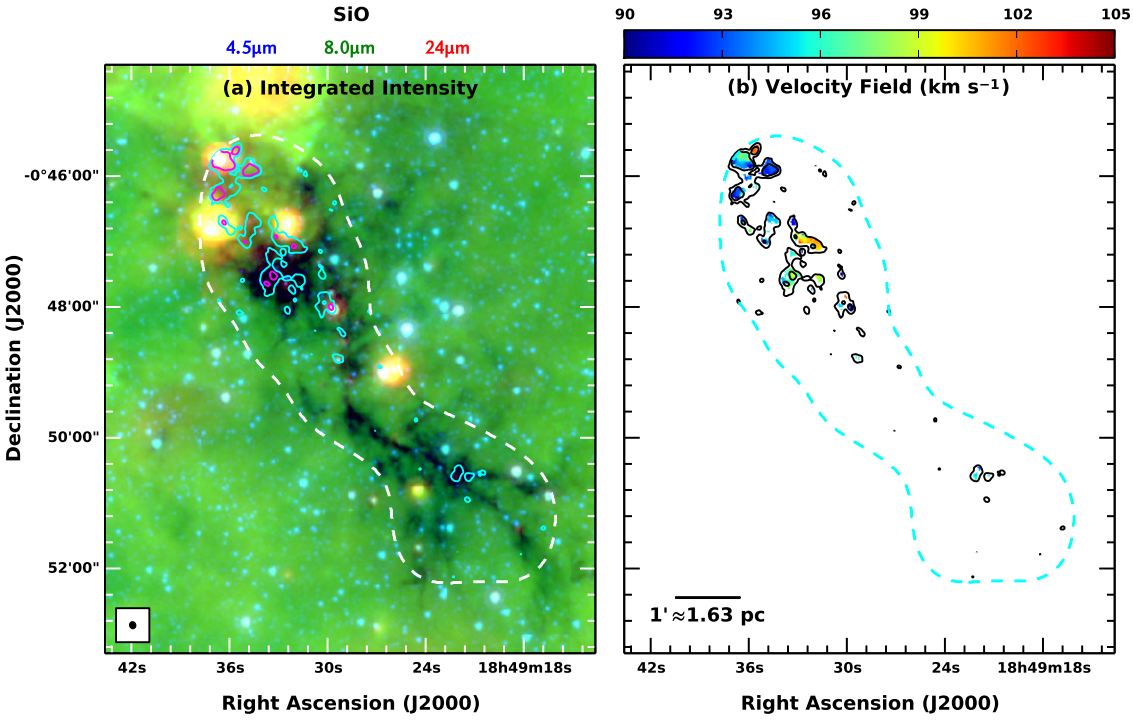

Fig. 4.9.— Same as Figure 4.3, but for SiO.

to H_2 of 10^{-8}, we see that H_2 column densities through this cloud range from about 10^{22} to over 10^{23} cm^{-2}. This is also a few times higher than the column densities in Sanhueza et al. (2012) calculated from 11″ resolution observations at 1.12 mm, and is probably due to beam dilution effects. They had a 38″ beam for the molecular lines in their study, compared to about 6″ in our CARMA observations and even smaller for our ammonia observations. We clearly see dense structures smaller than 38″. This also seems to explain observations SiO J=2-1 line from Jiménez-Serra et al. (2010). They reported SiO column densities between 5×10^{10} and 4×10^{11} cm^{-2} and fractional abundances from 5×10^{-10} to greater than 10^{-8} towards cores with high linewidths, using the IRAM 30 m at 28″ resolution and modeling with the large velocity gradient (LVG) approximation. When we smooth our SiO data to 38″ resolution and repeat

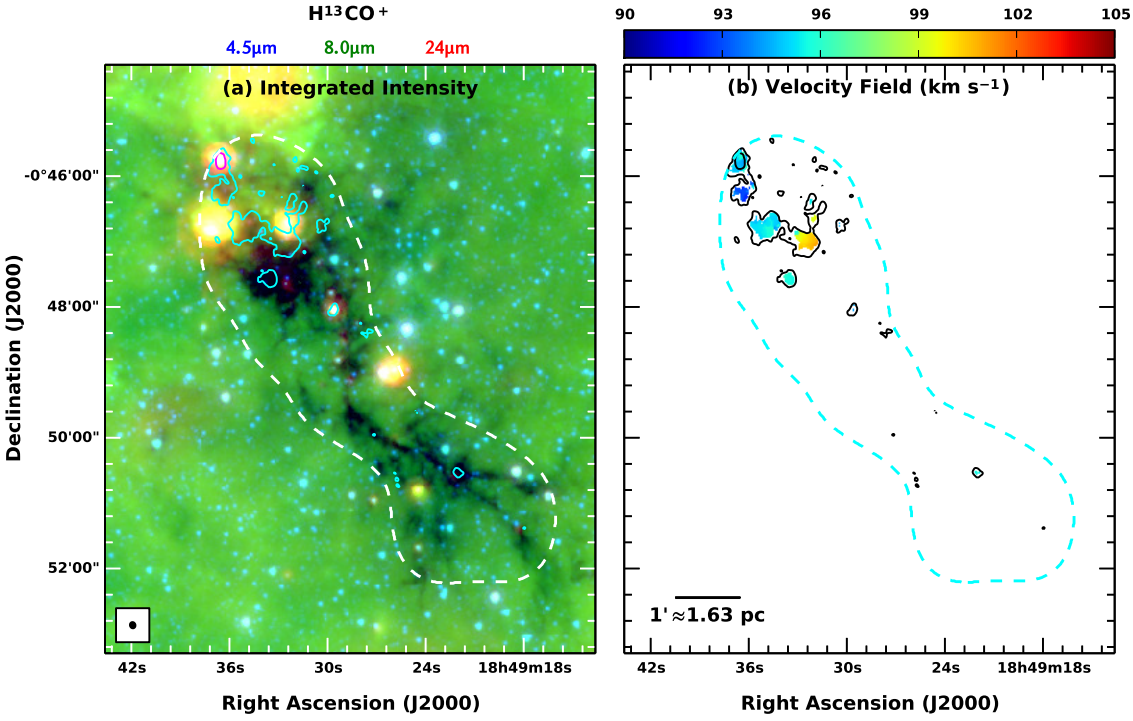

Fig. 4.10.— Same as Figure 4.3, but for $H^{13}CO^+$.

the fitting process, the column densities are a factor of about 5 to 7 lower at the peak locations. The discrepancies in column density seem explained by beam dilution, while we still recover similar fractional abundances in similar environments.

For a more direct comparison, we look to Sanhueza et al. (2013). They observed G028.23-00.19 with CARMA, using an identical observational scheme as we observed G031.97+00.07. They reported peak column densities of N_2H^+ and SiO of 1.7×10^{13} cm^{-2} and 8.1×10^{12} cm^{-2}, respectively, and fractional abundances of 4.3×10^{-10} and 7.5×10^{-10}, respectively. These fractional abundances are again in good agreement with ours, and the column densities are within a factor of a few. Since G028.23-00.19 is in our sample from Chapter 3, we can compare it to G031.97+00.07 in NH_3. We see that the total column density of individual lines of sight from G031.97+00.07 is

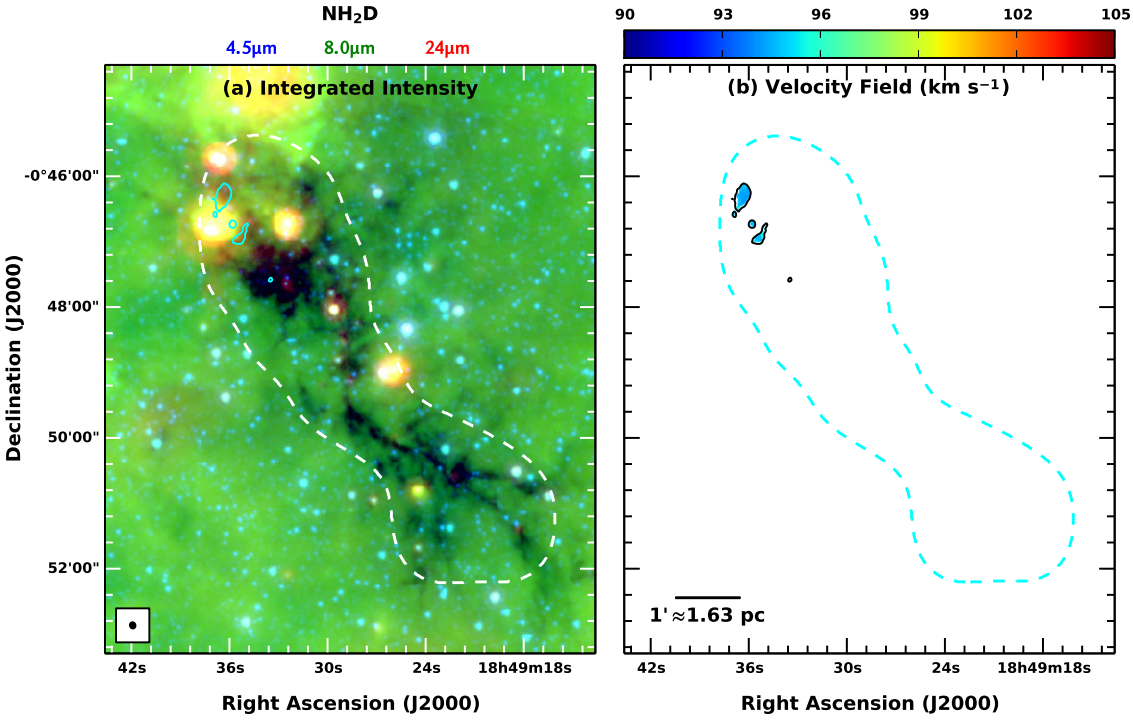

Fig. 4.11.— Same as Figure 4.3, but for NH_2D.

typically a factor of two higher than G028.23-00.19, so it is no surprise that N_2H^+ and SiO would also have slightly higher column densities and the same fractional abundances.

4.5 Summary & Future Work

We have presented CARMA observations of the IRDC G031.97+00.07, a several parsec long cloud with extensive filamentary and clumpy structure and complex kinematics. It contains apparently quiescent gas as high in column density as a few times 10^{23} cm^{-2}, embedded protostars, and young H II regions, making it an excellent laboratory for studying diverse conditions within IRDCs. The analysis is in its preliminary stages, but we already see promising results. We have significant detections of all

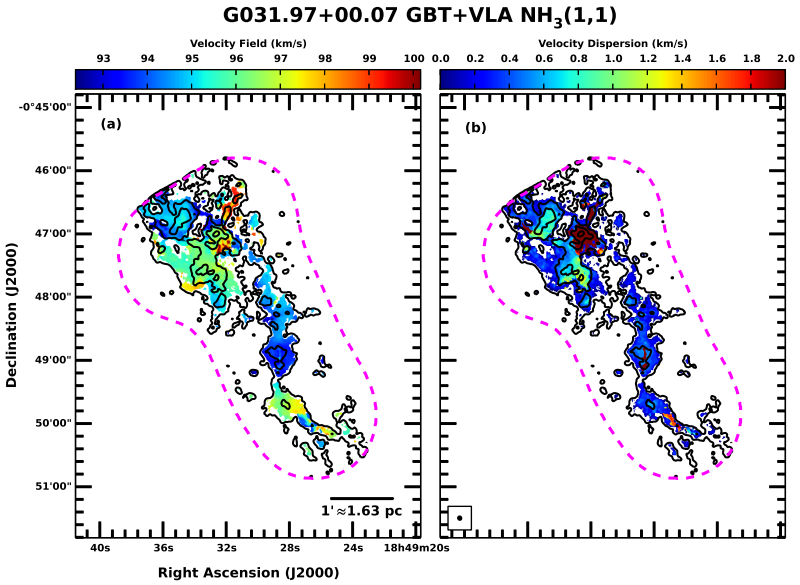

Fig. 4.12.— Moment 1 and moment 2 maps showing the velocity field ($\langle v_{(1,1)} \rangle$) and velocity dispersion ($\langle v^2_{(1,1)} \rangle$), respectively, from the NH_3 (1,1) emission in G031.97+00.07. (Repeated from Figure 3.19 for comparison to CARMA data.)

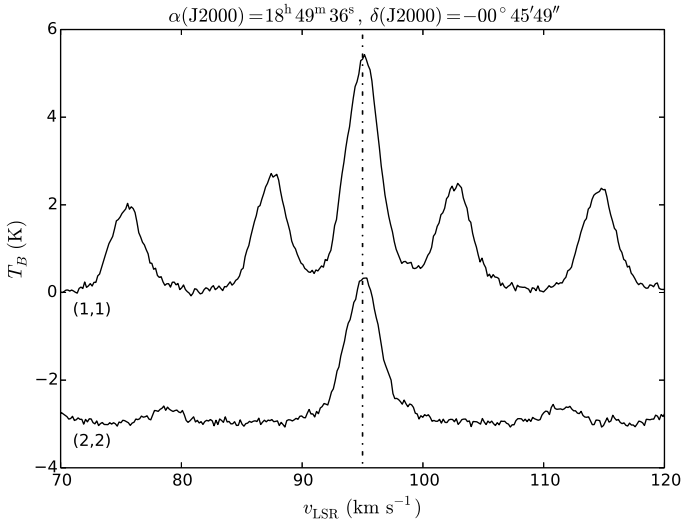

Fig. 4.13.— Spectra of the NH_3 (1,1) and (2,2) lines as observed by the GBT towards the bright IR source at the northeastern end of the cloud. A vertical black dashed-dotted line at 95 km s^{-1} is shown for comparing the line centers to those in Figure 4.2. The brightness temperature scale assumes a beam filling factor of unity.

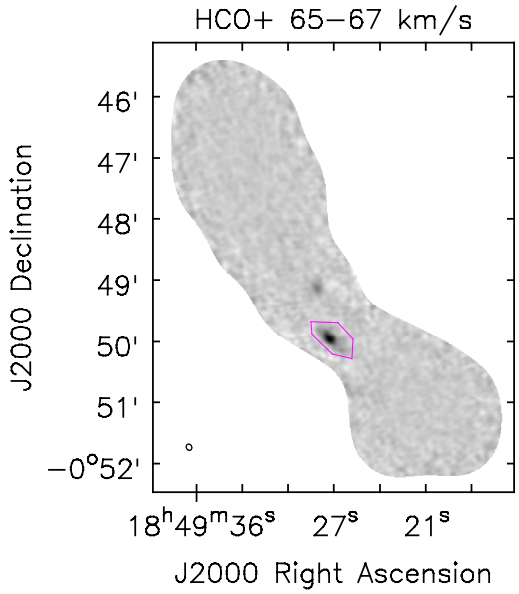

Fig. 4.14.— An integrated intensity map of HCO^+ over the velocity range 65 to 67 km s^{-1}. The magenta polygon shows the approximate extent of the cloud.

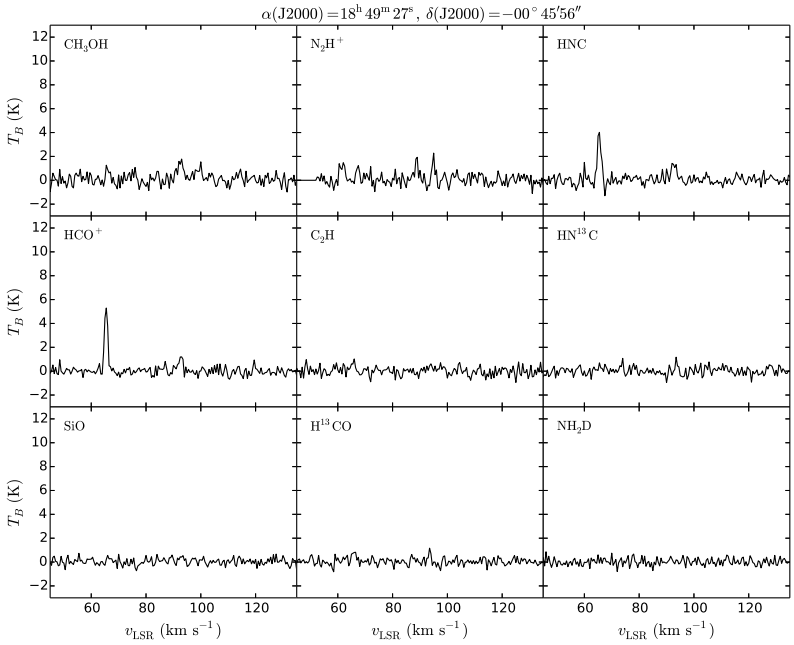

Fig. 4.15.— Spectra of HCO^+ and HNC showing the second cloud 30 km s^{-1} from the main cloud. The brightness temperature scale assumes a beam filling factor of unity.

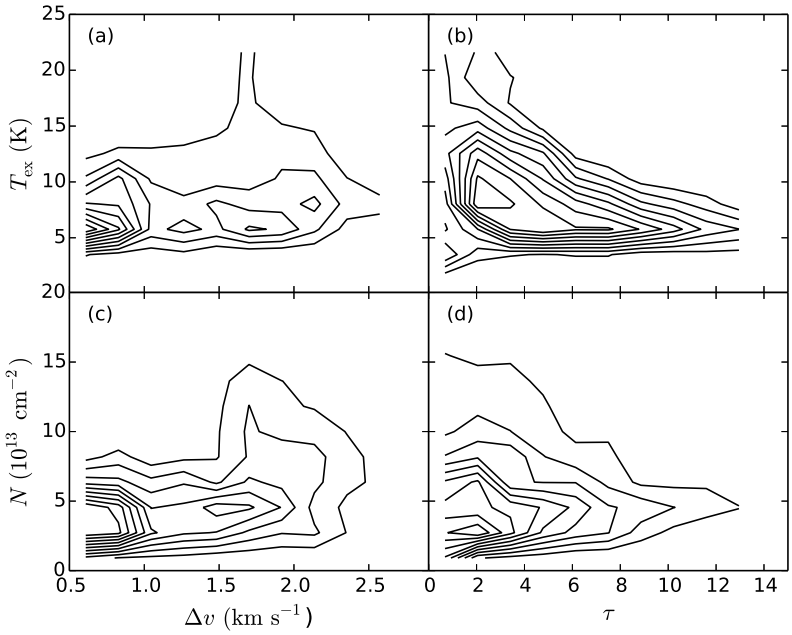

Fig. 4.16.— Plots of the results of N_2H^+ fitting. The black contours show the density of all lines of sight.

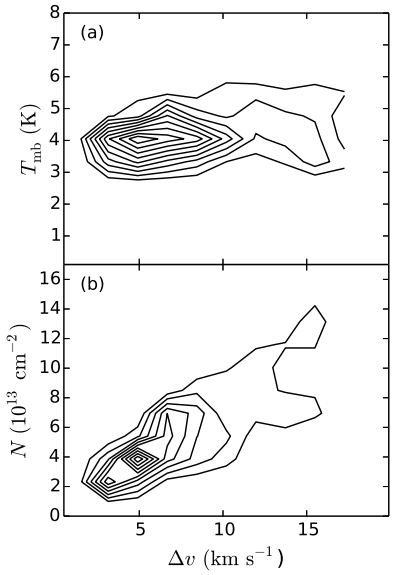

Fig. 4.17.— Plots of the results of SiO fitting. The black contours show the density of all lines of sight.

nine dense gas tracers, and from the moment maps we can discern chemical differentiation in the cloud. The difference in chemistry between deeply embedded and more evolved protostars is expected, but there is some hint of differences between different clumps in the quiescent gas. The range of relative abundances of N_2H^+ and SiO are in agreement with studies of similar IRDC environments, though we extend to higher overall column density.

We have a spectral line fitting routine that works well for N_2H^+ and SiO, gives results consistent with the NH_3 fitting, and can be easily applied to the other species. We detected an anomalous second cloud at a velocity well separated from the main IRDC that is apparently along the same line of sight but unrelated. The SiO emission is generally associated with bright IR sources and has high linewidths (> 10 km s^{-1}), consistent with molecular outflows from protostars. There is some SiO emission coincident with dark gas that may result from clump-clump collisions, however we cannot exclude the possibility of outflows from undetected protostars or that the shocks from stronger jets or the expanding H II regions has propagated into this gas. We do not see widespread weaker, narrower SiO emission throughout the cloud as was seen in G035.39-00.33.

There is significant future work to be done on these data. Spectral line fitting should be completed for nine dense gas tracers. Care will be needed to account for the self-absorption of HCO^+ and HNC and the blended lines of different CH_3OH transitions (generally 3 transitions are detected, though a fourth is seen towards the bright IR source at the northeastern end of the cloud). The isotopologues $H^{13}CO^+$ and $HN^{13}C$ can be used to deal with the optical depth effects in the self-absorbed profiles. We also detect a second component of the hyperfine structure of C_2H towards the bright IR source, and so we can estimate the optical depth of this line towards

that source. We can further compare NH_3 and NH_2D to study deuteration in this cloud. However, to make a more direct comparison of the data from Chapter 3 with the CARMA data, the VLA data should be tapered to the same resolution and, baring corresponding total power data for the CARMA observations, the GBT data should be excluded from this comparison. Finally, we should attempt to perform clump deconvolution on these data so we can fit multiple velocity components and analyze the physical and chemical properties of the clumps as in Chapter 3. Whether it is best to do this for one line and impose those assignments on all the lines or to do it independently, and how successful it will be given the lower angular and spectral resolution and signal-to-noise ratio is yet to be seen.

Chapter 5

Conclusions & Future Work

The importance of triggered star formation is a key open question in understanding star formation on Galactic scales, but it is important to understand whether the presence or absence of triggering around any given H II region can be reliably evaluated based on existing survey data. We have performed SED fitting on a large number of infrared point sources around several H II regions and identified 458 objects that are consistent with YSOs. We report properties of the individual candidates, including mass, evolutionary stage, and accretion rate, based on the physical parameters of the best matching model SEDs. The distribution of the YSOs along the bright rims of infrared bubbles as compared to the field populations, as well as their relatively early evolutionary state, provides evidence that triggered star formation is at work. We find that the regions with cometary morphology are the strongest candidates for triggered star formation.

We searched for further evidence of triggered star formation by quantitatively comparing the predictions of "collect and collapse" (CnC) and "radiatively driven implosion" (RDI) triggering models to observations for 6 H II regions spanning a range of morphologies. To evaluate the consistency of models and data from as many angles as possible, we combined publicly available MIR, cm continuum, and ^{13}CO (1-0) surveys to constrain the properties of YSOs and ionized and molecular gas. While the data are insufficient to draw firm conclusions about the importance of triggering across the whole galaxy, the results suggest ongoing triggered star formation in our sample. While RDI remains difficult to test quantitatively, CnC is a plausible scenario for most of the regions in our sample when properties of the molecular gas are compared to the predictions of analytical models.

Better analytical models and simulations, as well as observational studies, of cometary H II regions are necessary to better constrain the importance of their trig-

gered star formation and to test whether the stronger evidence of triggering in such regions compared to closed bubbles is true beyond this particular sample. Simulations of round bubbles have been fairly successful in reproducing the properties of the molecular gas and triggered star formation predicted by the simple analytical models of CnC, but we need similar simulations of cometary regions to see if and how the properties of the molecular gas and the efficiency of triggering change. The data used in this work are from large surveys and thus sufficient for repeating this analysis on a larger sample, including more cometary regions; these regions have been neglected in the past because of the early focus on cataloging closed bubbles and because closed bubbles are more easily compared to the available analytical models and simulations, but not for a lack of data.

Ideally, studies of this type would be improved with higher resolution molecular observations using tracers such as NH_3 such that the temperatures and column densities can be more precisely determined. In our sample, molecular clumps consistent with CnC are predicted to be a few parsecs in size with peak-to-peak separations of about half a parsec projected onto the sky; 1 pc seen at 4 kpc away is approximately $50''$, only marginally resolved by the BU-GRS $46''$ beam. A real region will certainly have a range of clump sizes and separations, but doing a more thoroughly comparison of these distributions with those seen in triggering simulations will likely require interferometers to resolve the smallest clumps. Even the average sizes will be skewed to larger values if the smallest clumps are not detected or appear as the size of the beam.

Additionally, we mapped the NH_3 and CCS in nine Infrared Dark Clouds, combining single dish and interferometric data from the GBT and the VLA. From fitting the NH_3 spectral lines, we probed the physical conditions of these regions. The kine-

matics seen in NH_3 reveal a diverse set of configurations and substructure. We see clouds with gradients in the velocity field and velocity dispersion, clouds with discrete clumps possibly interacting with each other, and clouds that clearly have both of these scenarios occurring simultaneously in different locations.

Protostars have a tendency to form at the interface of different subclouds. We find that these clumps are typically near virial equilibrium and can easily be supported by typical molecular cloud magnetic field strengths, so these structures may survive for multiple free-fall times. It is possible that all of these IRDCs are consistent with hub-filament structure. High resolution studies of other physical probes, including shock tracers like SiO, are necessary to further test whether the gas is in fact colliding in these regions. The signal-to-noise ratio of the CCS line is typically weak, and so deeper observations and observations of other CCS lines are necessary to better probe the possible chemical differentiation and evolution in IRDCs.

The interplay between IRDC and H II regions may also be important for the formation of massive stars. In Chapter 2, we identify a small number of small IRDCs associated with the H II regions we studied and YSOs coincident with these IRDCs, but the interaction, if any, between the IRDCs and the H II regions is not apparent from the available data. Battersby et al. (2014b) notes that G031.97+00.07 is part of a larger molecular complex as seen by the BU-GRS ^{13}CO J=1-0 data and may have been formed or shaped by the expansion of three neighboring IR bright bubbles. One bubble in particular appears to be colliding with the IRDC at the northeastern end where we see the most advanced star formation, possibly an instance of CnC triggered star formation. Xu et al. (2013) also proposed that the star formation in G038.95-00.47 may be triggered by RDI, powered by adjacent H II regions.

We also have presented CARMA observations of the IRDC G031.97+00.07. The

analysis is in its preliminary stages, but we already see promising results. We have significant detections of all nine dense gas tracers, and from the moment maps we can discern chemical differentiation in the cloud. We have a spectral line fitting routine that works well for N_2H^+ and SiO, gives results consistent with the NH_3 fitting, and can be easily applied to the other species. The SiO emission is generally associated with protostellar IR sources and has high linewidths (> 10 km s^{-1}), consistent with molecular outflows from protostars.

There is significant future work to be done on the CARMA data. Spectral line fitting should be completed for nine dense gas tracers. To make a more direct comparison of the data from Chapter 3 with the CARMA data, the VLA data should be tapered to the same resolution and, baring corresponding total power data for the CARMA observations, the GBT data should be excluded from this comparison. We should attempt to perform clump deconvolution on these data so we can fit multiple velocity components and analyze the physical and chemical properties of the clumps as in Chapter 3.

This research could be expanded to a larger sample of IRDCs and a more comprehensive set of molecular tracers observed at high resolution and high sensitivity. However, it is probably more useful to expand the area around IRDCs that are observed rather than increasing the number of IRDCs observed, i.e. studying the network of filaments apparently associated with the IRDCs in, or similar to IRDCs in, this sample. Studies typically focus on the largest and darkest IRDCs, which look consistent with the hubs at the center of larger complexes. Studying these lower contrast filaments and clumps across many parsecs, particularly their kinematics, dense core population, and star formation activity, would help discern whether molecular gas is flowing along these filaments all the way to the central clouds or if they are

simply lower column density analogues of the larger clouds. Studies of this nature would necessarily need to be deeper in order to detect molecular tracers in the lower column density environments, and interferometers would still be necessary to resolve the substructure.

For the foreseeable future, this work will draw heavily from radio data. Additional research into IRDCs will require ample molecular line observations to explore the physical conditions, kinematics, chemistry, and magnetic fields across a significant sample of these clouds. The forefront of star formation and astrochemical research will make heavy use of observatories including the GBT, the Jansky Very Large Array (JVLA), CARMA, and the Atacama Large Millimeter/submillimeter Array (ALMA), complimented by the publically available infrared surveys from *Spitzer* and *Herschel*.

The GBT is uniquely important to these studies. High signal-to-noise is required to make accurate measurements of the magnetic field through Zeeman splitting, and the molecular tracers that work for this approach are not very abundant in IRDCs. Furthermore, fast mapping capability is needed in order to map larger areas around the primary clouds, to investigate the fainter filaments that are part of the larger molecular cloud structure and may be feeding the formation and evolution of IRDCs, and for observing a statistically significant number of these objects. The ongoing instrumentation upgrades, including the new spectrometer, VEGAS, and the W-band focal plane array, Argus, will further improve the ability of the GBT to observe molecular transitions. The large studies of several dozen to hundreds of IRDCs use only single-dish observations and concentrate on whole-cloud properties or pointed observations toward only the cores, while most detailed studies of IRDCs focus on one or a few objects. A small number of studies, including work presented here, have performed detailed, high-resolution studies on slightly larger samples in a uniform

way. This has begun to reveal range in structure and complexity in these objects, and surely this cannot be considered closed until a larger diverse study is performed.

It will also be critical to use the JVLA in tandem with the GBT to fully explore the structure of IRDCs, as many of the features, including the dense cores, will not be resolved by the GBT. Interferometers alone are not sufficient, however, because a significant amount of emission is on extended spatial scales. The data presented here, which yields interesting results, is from circa 2005 before the JVLA upgrade was completed, and so we can expect to do even better in future observations. I also plan to propose for ALMA observations to gain a richer understanding of the chemistry of these regions at high resolution. Early ALMA observations of IRDC cores have already begun to reveal incredible details of the structures associated with protostars, even at these distances greater than 1 kpc. Other facilities such as CARMA and the SMA are also logical choices for complimentary observations.

Major outstanding questions surround the role of filaments in general in massive star formation and origin and structure of these filaments. *Spitzer* and *Herschel* have shown that complex networks of filamentary structures are ubiquitous across the Milky Way, and in particular are associated with star forming regions (André et al. 2010; Mallick et al. 2013). The population of IRDCs is a subset of these filaments that have high enough column density, are close enough, and appear in front of a bright enough IR background to be seen in contrast, but there are certainly physically similar structures that are not seen in this way. Studies of giant molecular filaments (GMF) have already shown that IRDCs are part of larger spatially and kinematically coherent structures that cross several degrees on the sky (Ragan et al. 2014). They are also part of larger molecular clouds, including more diffuse envelopes and IR-bright bubbles. The proposed hub-filament structure for IRDCs may be relevant not only

for the small scale (on the order of parsecs), but also on the larger scales of GMFs. Studies of gradients in the velocity fields and velocity dispersions along the filaments of IRDCs have been interpreted as evidence of molecular gas flowing towards hubs of star formation, but the interpretation is still ambiguous because of projection effects (Peretto et al. 2014). High resolution maps of dense gas tracers with the JVLA, CARMA, ALMA, etc. across the extent of the hub-filament structure are necessary to further investigate whether this interpretation is valid, e.g. SiO emission consistent with colliding flows or clumps.

The role that magnetic fields play in structure and kinematics of these filaments is also debated. Theoretical models have predicted that the magnetic fields may run parallel to or perpendicular to the major axes of filaments depending on the specific conditions, and Li et al. (2013) indeed found that the orientation of magnetic fields around filamentary molecular clouds in the Gould Belt were preferentially one of these two orientations, but not randomly distributed. Those measurements were made with the polarization of background starlight through dust grains aligned in the magnetic field, which is difficult to apply to the interior of IRDCs because of the high extinction. The TADPOL survey of lower mass star forming regions (Hull et al. 2013) has shown that the directions and strengths of the magnetic fields varies widely between different star forming cores. Given the relatively heterogeneous structure of IRDCs, we should expect similar complexity. In principle, the strength of the magnetic fields in IRDCs and other filamentary clouds can measured from Zeeman splitting of molecular emission lines, but in practice, this can be a difficult measurement. Ultimately the high resolution of interferometers will probably be necessary to disentangle the complex structure.

Aside from the acquisition of data, this work can be extended by generalizing the

Python code used to fit my spectral line observations of ammonia and other molecular tracers to determine physical characteristics, such as temperature and density of interstellar gas. With the increasing amount of research in molecular spectroscopy, there is a need for a general use tool like my fitting routine for more generalized situations and many other molecules. The current code could be integrated with CASA that can be used by the astronomical community at large.

Appendix A

YSOs in H II Regions Identified by SED Fitting

Table A.1:: YSOs identified by SED fitting

YSO	Stage[1]	$\frac{\chi^2_{\rm best}}{n_{\rm data}}$	24 μm?	$\log\left[\frac{M_*}{M_\odot}\right]$[2]	$\log\left[\frac{L_*}{L_\odot}\right]$	$\log\left[\frac{\dot{M_{\rm env}}}{M_\odot\ {\rm yr}^{-1}}\right]$[3]	$\log\left[\frac{M_{\rm disk}}{M_\odot}\right]$
			G028.83-0.25				
G028.6534-00.2539	III	2.89	N	14.6±0.0	4.3±0.0	0.0±0.0	-8.0±0.0
G028.6608-00.2305	II	3.00	N	5.5±1.4	3.0±3.1	0.0±0.0	-2.1±-1.7
G028.6788-00.2786	I	0.05	N	3.8±1.1	2.3±2.6	-4.7±-4.1	-1.7±-1.4
G028.6879-00.2739	I	0.31	Y	3.6±1.3	2.0±2.1	-4.1±-3.8	-1.5±-1.2
G028.6962-00.2913	I	0.47	Y	5.0±1.6	2.9±3.1	-4.8±-3.9	-1.9±-1.5
G028.7020-00.2101	I	0.71	N	2.7±0.9	1.7±1.7	-5.5±-4.9	-2.1±-1.7
G028.7166-00.2231	I	0.01	N	2.0±1.1	1.5±1.9	-5.4±-4.8	-2.2±-1.8
G028.7190-00.1813	II	0.67	Y	4.3±1.1	2.6±2.9	-6.0±-4.8	-2.1±-1.7
G028.7191-00.2083	I	2.06	Y	1.1±1.2	1.7±2.1	-4.5±-4.0	-1.8±-1.6
G028.7347-00.1769	II	0.01	Y	4.5±1.0	2.6±2.6	-6.2±-4.8	-2.0±-1.6
G028.7496-00.1716	II	1.41	N	4.6±1.2	2.7±2.8	-8.5±-7.0	-2.9±-2.2
G028.7516-00.1568	I	0.07	Y	2.9±1.1	1.9±2.1	-5.0±-4.5	-1.9±-1.5
G028.7580-00.2214	II	2.79	N	3.7±0.8	2.2±2.2	-6.3±-5.8	-2.3±-1.7
G028.7632-00.1127	II	2.74	N	6.2±1.8	3.2±3.5	0.0±0.0	-3.3±-2.3
G028.7739-00.2546	II	2.31	N	7.9±4.1	3.8±3.9	0.0±0.0	-2.8±-2.1
G028.7798-00.1671	I	0.02	Y	3.0±1.2	2.1±2.4	-5.1±-4.6	-1.9±-1.6
G028.7814-00.1640	II	1.40	N	4.8±1.5	2.8±3.1	-7.4±-6.3	-2.2±-1.6
G028.7858-00.2205	II	2.44	N	12.4±4.0	4.2±3.9	0.0±0.0	-2.3±-1.8
G028.7876-00.1205	II	1.09	N	3.6±1.0	2.3±2.4	-5.8±-5.2	-2.1±-1.6
G028.7940-00.2754	I	0.94	N	3.0±0.9	1.9±2.1	-5.2±-4.7	-2.0±-1.6
G028.7994-00.1891	III	2.24	N	14.6±0.0	4.3±0.0	0.0±0.0	-8.0±0.0
G028.8008-00.2659	I	0.35	N	4.2±1.2	2.5±2.8	-5.1±-4.5	-1.8±-1.4
G028.8023-00.1158	II	0.14	Y	3.8±0.9	2.3±2.5	-5.6±-4.5	-2.0±-1.6
G028.8105-00.2803	II	2.04	N	5.8±1.7	3.1±3.4	-10.5±-9.5	-2.9±-2.1
G028.8116-00.2211	I	0.07	N	3.6±1.3	2.3±2.6	-4.9±-4.3	-1.8±-1.4
G028.8130-00.2935	I	0.11	N	2.5±1.0	1.7±2.0	-5.3±-4.7	-2.1±-1.7
G028.8299-00.2532	I	0.39	N	6.2±2.0	3.1±3.2	-4.1±-3.6	-1.3±-0.9
G028.8315-00.3123	I	0.49	Y	2.4±1.5	2.0±2.4	-5.0±-4.4	-1.9±-1.6
G028.8318-00.2808	II	0.08	N	3.0±0.9	2.0±2.2	-5.7±-4.9	-2.1±-1.7
G028.8352-00.2354	I	0.04	N	4.1±1.4	2.5±2.8	-4.8±-4.2	-1.8±-1.4
G028.8365-00.3594	II	0.17	N	4.0±1.3	2.5±2.8	-6.3±-5.2	-2.4±-1.8
G028.8382-00.2051	I	0.15	N	3.5±1.0	2.2±2.5	-5.0±-4.3	-2.0±-1.6
G028.8476-00.2657	II	1.72	N	6.8±2.0	3.4±3.6	0.0±0.0	-5.2±-4.1
G028.8540-00.2793	I	0.01	N	2.9±1.0	1.9±2.2	-5.4±-4.8	-2.0±-1.6

YSO	Stage[1]	$\left[\frac{\chi^2_{\rm best}}{n_{\rm data}}\right]$	24 μm?	$\log\left[\frac{M_*}{M_\odot}\right]$[2]	$\log\left[\frac{L_*}{L_\odot}\right]$	$\log\left[\frac{\dot{M_{\rm env}}}{M_\odot\ {\rm yr}^{-1}}\right]$[3]	$\log\left[\frac{M_{\rm disk}}{M_\odot}\right]$
G028.8547-00.2192	I	1.80	Y	2.8±1.8	2.3±2.5	-4.0±-3.6	-1.6±-1.4
G028.8573-00.2184	I	0.54	Y	1.6±1.3	1.8±2.2	-4.3±-4.0	-1.7±-1.5
G028.8750-00.1296	I	0.80	N	2.8±1.1	1.8±2.0	-5.0±-4.6	-1.9±-1.5
G028.8781-00.3573	II	0.29	N	2.8±1.5	2.3±2.9	-5.8±-5.2	-2.2±-1.8
G028.8814-00.3291	II	0.37	Y	3.9±1.3	2.5±2.8	-5.4±-4.7	-2.0±-1.6
G028.8884-00.1148	II	2.24	N	4.7±1.4	2.8±2.9	-6.4±-5.6	-2.2±-1.7
G028.9004-00.3328	III	2.66	N	14.6±0.0	4.3±0.0	0.0±0.0	-8.0±0.0
G028.9145-00.2258	I	1.60	N	3.1±0.8	1.8±2.0	-5.4±-4.8	-2.0±-1.6
G028.9191-00.2304	I	0.10	Y	1.1±1.0	1.6±2.0	-4.9±-5.0	-1.9±-1.7
G028.9198-00.2283	I	1.39	Y	5.0±1.7	2.9±3.1	-4.2±-3.6	-1.8±-1.4
G028.9249-00.1749	II	2.57	N	4.1±1.7	2.8±3.4	-7.8±-6.7	-2.4±-1.8
G028.9277-00.1678	I	0.08	N	2.2±1.0	1.5±1.9	-5.4±-4.7	-2.2±-1.8
G028.9311-00.2275	I	0.10	Y	2.1±1.4	1.8±2.3	-5.0±-4.4	-2.0±-1.6
G028.9450-00.2436	II	0.42	N	3.5±1.1	2.2±2.3	-5.5±-5.1	-1.9±-1.5
M028.7228-00.3030	I	0.66	Y	2.9±1.3	2.0±2.4	-4.8±-4.4	-1.8±-1.5
M028.7905-00.2439	I	0.96	Y	4.0±1.8	2.5±2.7	-4.0±-3.6	-1.5±-1.2
M028.8217-00.2235	I	2.66	Y	6.0±1.8	2.8±2.8	-4.0±-3.7	-1.1±-0.9
M028.9096-00.1618	I	1.22	Y	2.8±1.4	2.0±2.2	-5.1±-5.1	-2.1±-1.7
				G041.10-0.15			
G040.9735-00.1553	I	0.19	Y	3.5±1.9	2.5±2.8	-4.9±-4.2	-1.8±-1.5
G040.9879-00.2920	I	1.17	Y	1.9±1.2	1.5±2.0	-5.0±-4.2	-2.1±-1.7
G041.0008-00.1363	I	0.25	Y	3.3±1.3	2.2±2.5	-4.8±-4.2	-1.8±-1.5
G041.0033-00.1247	I	0.09	Y	1.9±1.2	1.6±1.9	-4.9±-4.5	-2.0±-1.7
G041.0061-00.1462	I	0.85	N	1.2±1.1	1.3±1.8	-4.8±-4.5	-2.0±-1.8
G041.0091-00.1607	I	1.11	N	2.1±1.2	1.7±2.1	-5.0±-4.5	-2.0±-1.7
G041.0290-00.1963	I	0.05	N	2.4±1.2	1.7±2.0	-4.9±-4.5	-1.9±-1.6
G041.0360-00.2221	I	0.10	Y	3.3±1.5	2.1±2.4	-4.1±-3.8	-1.6±-1.3
G041.0400-00.0973	I	2.38	N	2.6±0.9	1.5±2.0	-4.8±-3.9	-1.8±-1.5
G041.0434-00.2076	I	0.14	N	3.6±1.3	2.3±2.6	-4.8±-4.3	-1.8±-1.4
G041.0439-00.2360	I	0.20	N	2.0±1.5	2.0±2.2	-4.5±-4.1	-1.7±-1.4
G041.0505-00.1885	I	0.01	N	2.3±1.3	1.8±2.1	-4.9±-4.4	-1.9±-1.6
G041.0519-00.0910	I	1.59	Y	2.8±1.6	2.2±2.5	-4.2±-3.8	-1.4±-1.2
G041.0533-00.1910	I	0.42	N	1.9±1.3	1.7±2.1	-4.8±-4.4	-1.9±-1.6
G041.0552-00.1035	I	0.01	N	3.1±1.6	2.3±2.7	-5.0±-4.5	-1.9±-1.5
G041.0643-00.2324	I	1.97	N	3.8±1.0	2.3±2.4	-5.1±-4.3	-2.1±-1.6
G041.0728-00.1238	I	0.80	Y	2.9±1.7	2.2±2.6	-4.3±-3.9	-1.5±-1.3
G041.0775-00.1884	I	0.01	N	3.0±0.8	2.0±2.2	-5.0±-4.4	-2.0±-1.6

YSO	Stage[1]	$\left[\frac{\chi^2_{\rm best}}{n_{\rm data}}\right]$	24 μm?	$\log\left[\frac{M_*}{M_\odot}\right]$[2]	$\log\left[\frac{L_*}{L_\odot}\right]$	$\log\left[\frac{\dot{M_{\rm env}}}{M_\odot\ {\rm yr}^{-1}}\right]$[3]	$\log\left[\frac{M_{\rm disk}}{M_\odot}\right]$
G041.0789-00.1279	I	1.90	N	2.5±1.1	1.6±1.8	-4.9±-4.4	-2.0±-1.6
G041.0791-00.2253	I	1.73	N	2.5±1.1	1.7±2.0	-5.1±-4.6	-1.9±-1.6
G041.0821-00.1121	I	0.10	N	1.7±1.1	1.4±1.7	-5.1±-4.6	-2.1±-1.8
G041.0827-00.1933	I	0.09	N	3.8±1.1	2.4±2.6	-5.2±-4.6	-2.0±-1.6
G041.0844-00.1679	I	0.01	N	3.0±1.0	2.0±2.2	-5.3±-4.5	-2.0±-1.7
G041.0963-00.3064	I	0.09	N	2.1±1.1	1.5±1.7	-5.2±-4.7	-2.1±-1.7
G041.1013-00.1197	I	0.01	N	2.7±1.4	2.1±2.3	-5.6±-4.9	-2.0±-1.6
G041.1054-00.1192	I	0.18	N	2.5±1.0	1.9±2.0	-4.5±-4.3	-1.9±-1.6
G041.1107-00.1935	I	0.31	N	3.1±0.9	2.0±2.2	-4.8±-4.3	-1.8±-1.5
G041.1121-00.1832	I	2.27	N	3.7±1.0	2.3±2.5	-4.9±-4.4	-1.9±-1.5
G041.1135-00.3356	I	0.60	N	2.8±1.0	1.7±1.8	-5.4±-5.0	-2.1±-1.7
G041.1160-00.1124	I	1.84	Y	2.1±1.4	1.8±2.2	-4.3±-4.0	-1.7±-1.5
G041.1196-00.1955	I	0.32	N	3.4±1.1	2.1±2.2	-4.7±-4.2	-1.9±-1.5
G041.1206-00.1255	II	2.82	N	4.0±1.1	2.5±2.7	-6.8±-5.6	-2.5±-1.8
G041.1248-00.2309	I	0.15	Y	6.0±1.3	2.7±2.5	-4.4±-4.5	-1.0±-0.8
G041.1315-00.2107	I	0.18	N	4.0±1.1	2.5±2.8	-4.7±-4.2	-1.8±-1.4
G041.1374-00.2111	I	1.16	N	4.5±1.2	2.6±2.8	-5.2±-4.5	-2.0±-1.5
G041.1388-00.0766	II	2.16	N	4.6±1.1	2.6±2.6	-5.6±-4.7	-2.3±-1.6
G041.1414-00.1581	I	0.53	N	1.1±1.1	1.4±1.9	-4.7±-4.4	-2.0±-1.7
G041.1447-00.1065	II	1.38	N	3.4±0.8	2.1±2.2	-6.5±-5.6	-2.3±-1.8
G041.1616-00.1840	I	0.33	Y	3.9±1.7	2.6±2.9	-4.5±-4.0	-1.7±-1.4
G041.1774-00.2689	I	0.80	Y	3.9±0.8	2.4±2.6	-5.1±-4.2	-1.9±-1.5
G041.1797-00.2242	II	1.38	N	5.0±1.3	2.8±3.0	-6.1±-5.4	-2.0±-1.5
G041.1840-00.1786	II	0.45	N	3.2±0.9	2.1±2.3	-5.5±-4.9	-2.0±-1.6
G041.1868-00.1844	I	0.03	Y	2.8±1.4	2.1±2.3	-5.1±-4.5	-1.9±-1.6
G041.1894-00.2005	II	1.16	N	4.1±1.0	2.5±2.5	-8.3±-7.3	-2.8±-2.1
G041.1957-00.1947	II	2.04	Y	4.5±1.1	2.7±2.8	-5.9±-4.7	-2.1±-1.6
G041.2037-00.1225	II	2.52	N	3.5±0.8	2.1±2.1	-5.9±-5.0	-2.2±-1.6
G041.2074-00.1813	I	0.20	N	2.0±1.2	1.7±2.0	-5.0±-4.5	-2.0±-1.7
G041.2110-00.3277	I	0.32	N	2.1±1.0	1.5±1.7	-5.2±-4.7	-2.1±-1.7
G041.2128-00.1932	I	0.88	N	3.0±1.1	2.0±2.3	-5.0±-4.5	-2.0±-1.6
G041.2151-00.2191	II	2.78	N	3.9±0.9	2.3±2.4	-6.4±-5.5	-2.3±-1.7
G041.2372-00.1732	I	1.42	N	2.2±0.9	1.6±1.6	-5.0±-4.6	-2.0±-1.7
G041.2377-00.2978	II	0.14	N	2.7±1.1	1.8±2.1	-5.8±-5.4	-2.1±-1.7
G041.2411-00.2435	I	0.43	Y	1.3±1.3	1.7±2.2	-4.7±-4.3	-1.8±-1.6
G041.2426-00.1020	I	0.16	N	2.6±0.9	1.7±1.8	-5.5±-5.1	-2.1±-1.7
G041.2441-00.2108	I	1.05	Y	3.3±1.1	2.1±2.2	-4.9±-4.4	-1.9±-1.5

YSO	Stage[1]	$\left[\frac{\chi^2_{\rm best}}{n_{\rm data}}\right]$	24 μm?	$\log\left[\frac{M_*}{M_\odot}\right]$[2]	$\log\left[\frac{L_*}{L_\odot}\right]$	$\log\left[\frac{\dot{M_{\rm env}}}{M_\odot\ {\rm yr}^{-1}}\right]$[3]	$\log\left[\frac{M_{\rm disk}}{M_\odot}\right]$
G041.2472-00.3503	I	0.10	Y	2.7±1.5	2.1±2.3	-5.0±-4.3	-2.0±-1.6
G041.2479-00.1583	I	0.01	N	1.9±1.1	1.5±1.8	-5.1±-4.6	-2.1±-1.8
G041.2517-00.0818	I	0.13	Y	3.1±1.4	2.0±2.4	-4.6±-4.3	-1.6±-1.4
G041.2541-00.2281	I	1.21	N	2.8±0.8	1.9±2.0	-5.3±-4.7	-2.1±-1.9
G041.2561-00.3402	I	0.72	Y	3.2±1.2	2.1±2.3	-4.9±-4.4	-1.9±-1.5
G041.2574-00.2835	II	0.54	N	2.5±1.0	1.5±1.7	-5.7±-5.2	-2.2±-1.8
G041.2588-00.2290	I	0.13	N	1.9±1.1	1.4±1.8	-5.1±-4.6	-2.1±-1.8
G041.2616-00.3511	II	2.58	N	3.9±0.9	2.4±2.4	-7.8±-6.9	-2.7±-1.9
G041.2618-00.1425	II	2.23	N	3.7±1.0	2.3±2.4	-6.6±-5.7	-2.4±-1.8
G041.2639-00.1049	I	0.30	N	0.7±0.8	1.2±1.6	-5.1±-4.6	-2.0±-1.8
G041.2691-00.1775	II	2.37	N	4.1±0.9	2.4±2.4	-7.3±-6.2	-2.6±-2.0
G041.2697-00.1151	II	1.16	N	3.0±0.5	1.9±1.8	-6.0±-4.9	-2.1±-1.7
G041.2726-00.1040	II	0.08	N	3.0±1.1	2.1±2.3	-6.1±-5.4	-2.2±-1.8
G041.2854-00.2190	I	0.07	Y	2.9±1.1	2.0±2.2	-5.2±-4.6	-1.8±-1.5
G041.2858-00.0862	I	0.12	Y	1.9±1.2	1.5±2.0	-4.7±-3.9	-2.0±-1.6
G041.2940-00.2937	I	1.23	Y	3.1±1.4	2.0±2.3	-4.2±-3.9	-1.8±-1.5
G041.2963-00.3250	II	0.17	N	2.8±1.2	1.9±2.1	-5.6±-5.1	-2.0±-1.7
G041.3061-00.2609	I	0.02	Y	2.5±1.1	1.7±2.0	-5.2±-4.6	-1.9±-1.6
G041.3083-00.1717	I	2.17	N	2.9±1.2	2.0±2.2	-4.3±-3.9	-1.7±-1.4
G041.3091-00.2766	II	2.52	N	3.2±0.6	2.0±1.9	-6.3±-5.4	-2.2±-1.7
G041.3098-00.1412	I	0.08	Y	3.0±1.4	2.2±2.5	-5.3±-4.6	-2.0±-1.6
G041.3114-00.2463	I	0.17	Y	2.8±1.5	2.2±2.7	-5.0±-4.4	-2.0±-1.6
G041.3119-00.3145	II	1.73	N	3.0±1.5	2.3±2.7	-6.1±-5.4	-2.3±-1.8
G041.3129-00.2256	I	1.15	Y	2.0±1.0	1.3±1.1	-4.8±-4.5	-2.0±-1.7
G041.3170-00.1687	I	1.06	N	3.0±0.9	1.9±2.1	-5.5±-4.8	-2.1±-1.7
G041.3255-00.1546	I	0.07	Y	1.0±1.0	1.4±1.8	-5.0±-4.6	-1.9±-1.7
G041.3266-00.1290	I	0.02	N	1.3±1.3	1.6±1.9	-5.0±-4.5	-2.0±-1.8
G041.3275-00.1869	I	0.05	N	5.1±1.6	2.9±3.1	-4.5±-4.0	-1.7±-1.3
G041.3301-00.1920	I	0.36	N	1.9±1.9	2.3±2.6	-4.5±-3.8	-1.6±-1.5
G041.3356-00.2144	I	0.20	Y	2.6±1.2	1.8±2.2	-5.0±-4.5	-2.0±-1.6
G041.3368-00.2167	I	1.23	N	1.8±1.4	1.8±2.0	-4.9±-4.4	-1.9±-1.7
G041.3475-00.1364	I	0.19	Y	4.5±1.5	2.5±2.6	-3.7±-3.4	-1.4±-1.2
G041.3524-00.0933	I	2.03	N	2.7±1.0	1.8±2.1	-5.4±-4.8	-2.1±-1.7
G041.3579-00.1541	II	0.85	N	3.2±0.9	2.0±2.2	-6.1±-5.2	-2.2±-1.7
G041.3590-00.2699	I	0.44	Y	1.8±1.5	1.8±2.2	-5.4±-4.9	-2.0±-1.8
G041.3671-00.2146	II	0.06	N	2.5±0.9	1.7±1.7	-5.9±-5.2	-2.1±-1.7
G041.3675-00.2060	I	0.37	N	2.0±1.0	1.4±1.6	-5.6±-5.1	-2.1±-1.8

YSO	Stage[1]	$\left[\frac{\chi^2_{\rm best}}{n_{\rm data}}\right]$	24 μm?	$\log\left[\frac{M_*}{M_\odot}\right]$[2]	$\log\left[\frac{L_*}{L_\odot}\right]$	$\log\left[\frac{\dot{M_{\rm env}}}{M_\odot\ {\rm yr}^{-1}}\right]$[3]	$\log\left[\frac{M_{\rm disk}}{M_\odot}\right]$
G041.3768-00.2891	II	0.05	N	3.1±0.5	1.9±1.8	-6.4±-5.2	-2.4±-1.9
M041.0097-00.1347	I	1.01	Y	2.1±1.1	1.4±1.3	-4.9±-4.7	-2.0±-1.6
M041.0600-00.1378	I	2.08	Y	3.9±1.3	2.1±1.8	-4.1±-3.8	-1.7±-1.4
M041.0670-00.2872	I	0.05	Y	2.6±1.4	2.0±2.2	-4.2±-3.9	-1.6±-1.4
M041.0739-00.2808	I	2.58	Y	3.4±1.5	2.3±2.6	-5.0±-4.5	-1.8±-1.5
M041.1334-00.1944	I	2.38	Y	3.2±1.6	2.2±2.4	-4.1±-3.8	-1.4±-1.2
M041.1898-00.2328	I	0.22	Y	3.6±1.3	2.0±2.1	-4.3±-4.0	-1.5±-1.3
M041.2243-00.1662	I	0.32	Y	3.3±1.4	2.0±2.3	-4.1±-3.8	-1.7±-1.4
M041.2332-00.1225	I	0.06	Y	3.3±1.4	2.1±2.3	-4.1±-3.8	-1.6±-1.3
M041.2628-00.1904	I	0.17	Y	2.9±1.2	1.8±1.9	-4.6±-4.2	-1.7±-1.4
M041.2862-00.1845	I	1.70	Y	1.9±1.4	1.6±2.0	-4.3±-3.7	-1.9±-1.5
M041.3296-00.2351	I	1.08	Y	3.2±1.9	2.4±2.7	-4.6±-4.2	-1.8±-1.5
G041.91-0.12 & G041.92+0.04							
G041.8040-00.1169	II	0.52	N	0.7±0.6	0.2±0.6	-7.0±-6.2	-3.3±-2.6
G041.8099+00.0894	I	0.33	N	0.4±0.5	0.6±0.9	-4.9±-4.7	-2.2±-2.0
G041.8105+00.0509	I	0.04	Y	0.9±0.8	0.8±1.3	-5.8±-5.3	-2.3±-2.0
G041.8136+00.0282	II	0.16	N	0.8±0.7	0.4±0.9	-6.3±-5.5	-2.8±-2.3
G041.8143+00.0305	II	0.30	N	0.7±0.6	0.4±1.1	-6.2±-5.4	-2.9±-2.3
G041.8144-00.0968	II	1.00	N	1.0±0.7	0.4±0.7	-7.0±-6.4	-2.9±-2.3
G041.8160-00.0963	II	0.41	N	1.1±0.8	0.6±1.0	-7.0±-6.5	-2.9±-2.3
G041.8166-00.1189	I	0.01	Y	0.8±0.8	0.7±1.5	-5.5±-4.5	-2.5±-2.0
G041.8175-00.1185	I	0.01	Y	0.9±0.9	0.9±1.5	-5.6±-5.0	-2.6±-2.1
G041.8176-00.1249	I	0.43	Y	0.6±0.8	1.1±1.6	-5.4±-5.6	-2.1±-2.0
G041.8205-00.1607	II	1.55	N	0.8±0.7	0.4±0.9	-6.5±-5.8	-2.9±-2.3
G041.8207-00.1729	II	0.01	Y	1.6±1.0	1.1±1.5	-6.2±-5.3	-2.4±-1.9
G041.8267+00.0866	II	0.02	N	0.8±0.7	0.5±1.0	-6.1±-5.5	-2.8±-2.3
G041.8303+00.0495	I	0.07	Y	1.0±1.2	1.3±1.6	-5.6±-5.2	-2.1±-2.0
G041.8307+00.0276	I	0.12	Y	1.1±1.0	1.0±1.6	-5.3±-4.8	-2.3±-1.9
G041.8329+00.0323	I	0.15	N	0.8±0.8	0.7±1.2	-5.6±-5.0	-2.5±-2.2
G041.8336+00.0914	II	1.89	N	0.9±0.7	0.3±0.7	-7.3±-6.5	-3.9±-3.1
G041.8360+00.0013	I	0.01	Y	0.9±1.0	1.1±1.7	-5.3±-5.0	-2.3±-1.9
G041.8377-00.1124	II	0.03	N	0.8±0.7	0.4±0.9	-6.2±-5.5	-2.8±-2.3
G041.8385-00.1294	II	0.63	N	0.9±0.7	0.5±0.9	-6.6±-5.9	-2.9±-2.3
G041.8394-00.0491	II	0.47	N	0.8±0.7	0.3±0.7	-6.8±-6.1	-3.0±-2.4
G041.8434-00.0104	I	0.06	Y	0.7±0.7	0.6±1.1	-5.4±-4.9	-2.4±-2.1
G041.8495+00.1513	II	0.12	N	1.1±0.8	0.7±1.2	-6.7±-6.2	-2.7±-2.2
G041.8532+00.0208	I	0.02	N	0.5±0.7	0.7±1.2	-5.2±-4.8	-2.3±-2.1

YSO	Stage[1]	$\left[\frac{\chi^2_{\rm best}}{n_{\rm data}}\right]$	24 μm?	$\log\left[\frac{M_*}{M_\odot}\right]$[2]	$\log\left[\frac{L_*}{L_\odot}\right]$	$\log\left[\frac{\dot{M_{\rm env}}}{M_\odot\ {\rm yr}^{-1}}\right]$[3]	$\log\left[\frac{M_{\rm disk}}{M_\odot}\right]$
G041.8553-00.1085	II	1.47	N	1.1±0.8	0.7±1.1	-6.8±-6.3	-2.8±-2.2
G041.8634-00.0435	I	2.56	Y	0.7±0.9	1.3±1.9	-4.9±-4.6	-2.1±-1.8
G041.8698-00.0939	I	0.02	Y	0.4±0.6	0.5±1.2	-5.3±-5.0	-2.4±-2.2
G041.8702+00.1484	I	0.13	Y	1.0±1.3	1.4±1.8	-5.7±-5.2	-2.2±-1.9
G041.8702-00.1304	II	1.03	N	1.4±0.8	0.7±0.9	-7.1±-6.4	-4.7±-3.6
G041.8744-00.1114	I	0.20	Y	1.0±0.9	0.9±1.4	-5.7±-5.2	-2.5±-2.0
G041.8801-00.1294	I	0.18	Y	2.9±1.5	2.2±2.5	-4.8±-4.2	-2.0±-1.6
G041.8816-00.0593	II	0.74	N	0.8±0.6	0.2±0.6	-7.1±-6.3	-3.5±-2.7
G041.8842-00.0914	I	0.33	Y	0.5±0.8	0.9±1.4	-5.3±-4.8	-2.2±-2.0
G041.8843-00.1093	II	0.45	N	0.5±0.3	0.1±0.1	-6.5±-6.1	-2.8±-2.4
G041.8868+00.0603	I	0.11	N	0.7±0.8	0.6±1.0	-6.0±-5.5	-2.5±-2.1
G041.8883+00.1058	II	0.61	N	1.0±1.1	1.3±1.9	-6.0±-5.9	-2.2±-2.0
G041.8900-00.1025	I	0.46	N	0.8±0.7	0.4±1.0	-6.0±-5.4	-2.7±-2.2
G041.8912-00.0532	I	0.06	Y	0.9±0.9	1.0±1.4	-5.5±-5.1	-2.2±-1.9
G041.8940+00.0523	II	1.78	N	0.8±0.6	0.3±0.8	-6.4±-5.7	-2.9±-2.3
G041.8997+00.1270	II	0.14	Y	2.4±1.2	1.8±2.2	-6.3±-5.4	-2.3±-1.8
G041.9021-00.1678	I	0.01	Y	0.5±0.9	1.1±1.7	-5.3±-5.0	-2.2±-2.0
G041.9063-00.1550	I	0.16	Y	4.0±1.2	2.5±2.7	-5.3±-4.4	-2.1±-1.6
G041.9250+00.0428	I	2.30	N	1.0±1.2	1.5±2.0	-4.8±-4.4	-2.1±-1.8
G041.9257+00.0327	I	0.10	N	0.5±0.5	0.2±0.6	-5.5±-5.2	-2.5±-2.2
G041.9270-00.1401	I	0.04	Y	1.3±1.1	1.2±1.7	-5.4±-4.9	-2.3±-1.8
G041.9336-00.1541	I	0.05	Y	1.0±0.9	0.8±1.3	-5.7±-5.1	-2.4±-2.0
G041.9344-00.1002	II	0.42	N	1.1±0.8	0.7±1.0	-6.7±-6.1	-2.8±-2.2
G041.9406-00.0746	I	0.39	Y	1.7±1.4	1.7±1.9	-4.8±-4.4	-2.1±-1.8
G041.9460-00.1067	II	1.48	N	1.0±0.7	0.4±0.8	-7.7±-7.0	-4.2±-3.2
G041.9488-00.0593	II	0.29	N	1.2±0.7	0.5±0.8	-7.6±-6.8	-4.6±-3.5
G041.9516-00.1445	II	0.25	N	0.9±0.8	0.5±0.8	-6.5±-5.8	-2.8±-2.2
G041.9536-00.0981	II	1.16	N	0.9±0.8	0.5±0.9	-6.5±-5.8	-2.8±-2.3
G041.9571+00.0745	I	0.01	N	0.5±0.7	0.7±1.3	-4.9±-4.8	-2.3±-2.0
G041.9585+00.0293	I	0.04	N	0.6±0.6	0.2±0.6	-6.1±-5.5	-2.8±-2.4
G041.9687-00.0111	I	0.38	Y	0.9±0.8	0.7±1.2	-5.6±-4.8	-2.6±-2.1
G041.9691-00.0610	I	0.31	N	0.7±1.0	0.9±1.2	-5.7±-5.2	-2.4±-2.2
G041.9708+00.0681	II	0.17	N	1.1±0.9	0.9±1.3	-6.6±-6.0	-2.3±-2.0
G041.9741-00.0292	II	1.31	N	1.0±0.8	0.5±1.0	-6.5±-5.8	-2.8±-2.3
G041.9754-00.1077	I	0.02	N	0.4±0.5	0.2±0.7	-5.5±-5.3	-2.6±-2.3
G041.9790+00.1338	II	2.22	N	0.9±0.7	0.4±0.8	-6.7±-6.1	-2.9±-2.3
G041.9833-00.1209	II	0.68	N	0.8±0.6	0.3±0.4	-7.0±-6.5	-3.1±-2.5

YSO	Stage[1]	$\left[\frac{\chi^2_{\rm best}}{n_{\rm data}}\right]$	24 μm?	$\log\left[\frac{M_*}{M_\odot}\right]$[2]	$\log\left[\frac{L_*}{L_\odot}\right]$	$\log\left[\frac{\dot{M_{\rm env}}}{M_\odot\ {\rm yr}^{-1}}\right]$[3]	$\log\left[\frac{M_{\rm disk}}{M_\odot}\right]$
G041.9871-00.1229	II	1.35	N	0.9±0.7	0.4±0.7	-6.6±-6.0	-2.7±-2.2
G041.9880-00.0366	II	0.03	N	1.0±0.8	0.7±1.1	-6.4±-5.9	-2.5±-2.1
G041.9911-00.0310	I	0.19	Y	3.2±1.7	2.4±2.6	-4.7±-4.2	-1.9±-1.5
G041.9979-00.0280	II	0.31	Y	1.1±0.8	0.7±1.2	-6.3±-5.6	-2.7±-2.2
G041.9985-00.0621	I	0.23	Y	1.5±1.2	1.4±1.8	-5.6±-4.9	-2.1±-1.8
G042.0008-00.0401	I	0.71	Y	0.5±0.6	0.9±1.5	-4.8±-4.6	-2.2±-1.9
G042.0009-00.0696	I	0.11	Y	0.6±0.7	0.7±1.3	-5.3±-4.9	-2.3±-2.0
G042.0141+00.0093	II	0.06	Y	2.1±1.2	1.7±2.1	-6.0±-5.2	-2.3±-1.8
G042.0228-00.0899	II	1.13	N	1.1±0.8	0.7±1.1	-7.0±-6.4	-2.9±-2.3
G042.0231+00.0173	I	0.41	Y	0.4±0.7	0.7±1.2	-5.1±-4.7	-2.2±-2.0
G042.0234-00.0461	I	0.87	N	0.4±0.7	0.5±1.1	-5.3±-5.1	-2.4±-2.2
G042.0352+00.0362	II	1.95	N	0.9±0.7	0.4±0.7	-6.7±-6.0	-3.0±-2.4
G042.0402-00.0725	I	0.62	Y	1.5±1.4	1.6±1.8	-5.6±-4.9	-2.2±-1.9
G042.0415+00.1356	II	1.07	N	1.0±0.7	0.4±0.8	-7.7±-7.0	-4.2±-3.2
G042.0430-00.0690	II	2.12	N	1.2±0.8	0.6±0.9	-6.9±-6.3	-2.9±-2.3
G042.0492+00.0390	II	0.42	N	0.9±0.7	0.4±0.9	-6.6±-5.8	-2.9±-2.3
G042.0498-00.0745	II	2.72	N	1.1±0.8	0.6±0.8	-6.5±-5.5	-2.8±-2.2
M041.8609-00.0378	I	0.13	Y	0.9±0.9	1.0±1.5	-4.9±-4.5	-2.2±-1.9
M041.8877-00.1379	I	0.24	Y	1.0±1.0	1.1±1.6	-4.5±-3.9	-2.2±-1.8
M041.9017-00.1513	I	0.02	N	1.2±1.0	1.1±1.6	-5.3±-4.8	-2.3±-1.9
M041.9285+00.0533	I	0.77	Y	1.1±1.5	1.6±2.0	-5.1±-4.5	-2.1±-1.9
M041.9407+00.0162	I	1.68	Y	0.4±0.5	0.6±1.1	-5.1±-4.9	-2.3±-2.0
M041.9573-00.0617	I	0.01	N	0.4±0.5	0.1±0.7	-5.5±-5.2	-2.5±-2.3
M041.9665+00.1483	I	0.01	Y	0.7±0.9	0.9±1.4	-5.3±-4.9	-2.4±-2.1
M041.9801+00.0672	I	0.33	Y	0.6±0.5	0.1±0.6	-5.7±-4.9	-2.8±-2.3
M042.0060+00.0868	I	1.47	Y	0.6±0.6	0.4±0.9	-5.0±-4.2	-2.5±-2.1
M042.0114-00.0329	I	0.21	Y	0.6±0.6	0.5±1.2	-5.6±-5.0	-2.5±-2.2
M042.0443-00.0375	I	0.11	Y	0.9±0.8	0.9±1.4	-5.4±-5.0	-2.4±-2.0
				G044.28+0.11			
G043.9606+00.0244	I	0.95	N	2.0±1.0	1.4±1.6	-5.4±-5.0	-2.1±-1.8
G043.9627+00.1631	II	0.23	N	2.3±1.1	1.6±1.8	-5.8±-5.4	-2.1±-1.7
G043.9646-00.1120	I	0.09	Y	2.4±1.3	1.8±2.1	-4.9±-4.4	-1.9±-1.6
G043.9686+00.0756	I	0.27	Y	3.0±1.2	2.0±2.2	-5.0±-4.5	-1.8±-1.5
G043.9705+00.0169	II	0.10	Y	5.5±1.3	3.0±3.1	-5.9±-4.6	-1.9±-1.6
G043.9725+00.0333	II	0.47	N	3.6±1.1	2.3±2.5	-6.6±-6.0	-2.2±-1.7
G043.9762+00.1150	I	0.05	Y	2.3±1.7	2.1±2.4	-5.3±-4.6	-2.1±-1.8
G043.9762+00.3216	II	0.25	N	3.7±0.9	2.3±2.5	-7.4±-6.7	-2.2±-1.7

YSO	Stage[1]	$\left[\frac{\chi^2_{\rm best}}{n_{\rm data}}\right]$	24 μm?	$\log\left[\frac{M_*}{M_\odot}\right]$[2]	$\log\left[\frac{L_*}{L_\odot}\right]$	$\log\left[\frac{\dot{M_{\rm env}}}{M_\odot\ {\rm yr}^{-1}}\right]$[3]	$\log\left[\frac{M_{\rm disk}}{M_\odot}\right]$
G043.9892+00.0504	II	0.61	Y	4.9±1.1	2.8±3.0	-6.0±-4.9	-1.8±-1.5
G043.9956+00.0060	II	0.09	N	3.8±0.9	2.3±2.5	-6.3±-5.5	-2.1±-1.6
G043.9984+00.1565	I	0.11	Y	2.7±1.2	1.9±2.2	-5.0±-4.4	-1.9±-1.6
G044.0032-00.1634	I	0.15	Y	1.9±1.2	1.6±1.9	-5.2±-4.7	-2.0±-1.7
G044.0048+00.2956	II	0.19	Y	4.7±1.3	2.7±2.9	-5.9±-4.7	-2.1±-1.6
G044.0119-00.0291	I	0.53	Y	4.4±1.4	2.7±2.9	-5.3±-4.4	-2.0±-1.5
G044.0125+00.3246	I	0.50	Y	6.2±2.4	3.3±3.4	-4.0±-3.4	-1.5±-1.2
G044.0130-00.0010	I	0.16	N	2.2±1.0	1.4±1.5	-5.4±-4.9	-2.2±-1.8
G044.0133-00.0046	I	0.03	N	3.3±1.1	2.1±2.2	-4.9±-4.5	-1.8±-1.5
G044.0212-00.1030	II	1.33	N	2.9±1.0	1.9±2.1	-5.9±-5.2	-2.0±-1.6
G044.0384-00.1203	II	0.21	N	2.9±1.0	2.0±2.3	-6.2±-5.1	-2.2±-1.8
G044.0405+00.0367	I	0.24	N	2.7±0.8	1.9±1.8	-5.1±-4.7	-1.8±-1.5
G044.0612+00.2287	I	0.92	Y	2.1±1.0	1.3±1.2	-5.0±-4.7	-2.3±-1.9
G044.0738+00.2972	I	0.38	Y	3.7±1.3	2.4±2.7	-4.9±-4.3	-1.9±-1.4
G044.0798+00.0307	I	0.13	Y	2.9±1.0	1.9±1.9	-4.8±-4.3	-1.8±-1.5
G044.0809+00.2654	I	0.04	Y	2.4±1.2	1.7±2.0	-5.1±-4.6	-1.9±-1.6
G044.0865+00.0862	II	0.12	N	2.1±1.0	1.4±1.6	-5.7±-5.2	-2.2±-1.8
G044.0964+00.1257	I	0.49	Y	3.5±1.0	2.2±2.4	-5.2±-4.5	-2.0±-1.5
G044.0976+00.0859	I	0.52	N	1.9±1.0	1.4±1.7	-5.6±-5.0	-2.1±-1.8
G044.1012+00.2308	I	0.01	Y	1.6±1.2	1.7±2.2	-4.6±-4.3	-1.7±-1.5
G044.1025-00.0754	II	0.19	N	2.7±1.1	1.8±2.1	-5.7±-5.3	-2.0±-1.7
G044.1039+00.2065	I	0.23	N	1.8±0.9	1.2±1.4	-5.6±-5.0	-2.3±-1.9
G044.1048+00.0722	I	0.36	Y	1.4±1.4	1.8±2.2	-5.0±-4.4	-1.9±-1.7
G044.1062+00.2294	I	0.13	Y	1.6±1.3	1.6±2.0	-5.1±-4.6	-2.0±-1.7
G044.1070+00.0689	II	0.05	N	3.5±1.0	2.3±2.5	-6.4±-5.5	-2.2±-1.7
G044.1087+00.1694	II	1.83	N	2.7±0.8	1.6±1.7	-5.8±-5.1	-2.1±-1.7
G044.1090+00.2448	II	0.06	N	3.0±0.7	2.0±1.9	-5.6±-4.6	-2.0±-1.6
G044.1105+00.0169	II	0.53	N	2.9±0.9	1.8±1.9	-5.9±-5.2	-2.1±-1.7
G044.1114+00.2527	II	0.22	Y	4.6±1.3	2.7±3.0	-5.7±-4.7	-2.0±-1.6
G044.1123+00.1704	I	1.30	N	2.7±1.4	2.1±2.2	-5.3±-4.6	-2.3±-1.9
G044.1124-00.0250	II	0.46	N	2.5±1.1	1.7±2.0	-5.6±-5.2	-2.1±-1.7
G044.1146+00.2107	I	0.04	N	1.0±1.0	1.2±1.7	-4.8±-4.5	-2.1±-1.8
G044.1200+00.2847	I	0.36	N	2.7±1.1	1.9±2.1	-5.3±-4.7	-1.9±-1.6
G044.1208+00.2609	I	0.44	N	2.0±1.0	1.4±1.6	-5.4±-4.8	-2.2±-1.8
G044.1352+00.1601	I	0.13	Y	5.3±2.5	3.1±3.3	-4.2±-3.6	-1.5±-1.2
G044.1443-00.0143	II	0.85	Y	6.0±1.2	3.1±3.2	-5.9±-4.7	-1.9±-1.6
G044.1492-00.1078	I	0.44	N	2.0±1.0	1.4±1.6	-5.6±-5.1	-2.2±-1.8

YSO	Stage[1]	$\left[\frac{\chi^2_{\rm best}}{n_{\rm data}}\right]$	24 μm?	$\log\left[\frac{M_*}{M_\odot}\right]$[2]	$\log\left[\frac{L_*}{L_\odot}\right]$	$\log\left[\frac{\dot{M_{\rm env}}}{M_\odot\ {\rm yr}^{-1}}\right]$[3]	$\log\left[\frac{M_{\rm disk}}{M_\odot}\right]$
G044.1495-00.0062	I	0.10	N	2.3±1.2	1.8±2.0	-5.4±-4.8	-2.0±-1.7
G044.1502-00.0132	II	0.57	N	3.4±0.7	2.2±2.1	0.0±0.0	-2.2±-1.7
G044.1510+00.1228	I	0.10	N	1.7±1.0	1.3±1.7	-5.5±-5.0	-2.3±-1.9
G044.1525-00.0462	I	0.44	N	1.6±1.2	1.5±1.9	-5.4±-5.0	-2.1±-1.8
G044.1589+00.1857	I	1.14	N	2.6±0.9	1.9±1.8	-5.3±-4.7	-2.2±-1.9
G044.1618+00.1951	II	0.05	N	3.0±1.1	2.0±2.3	-5.9±-5.5	-2.1±-1.7
G044.1635+00.1424	I	0.11	N	2.4±0.9	1.7±1.8	-5.5±-4.9	-2.2±-1.8
G044.1648-00.1874	I	0.18	Y	2.1±1.1	1.4±1.6	-5.2±-4.6	-2.0±-1.7
G044.1658+00.2363	I	0.01	N	0.9±1.0	1.3±1.7	-4.9±-4.5	-2.1±-1.8
G044.1675-00.0160	I	0.90	N	2.0±1.0	1.3±1.5	-5.5±-5.0	-2.2±-1.8
G044.1682-00.1194	I	1.57	N	1.6±1.0	1.2±1.6	-5.6±-5.1	-2.3±-1.9
G044.1683+00.3150	II	0.21	Y	4.8±1.4	2.8±3.1	-5.4±-4.4	-2.1±-1.6
G044.1687+00.1365	I	0.09	N	2.3±1.2	1.7±2.1	-5.2±-4.7	-2.0±-1.6
G044.1707+00.0022	II	0.12	N	3.5±0.8	2.2±2.2	-6.0±-5.2	-2.2±-1.6
G044.1707+00.0747	I	0.05	N	2.6±1.1	1.8±2.1	-5.5±-5.0	-2.0±-1.6
G044.1737+00.0046	I	0.05	Y	1.8±1.4	1.8±2.3	-4.5±-3.8	-1.7±-1.5
G044.1799-00.0471	II	0.81	N	4.2±1.3	2.6±3.2	-7.2±-6.6	-2.1±-1.6
G044.1827+00.3155	I	0.01	Y	1.9±1.5	1.8±2.1	-4.5±-4.1	-1.7±-1.3
G044.1877-00.0413	I	0.18	Y	1.3±1.1	1.5±2.1	-4.7±-3.8	-2.0±-1.6
G044.1889-00.1364	I	0.16	Y	1.9±1.1	1.4±1.7	-5.2±-4.7	-2.1±-1.7
G044.1901-00.0054	II	0.03	N	2.4±1.1	1.7±2.0	-5.7±-5.1	-2.1±-1.7
G044.1904+00.1207	I	0.80	Y	3.5±1.5	2.4±2.5	-4.7±-4.0	-2.1±-1.8
G044.1963+00.3353	I	0.16	Y	2.2±1.1	1.5±1.8	-5.2±-4.6	-2.0±-1.7
G044.1981+00.1411	I	0.07	Y	3.3±1.2	2.1±2.4	-4.8±-4.2	-1.8±-1.5
G044.2055-00.0681	II	0.09	N	3.2±1.1	2.1±2.2	-6.0±-5.2	-2.1±-1.6
G044.2084+00.3072	I	0.11	N	2.0±1.1	1.4±1.7	-5.5±-5.1	-2.1±-1.8
G044.2124-00.0023	II	0.43	N	3.5±0.9	2.2±2.3	-6.8±-5.8	-2.3±-1.8
G044.2174+00.1409	I	0.30	N	2.5±1.0	1.6±1.8	-5.5±-5.1	-2.1±-1.7
G044.2268+00.1381	I	0.10	Y	3.3±1.3	2.2±2.5	-4.8±-4.2	-1.8±-1.5
G044.2283+00.0528	I	1.11	Y	5.1±2.0	3.0±3.2	-4.0±-3.5	-1.7±-1.3
G044.2291+00.2043	I	1.60	Y	2.5±1.1	1.5±1.6	-4.7±-4.4	-1.9±-1.6
G044.2304+00.1245	I	0.15	Y	2.7±1.1	1.9±2.0	-5.3±-4.7	-1.9±-1.6
G044.2311+00.1384	I	0.23	Y	3.7±1.1	2.3±2.5	-5.3±-4.5	-1.9±-1.5
G044.2313-00.1197	I	0.30	Y	3.8±1.2	2.4±2.6	-5.1±-4.3	-2.0±-1.5
G044.2324+00.1491	II	1.23	N	2.9±0.8	1.8±1.8	-5.8±-5.2	-2.2±-1.7
G044.2356+00.3039	I	1.36	Y	2.2±1.1	1.3±1.3	-5.1±-4.7	-2.1±-1.7
G044.2360+00.1544	I	1.28	Y	4.1±1.7	2.6±3.0	-4.7±-4.1	-1.6±-1.4

YSO	Stage[1]	$\left[\frac{\chi^2_{\rm best}}{n_{\rm data}}\right]$	24 μm?	$\log\left[\frac{M_*}{M_\odot}\right]$[2]	$\log\left[\frac{L_*}{L_\odot}\right]$	$\log\left[\frac{\dot{M_{\rm env}}}{M_\odot\ {\rm yr}^{-1}}\right]$[3]	$\log\left[\frac{M_{\rm disk}}{M_\odot}\right]$
G044.2435-00.1291	I	0.11	Y	5.1±1.5	2.6±2.8	-3.9±-3.5	-1.3±-1.0
G044.2565+00.1257	I	0.01	N	2.8±1.0	1.9±2.1	-5.1±-4.5	-2.0±-1.7
G044.2614+00.0458	I	2.49	Y	4.3±1.0	2.6±2.7	-5.3±-4.3	-2.1±-1.7
G044.2627+00.0365	I	0.03	Y	2.2±1.2	1.8±2.1	-4.9±-4.5	-1.8±-1.6
G044.2643-00.1449	I	0.28	Y	3.0±1.0	1.9±2.2	-5.3±-4.6	-1.9±-1.6
G044.2767+00.0120	I	0.34	Y	1.7±1.1	1.3±1.5	-4.9±-4.5	-2.3±-2.0
G044.2820-00.0941	I	0.16	Y	3.1±1.1	2.0±2.2	-4.9±-4.3	-1.8±-1.5
G044.2828-00.0822	I	1.75	Y	2.8±1.1	1.7±1.8	-4.9±-4.5	-1.8±-1.5
G044.2845+00.0153	I	0.85	Y	3.3±1.1	1.9±2.1	-4.9±-4.4	-1.8±-1.5
G044.2887-00.1376	I	1.55	Y	1.6±1.2	1.5±1.9	-4.8±-4.5	-1.9±-1.6
G044.2906+00.0339	I	2.23	Y	4.0±1.7	2.2±2.2	-4.1±-3.8	-1.2±-1.1
G044.2920-00.1829	I	1.29	N	1.7±1.0	1.3±1.7	-5.5±-5.0	-2.2±-1.8
G044.2939+00.0280	I	0.18	N	1.8±1.1	1.6±1.7	-4.8±-4.5	-1.9±-1.6
G044.2945-00.2496	I	0.03	N	2.2±1.1	1.6±1.9	-5.6±-5.1	-2.1±-1.7
G044.2957+00.2187	I	1.38	N	2.6±0.9	1.8±1.9	-5.1±-4.6	-2.1±-1.8
G044.2962-00.0763	II	0.04	N	3.5±0.7	2.1±2.1	-6.1±-5.3	-2.2±-1.6
G044.2964-00.1255	II	0.08	N	2.0±0.9	1.3±1.6	-5.7±-5.1	-2.2±-1.8
G044.2979-00.0762	II	0.79	Y	4.1±0.8	2.4±2.5	-5.9±-4.8	-2.0±-1.6
G044.3038+00.0518	I	2.90	N	3.1±0.8	1.8±1.6	-4.8±-4.5	-1.9±-1.5
G044.3102+00.0410	I	0.28	Y	7.5±1.8	3.2±3.2	-3.7±-3.3	-1.0±-0.8
G044.3111+00.0282	I	0.57	Y	2.5±1.3	2.1±2.0	-4.1±-4.1	-1.3±-1.2
G044.3155+00.1392	I	1.99	N	1.9±1.0	1.3±1.6	-5.6±-5.1	-2.2±-1.8
G044.3217-00.1019	II	0.79	N	3.5±0.7	2.1±2.1	-6.5±-5.3	-2.3±-1.7
G044.3225+00.0398	I	0.31	N	0.6±0.2	1.2±0.8	-3.9±-4.1	-1.5±-1.5
G044.3260-00.0125	II	0.22	N	3.6±0.8	2.2±2.3	-6.8±-6.2	-2.2±-1.7
G044.3293-00.0814	II	1.73	N	2.9±1.0	1.9±2.1	-6.0±-5.3	-2.2±-1.8
G044.3306+00.1283	I	0.47	Y	1.3±1.3	1.6±2.0	-5.3±-4.9	-2.0±-1.8
G044.3390+00.2760	II	0.70	N	2.6±0.8	1.8±1.8	-6.3±-5.5	-2.3±-1.9
G044.3469-00.0435	II	0.26	N	3.0±0.9	1.9±2.1	-5.8±-5.1	-2.0±-1.7
G044.3514+00.3233	I	0.44	N	1.3±1.4	1.6±1.9	-5.3±-4.6	-2.2±-2.0
G044.3519+00.1663	II	0.63	N	2.5±0.7	1.7±1.7	-5.9±-5.0	-2.1±-1.8
G044.3597+00.1712	I	0.72	Y	1.9±1.8	2.2±2.6	-4.9±-4.4	-1.6±-1.4
G044.3614-00.1838	II	0.52	N	2.9±0.6	1.9±1.8	-5.9±-4.9	-2.6±-2.1
G044.3740+00.1572	II	1.88	N	2.0±1.0	1.4±1.7	-5.7±-5.2	-2.2±-1.8
G044.3815+00.3038	I	0.53	Y	2.0±1.1	1.5±1.7	-5.0±-4.6	-2.0±-1.7
G044.3855-00.0638	I	0.14	N	1.7±1.0	1.2±1.4	-5.5±-5.0	-2.3±-1.9
G044.3894-00.0715	I	1.86	Y	2.6±0.9	1.5±1.2	-4.8±-4.4	-2.2±-2.0

YSO	Stage[1]	$\left[\frac{\chi^2_{\rm best}}{n_{\rm data}}\right]$	24 μm?	$\log\left[\frac{M_*}{M_\odot}\right]$[2]	$\log\left[\frac{L_*}{L_\odot}\right]$	$\log\left[\frac{\dot{M_{\rm env}}}{M_\odot\ {\rm yr}^{-1}}\right]$[3]	$\log\left[\frac{M_{\rm disk}}{M_\odot}\right]$
G044.3907-00.2170	I	1.15	Y	3.0±1.1	1.8±1.9	-4.8±-4.4	-1.7±-1.4
G044.3937-00.1398	I	0.68	Y	3.9±0.7	1.9±1.8	-4.9±-4.3	-1.7±-1.4
G044.3956-00.1457	I	0.02	Y	2.0±1.3	1.7±2.0	-5.0±-4.5	-1.9±-1.6
G044.3979-00.0019	I	0.54	Y	3.2±1.8	2.4±2.6	-4.7±-4.1	-1.9±-1.6
G044.4023-00.0334	II	0.32	N	3.6±0.7	2.2±2.1	-7.0±-6.1	-2.3±-1.8
G044.4044+00.0073	II	0.01	N	3.2±1.0	2.2±2.4	-6.7±-6.1	-2.3±-1.8
G044.4074+00.1143	I	0.83	N	3.1±0.9	2.1±1.9	-5.4±-5.0	-2.5±-2.0
G044.4076+00.1168	I	0.03	N	1.6±1.0	1.3±1.6	-5.4±-5.0	-2.1±-1.8
G044.4080+00.3230	I	0.06	N	1.8±1.1	1.4±1.8	-5.5±-5.0	-2.2±-1.8
G044.4132+00.0989	I	1.42	Y	3.0±0.9	1.9±1.8	-4.9±-4.3	-1.8±-1.5
G044.4156-00.2563	II	0.81	N	1.9±1.0	1.3±1.6	-5.7±-5.2	-2.2±-1.8
G044.4164+00.0950	I	1.84	Y	4.2±1.9	2.7±2.9	-4.3±-3.6	-1.8±-1.4
G044.4195+00.0180	I	0.03	N	1.2±1.3	1.6±2.0	-5.5±-5.6	-1.9±-1.8
G044.4235-00.2013	I	0.07	Y	2.6±1.1	1.8±2.1	-5.1±-4.5	-2.0±-1.6
G044.4254-00.1036	I	0.18	Y	2.2±1.3	1.7±2.1	-4.7±-4.3	-1.8±-1.5
G044.4262+00.3348	II	0.36	N	2.2±0.9	1.4±1.7	-5.9±-5.4	-2.3±-1.8
G044.4285-00.1532	II	0.37	N	2.8±0.9	1.7±1.8	-5.9±-5.4	-2.1±-1.7
G044.4295+00.0964	II	0.03	N	2.4±1.1	1.7±2.0	-5.7±-5.3	-2.1±-1.7
G044.4395+00.0282	I	0.07	Y	3.6±1.4	2.3±2.6	-4.9±-4.3	-1.7±-1.4
G044.4565-00.2569	I	0.38	N	1.8±1.2	1.5±1.9	-5.6±-5.1	-2.1±-1.8
G044.4606-00.0667	I	0.06	Y	4.2±1.3	2.6±2.9	-5.0±-4.2	-1.9±-1.5
G044.4710+00.0567	I	0.67	Y	3.9±1.3	2.5±2.8	-4.9±-4.2	-1.9±-1.5
G044.4715-00.1034	I	0.07	N	2.3±0.8	1.6±1.8	-5.5±-4.8	-2.0±-1.8
G044.4733+00.3238	I	0.18	Y	2.7±1.8	2.3±2.6	-4.9±-4.3	-1.8±-1.6
G044.4739-00.1259	I	0.59	N	2.2±0.9	1.6±1.8	-5.0±-4.6	-1.9±-1.7
G044.4761-00.1249	II	0.18	N	2.9±0.9	1.9±2.1	-6.0±-5.3	-2.1±-1.7
G044.4790+00.0670	I	0.94	Y	2.8±1.4	2.2±2.4	-4.8±-4.2	-2.0±-1.6
G044.4892-00.1523	I	0.36	Y	2.3±1.3	1.8±2.1	-4.7±-4.2	-1.7±-1.5
G044.4910-00.1501	I	0.83	Y	4.9±1.4	2.8±3.0	-5.0±-4.1	-1.9±-1.5
G044.4918-00.1436	II	1.49	N	3.1±0.7	2.0±2.2	-6.1±-5.1	-2.4±-2.0
G044.5012-00.0899	I	0.03	Y	3.8±1.9	2.6±2.8	-4.6±-4.0	-1.7±-1.5
G044.5481-00.2227	I	0.02	N	1.9±1.1	1.6±1.9	-5.3±-4.7	-2.1±-1.8
G044.5598-00.2132	II	1.51	N	3.6±0.7	2.2±2.1	-7.3±-6.6	-2.3±-1.7
G044.5780-00.1323	I	0.03	N	2.2±1.1	1.5±1.7	-5.3±-4.9	-2.1±-1.7
G044.5964-00.0450	II	0.15	Y	4.8±1.1	2.7±2.9	-6.0±-4.6	-1.9±-1.6
G044.5972-00.0465	II	0.02	N	3.6±0.9	2.3±2.4	-5.8±-4.8	-2.2±-1.8
M044.0412+00.1991	I	0.28	Y	1.7±1.6	1.9±2.3	-4.9±-4.3	-2.0±-1.8

YSO	Stage[1]	$\left[\frac{\chi^2_{\rm best}}{n_{\rm data}}\right]$	24 μm?	$\log\left[\frac{M_*}{M_\odot}\right]$[2]	$\log\left[\frac{L_*}{L_\odot}\right]$	$\log\left[\frac{\dot{M_{\rm env}}}{M_\odot\ {\rm yr}^{-1}}\right]$[3]	$\log\left[\frac{M_{\rm disk}}{M_\odot}\right]$
M044.1425-00.0221	I	1.33	Y	3.0±1.3	2.2±2.4	-4.8±-4.3	-2.2±-1.8
M044.2117-00.0619	I	0.23	Y	3.1±1.1	2.0±2.2	-5.0±-4.5	-1.9±-1.5
M044.2187+00.0270	I	0.64	Y	3.5±2.3	2.6±2.8	-4.4±-4.0	-1.8±-1.5
M044.2203-00.0607	I	1.01	Y	3.0±1.7	2.2±2.5	-4.7±-4.1	-1.8±-1.5
M044.2248+00.1803	I	1.50	Y	1.6±1.2	1.5±1.9	-4.7±-4.4	-1.8±-1.6
M044.2250+00.3022	I	0.26	Y	1.6±1.2	1.4±1.9	-4.8±-3.9	-2.2±-1.8
M044.2437+00.0278	I	1.34	Y	2.8±1.5	2.1±2.4	-4.6±-4.1	-1.7±-1.5
M044.2488-00.1309	I	1.03	N	4.0±1.0	2.3±2.3	-4.6±-4.1	-1.9±-1.4
M044.2728+00.0507	I	0.38	Y	2.0±1.3	1.8±2.1	-4.3±-3.8	-1.8±-1.5
M044.2741+00.1080	I	2.05	N	5.3±1.3	2.9±3.0	-5.2±-4.7	-1.8±-1.3
M044.2896+00.0525	I	0.57	Y	1.6±1.2	1.8±2.2	-4.3±-4.0	-1.6±-1.5
M044.2938-00.1577	I	0.14	Y	2.5±1.5	2.0±2.2	-4.2±-3.9	-1.8±-1.5
M044.2997+00.0594	II	2.68	N	4.8±1.1	2.7±2.7	-6.6±-5.8	-2.4±-1.8
M044.3192-00.2035	I	0.01	Y	0.7±0.8	0.8±1.6	-4.9±-4.0	-2.3±-1.8
M044.3223-00.2178	I	0.26	Y	2.1±1.2	1.6±1.9	-4.8±-4.4	-1.9±-1.6
M044.3473+00.0862	I	0.54	Y	1.8±1.3	1.7±2.0	-4.4±-4.0	-1.9±-1.6
M044.3835+00.2162	I	0.61	Y	2.2±1.2	1.7±2.0	-5.2±-4.6	-2.1±-1.7
M044.4261-00.1467	I	0.20	Y	2.2±1.5	1.9±2.2	-5.0±-4.4	-2.0±-1.7
M044.4586+00.0536	I	0.69	Y	2.6±1.4	2.0±2.3	-4.7±-4.1	-1.8±-1.5
M044.5243-00.2384	I	1.94	Y	1.9±1.6	2.0±2.3	-4.6±-4.2	-1.9±-1.7
M044.5309-00.1142	I	0.55	Y	2.4±1.2	1.7±1.9	-4.8±-4.4	-1.8±-1.5
M044.5767-00.2183	I	0.72	Y	1.7±1.4	1.8±2.2	-4.6±-4.2	-1.9±-1.6
				G044.34-0.82			
G044.2020-00.7828	I	1.62	Y	1.5±1.8	2.0±2.3	-4.7±-4.0	-2.0±-1.9
G044.2039-00.7794	I	0.20	N	2.1±1.1	1.5±1.7	-5.6±-5.1	-2.1±-1.8
G044.2176-00.8876	II	1.95	N	2.6±0.9	1.6±1.7	-5.8±-5.3	-2.2±-1.8
G044.2198-00.7454	II	0.20	Y	3.9±0.8	2.4±2.5	-6.1±-4.8	-2.0±-1.6
G044.2304-00.8282	I	1.77	Y	2.1±1.4	1.8±2.1	-4.7±-4.0	-2.0±-1.6
G044.2360-00.8404	I	0.03	Y	1.9±1.3	1.8±2.1	-4.9±-4.6	-1.7±-1.5
G044.2364-00.8392	I	0.05	Y	2.0±0.9	1.5±1.3	-4.6±-4.8	-1.7±-1.5
G044.2781-00.7849	II	0.07	N	2.7±0.9	1.7±1.8	-5.9±-5.3	-2.1±-1.7
G044.2801-00.7782	II	0.01	N	3.2±0.8	2.0±2.2	-6.4±-5.4	-2.2±-1.7
G044.3007-00.7681	I	0.05	Y	4.2±0.8	2.4±2.5	-5.3±-4.5	-1.9±-1.5
G044.3017-00.8180	I	1.46	N	3.9±1.2	2.5±3.0	-5.0±-4.4	-2.1±-1.6
G044.3080-00.9397	I	0.08	Y	1.1±0.9	1.3±1.6	-4.6±-4.4	-1.9±-1.7
G044.3129-00.8567	I	0.38	N	2.5±1.5	2.1±2.8	-5.5±-5.0	-2.1±-1.7
G044.3245-00.8201	I	0.87	N	4.2±1.0	2.4±2.3	-5.1±-4.9	-1.3±-1.2

YSO	Stage[1]	$\left[\frac{\chi^2_{\rm best}}{n_{\rm data}}\right]$	24 μm?	$\log\left[\frac{M_*}{M_\odot}\right]$[2]	$\log\left[\frac{L_*}{L_\odot}\right]$	$\log\left[\frac{\dot{M_{\rm env}}}{M_\odot\ {\rm yr}^{-1}}\right]$[3]	$\log\left[\frac{M_{\rm disk}}{M_\odot}\right]$
G044.3351-00.8243	I	0.91	Y	3.0±1.9	2.4±2.6	-4.7±-3.9	-1.5±-1.3
G044.3446-00.8155	II	1.31	Y	4.7±1.6	2.8±3.0	-6.1±-4.7	-1.9±-1.5
G044.3450-00.7219	II	0.15	N	3.4±0.9	2.1±2.2	-6.5±-6.0	-2.2±-1.7
G044.3677-00.7947	I	0.23	N	2.1±0.9	1.5±1.6	-5.0±-4.7	-2.0±-1.7
G044.3700-00.7479	II	0.10	N	2.3±1.1	1.6±1.8	-5.7±-5.3	-2.1±-1.7
G044.3713-00.8245	I	0.05	N	2.0±1.1	1.5±1.7	-5.1±-4.6	-2.1±-1.7
G044.3764-00.7726	II	0.10	N	2.5±1.0	1.7±1.8	-5.8±-5.2	-2.0±-1.7
G044.3868-00.8891	I	0.04	N	1.9±1.0	1.4±1.7	-5.5±-5.0	-2.1±-1.8
G044.3962-00.7668	I	1.42	Y	5.4±1.8	3.0±3.2	-5.2±-4.3	-1.7±-1.5
G044.4011-00.7711	I	0.04	N	1.9±1.0	1.4±1.7	-5.2±-4.7	-2.1±-1.8
G044.4031-00.7587	I	1.36	Y	2.6±1.6	2.2±2.5	-4.8±-4.3	-1.8±-1.5
G044.4585-00.8751	II	0.04	N	2.4±1.1	1.6±1.9	-5.8±-5.3	-2.1±-1.7
M044.2451-00.8082	I	1.64	N	1.2±0.8	0.7±1.1	-5.9±-5.3	-2.6±-2.2
M044.3341-00.8174	II	0.08	N	4.6±1.4	2.8±3.0	-5.6±-4.5	-2.0±-1.6
M044.3358-00.8221	I	1.42	Y	3.9±1.5	2.3±2.5	-4.0±-3.7	-1.6±-1.3
M044.3397-00.8165	I	0.39	N	3.3±1.4	2.3±2.6	-5.4±-4.8	-2.0±-1.6
M044.3418-00.8073	I	1.98	Y	5.0±0.8	2.6±2.5	-4.6±-4.0	-1.8±-1.4
M044.3526-00.8261	I	0.34	N	3.5±1.0	2.2±2.3	-5.0±-4.4	-1.9±-1.5
M044.3608-00.8227	II	1.27	N	5.1±1.2	2.9±3.1	-5.8±-5.1	-2.0±-1.5
M044.3987-00.7884	I	0.23	Y	2.0±1.2	1.5±1.9	-5.1±-4.5	-2.1±-1.7
M044.4380-00.9562	I	0.17	Y	2.8±1.0	1.9±2.2	-5.4±-4.8	-2.0±-1.6

[1]See §2.2.2 for explanation of evolutionary stages.

[2]Values for all quantities are determined by the parameters of model SEDs that fit the source such that $\left(\chi^2 - \chi^2_{\rm best}\right)/n_{\rm data} < 6$. Averages and uncertainties are the mean and standard deviation values of the fit parameters weighted by the probability of the corresponding model, $\exp\left(-\chi^2/2\right)$ (See §2.2.2). Uncertainties of 0.0 indicate no spread in the models that fit the data.

[3]The data are sometimes fit by disk-only models with no accreting envelope, represented by a value of 0.0.

Appendix B

Molecular Gas Clump Parameters Around H II Regions

Table B.1:: Molecular Gas Clump Parameters

$\ell_{\rm peak}$ (deg)	$b_{\rm peak}$ (deg)	$v_{\rm peak}$ (km s^{-1})	$R_{\rm cl}$[1] (pc)	$\sigma_{\rm cl}$ (km s^{-1})	$d_{\rm cl}$[2] (pc)	$N_{\rm cl}(H_2)$[3] (10^{21} cm^{-2})	$n_{\rm cl}(H_2)$ (cm^{-3})	$M_{\rm cl}(H_2)$ ($M_\odot$)	$\alpha_{\rm vir}$[4]
G028.83-0.25 (83.8-90.0 km s^{-1})									
28.850	-0.24	88.26	4.3	1.9	1.7	18.7	274	6103	0.5
28.844	-0.21	85.93	3.3	1.6	3.2	11.0	228	2311	0.8
28.887	-0.20	85.93	3.1	1.2	1.6	5.4	108	899	1.1
28.887	-0.22	87.41	3.5	1.0	1.1	7.1	121	1518	0.5
28.868	-0.24	86.14	2.7	1.5	1.7	7.4	298	1671	0.9
28.887	-0.23	85.93	2.1	1.2	1.1	5.2	233	625	1.0
28.887	-0.26	85.93	2.9	1.6	2.1	6.5	141	1010	1.8
28.795	-0.23	86.14	3.7	2.0	4.5	4.8	99	1478	2.1
28.868	-0.30	87.20	3.9	1.8	4.0	3.9	97	1645	2.0
G028.83-0.25 (91.9-98.8 km s^{-1})									
28.930	-0.22	95.63	3.4	3.0	4.3	21.8	684	7668	1.0
28.850	-0.23	96.48	4.3	2.7	1.1	18.4	378	8899	0.8
28.893	-0.30	94.78	3.4	1.2	6.7	3.7	116	1328	0.8
28.893	-0.16	96.48	4.0	1.4	1.8	5.7	152	2822	0.6
28.819	-0.32	95.20	3.1	2.0	1.8	5.2	169	1408	2.1
28.819	-0.29	95.41	2.4	0.7	1.8	2.7	110	468	0.5
28.850	-0.16	97.96	3.3	1.2	1.3	3.6	112	1208	0.7
28.801	-0.13	96.69	2.9	1.4	5.2	4.8	173	1194	1.1
28.825	-0.27	96.05	3.0	1.5	1.8	4.5	155	1210	1.1
28.875	-0.15	97.54	2.8	1.0	1.8	2.3	100	637	0.9
28.838	-0.17	98.60	3.4	0.8	1.3	2.5	84	957	0.4
28.801	-0.31	94.99	2.2	1.2	1.8	2.8	133	426	1.5
28.776	-0.24	96.69	2.8	0.8	3.8	2.3	59	391	0.9
28.825	-0.24	98.81	3.6	0.7	1.3	1.3	37	506	0.5
28.795	-0.28	94.99	2.0	0.9	2.5	2.0	105	236	1.5
28.912	-0.18	94.35	2.9	1.6	2.4	2.3	83	562	2.7

$\ell_{\rm peak}$ (deg)	$b_{\rm peak}$ (deg)	$v_{\rm peak}$ (km s^{-1})	$R_{\rm cl}$[1] (pc)	$\sigma_{\rm cl}$ (km s^{-1})	$d_{\rm cl}$[2] (pc)	$N_{\rm cl}(H_2)$[3] (10^{21} cm^{-2})	$n_{\rm cl}(H_2)$ (cm^{-3})	$M_{\rm cl}(H_2)$ ($M_\odot$)	$\alpha_{\rm vir}$[4]
28.838	-0.23	92.44	4.3	1.0	1.1	2.3	52	1207	0.7
G041.10-0.15									
41.128	-0.22	60.34	2.4	1.4	1.0	11.5	364	1514	0.7
41.140	-0.20	60.98	2.4	1.3	1.5	9.7	214	863	0.9
41.035	-0.23	60.76	1.9	1.5	1.5	11.0	187	391	2.5
41.085	-0.12	63.95	2.1	1.5	0.0	11.2	269	773	1.2
41.134	-0.23	58.64	2.7	1.1	0.9	7.3	199	1122	0.5
41.054	-0.25	60.13	2.2	1.5	0.4	8.1	309	908	1.2
41.165	-0.17	59.91	2.1	1.4	1.4	7.2	260	747	1.4
41.103	-0.23	59.28	2.5	2.2	1.9	10.8	190	848	2.7
41.171	-0.19	61.83	2.6	1.2	1.2	5.2	157	794	0.9
41.189	-0.22	58.00	2.6	1.1	0.9	4.9	164	794	0.8
41.048	-0.25	65.65	2.3	1.1	0.4	5.6	225	774	0.8
41.066	-0.24	65.44	2.1	1.2	1.0	4.7	158	422	1.8
41.202	-0.22	58.85	1.6	0.7	0.9	3.2	184	226	0.6
41.042	-0.26	64.80	2.3	1.1	1.0	3.6	147	506	1.2
41.085	-0.12	65.23	1.8	0.8	0.0	2.7	124	212	1.2
41.066	-0.10	62.68	1.8	1.0	0.6	3.2	107	189	1.8
41.183	-0.20	59.28	1.8	1.4	1.0	5.8	354	591	1.4
41.128	-0.25	56.51	2.6	1.7	1.0	6.8	125	643	2.6
41.134	-0.16	62.68	1.9	1.3	1.8	4.3	178	349	1.9
41.208	-0.20	60.13	1.8	0.8	1.0	3.0	164	289	0.7
41.189	-0.19	59.49	1.4	1.1	1.3	4.0	249	201	2.0
41.060	-0.09	61.83	1.7	0.6	0.0	2.2	73	112	1.3
41.097	-0.12	65.44	2.2	1.6	0.9	4.5	136	437	2.8
41.214	-0.11	65.65	1.5	1.2	1.5	3.3	200	200	2.2
41.165	-0.12	63.31	2.0	1.1	0.6	3.2	111	249	1.9
41.115	-0.13	64.16	2.1	1.0	0.9	2.6	114	327	1.2

$\ell_{\rm peak}$ (deg)	$b_{\rm peak}$ (deg)	$v_{\rm peak}$ (km s^{-1})	$R_{\rm cl}$[1] (pc)	$\sigma_{\rm cl}$ (km s^{-1})	$d_{\rm cl}$[2] (pc)	$N_{\rm cl}(H_2)$[3] (10^{21} cm^{-2})	$n_{\rm cl}(H_2)$ (cm^{-3})	$M_{\rm cl}(H_2)$ ($M_\odot$)	$\alpha_{\rm vir}$[4]
40.992	-0.25	65.44	1.8	1.1	1.3	2.6	137	229	2.2
40.992	-0.27	65.23	1.5	1.4	1.3	2.8	194	186	3.9
41.183	-0.29	60.13	1.7	1.5	1.8	3.2	190	275	3.5
41.183	-0.11	62.89	1.9	1.2	1.5	2.7	126	264	2.3
41.005	-0.23	66.08	2.1	1.0	1.5	2.2	86	230	1.7
41.054	-0.21	66.50	2.5	1.3	1.8	3.3	102	451	1.8
40.974	-0.27	65.23	1.5	0.9	1.3	2.3	154	165	1.9
41.060	-0.09	60.76	1.6	1.1	0.0	2.4	76	88	4.6
41.183	-0.15	54.60	1.8	0.7	1.2	1.5	59	96	1.8
41.115	-0.14	62.89	1.6	0.8	0.9	2.1	103	127	1.4
41.079	-0.25	57.58	1.9	1.0	1.0	1.6	76	163	2.4
40.992	-0.21	64.80	1.6	1.0	1.5	2.3	65	78	4.0
41.158	-0.13	65.23	1.6	1.0	0.6	1.7	129	149	2.2
41.195	-0.14	59.49	1.9	1.6	0.6	2.2	119	249	4.3
41.214	-0.24	60.98	1.4	0.9	0.9	1.8	134	114	2.1
41.214	-0.23	62.04	1.6	0.7	0.9	1.3	103	133	1.1
41.189	-0.26	59.91	2.1	1.3	0.4	2.0	106	277	2.9
41.208	-0.15	60.98	1.8	0.8	0.6	1.2	61	104	1.7
41.146	-0.24	62.25	2.1	1.0	0.4	2.1	82	230	1.7
41.085	-0.19	59.49	1.4	1.0	2.2	1.6	66	56	5.1
41.177	-0.27	60.76	1.9	0.7	1.0	1.4	71	149	1.2
41.048	-0.29	58.21	1.6	1.1	2.2	1.9	120	139	3.2
41.214	-0.14	65.23	1.6	1.0	0.6	1.7	95	106	2.8
41.208	-0.19	60.98	1.5	1.0	1.3	2.0	159	141	2.0
41.189	-0.14	66.71	1.7	1.1	0.6	1.8	90	123	3.4
41.091	-0.14	62.25	1.5	1.1	1.2	1.7	117	116	2.9
41.146	-0.23	63.10	2.1	0.6	0.4	1.3	60	157	1.0
40.992	-0.17	67.99	1.8	0.8	3.0	1.4	53	96	2.4
41.054	-0.17	65.44	1.7	1.2	1.9	1.3	43	62	8.0

$\ell_{\rm peak}$ (deg)	$b_{\rm peak}$ (deg)	$v_{\rm peak}$ (km s^{-1})	$R_{\rm cl}$[1] (pc)	$\sigma_{\rm cl}$ (km s^{-1})	$d_{\rm cl}$[2] (pc)	$N_{\rm cl}(H_2)$[3] (10^{21} cm^{-2})	$n_{\rm cl}(H_2)$ (cm^{-3})	$M_{\rm cl}(H_2)$ ($M_\odot$)	$\alpha_{\rm vir}$[4]
41.189	-0.25	60.98	1.2	0.7	0.4	0.7	84	40	2.9
41.085	-0.28	65.65	1.2	1.3	1.0	1.7	85	46	8.9
41.122	-0.21	64.80	2.0	1.6	1.0	2.0	84	201	5.9
41.202	-0.12	64.38	1.8	0.9	1.2	1.1	60	105	2.7
41.079	-0.15	61.83	1.6	1.1	1.2	1.8	86	96	3.9
41.183	-0.23	62.89	1.3	0.9	1.0	0.9	84	51	4.0
41.091	-0.27	55.88	1.8	1.6	1.0	2.8	72	113	9.0
G041.91-0.12									
41.851	-0.09	18.80	1.0	1.3	0.7	7.1	372	92	4.4
41.869	-0.12	16.89	0.6	1.7	0.4	4.8	578	38	10.6
41.882	-0.13	14.55	0.6	1.1	0.4	3.4	315	17	8.7
41.839	-0.12	17.53	0.5	0.9	0.7	1.7	295	12	7.6
41.888	-0.15	14.55	0.5	1.0	0.5	1.4	159	6	16.2
41.851	-0.14	16.89	0.5	1.4	0.7	1.4	226	8	23.1
G041.92+0.04									
41.825	0.05	16.46	0.6	1.2	0.6	3.6	584	30	5.0
41.832	0.03	15.83	0.6	1.0	0.2	3.1	321	22	6.2
41.838	0.02	14.76	0.7	0.7	0.2	2.3	182	19	3.6
41.936	0.08	19.44	0.7	1.1	0.5	2.3	256	20	8.4
41.961	-0.00	17.53	0.7	1.1	0.3	2.5	292	27	6.1
41.955	-0.01	16.89	0.7	1.2	0.3	1.9	216	19	10.7
41.924	0.05	16.25	0.6	1.5	0.8	2.8	317	17	15.7
41.924	0.10	17.95	0.7	1.3	0.5	3.3	301	36	7.1
41.899	0.10	16.25	0.6	1.3	0.1	2.3	343	27	9.3
41.936	0.01	16.46	0.8	1.6	0.3	2.1	159	23	19.3
41.967	0.02	19.65	0.7	1.1	0.3	1.6	191	20	8.4
41.850	0.03	17.31	0.8	0.6	0.3	1.1	165	27	2.7
41.899	0.11	17.10	0.6	0.7	0.1	1.5	271	15	3.6

$\ell_{\rm peak}$ (deg)	$b_{\rm peak}$ (deg)	$v_{\rm peak}$ (km s^{-1})	$R_{\rm cl}$[1] (pc)	$\sigma_{\rm cl}$ (km s^{-1})	$d_{\rm cl}$[2] (pc)	$N_{\rm cl}(H_2)$[3] (10^{21} cm^{-2})	$n_{\rm cl}(H_2)$ (cm^{-3})	$M_{\rm cl}(H_2)$ ($M_\odot$)	$\alpha_{\rm vir}$[4]
41.948	0.00	17.74	0.7	0.9	0.3	1.7	177	14	7.1
41.967	0.03	19.01	0.6	0.8	0.3	1.2	194	10	7.0
41.856	0.01	16.46	0.7	1.1	0.4	2.1	268	22	7.0
G044.28+0.11									
43.999	-0.01	64.74	2.1	1.9	2.7	15.9	450	1235	1.4
44.306	0.04	56.88	3.2	2.4	2.4	16.2	334	3286	1.4
44.109	0.15	55.18	2.2	1.8	2.3	9.7	400	1173	1.4
44.275	0.04	56.88	2.7	2.0	1.7	9.7	260	1525	1.3
44.128	-0.01	59.43	2.2	1.5	1.3	6.2	218	712	1.7
44.245	0.15	58.15	2.8	1.2	1.5	5.9	186	1123	0.7
44.134	0.08	61.98	2.4	2.0	2.7	5.8	177	703	2.8
44.042	-0.02	66.23	1.7	1.0	1.3	3.2	165	219	1.6
44.029	-0.03	66.86	1.7	0.8	1.3	2.9	163	233	0.9
44.226	0.15	59.43	2.7	0.9	1.5	3.5	96	558	0.8
44.116	0.21	54.54	2.4	1.5	0.5	4.3	138	527	1.9
44.165	0.10	59.21	3.1	1.6	2.7	4.2	93	846	1.9
44.263	0.02	65.16	2.1	0.9	1.7	2.5	124	331	1.1
44.048	0.04	57.73	2.5	1.2	1.4	3.8	125	539	1.5
44.189	-0.01	58.79	2.8	1.1	1.5	4.0	89	564	1.4
44.177	0.19	59.43	3.0	1.9	3.4	4.9	134	1056	2.6
44.066	0.14	58.36	2.8	1.4	0.9	3.9	126	763	1.6
44.245	0.01	66.01	2.1	1.6	1.7	5.3	149	408	2.9
44.066	0.05	58.79	2.7	0.6	0.5	2.1	65	389	0.5
44.066	0.04	60.91	2.6	1.1	0.0	3.1	104	520	1.3
44.269	0.18	57.30	2.6	1.0	3.4	3.5	122	603	1.0
44.085	0.09	58.15	2.3	1.9	3.1	4.7	118	427	4.7
44.066	0.06	60.06	2.8	0.8	0.5	2.1	70	423	0.9
44.312	-0.02	65.38	3.0	1.6	4.2	4.6	129	1011	1.6

$\ell_{\rm peak}$ (deg)	$b_{\rm peak}$ (deg)	$v_{\rm peak}$ (km s^{-1})	$R_{\rm cl}$[1] (pc)	$\sigma_{\rm cl}$ (km s^{-1})	$d_{\rm cl}$[2] (pc)	$N_{\rm cl}(H_2)$[3] (10^{21} cm^{-2})	$n_{\rm cl}(H_2)$ (cm^{-3})	$M_{\rm cl}(H_2)$ ($M_\odot$)	$\alpha_{\rm vir}$[4]
44.066	0.04	59.64	2.2	0.7	0.0	2.0	96	308	0.6
44.066	0.13	59.21	3.1	0.9	0.9	2.7	66	566	0.9
44.275	0.07	58.79	3.1	1.4	1.9	4.5	98	878	1.4
44.146	-0.01	63.46	2.2	2.2	1.5	6.4	210	644	3.8
44.195	-0.03	57.73	2.1	1.0	1.3	2.9	127	325	1.3
44.263	0.12	59.85	2.7	1.0	2.3	2.9	71	417	1.4
44.208	-0.04	57.09	2.0	0.8	1.3	2.5	108	262	0.9
44.116	0.22	53.69	2.3	1.0	0.5	2.7	113	392	1.2
44.202	0.04	57.51	2.5	1.3	2.5	3.7	150	693	1.4
44.116	-0.00	64.10	1.6	1.2	1.3	3.6	245	301	2.0
44.220	0.18	58.15	2.9	1.1	1.9	2.6	75	512	1.5
44.189	0.01	57.30	2.3	1.3	1.9	4.2	139	483	1.7
44.269	0.09	58.58	2.7	1.3	1.9	4.3	135	761	1.3
44.239	0.04	55.81	3.2	2.0	1.9	3.6	78	727	4.0
44.128	0.13	56.45	2.8	1.6	2.3	3.5	88	533	2.4
44.337	0.11	57.73	2.8	1.1	4.2	3.1	82	542	1.3
44.331	-0.08	65.59	1.9	1.6	4.9	4.2	189	361	2.8
44.362	0.16	56.66	1.9	0.8	4.2	2.0	125	245	1.1
44.275	0.24	57.30	2.0	0.9	4.2	2.4	139	313	1.2
44.036	-0.05	65.80	1.9	2.4	1.5	5.8	200	403	6.1
G044.34+0.11									
44.302	-0.81	61.08	2.8	1.4	1.6	6.1	201	1234	1.0
44.395	-0.76	64.48	2.6	1.4	1.8	8.3	174	894	1.5
44.321	-0.81	61.08	2.6	1.0	1.1	4.3	162	833	0.7
44.333	-0.81	60.65	2.8	1.3	0.7	6.8	158	1017	1.1
44.327	-0.82	61.93	3.5	1.0	0.7	5.0	127	1583	0.5
44.388	-0.79	64.05	2.6	1.3	1.6	4.0	133	685	1.3
44.333	-0.84	64.26	2.2	1.1	1.6	4.1	175	545	1.1

$\ell_{\rm peak}$ (deg)	$b_{\rm peak}$ (deg)	$v_{\rm peak}$ (km s^{-1})	$R_{\rm cl}$[1] (pc)	$\sigma_{\rm cl}$ (km s^{-1})	$d_{\rm cl}$[2] (pc)	$N_{\rm cl}(H_2)$[3] (10^{21} cm^{-2})	$n_{\rm cl}(H_2)$ (cm^{-3})	$M_{\rm cl}(H_2)$ ($M_\odot$)	$\alpha_{\rm vir}$[4]
44.407	-0.78	60.44	2.2	1.3	1.6	2.5	137	407	2.1
44.432	-0.78	61.29	2.0	1.0	1.5	2.8	139	315	1.3
44.376	-0.81	64.48	2.5	1.4	1.8	3.5	146	656	1.5
44.364	-0.88	64.69	2.4	1.4	4.2	3.7	155	652	1.8
44.432	-0.76	60.44	1.9	0.9	1.5	2.3	150	321	1.0
44.413	-0.80	65.11	2.5	0.8	1.6	2.4	85	386	1.0

[1]Clump effective radius
[2]Nearest neighbor (peak-to-peak) separation
[3]Peak column density
[4]$M_{\rm vir}/M_{\rm cl}$

Appendix C

Spectral Line Fitter User Manual

This appendix serves as basic instructions for using the spectral line fitter described in 3.4.3 for general data cubes of molecular emission line spectra. Implementations of this fitter for single-pointing spectra and absorption lines exist, but are yet to be thoroughly tested. The fitter routine is written in Python and tested most thoroughly in version 2.7.8. It requires use of the packages `os`, `sys`, `numpy`, `pyfits`, `nmpfit`, `numerixenv`, `pdb`, and `matplotlib`. The only two of these packages not typically included with python installations are `nmpfit`, the python version of the least-squares mpfit package available for IDL, and `numerixenv`. The package `numerixenv` is available at `http://stsdas.stsci.edu/pyraf/stscidocs/pytools_pkg/pytools_api/pytools.numerixenv-module.html`, and `nmpfit` is available at `https://trac.stsci.edu/ssb/stsci_python/browser/stsci_python/trunk/pytools/lib/nmpfit.py?rev=675` (note that this version contains a small error; uncomment lines 1343-1344 and comment line 1345, otherwise the reported covariance matrix will be incorrect). The documentation for `nmpfit` is at `http://cars9.uchicago.edu/software/python/mpfit.html` though users may also want to consult the IDL documentation at `http://www.physics.wisc.edu/~craigm/idl/fitting.html` and `http://www.physics.wisc.edu/~craigm/idl/down/mpfit.pro` for additional details, but be aware that there are some differences between the python and IDL versions, such as in the data weighting options.

The fitting routine is designed to operate without any manual input for the user, but a set of files are required before running the fitter. These are: the data cube(s), corresponding signal-to-noise ratio (SNR) moment maps and RMS maps, and maximum value, velocity field, and velocity dispersion moment maps for each clump. When fitting multiple lines simultaneously, such as NH_3 (1,1) and (2,2), two data cubes of equal size and expanse in position-position-velocity space, as well as SNR

and RMS maps for both lines, are necessary. Regions may be treated as a single clump if no clump deconvolution was previously performed, but the fitter will only be able to handle one velocity component per line of sight in this case. Note that the assignment cubes themselves from clump deconvolution are not required, and so you may use any algorithm of your choice, even manual assignment. It is sufficient for the fitter to determine the two dimensional extent of the clumps and guesses for the amplitudes, velocity centers, and velocity widths from the moment maps alone.

The SNR, RMS, and moment maps are made easily in CASA from the primarily beam corrected data cubes using the `immoments` task. The RMS maps can be made via

```
immoments(imagename='datacube',
outfile='datacube.mom.rms',
moments=[6],
chans='chan1~chan2,chan3~chan4')
```

where some care is taken to choose ranges of line-free channels. The RMS maps have two primary uses: (1) making the SNR map with the task `immath`, which in turn can be used to mask the data to only include lines of sight with arbitrarily significant emission, and, more importantly, (2) for calculating the χ^2 value for each spectrum, i.e. `nmpfit` considers the differences between the data and the model in units of the RMS value for the spectrum. In principle this value can be specified per data point as a way to weight the data; in practice this fitter uses a single RMS value across a spectrum, and the value varies from spectrum to spectrum across the image. The SNR map is only used for masking the data; if the data are already sufficiently masked, including any mask on the clump moment maps, then the SNR map is not critical, though the lines of code referring to the SNR map will need to be commented

if it is not provided. The SNR maps could refer to either the peak SNR or integrated SNR, depending on how the user wants to mask.

The moment maps can be also be created in CASA via

```
immoments(imagename='datacube',
moments=[0,1,2,8],
mask='assignment==clump',
outfile='datacube.mom') ,
```

which also creates an integrated intensity map that can be used to generate the SNR map if created over the entire region instead of an individual clump. The mask parameter is optional if there exists a clump assignment cube and the moment maps are being made for each clump. Otherwise, the `chans` parameter should be used to select channels of line emission if the entire region is being treated as a single clump. All the data cubes and maps should be exported from CASA into FITS files for the fitter before proceeding.

The fitter operates in velocity (m s^{-1}) and main beam temperature (K) units, however the data cubes are assumed to be in Jy $beam^{-1}$ and can either be in km s^{-1}, m s^{-1}, or Hz. The fitter (within the custom function `frequencyscale`) checks the header keyword `CTYPE3`; if it is `'VELO'` or `'VRAD'` the fitter takes the keywords `NAXIS3`, `CRVAL3`, `CDELT3`, and `CRPIX3` to compute the velocity scale, assumed to be in m s^{-1} unless the keyword `CUNIT3` is `'km/s'` and then the scale is converted to m s^{-1}. For any other values of `CTYPE3` the spectral axis is assumed to be in Hz and is converted to m s^{-1} using the keywords `NAXIS3`, `CRVAL3`, `CDELT3`, and `CRPIX3` and the nonrelativistic radio velocity definition of the Doppler shift. The amplitude scale is converted with the custom function `jybeam2tmb`, which requires the dimensions of the beam provided by the header keywords `BMAJ` and `BMIN`, assumed to be specified

in degrees. Future versions of the fitter will be made more flexible and careful with units and header keywords.

The fitter uses an auxiliary file (e.g. `ammonia.py`) containing information specific the molecular line(s) being fit. This file must contain: (1) a list of lines to fit (e.g. '11' or '1-0'), (2) a dictionary of rest frequencies in GHz for the lines, (3) a dictionary of frequency offsets for the hyperfine components in GHz from the line rest frequency if they are to be considered for fitting the optical depth, (4) a dictionary of relative intensities of the hyperfine components if they are to be considered for fitting the optical depth (the absolute scaling of intensities is irrelevant), (5) functions that describe the line shape with all the fine and hyperfine structure, (6) dictionary for `nmpfit` that specifies limits on the fit parameters (see `nmpfit` documentation), (7) a function for computing the column density, (8) initial guesses for the clump-averaged spectra fit parameters except the velocity center (the routine is fairly insensitive to these values), (9) a function to convert rotation temperature to kinetic temperature, if applicable, and (10) physical parameters specific to the line(s) and functions. An example of such a file for ammonia (1,1) and (2,2) is given at the end of this appenidx in §C.1.

The fitting code may be manually updated in multiple places for a specific project:

→ `maxiter = 500`

the maximum number of iterations for `nmpfit` to perform on a fit; spectra that hit this limit are rejected by the fitter

→ `lines = ['11','22']`

specifying the particular lines of a molecule to fit

→ `snrlimit = {'11':0.,'22':0.}`

the minimum SNR to try fitting; uses AND logic for multiple lines; 0 is a safe choice if data are masked already or have clump assignments

→ `Tc = {'11':  0.,'22':  0.}`

the background continuum temperature not including the CMB; should be 0 for emission line data if they are baseline subtracted; this is critical for absorption line fitting

→ `nparams = 5`

the number of parameters to fit per velocity component; e.g. ammonia fitter uses velocity center, velocity width, optical depth, excitation temperature, and rotation temperature

→ `execfile('ammonia.py')`

this is the auxiliary file that contains information specific to the molecular line(s) being fit

→ `regions=['reg1','reg2',...]`

for specifying the region names

→ `clumps={'reg1':['clump1','clump2',...]...}`

for specifying the clump assignment numbers

→ `for reg in range(0,9):`

regions to loop over

→ `datacube[line],hdrcube[line] =`
`loaddatacube(root+region+'_'+line+'_Combined.fits')`

path to data cube; header keywords are read from the first data cube only, so other data cubes and moment maps must match

→ `snr[line],dummy = loaddatacube(root+region+'_Combined_'+line+'.mom.snr.fits')`

path to SNR map

→ `rms,dummy = loaddatacube(root+region+'_Combined_11.mom.rms.fits')`

path to RMS map

→ `for mo in mom:  clumpdata[clnm][mo],dummy = loaddatacube(root+region+'_Combined_11.mom.'+mo+'.fits')`

path to moment maps

→ `mom = ('maximum','weighted_coord','weighted_dispersion_coord')`

labels for the moment map names

→ `included[clnm] = (~numpy.isnan(clumpdata[clnm]['weighted_dispersion_coord'])) * (snr['11'] > snrlimit['11']) * (snr['22'] > snrlimit['22'])`

can change the masking here, especially if user does not want to mask based on SNR

The fitter produces a suite of output files in the directory where it is run. For each clump, the fitter first attempts to fit the spectrum averaged over the extent of the clump. An image of the averaged spectrum with the fit is printed to

`region_Clump#_IntegratedFit.png`,

and the fit parameters and covariance matrix are printed to the command line. The covariance matrix can be used to generate error ellipses. The other outputs take the form of `parameter.region_#_out.fits`, where `#` is the clump assignment number. The files beginning with `specfit` and `resid` are cubes with the model spectrum and the residuals, respectively, and are the same size as the input data in the same amplitude units and with a velocity axis. All of the other outputs are two dimensional maps with the same extent as the input data. The fit parameters outputs are named `velocity`, `fwhm`, `tau11`, `tex`, and `trot`, and the formal uncertainties are named `dvelocity`, `dfwhm`, `dtau11`, `dtex`, and `dtrot`. Each clump will have additional outputs `nnh3` for the column density and `tkin` for the kinetic temperature. The outputs that exist for each region (but not for each clump) include: (1) `nnh3.region_total_out.fits` with the column densities of all the clumps summed along the line of sight, (2) `mask.region_out.fits` that has a map of all the lines of sight for which a fit was output (this excludes any spectra that were manually masked in any of the input files, the SNR was below the fit threshold, the fit did not converge, the maximum number of fit iterations was reached, or at least one of the best fits parameters matched the initial guess or the upper or lower limits on the values), (3) `ncomponents.region_out.fits` has the number of velocity components fit along each line of sight, (4) `reducechisq.region_out.fits` has the the reduced χ^2 value for each fit, and (5) `status.region_out.fits` has the status flag of the fit result. Refer to the `nmpfit` documentation for status flags, except for the following user-specified flags: -1 if at least one best fit parameter matches the lower limit on the allowed range, -2 if at least one best fit parameter matches the upper limit on the allowed range, and -3 if at least one best fit parameter matches the initial guess. If more than one of these conditions is met, these status flags can only indicate that at

least one case was true (whichever was last found to be true).

To run the fitter, put the scripts `clump_fitter.py` and `ammonia.py` (or other versions of the fitter and auxiliary file) in the directory where you want the outputs, and run `python clump_fitter.py`. If there are no errors, the fitter will loop over each region, print the best fit parameters and covariance matices for the average spectrum of each clump, then print the columns in the data cube it is looping over, and finally print `DONE` when it reaches completion.

C.1 Example Auxiliary File `ammonia.py`

```
#### Important constants
## (1,1) Einstein A coefficient
a11 = 1.68e-7 # Hz
## rotational constants
brot = 2.98117e11 # Hz
crot = 1.86726e11 # Hz

## List of lines that we can do
JKlines=numpy.array(['11','22'])

## Rest frequencies from splatalogue
restfreq = { '11': 23.69450,'22': 23.72263}

## List of hyperfine component frequency offsets from center
## (1,1) & (2,2) in velocity from Kukolich
components = { '11': -1.* restfreq['11']*((1e3*
numpy.array([19.452700,19.984400,8.0195000,7.6023000,7.4831000,
0.59540000,0.45620000,0.44170000,0.32260000,0.059100000,0.0000000,-0.080100000,-0.11910000,
-7.1014000,-7.2406000,-7.6823000,-19.276300,-19.415500]))/c),
'22': -1.* restfreq['22']*((1e3*
numpy.array([-26.526000,-26.011000,-25.951000,-16.382000,-16.370000,-15.854000,
-0.58900000,-0.53100000,-0.50200000,-0.013000000,-0.0040000000,0.013000000,0.52400000,0.52800000,0.56200000,
15.865000,16.379000,16.392000,25.950000,26.011000,26.526000]))/c)}
```

```
## Relative strengths of hyperfine components
## (1,1) & (2,2) from Kukolich
scale = { '11': numpy.array([0.44,0.22,0.28,0.50,0.06,
0.11,0.06,0.10,0.90,0.06,1.40,0.28,0.10,0.28,0.06,0.50,0.22,0.44]),
'22': numpy.array([0.02,0.18,0.10,0.178,0.124,0.01,
0.10,0.05,0.056,0.70,2.387,1.278,0.05,0.056,0.10,0.01,0.124,0.178,0.10,0.18,0.02])}
## Normalize each JK line since only relative strengths matter
for s in range(len(scale)):
scale[str(s+1)+str(s+1)] = scale[str(s+1)+str(s+1)]/numpy.sum(scale[str(s+1)+str(s+1)])

## Statistical weights
## accounts for rotational degeneracy, K degeneracy, and nuclear spin degeneracy
gJK = {JKlines[j]: 4*(2*(j+1.)+1)*(1+numpy.round(numpy.mod(j,3)/3.)) for j in range(len(JKlines))}

## Dipole moment dependence on (J,J) since constants cancel
## |mu(J,K)|^2 ~ K^2/(J(J+1)) ~ J(J+1)
mu2 = {JKlines[j]: (j+1.)/(j+2.) for j in range(len(JKlines))}

## Energy of lower level from splatalogue [1/cm]
EL = {'11': 16.172,'22': 44.794}

## Each hyperfine component is a gaussian
## Parametrize everything by (1,1) center and (1,1) FWHM
## This does not account for the spectral resolution (at least the channel width; more if
## the data were smoothed) so the resulting "observed" width is not the "true" width
def gaussiancomponent(p, freq, JK, i):
return( scale[JK][i]*numpy.exp(-4.*numpy.log(2.)*
(freq - p[0]*(restfreq[JK]/restfreq['11']) - components[JK][i])**2./
((p[1]*restfreq[JK]/restfreq['11'])**2.) ) )

## Sum the hyperfine components for a single (J,K) line
def hyperfinestructure(p, freq, JK):
## first the generic shape of the optical depth profile
shape = numpy.zeros(freq.size)
for i in range(len(components[JK])): shape += gaussiancomponent(p, freq, JK, i)
## scale by ratios of constants for (J,K) compared to the (1,1) line
shape = shape*((restfreq[JK]/restfreq['11'])*(mu2[JK]/mu2['11'])*(gJK[JK]/gJK['11'])*
numpy.exp(-1.43877696*(EL[JK]-EL['11'])/p[4]) )
# (1/cm)/(Boltzmann constant)*(Planck's constant)*c = 1.43877696 kelvin
```

```
## Turn the optical depth into main beam temperature profile
F = ((Jfunct(p[3],freq) - Jfunct(Tc[JK] + Tcmb,freq)) * ( 1. - numpy.exp( -1.*(p[2])*shape ) ) )
return(F)

## Sum of (J,K) lines for the complete spectrum
def specline(p, freq, lines):
# p=[central frequency, frequency FWHM, (1,1) main tau, Tex, Trot]
shape = numpy.zeros(freq.size)
for line in lines:
for m in range(len(p)/nparams):
## calculate contribution from different velocity components
## clumps not along a particular LOS should have the initial guess for the
## center at 0 km/s. This should change if vLSR gets close to 0
if (p[1+m*nparams] != 0):
shape += hyperfinestructure(p[nparams*m:nparams*(m+1)], freq, line)
return(shape)

## Set constraints on fit parameters
def setparinfo(p, nparams, freq, Tcmb):
parinfo = [{}]*len(p)
## Need to do this for every component
for m in range(len(p)/nparams):
for n in range(nparams):
## Don't bother with parameters for components not along this LOS
if (p[1+m*nparams] == 0):
parinfo[n+m*nparams] = {'value':0, 'fixed':1, 'limited':[0,0],
'limits':[0,0],  'parname':'','step':0,'mpside':0, 'mpmaxstep':0,'tied':'', 'mpprint':0}
else:
if (n == 0):
parinfo[n+m*nparams] = {'value':p[n+m*nparams], 'fixed':0, 'limited':[1,1],
'limits':[p[0+m*nparams]-5*p[1+m*nparams],p[0+m*nparams]+5*p[1+m*nparams]],
'parname':'Central Frequency','step':0,'mpside':0,
'mpmaxstep':(numpy.abs(freq[1]-freq[0])/2.),'tied':'', 'mpprint':1}
if (n == 1):
parinfo[n+m*nparams] = {'value':p[n+m*nparams], 'fixed':0, 'limited':[1,1],
'limits':[0,5*p[1+m*nparams]],  'parname':'Frequency Width','step':0,'mpside':0,
'mpmaxstep':(numpy.abs(freq[1]-freq[0])/2.),'tied':'', 'mpprint':1}
if (n == 2):
parinfo[n+m*nparams] = {'value':p[n+m*nparams], 'fixed':0, 'limited':[1,1],
```

```
'limits':[0,20.],  'parname':'(1,1) Main Optical Depth','step':0,'mpside':0,
'mpmaxstep':0.1,'tied':'', 'mpprint':1}
if (n == 3):
parinfo[n+m*nparams] = {'value':p[n+m*nparams], 'fixed':0, 'limited':[1,1],
'limits':[Tcmb,20.],  'parname':'Tex','step':0,'mpside':0, 'mpmaxstep':0.1,'tied':'', 'mpprint':1}
if (n == 4):
parinfo[n+m*nparams] = {'value':p[n+m*nparams], 'fixed':0, 'limited':[1,1],
'limits':[Tcmb,40.],  'parname':'Trot','step':0,'mpside':0, 'mpmaxstep':0.1,'tied':'', 'mpprint':1}
return(parinfo)

## Ammonia partition function for column density calculation
def partition(J,trot):
orthopara = numpy.mod(J,3)
S = 1
if (orthopara == 0): S = 2
return( (2*J + 1) * S * numpy.exp(-1.*h*(brot*J*(J+1)+(crot-brot)*J**2)/kB/trot) )

## Kinetic temperature following Rosolowsky
def kinetictemp(results):
return(results[:,:,4]/(1.-results[:,:,4]/42.*numpy.log(1.+1.1*numpy.exp(-16./results[:,:,4]))))

## Column density of (1,1)
def N11(results):
return(4.*(restfreq['11']*1e9)**2/(c*1e2)**2 * numpy.sqrt(numpy.pi**3/numpy.log(2.)) * (1./1.) * 1./a11 * results[:,:,2
(results[:,:,1]*1e9) * (1. + numpy.exp(-1.*h*(restfreq['11']*1e9)/kB/results[:,:,3]))/(
1. - numpy.exp(-1.*h*(restfreq['11']*1e9)/kB/results[:,:,3])) / 1e15)

## Total ammonia column density
def NNH3(results):
z11 = partition(1,results[:,:,4])
z = z11
for i in range(2,101): z += partition(i,results[:,:,4])
return(N11(results) * z/z11)

## Completely blind initial guesses for averaged spectrum fit
## We'll get the line center from the maximum in the data
def initialguesses():
return(numpy.array([0., 1e-4, 5., 5., 20.]))
```

Appendix D

Molecular Gas Clumps in IRDC Sample

Table D.1:: Clump Properties

Peak Coordinates			cprops		*Herschel*	Spectral Line Fitting				*Spitzer*
R.A. (J2000)	Decl. (J2000)	$v_{\rm LSR}$	$R_{\rm eff}$	A_0	70 μm	$\langle\sigma_{\rm line}\rangle$	$\langle\tau_0\rangle$	$\langle T_K\rangle$	$\langle N({\rm NH_3})\rangle$	$\langle\tau_{24\mu{\rm m}}\rangle$[1]
hh:mm:ss	dd:mm:ss	(km s^{-1})	(pc)		source?	(km s^{-1})		(K)	(10^{23} cm^{-2})	
G010.74-00.13 ($f_{\rm fore}=0.095$)[2]										
18:09:45	-19:42:29	28.50	0.17	2.1	N	1.0	7.3	14.1	0.8	0.35
18:09:45	-19:42:07	28.50	0.16	1.2	Y	1.0	8.3	15.1	1.1	0.34
18:09:44	-19:42:06	29.16	0.11	2.1	N	0.7	7.9	14.0	0.6	0.37
18:09:46	-19:41:47	29.82	0.16	2.5	Y	1.0	8.1	14.7	0.9	0.27
G022.56-00.20 ($f_{\rm fore}=0.173$)										
18:33:00	-09:19:59	74.84	0.15	3.0	Y	1.3	6.7	16.5	1.0	0.20
18:33:01	-09:19:56	76.82	0.09	1.6	N	1.6	6.0	15.7	0.9	0.19
18:33:00	-09:20:04	78.14	0.09	2.8	N	1.6	5.1	16.3	0.7	0.22
G024.60+00.08 ($f_{\rm fore}=0.127$)										
18:35:40	-07:18:36	52.49	0.12	1.4	Y	1.4	4.5	19.8	0.8	0.19
18:35:39	-07:18:55	53.15	0.17	1.5	N	0.8	6.1	14.0	0.6	0.28
18:35:40	-07:19:06	53.81	0.09	1.2	N	0.6	6.1	14.2	0.4	0.23
18:35:40	-07:18:31	53.81	0.10	1.2	N	1.0	4.5	18.1	0.6	0.15
18:35:41	-07:18:03	53.81	0.03	3.4	N	0.3	8.4	11.7	0.6	0.06
18:35:41	-07:19:08	54.14	0.05	1.6	N	0.4	5.6	16.0	0.4	0.19
G028.23-00.19 ($f_{\rm fore}=0.220$)										
18:43:31	-04:13:23	79.15	0.09	1.5	N	1.2	12.2	13.9	1.5	0.84
18:43:30	-04:13:09	79.81	0.08	1.3	N	1.0	9.5	13.6	0.8	0.77
18:43:30	-04:12:59	80.14	0.08	1.8	N	1.5	6.2	12.3	0.8	0.70
18:43:29	-04:12:34	80.14	0.05	1.8	N	0.9	4.6	13.8	0.4	...
18:43:29	-04:12:27	80.14	0.06	2.9	N	1.1	3.5	14.6	0.4	0.44
18:43:30	-04:12:30	80.80	0.06	4.4	N	1.1	9.9	13.1	0.9	0.63
18:43:30	-04:13:32	81.13	0.05	1.7	N	0.8	8.5	14.0	0.7	0.67
18:43:29	-04:12:51	81.13	0.04	1.8	N	1.2	13.0	11.4	1.2	0.56
G031.97+00.07 ($f_{\rm fore}=0.328$)										
18:49:29	-00:48:53	93.85	0.18	1.3	N	1.0	7.6	15.3	0.9	0.15
18:49:26	-00:49:52	94.18	0.09	2.0	N	0.6	7.3	12.9	0.5	0.29
18:49:31	-00:47:09	94.18	0.10	1.2	N	2.3	4.3	18.9	0.9	0.12
18:49:28	-00:48:30	94.51	0.17	1.5	N	1.2	4.7	18.1	0.6	0.18
18:49:29	-00:48:03	94.51	0.17	1.9	Y	1.3	5.5	18.1	0.7	0.18
18:49:30	-00:47:23	94.51	0.07	1.7	N	0.7	6.6	16.4	0.6	0.17
18:49:30	-00:48:18	94.84	0.07	2.9	N	1.0	6.1	16.5	0.5	0.28
18:49:32	-00:48:04	94.84	0.17	1.5	N	1.7	5.4	17.1	0.9	0.29
18:49:30	-00:46:46	94.84	0.08	1.4	N	1.6	4.4	16.9	0.7	0.14
18:49:32	-00:46:29	94.84	0.08	2.3	N	1.8	2.8	19.5	0.6	...
18:49:26	-00:50:28	95.50	0.06	3.4	N	1.1	6.8	12.7	0.8	0.28
18:49:31	-00:47:17	95.50	0.10	1.3	N	1.8	3.6	17.3	0.6	0.25
18:49:33	-00:47:15	95.50	0.16	1.7	N	2.2	5.4	18.4	1.1	0.14
18:49:24	-00:50:07	95.83	0.09	3.3	N	1.0	5.6	13.8	0.5	0.29
18:49:34	-00:46:44	95.83	0.28	1.1	Y	1.8	5.2	18.9	1.2	0.01
18:49:28	-00:49:39	96.49	0.18	2.0	N	0.9	7.2	13.2	0.8	0.28
18:49:33	-00:47:33	96.49	0.25	2.1	N	1.7	6.6	16.7	1.2	0.25
18:49:25	-00:50:09	96.82	0.08	4.7	N	1.5	7.4	12.2	1.0	0.25
18:49:31	-00:46:46	98.47	0.06	2.1	N	1.3	4.1	18.0	0.5	...
18:49:32	-00:46:59	99.46	0.18	1.3	Y	2.0	6.3	18.0	1.2	0.12

Peak Coordinates			cprops		*Herschel*	Spectral Line Fitting				*Spitzer*
R.A. (J2000)	Decl. (J2000)	$v_{\rm LSR}$	$R_{\rm eff}$	A_0	70 μm	$\langle\sigma_{\rm line}\rangle$	$\langle\tau_0\rangle$	$\langle T_K\rangle$	$\langle N({\rm NH_3})\rangle$	$\langle\tau_{24\mu{\rm m}}\rangle$[1]
hh:mm:ss	dd:mm:ss	(km s^{-1})	(pc)		source?	(km s^{-1})		(K)	(10^{23} cm^{-2})	
18:49:31	-00:46:41	99.46	0.12	2.5	N	0.9	5.4	17.6	0.6	0.05
G032.70-00.30 ($f_{\rm fore}$ = 0.289)										
18:52:03	-00:21:09	89.83	0.04	1.3	N	0.5	4.9	10.5	0.5	0.31
18:52:05	-00:20:54	90.16	0.08	3.7	Y	0.8	5.2	14.3	0.5	0.25
18:52:07	-00:20:06	90.82	0.05	2.0	N	0.4	3.6	12.6	0.3	0.32
G034.43+00.24 ($f_{\rm fore}$ = 0.058)										
18:53:17	01:23:45	55.86	0.10	2.1	N	1.4	5.7	19.7	0.8	0.01
18:53:17	01:24:32	56.19	0.08	2.0	N	1.6	5.3	18.9	1.3	···
18:53:17	01:26:52	56.19	0.05	1.8	N	0.6	6.5	12.8	0.5	0.01
18:53:18	01:24:51	56.52	0.08	1.1	Y	2.6	4.4	24.6	2.0	···
18:53:18	01:26:37	56.52	0.04	2.8	N	0.4	6.6	11.9	0.5	0.01
18:53:16	01:26:30	56.85	0.04	2.6	Y	1.3	6.5	13.6	0.9	···
18:53:15	01:26:58	56.85	0.02	2.2	N	0.4	9.4	13.1	0.6	···
18:53:17	01:23:59	57.18	0.02	1.9	N	1.2	4.7	13.8	0.7	···
18:53:21	01:23:08	57.51	0.02	2.5	N	0.4	8.6	11.2	0.6	0.00
18:53:18	01:25:25	57.51	0.08	1.4	Y	2.3	4.3	27.9	1.8	···
18:53:19	01:26:27	57.51	0.09	2.5	N	1.0	5.6	14.1	0.7	0.04
18:53:19	01:24:29	57.84	0.14	2.7	Y	1.7	6.1	20.6	1.6	0.01
18:53:18	01:25:37	58.17	0.11	1.2	N	1.5	5.5	19.8	1.3	···
18:53:19	01:23:13	58.50	0.05	2.3	N	1.0	6.7	14.7	0.8	···
18:53:18	01:25:13	58.50	0.06	1.6	N	1.5	6.0	21.3	1.7	···
18:53:19	01:27:49	58.50	0.13	2.9	Y	1.1	6.3	13.9	0.9	0.06
18:53:20	01:28:21	59.49	0.09	1.4	Y	1.2	5.2	20.3	1.1	0.05
18:53:21	01:26:57	59.82	0.02	1.8	N	0.9	5.4	13.8	0.7	0.01
G035.39-00.33 ($f_{\rm fore}$ = 0.131)										
18:57:08	02:08:25	42.53	0.09	2.1	N	0.8	7.1	12.8	0.7	0.20
18:57:10	02:07:36	44.84	0.14	1.6	N	0.8	7.9	14.2	0.8	0.34
18:57:09	02:07:08	45.17	0.04	1.9	N	0.4	6.7	11.8	0.5	0.27
18:57:09	02:08:18	45.17	0.09	1.4	Y	1.0	5.2	14.4	0.6	0.23
18:57:07	02:08:41	45.17	0.03	2.0	N	0.7	5.2	14.0	0.7	0.25
18:57:08	02:07:52	45.50	0.10	1.3	Y	0.9	7.4	13.5	0.8	0.32
18:57:09	02:07:52	45.50	0.11	1.8	Y	1.0	5.3	14.5	0.6	0.26
18:57:08	02:08:03	45.50	0.13	1.4	Y	0.7	8.1	13.9	0.7	0.29
G038.95-00.47 ($f_{\rm fore}$ = 0.131)										
19:04:07	05:08:47	42.16	0.10	1.3	N	1.2	5.2	17.6	0.9	0.23
19:04:10	05:09:14	42.16	0.04	2.0	N	0.6	4.9	22.9	0.3	0.22
19:04:06	05:08:50	42.49	0.07	1.9	Y	1.3	4.0	13.2	0.6	0.16
19:04:08	05:09:30	42.49	0.10	1.7	Y	1.3	3.8	15.1	0.5	0.16
19:04:10	05:08:43	42.82	0.04	1.1	N	0.6	4.5	13.6	0.5	0.24
19:04:10	05:08:54	42.82	0.05	1.6	N	1.1	3.9	15.0	0.5	0.10
19:04:08	05:08:56	42.82	0.10	2.0	Y	1.3	3.2	15.3	0.5	0.26
19:04:08	05:09:09	42.82	0.11	1.1	N	1.0	3.4	17.1	0.4	0.27
19:04:07	05:09:46	42.82	0.08	1.4	Y	1.1	4.9	18.3	0.8	0.27
19:04:10	05:09:05	43.15	0.04	1.3	N	0.8	4.2	15.0	0.4	0.17

[1] $\tau_{24\mu{\rm m}}$ cannot be computed for some clumps because IR emission covers their entire angular extent or the contrast with the background is too low.

[2] $f_{\rm fore}$ is the estimated fraction of diffuse galactic IR emission that is foreground to the cloud, and is used to calculate $\tau_{24\mu{\rm m}}$ (see §3.4.2).

Appendix E

Stability of Molecular Gas Clumps

Table E.1:: Clump Stability

$M_{\rm cl}$[1] ($M_\odot$)	$t_{\rm ff,sph}$ (Myr)	$t_{\rm ff,cyl}$ (Myr)	$M_{\rm vir,sph}$ ($M_\odot$)	$M_{\rm vir,cyl}$ ($M_\odot$)	$\alpha_{\rm vir,sph}$	$\alpha_{\rm vir,cyl}$	c_s (km s^{-1})	$\mathcal{M}$	$B_{\rm min}$ (mG)
G010.74-00.13									
409	0.06	0.10	217	152	0.53	0.37	0.26	3.9	1.37
454	0.05	0.05	171	91	0.38	0.20	0.27	3.5	1.88
112	0.06	0.10	59	41	0.53	0.36	0.26	2.5	0.87
348	0.06	0.12	195	149	0.56	0.43	0.27	3.8	1.36
G022.56-00.20									
486	0.05	0.11	287	238	0.59	0.49	0.29	4.4	2.09
162	0.04	0.05	264	158	1.63	0.97	0.28	5.6	1.95
103	0.04	0.10	257	207	2.50	2.01	0.28	5.5	1.33
G024.60+00.08									
174	0.05	0.06	271	155	1.56	0.89	0.31	4.5	1.28
243	0.07	0.09	136	80	0.56	0.33	0.26	3.2	0.88
63	0.06	0.06	40	21	0.63	0.33	0.27	2.2	0.72
88	0.05	0.05	119	63	1.36	0.72	0.30	3.5	0.99
6	0.04	0.10	3	3	0.52	0.46	0.24	1.2	0.67
14	0.05	0.06	10	6	0.70	0.42	0.28	1.4	0.59
G028.23-00.19									
199	0.03	0.04	156	91	0.78	0.46	0.26	4.5	2.34
80	0.04	0.04	85	46	1.06	0.57	0.26	3.7	1.30
99	0.04	0.05	199	128	2.01	1.30	0.25	6.0	1.73
21	0.03	0.05	41	26	1.93	1.24	0.26	3.3	1.05
24	0.05	0.11	82	67	3.45	2.81	0.27	4.1	0.72
41	0.03	0.12	74	74	1.81	1.81	0.25	4.2	1.31
42	0.03	0.04	32	20	0.77	0.48	0.26	2.9	1.84
28	0.02	0.03	58	38	2.09	1.36	0.24	5.0	2.30
G031.97+00.07									
871	0.04	0.05	212	118	0.24	0.13	0.28	3.7	2.89

$M_{\rm cl}$[1] ($M_\odot$)	$t_{\rm ff,sph}$ (Myr)	$t_{\rm ff,cyl}$ (Myr)	$M_{\rm vir,sph}$ ($M_\odot$)	$M_{\rm vir,cyl}$ ($M_\odot$)	$\alpha_{\rm vir,sph}$	$\alpha_{\rm vir,cyl}$	c_s (km s^{-1})	$\mathcal{M}$	$B_{\rm min}$ (mG)
103	0.05	0.08	36	24	0.35	0.24	0.25	2.2	1.18
116	0.05	0.05	631	336	5.43	2.89	0.31	7.5	1.14
454	0.05	0.07	301	179	0.66	0.39	0.30	4.1	1.62
408	0.06	0.09	319	210	0.78	0.51	0.30	4.2	1.45
59	0.04	0.05	39	24	0.65	0.41	0.29	2.5	1.37
59	0.04	0.10	87	71	1.46	1.20	0.29	3.5	1.16
551	0.05	0.06	568	335	1.03	0.61	0.29	5.8	1.95
104	0.04	0.04	225	129	2.17	1.25	0.29	5.5	1.77
93	0.04	0.08	300	219	3.21	2.35	0.31	5.7	1.40
96	0.03	0.07	91	80	0.94	0.83	0.25	4.5	2.63
26	0.10	0.11	383	212	14.81	8.20	0.29	6.3	0.28
715	0.04	0.06	895	560	1.25	0.78	0.30	7.2	2.71
109	0.04	0.11	95	84	0.87	0.77	0.26	3.7	1.54
2759	0.05	0.04	1082	536	0.39	0.19	0.31	5.9	3.47
654	0.05	0.08	177	119	0.27	0.18	0.26	3.6	2.00
2110	0.05	0.08	817	566	0.39	0.27	0.29	5.8	3.39
102	0.03	0.13	209	218	2.04	2.13	0.25	6.2	1.78
37	0.04	0.06	104	72	2.84	1.96	0.30	4.2	1.14
826	0.04	0.05	786	436	0.95	0.53	0.30	6.5	2.69
219	0.05	0.09	120	91	0.55	0.41	0.30	3.1	1.59
G032.70-00.30									
17	0.03	0.03	9	5	0.54	0.29	0.23	2.0	1.32
79	0.04	0.12	54	50	0.69	0.63	0.27	2.9	1.31
14	0.05	0.08	9	6	0.65	0.44	0.25	1.5	0.54
G034.43+00.24									
24	0.10	0.17	222	154	9.27	6.43	0.31	4.5	0.27
59	0.04	0.07	216	149	3.65	2.51	0.31	5.1	1.06
12	0.06	0.09	25	16	2.12	1.36	0.25	2.4	0.39

$M_{\rm cl}$[1] ($M_\odot$)	$t_{\rm ff,sph}$ (Myr)	$t_{\rm ff,cyl}$ (Myr)	$M_{\rm vir,sph}$ ($M_\odot$)	$M_{\rm vir,cyl}$ ($M_\odot$)	$\alpha_{\rm vir,sph}$	$\alpha_{\rm vir,cyl}$	c_s (km s^{-1})	$\mathcal{M}$	$B_{\rm min}$ (mG)
96	0.04	0.04	670	342	6.97	3.55	0.35	7.5	1.41
5	0.06	0.14	6	5	1.35	1.09	0.24	1.5	0.31
7	0.04	0.09	71	54	10.43	8.04	0.26	5.0	0.53
3	0.04	0.06	4	3	1.50	1.06	0.26	1.5	0.48
3	0.04	0.06	43	28	16.55	11.03	0.26	4.6	0.42
3	0.04	0.08	5	4	1.98	1.50	0.24	1.8	0.44
59	0.04	0.05	449	254	7.56	4.27	0.37	6.1	1.06
37	0.07	0.14	103	78	2.79	2.10	0.26	3.8	0.48
196	0.06	0.14	489	385	2.49	1.96	0.32	5.4	1.01
116	0.06	0.06	305	163	2.63	1.41	0.31	4.9	0.97
16	0.05	0.09	59	43	3.65	2.64	0.27	3.6	0.58
55	0.04	0.05	156	96	2.86	1.75	0.33	4.5	1.41
116	0.07	0.16	176	144	1.51	1.24	0.26	4.1	0.74
76	0.05	0.06	146	83	1.91	1.09	0.32	3.7	0.93
3	0.03	0.05	20	13	7.53	4.87	0.26	3.5	0.62
G035.39-00.33									
58	0.06	0.10	73	50	1.27	0.87	0.25	3.3	0.74
249	0.06	0.07	117	71	0.47	0.28	0.27	3.1	1.23
12	0.05	0.07	9	6	0.78	0.51	0.24	1.7	0.59
55	0.06	0.06	93	52	1.70	0.95	0.27	3.6	0.76
6	0.04	0.07	19	13	3.41	2.33	0.26	2.7	0.55
126	0.05	0.05	107	57	0.84	0.45	0.26	3.6	1.21
106	0.06	0.08	125	79	1.18	0.75	0.27	3.7	0.89
187	0.06	0.07	74	42	0.39	0.23	0.26	2.6	1.05
G038.95-00.47									
115	0.05	0.05	173	94	1.51	0.82	0.30	4.2	1.22
1	0.10	0.16	16	11	12.00	8.22	0.34	1.8	0.10
26	0.06	0.10	155	104	5.88	3.93	0.26	5.3	0.50

$M_{\rm cl}$[1] ($M_\odot$)	$t_{\rm ff,sph}$ (Myr)	$t_{\rm ff,cyl}$ (Myr)	$M_{\rm vir,sph}$ ($M_\odot$)	$M_{\rm vir,cyl}$ ($M_\odot$)	$\alpha_{\rm vir,sph}$	$\alpha_{\rm vir,cyl}$	c_s (km s^{-1})	$\mathcal{M}$	$B_{\rm min}$ (mG)
71	0.06	0.09	207	129	2.94	1.82	0.27	4.8	0.70
7	0.06	0.05	17	9	2.50	1.27	0.26	2.2	0.38
9	0.07	0.09	75	45	8.59	5.18	0.27	4.1	0.33
55	0.07	0.11	192	130	3.48	2.36	0.28	4.7	0.60
61	0.08	0.07	120	61	1.96	0.99	0.29	3.3	0.50
68	0.05	0.05	112	64	1.65	0.94	0.30	3.6	1.05
6	0.06	0.07	35	19	5.95	3.29	0.27	3.0	0.30

[1]Clumps appear in the same order as Table 3.4.

References

Adams, F. C., Lada, C. J., & Shu, F. H. 1987, Astrophysical Journal, 312, 788

Aguirre, J. E., Ginsburg, A. G., Dunham, M. K., Drosback, M. M., Bally, J., Battersby, C., Bradley, E. T., Cyganowski, C., Dowell, D., Evans, N. J. I., Glenn, J., Rosolowsky, E., Stringfellow, G. S., Walawender, J., & Williams, J. P. 2011, The Astrophysical Journal Supplement, 192, 4

Allen, L. E., Calvet, N., D'Alessio, P., Merín, B., Hartmann, L., Megeath, S. T., Gutermuth, R. A., Muzerolle, J., Pipher, J. L., Myers, P. C., & Fazio, G. G. 2004, The Astrophysical Journal Supplement Series, 154, 363

Alves, J., Lada, C. J., Lada, E. A., Kenyon, S. J., & Phelps, R. 1998, The Astrophysical Journal, 506, 292

Anderson, L. D. & Bania, T. M. 2009, The Astrophysical Journal, 690, 706

André, P., Men'shchikov, A., Bontemps, S., Könyves, V., Motte, F., Schneider, N., Didelon, P., Minier, V., Saraceno, P., Ward-Thompson, D., Di Francesco, J., White, G., Molinari, S., Testi, L., Abergel, A., Griffin, M., Henning, T., Royer, P., Merin, B., Vavrek, R., Attard, M., Arzoumanian, D., Wilson, C. D., Ade, P., Aussel, H., Baluteau, J.-P., Benedettini, M., Bernard, J.-P., Blommaert, J. A. D. L., Cambrésy, L., Cox, P., di Giorgio, A., Hargrave, P., Hennemann, M., Huang, M., Kirk, J.,

Krause, O., Launhardt, R., Leeks, S., Le Pennec, J., Li, J. Z., Martin, P. G., Maury, A., Olofsson, G., Omont, A., Peretto, N., Pezzuto, S., Prusti, T., Roussel, H., Russeil, D., Sauvage, M., Sibthorpe, B., Sicilia-Aguilar, A., Spinoglio, L., Waelkens, C., Woodcraft, A., & Zavagno, A. 2010, Astronomy and Astrophysics, 518, L102

Ballesteros-Paredes, J., Hartmann, L. W., Vázquez-Semadeni, E., Heitsch, F., & Zamora-Avilés, M. A. 2011, Monthly Notices of the Royal Astronomical Society, 411, 65

Battersby, C., Bally, J., Dunham, M., Ginsburg, A., Longmore, S., & Darling, J. 2014a, The Astrophysical Journal, 786, 116

Battersby, C., Bally, J., Jackson, J. M., Ginsburg, A., Shirley, Y. L., Schlingman, W., & Glenn, J. 2010, The Astrophysical Journal, 721, 222

Battersby, C., Ginsburg, A., Bally, J., Longmore, S., Dunham, M., & Darling, J. 2014b, The Astrophysical Journal, 787, 113

Beaumont, C. N. & Williams, J. P. 2010, The Astrophysical Journal, 709, 791

Benjamin, R. A., Churchwell, E., Babler, B. L., Bania, T. M., Clemens, D. P., Cohen, M., Dickey, J. M., Indebetouw, R., Jackson, J. M., Kobulnicky, H. A., Lazarian, A., Marston, A. P., Mathis, J. S., Meade, M. R., Seager, S., Stolovy, S. R., Watson, C., Whitney, B. A., Wolff, M. J., & Wolfire, M. G. 2003, The Publications of the Astronomical Society of the Pacific, 115, 953

Beuther, H. & Steinacker, J. 2007, The Astrophysical Journal, 656, L85

Bisbas, T. G., Wünsch, R., Whitworth, A. P., Hubber, D. A., & Walch, S. 2011, The Astrophysical Journal, 736, 142

Blake, G. A., Sutton, E. C., Masson, C. R., & Phillips, T. G. 1987, Astrophysical Journal, 315, 621

Bowers, P. F. & Knapp, G. R. 1989, Astrophysical Journal, 347, 325

Brogan, C. L., Hunter, T. R., Cyganowski, C. J., Friesen, R. K., Chandler, C. J., & Indebetouw, R. 2011, The Astrophysical Journal Letters, 739, L16

Brott, I. & Hauschildt, P. H. 2005, in "Proceedings of the Gaia Symposium "The Three-Dimensional Universe with Gaia" (ESA SP-576). Held at the Observatoire de Paris-Meudon, 565

Busquet, G., Palau, A., Estalella, R., Girart, J. M., Sánchez-Monge, Á., Viti, S., Ho, P. T. P., & Zhang, Q. 2010, Astronomy and Astrophysics, 517, L6

Butler, M. J. & Tan, J. C. 2009, The Astrophysical Journal, 696, 484

Carey, S. J., Clark, F. O., Egan, M. P., Price, S. D., Shipman, R. F., & Kuchar, T. A. 1998, The Astrophysical Journal, 508, 721

Carey, S. J., Feldman, P. A., Redman, R. O., Egan, M. P., MacLeod, J. M., & Price, S. D. 2000, The Astrophysical Journal, 543, L157

Carey, S. J., Noriega-Crespo, A., Mizuno, D. R., Shenoy, S., Paladini, R., Kraemer, K. E., Price, S. D., Flagey, N., Ryan, E., Ingalls, J. G., Kuchar, T. A., Pinheiro Gonçalves, D., Indebetouw, R., Billot, N., Marleau, F. R., Padgett, D. L., Rebull, L. M., Bressert, E., Ali, B., Molinari, S., Martin, P. G., Berriman, G. B., Boulanger, F., Latter, W. B., Miville-Deschenes, M. A., Shipman, R., & Testi, L. 2009, Publications of the Astronomical Society of the Pacific, 121, 76

Caselli, P., Hartquist, T. W., & Havnes, O. 1997, Astronomy and Astrophysics, 322, 296

Caselli, P. & Myers, P. C. 1995, Astrophysical Journal v.446, 446, 665

Chandrasekhar, S. & Fermi, E. 1953, Astrophysical Journal, 118, 116

Chen, S. & Huang, M. 2010, Research in Astronomy and Astrophysics, 10, 777

Chira, R. A., Beuther, H., Linz, H., Schuller, F., Walmsley, C. M., Menten, K. M., & Bronfman, L. 2013, Astronomy and Astrophysics, 552, 40

Churchwell, E., Babler, B. L., Meade, M. R., Whitney, B. A., Benjamin, R., Indebetouw, R., Cyganowski, C., Robitaille, T. P., Povich, M., Watson, C., & Bracker, S. 2009, Publications of the Astronomical Society of the Pacific, 121, 213

Churchwell, E., Povich, M. S., Allen, D., Taylor, M. G., Meade, M. R., Babler, B. L., Indebetouw, R., Watson, C., Whitney, B. A., Wolfire, M. G., Bania, T. M., Benjamin, R. A., Clemens, D. P., Cohen, M., Cyganowski, C. J., Jackson, J. M., Kobulnicky, H. A., Mathis, J. S., Mercer, E. P., Stolovy, S. R., Uzpen, B., Watson, D. F., & Wolff, M. J. 2006, The Astrophysical Journal, 649, 759

Churchwell, E., Watson, D. F., Povich, M. S., Taylor, M. G., Babler, B. L., Meade, M. R., Benjamin, R. A., Indebetouw, R., & Whitney, B. A. 2007, The Astrophysical Journal, 670, 428

Cohen, M., Green, A. J., Meade, M. R., Babler, B., Indebetouw, R., Whitney, B. A., Watson, C., Wolfire, M., Wolff, M. J., Mathis, J. S., & Churchwell, E. B. 2007, Monthly Notices of the Royal Astronomical Society, 374, 979

Condon, J. J. 1992, In: Annual review of astronomy and astrophysics. Vol. 30 (A93-25826 09-90), 30, 575

Crutcher, R. M. 2012, Annual Review of Astronomy and Astrophysics, 50, 29

Cyganowski, C. J., Brogan, C. L., Hunter, T. R., & Churchwell, E. 2009, The Astrophysical Journal, 702, 1615

Cyganowski, C. J., Whitney, B. A., Holden, E., Braden, E., Brogan, C. L., Churchwell, E., Indebetouw, R., Watson, D. F., Babler, B. L., Benjamin, R., Gomez, M., Meade, M. R., Povich, M. S., Robitaille, T. P., & Watson, C. 2008, The Astronomical Journal, 136, 2391

Dale, J. E., Bonnell, I. A., & Whitworth, A. P. 2007a, Monthly Notices of the Royal Astronomical Society, 375, 1291

Dale, J. E., Clark, P. C., & Bonnell, I. A. 2007b, Monthly Notices of the Royal Astronomical Society, 377, 535

Daniel, F., Cernicharo, J., & Dubernet, M.-L. 2006, The Astrophysical Journal, 648, 461

Daniel, F., Gerin, M., Roueff, E., Cernicharo, J., Marcelino, N., Lique, F., Lis, D. C., Teyssier, D., Biver, N., & Bockelee-Morvan, D. 2013, Astronomy and Astrophysics, 560, 3

De Buizer, J. M. & Vacca, W. D. 2010, The Astronomical Journal, 140, 196

Deharveng, L., Lefloch, B., Kurtz, S., Nadeau, D., Pomarès, M., Caplan, J., & Zavagno, A. 2008, Astronomy and Astrophysics, 482, 585

Deharveng, L., Schuller, F., Anderson, L. D., Zavagno, A., Wyrowski, F., Menten, K. M., Bronfman, L., Testi, L., Walmsley, C. M., & Wienen, M. 2010, Astronomy and Astrophysics, 523, 6

Deharveng, L., Zavagno, A., & Caplan, J. 2005, Astronomy and Astrophysics, 433, 565

Devine, K. E., Chandler, C. J., Brogan, C., Churchwell, E., Indebetouw, R., Shirley, Y., & Borg, K. J. 2011, The Astrophysical Journal, 733, 44

Di Francesco, J., Andre, P., & Myers, P. C. 2004, The Astrophysical Journal, 617, 425

Draine, B. T. 2003, Annual Review of Astronomy &Astrophysics, 41, 241

Dunham, M. K., Rosolowsky, E., Evans, N. J. I., Cyganowski, C., & Urquhart, J. S. 2011, The Astrophysical Journal, 741, 110

Dyson, J. E. & Williams, D. A. 1980, New York

Egan, M. P., Shipman, R. F., Price, S. D., Carey, S. J., Clark, F. O., & Cohen, M. 1998, Astrophysical Journal Letters v.494, 494, L199

Elmegreen, B. G. & Lada, C. J. 1977, Astrophysical Journal, 214, 725

Engelbracht, C. W., Blaylock, M., Su, K. Y. L., Rho, J., Rieke, G. H., Muzerolle, J., Padgett, D. L., Hines, D. C., Gordon, K. D., Fadda, D., Noriega-Crespo, A., Kelly, D. M., Latter, W. B., Hinz, J. L., Misselt, K. A., Morrison, J. E., Stansberry, J. A., Shupe, D. L., Stolovy, S., Wheaton, W. A., Young, E. T., Neugebauer, G., Wachter, S., Pérez-González, P. G., Frayer, D. T., & Marleau, F. R. 2007, The Publications of the Astronomical Society of the Pacific, 119, 994

Everett, J. E. & Churchwell, E. 2010, The Astrophysical Journal, 713, 592

Falgarone, E., Puget, J. L., & Pérault, M. 1992, Astronomy and Astrophysics (ISSN 0004-6361), 257, 715

Fazio, G. G., Hora, J. L., Allen, L. E., Ashby, M. L. N., Barmby, P., Deutsch, L. K., Huang, J.-S., Kleiner, S., Marengo, M., Megeath, S. T., Melnick, G. J., Pahre, M. A., Patten, B. M., Polizotti, J., Smith, H. A., Taylor, R. S., Wang, Z., Willner, S. P., Hoffmann, W. F., Pipher, J. L., Forrest, W. J., McMurty, C. W., McCreight, C. R., McKelvey, M. E., McMurray, R. E., Koch, D. G., Moseley, S. H., Arendt, R. G., Mentzell, J. E., Marx, C. T., Losch, P., Mayman, P., Eichhorn, W., Krebs, D., Jhabvala, M., Gezari, D. Y., Fixsen, D. J., Flores, J., Shakoorzadeh, K., Jungo, R., Hakun, C., Workman, L., Karpati, G., Kichak, R., Whitley, R., Mann, S., Tollestrup, E. V., Eisenhardt, P., Stern, D., Gorjian, V., Bhattacharya, B., Carey, S., Nelson, B. O., Glaccum, W. J., Lacy, M., Lowrance, P. J., Laine, S., Reach, W. T., Stauffer, J. A., Surace, J. A., Wilson, G., Wright, E. L., Hoffman, A., Domingo, G., & Cohen, M. 2004, The Astrophysical Journal Supplement Series, 154, 10

Fontani, F., Cesaroni, R., & Furuya, R. S. 2010, Astronomy and Astrophysics, 517, 56

Friesen, R. K., Di Francesco, J., Shirley, Y. L., & Myers, P. C. 2009, The Astrophysical Journal, 697, 1457

Gibson, D., Plume, R., Bergin, E., Ragan, S., & Evans, N. 2009, The Astrophysical Journal, 705, 123

Gómez, L., Wyrowski, F., Pillai, T., Leurini, S., & Menten, K. M. 2011, Astronomy and Astrophysics, 529, 161

Hacar, A., Tafalla, M., Kauffmann, J., & Kovacs, A. 2013, Astronomy and Astrophysics, 554, 55

Heiderman, A., Evans, N. J. I., Allen, L. E., Huard, T., & Heyer, M. 2010, The Astrophysical Journal, 723, 1019

Helfand, D. J., Becker, R. H., White, R. L., Fallon, A., & Tuttle, S. 2006, The Astronomical Journal, 131, 2525

Hennebelle, P., Pérault, M., Teyssier, D., & Ganesh, S. 2001, Astronomy and Astrophysics, 365, 598

Henney, W. J., Arthur, S. J., de Colle, F., & Mellema, G. 2009, Monthly Notices of the Royal Astronomical Society, 398, 157

Henning, T., Linz, H., Krause, O., Ragan, S., Beuther, H., Launhardt, R., Nielbock, M., & Vasyunina, T. 2010, Astronomy and Astrophysics, 518, L95

Henshaw, J. D., Caselli, P., Fontani, F., Jiménez-Serra, I., & Tan, J. C. 2014, Monthly Notices of the Royal Astronomical Society, 440, 2860

Hernandez, A. K. & Tan, J. C. 2011, The Astrophysical Journal, 730, 44

Hernandez, A. K., Tan, J. C., Kainulainen, J., Caselli, P., Butler, M. J., Jiménez-Serra, I., & Fontani, F. 2012, The Astrophysical Journal Letters, 756, L13

Heyer, M., Krawczyk, C., Duval, J., & Jackson, J. M. 2009, The Astrophysical Journal, 699, 1092

Hirota, T., Ohishi, M., & Yamamoto, S. 2009, The Astrophysical Journal, 699, 585

Ho, P. T. P. & Townes, C. H. 1983, IN: Annual review of astronomy and astrophysics. Volume 21 (A84-10851 01-90). Palo Alto, 21, 239

Høg, E., Fabricius, C., Makarov, V. V., Urban, S., Corbin, T., Wycoff, G., Bastian, U., Schwekendiek, P., & Wicenec, A. 2000, Astronomy and Astrophysics, 355, L27

Hull, C. L. H., Plambeck, R. L., Kwon, W., Bower, G. C., Carpenter, J. M., Crutcher, R. M., Fiege, J. D., Franzmann, E., Hakobian, N. S., Heiles, C., Houde, M., Hughes, A. M., Lamb, J. W., Looney, L. W., Marrone, D. P., Matthews, B. C., Pillai, T., Pound, M. W., Rahman, N., Sandell, G., Stephens, I. W., Tobin, J. J., Vaillancourt, J. E., Volgenau, N. H., & Wright, M. C. H. 2013, arXiv.org, 6653

Indebetouw, R., Brogan, C., Chen, C. H. R., Leroy, A., Johnson, K., Muller, E., Madden, S., Cormier, D., Galliano, F., Hughes, A., Hunter, T., Kawamura, A., Kepley, A., Lebouteiller, V., Meixner, M., Oliveira, J. M., Onishi, T., & Vasyunina, T. 2013, The Astrophysical Journal, 774, 73

Indebetouw, R., Mathis, J. S., Babler, B. L., Meade, M. R., Watson, C., Whitney, B. A., Wolff, M. J., Wolfire, M. G., Cohen, M., Bania, T. M., Benjamin, R. A., Clemens, D. P., Dickey, J. M., Jackson, J. M., Kobulnicky, H. A., Marston, A. P., Mercer, E. P., Stauffer, J. R., Stolovy, S. R., & Churchwell, E. 2005, The Astrophysical Journal, 619, 931

Indebetouw, R., Robitaille, T. P., Whitney, B. A., Churchwell, E., Babler, B., Meade, M., Watson, C., & Wolfire, M. 2007, The Astrophysical Journal, 666, 321

Israel, F. P. 1978, Astronomy and Astrophysics, 70, 769

Jackson, J. M., Finn, S. C., Rathborne, J. M., Chambers, E. T., & Simon, R. 2008, The Astrophysical Journal, 680, 349

Jackson, J. M., Rathborne, J. M., Shah, R. Y., Simon, R., Bania, T. M., Clemens, D. P., Chambers, E. T., Johnson, A. M., Dormody, M., Lavoie, R., & Heyer, M. H. 2006, The Astrophysical Journal Supplement Series, 163, 145

Jiang, B., Chen, Y., Wang, J., Su, Y., Zhou, X., Safi-Harb, S., & DeLaney, T. 2010, The Astrophysical Journal, 712, 1147

Jiménez-Serra, I., Caselli, P., Fontani, F., Tan, J. C., Henshaw, J. D., Kainulainen, J., & Hernandez, A. K. 2014, Monthly Notices of the Royal Astronomical Society, 439, 1996

Jiménez-Serra, I., Caselli, P., Tan, J. C., Hernandez, A. K., Fontani, F., Butler, M. J., & Van Loo, S. 2010, Monthly Notices of the Royal Astronomical Society, 406, 187

Kauffmann, J., Pillai, T., Shetty, R., Myers, P. C., & Goodman, A. A. 2010, The Astrophysical Journal, 716, 433

Kendrew, S., Simpson, R., Bressert, E., Povich, M. S., Sherman, R., Lintott, C. J., Robitaille, T. P., Schawinski, K., & Wolf-Chase, G. 2012, The Astrophysical Journal, 755, 71

Kim, G., Lee, C. W., Kim, J., Lee, Y., Ballesteros-Paredes, J., Myers, P. C., & Kurtz, S. 2010, Journal of the Korean Astronomical Society, 43, 9

Koenig, X. P., Allen, L. E., Gutermuth, R. A., Hora, J. L., Brunt, C. M., & Muzerolle, J. 2008, The Astrophysical Journal, 688, 1142

Kroupa, P. 2001, Monthly Notices of the Royal Astronomical Society, 322, 231

Kukolich, S. G. 1967, Physical Review, 156, 83

Kurayama, T., Nakagawa, A., Sawada-Satoh, S., Sato, K., Honma, M., Sunada, K., Hirota, T., & Imai, H. 2011, Publications of the Astronomical Society of Japan, 63, 513

Lada, C. J., Alves, J., & Lada, E. A. 1999, The Astrophysical Journal, 512, 250

Lai, S.-P., Velusamy, T., Langer, W. D., & Kuiper, T. B. H. 2003, The Astronomical Journal, 126, 311

Langer, W. D. & Penzias, A. A. 1990, Astrophysical Journal, 357, 477

Lefloch, B. & Lazareff, B. 1994, Astronomy and Astrophysics (ISSN 0004-6361), 289, 559

Li, H.-b., Fang, M., Henning, T., & Kainulainen, J. 2013, Monthly Notices of the Royal Astronomical Society, 436, 3707

Lo, N., Cunningham, M. R., Jones, P. A., Bains, I., Burton, M. G., Wong, T., Muller, E., Kramer, C., Ossenkopf, V., Henkel, C., Deragopian, G., Donnelly, S., & Ladd, E. F. 2009, Monthly Notices of the Royal Astronomical Society, 395, 1021

Lockman, F. J. 1989, Astrophysical Journal Supplement Series (ISSN 0067-0049), 71, 469

Lockman, F. J., Pisano, D. J., & Howard, G. J. 1996, Astrophysical Journal v.472, 472, 173

Lu, X., Zhang, Q., Liu, H. B., Wang, J., & Gu, Q. 2014, arXiv.org, 7933

Mallick, K. K., Kumar, M. S. N., Ojha, D. K., Bachiller, R., Samal, M. R., & Pirogov, L. 2013, The Astrophysical Journal, 779, 113

Marka, C., Schreyer, K., Launhardt, R., Semenov, D. A., & Henning, T. 2012, Astronomy and Astrophysics, 537, 4

Martín-Pintado, J., Bachiller, R., & Fuente, A. 1992, Astronomy and Astrophysics, 254, 315

Morgan, L. K., Figura, C. C., Urquhart, J. S., & Thompson, M. A. 2010, Monthly Notices of the Royal Astronomical Society, 408, 157

Motoyama, K. & Yoshida, T. 2003, Monthly Notice of the Royal Astronomical Society, 344, 461

Myers, P. C. 2009, The Astrophysical Journal, 700, 1609

Oka, T., Hasegawa, T., Sato, F., Tsuboi, M., Miyazaki, A., & Sugimoto, M. 2001, The Astrophysical Journal, 562, 348

Osorio, M., Anglada, G., Lizano, S., & D'Alessio, P. 2009, The Astrophysical Journal, 694, 29

Ossenkopf, V. & Henning, T. 1994, Astronomy and Astrophysics (ISSN 0004-6361), 291, 943

Pandian, J. D., Goldsmith, P. F., & Deshpande, A. A. 2007, The Astrophysical Journal, 656, 255

Paron, S., Petriella, A., & Ortega, M. E. 2011, Astronomy and Astrophysics, 525, 132

Peretto, N. & Fuller, G. A. 2009, Astronomy and Astrophysics, 505, 405

Peretto, N., Fuller, G. A., André, P., Arzoumanian, D., Rivilla, V. M., Bardeau, S., Duarte Puertas, S., Guzman Fernandez, J. P., Lenfestey, C., Li, G. X., Olguin,

F. A., Röck, B. R., de Villiers, H., & Williams, J. 2014, Astronomy and Astrophysics, 561, 83

Pickett, H. M., Poynter, R. L., Cohen, E. A., Delitsky, M. L., Pearson, J. C., & Müller, H. S. P. 1998, Journal of Quantitative Spectroscopy and Radiative Transfer, 60, 883

Pillai, T., Wyrowski, F., Carey, S. J., & Menten, K. M. 2006a, Astronomy and Astrophysics, 450, 569

Pillai, T., Wyrowski, F., Menten, K. M., & Krügel, E. 2006b, Astronomy and Astrophysics, 447, 929

Pineda, J. E., Goodman, A. A., Arce, H. G., Caselli, P., Foster, J. B., Myers, P. C., & Rosolowsky, E. W. 2010, The Astrophysical Journal Letters, 712, L116

Pineda, J. E., Goodman, A. A., Arce, H. G., Caselli, P., Longmore, S., & Corder, S. 2011, The Astrophysical Journal Letters, 739, L2

Pomarès, M., Zavagno, A., Deharveng, L., Cunningham, M., Jones, P., Kurtz, S., Russeil, D., Caplan, J., & Comerón, F. 2009, Astronomy and Astrophysics, 494, 987

Pon, A., Johnstone, D., & Heitsch, F. 2011, The Astrophysical Journal, 740, 88

Ragan, S. E., Bergin, E. A., & Wilner, D. 2011, The Astrophysical Journal, 736, 163

Ragan, S. E., Heitsch, F., Bergin, E. A., & Wilner, D. 2012, The Astrophysical Journal, 746, 174

Ragan, S. E., Henning, T., & Beuther, H. 2013, Astronomy and Astrophysics, 559, 79

Ragan, S. E., Henning, T., Tackenberg, J., Beuther, H., Johnston, K. G., Kainulainen, J., & Linz, H. 2014, arXiv.org, 1450

Rathborne, J. M., Garay, G., Jackson, J. M., Longmore, S., Zhang, Q., & Simon, R. 2011, The Astrophysical Journal, 741, 120

Rathborne, J. M., Jackson, J. M., Chambers, E. T., Simon, R., Shipman, R., & Frieswijk, W. 2005, The Astrophysical Journal, 630, L181

Rathborne, J. M., Jackson, J. M., & Simon, R. 2006, The Astrophysical Journal, 641, 389

Rathborne, J. M., Simon, R., & Jackson, J. M. 2007, The Astrophysical Journal, 662, 1082

Reich, W., Fuerst, E., Haslam, C. G. T., Steffen, P., & Reif, K. 1984, Astronomy and Astrophysics Supplement Series (ISSN 0365-0138), 58, 197

Reid, M. J., Menten, K. M., Zheng, X. W., Brunthaler, A., Moscadelli, L., Xu, Y., Zhang, B., Sato, M., Honma, M., Hirota, T., Hachisuka, K., Choi, Y. K., Moellenbrock, G. A., & Bartkiewicz, A. 2009, The Astrophysical Journal, 700, 137

Ridge, N. A., Wilson, T. L., Megeath, S. T., Allen, L. E., & Myers, P. C. 2003, The Astronomical Journal, 126, 286

Rieke, G. H., Young, E. T., Engelbracht, C. W., Kelly, D. M., Low, F. J., Haller, E. E., Beeman, J. W., Gordon, K. D., Stansberry, J. A., Misselt, K. A., Cadien, J., Morrison, J. E., Rivlis, G., Latter, W. B., Noriega-Crespo, A., Padgett, D. L., Stapelfeldt, K. R., Hines, D. C., Egami, E., Muzerolle, J., Alonso-Herrero, A., Blaylock, M., Dole, H., Hinz, J. L., Le Floc'h, E., Papovich, C., Pérez-González,

P. G., Smith, P. S., Su, K. Y. L., Bennett, L., Frayer, D. T., Henderson, D., Lu, N., Masci, F., Pesenson, M., Rebull, L., Rho, J., Keene, J., Stolovy, S., Wachter, S., Wheaton, W., Werner, M. W., & Richards, P. L. 2004, The Astrophysical Journal Supplement Series, 154, 25

Robitaille, T. P., Meade, M. R., Babler, B. L., Whitney, B. A., Johnston, K. G., Indebetouw, R., Cohen, M., Povich, M. S., Sewilo, M., Benjamin, R. A., & Churchwell, E. 2008, The Astronomical Journal, 136, 2413

Robitaille, T. P., Whitney, B. A., Indebetouw, R., & Wood, K. 2007, The Astrophysical Journal Supplement Series, 169, 328

Robitaille, T. P., Whitney, B. A., Indebetouw, R., Wood, K., & Denzmore, P. 2006, The Astrophysical Journal Supplement Series, 167, 256

Rosolowsky, E. & Leroy, A. 2006, The Publications of the Astronomical Society of the Pacific, 118, 590

Rosolowsky, E. W., Pineda, J. E., Foster, J. B., Borkin, M. A., Kauffmann, J., Caselli, P., Myers, P. C., & Goodman, A. A. 2008, The Astrophysical Journal Supplement Series, 175, 509

Sakai, T., Sakai, N., Kamegai, K., Hirota, T., Yamaguchi, N., Shiba, S., & Yamamoto, S. 2008, The Astrophysical Journal, 678, 1049

Salpeter, E. E. 1955, Astrophysical Journal, 121, 161

Sandford, M. T. I., Whitaker, R. W., & Klein, R. I. 1982, Astrophysical Journal, 260, 183

Sanhueza, P., Garay, G., Bronfman, L., Mardones, D., May, J., & Saito, M. 2010, The Astrophysical Journal, 715, 18

Sanhueza, P., Jackson, J. M., Foster, J. B., Garay, G., Silva, A., & Finn, S. C. 2012, The Astrophysical Journal, 756, 60

Sanhueza, P., Jackson, J. M., Foster, J. B., Jiménez-Serra, I., Dirienzo, W. J., & Pillai, T. 2013, The Astrophysical Journal, 773, 123

Schilke, P., Walmsley, C. M., Pineau Des Forêts, G., & Flower, D. R. 1997, Astronomy and Astrophysics, 321, 293

Schneider, S. & Elmegreen, B. G. 1979, Astrophysical Journal Supplement Series, 41, 87

Scott, G. B. I., Freeman, C. G., & McEwan, M. J. 1997, Monthly Notices of the Royal Astronomical Society, 290, 636

Shah, R. Y. & Wootten, A. 2001, The Astrophysical Journal, 554, 933

Simon, R., Jackson, J. M., Clemens, D. P., Bania, T. M., & Heyer, M. H. 2001, The Astrophysical Journal, 551, 747

Simon, R., Jackson, J. M., Rathborne, J. M., & Chambers, E. T. 2006a, The Astrophysical Journal, 639, 227

Simon, R., Rathborne, J. M., Shah, R. Y., Jackson, J. M., & Chambers, E. T. 2006b, The Astrophysical Journal, 653, 1325

Simpson, R. J., Povich, M. S., Kendrew, S., Lintott, C. J., Bressert, E., Arvidsson, K., Maddison, S., Schawinski, K., Sherman, R., Smith, A. M., & Wolf-Chase, G. 2012, Monthly Notices of the Royal Astronomical Society, 3404

Skrutskie, M. F., Cutri, R. M., Stiening, R., Weinberg, M. D., Schneider, S., Carpenter, J. M., Beichman, C., Capps, R., Chester, T., Elias, J., Huchra, J., Liebert, J., Lonsdale, C., Monet, D. G., Price, S., Seitzer, P., Jarrett, T., Kirkpatrick, J. D., Gizis, J. E., Howard, E., Evans, T., Fowler, J., Fullmer, L., Hurt, R., Light, R., Kopan, E. L., Marsh, K. A., McCallon, H. L., Tam, R., Van Dyk, S., & Wheelock, S. 2006, The Astronomical Journal, 131, 1163

Smith, L. J., Norris, R. P. F., & Crowther, P. A. 2002, Monthly Notice of the Royal Astronomical Society, 337, 1309

Snider, K. D., Hester, J. J., Desch, S. J., Healy, K. R., & Bally, J. 2009, The Astrophysical Journal, 700, 506

Sridharan, T. K., Beuther, H., Schilke, P., Menten, K. M., & Wyrowski, F. 2002, The Astrophysical Journal, 566, 931

Stil, J. M., Taylor, A. R., Dickey, J. M., Kavars, D. W., Martin, P. G., Rothwell, T. A., Boothroyd, A. I., Lockman, F. J., & McClure-Griffiths, N. M. 2006, The Astronomical Journal, 132, 1158

Suzuki, H., Yamamoto, S., Kaifu, N., Ishikawa, S.-I., Hirahara, Y., & Takano, S. 1992, Astrophysical Journal, 392, 551

Swift, J. J. 2009, The Astrophysical Journal, 705, 1456

Tafalla, M., Myers, P. C., Caselli, P., & Walmsley, C. M. 2004, Astronomy and Astrophysics, 416, 191

Tafalla, M., Myers, P. C., Caselli, P., Walmsley, C. M., & Comito, C. 2002, The Astrophysical Journal, 569, 815

Thompson, M. A., Urquhart, J. S., Moore, T. J. T., & Morgan, L. K. 2012, Monthly Notices of the Royal Astronomical Society, 2286

Tiné, S., Roueff, E., Falgarone, E., Gerin, M., & Pineau Des Forêts, G. 2000, Astronomy and Astrophysics, 356, 1039

Tucker, K. D., Kutner, M. L., & Thaddeus, P. 1974, Astrophysical Journal, 193, L115

Turner, B. E. & Thaddeus, P. 1977, Astrophysical Journal, 211, 755

Urquhart, J. S., Hoare, M. G., Purcell, C. R., Lumsden, S. L., Oudmaijer, R. D., Moore, T. J. T., Busfield, A. L., Mottram, J. C., & Davies, B. 2009, Astronomy and Astrophysics, 501, 539

Urquhart, J. S., Morgan, L. K., Figura, C. C., Moore, T. J. T., Lumsden, S. L., Hoare, M. G., Oudmaijer, R. D., Mottram, J. C., Davies, B., & Dunham, M. K. 2011, Monthly Notices of the Royal Astronomical Society, 418, 1689

Urquhart, J. S., Thompson, M. A., Morgan, L. K., Pestalozzi, M. R., White, G. J., & Muna, D. N. 2007, Astronomy and Astrophysics, 467, 1125

Vacca, W. D., Garmany, C. D., & Shull, J. M. 1996, Astrophysical Journal v.460, 460, 914

Vasyunina, T., Linz, H., Henning, T., Zinchenko, I., Beuther, H., & Voronkov, M. 2011, Astronomy and Astrophysics, 527, 88

Walch, S., Whitworth, A., Bisbas, T., Hubber, D. A., & Wuensch, R. 2011, arXiv.org, 3478

Walsh, A. J., Burton, M. G., Hyland, A. R., & Robinson, G. 1998, Monthly Notices of the Royal Astronomical Society, 301, 640

Wang, Y., Zhang, Q., Pillai, T., Wyrowski, F., & Wu, Y. 2008, The Astrophysical Journal, 672, L33

Wang, Y., Zhang, Q., Rathborne, J. M., Jackson, J., & Wu, Y. 2006, The Astrophysical Journal, 651, L125

Watson, C., Hanspal, U., & Mengistu, A. 2010, The Astrophysical Journal, 716, 1478

Watson, C., Povich, M. S., Churchwell, E. B., Babler, B. L., Chunev, G., Hoare, M., Indebetouw, R., Meade, M. R., Robitaille, T. P., & Whitney, B. A. 2008, The Astrophysical Journal, 681, 1341

Whitney, B. A., Indebetouw, R., Bjorkman, J. E., & Wood, K. 2004, The Astrophysical Journal, 617, 1177

Whitworth, A. P., Bhattal, A. S., Chapman, S. J., Disney, M. J., & Turner, J. A. 1994, Monthly Notices of the Royal Astronomical Society, 268, 291

Williams, J. P., de Geus, E. J., & Blitz, L. 1994, The Astrophysical Journal, 428, 693

Wilson, T. L., Rohlfs, K., & Hüttemeister, S. 2009, Tools of Radio Astronomy

Wood, D. O. S. & Churchwell, E. 1989, Astrophysical Journal Supplement Series (ISSN 0067-0049), 69, 831

Wood, D. O. S., Myers, P. C., & Daugherty, D. A. 1994, Astrophysical Journal Supplement Series (ISSN 0067-0049), 95, 457

Xu, J.-L., Wang, J.-J., & Liu, X.-L. 2013, Astronomy and Astrophysics, 559, 113

Ybarra, J. E., Lada, E. A., Balog, Z., Fleming, S. W., & Phelps, R. L. 2010, The Astrophysical Journal, 714, 469

Zavagno, A., Anderson, L. D., Russeil, D., Morgan, L., Stringfellow, G. S., Deharveng, L., Rodón, J. A., Robitaille, T. P., Mottram, J. C., Schuller, F., Testi, L., Billot, N., Molinari, S., di Gorgio, A., Kirk, J. M., Brunt, C., Ward-Thompson, D., Traficante, A., Veneziani, M., Faustini, F., & Calzoletti, L. 2010a, Astronomy and Astrophysics, 518, L101

Zavagno, A., Deharveng, L., Comerón, F., Brand, J., Massi, F., Caplan, J., & Russeil, D. 2006, Astronomy and Astrophysics, 446, 171

Zavagno, A., Pomarès, M., Deharveng, L., Hosokawa, T., Russeil, D., & Caplan, J. 2007, Astronomy and Astrophysics, 472, 835

Zavagno, A., Russeil, D., Motte, F., Anderson, L. D., Deharveng, L., Rodón, J. A., Bontemps, S., Abergel, A., Baluteau, J.-P., Sauvage, M., André, P., Hill, T., & White, G. J. 2010b, Astronomy and Astrophysics, 518, L81

Zhang, S. B., Yang, J., Xu, Y., Pandian, J. D., Menten, K. M., & Henkel, C. 2011, The Astrophysical Journal Supplement, 193, 10

Zinnecker, H. & Yorke, H. W. 2007, Annual Review of Astronomy and Astrophysics, 45, 481

Zuckerman, B. 1973, Astrophysical Journal, 183, 863